Natural Radioactive Background Suppression in ^{76}Ge Neutrinoless Double-β Decay Experiments

Nicholas W. Ruof

A dissertation
submitted in partial fulfillment of the
requirements for the degree of

Doctor of Philosophy

University of Washington

2023

Reading Committee:
Jason Detwiler, Chair
Alvaro Chavarria
Stephen Sharpe

Program Authorized to Offer Degree:
Physics

University of Washington

Abstract

Natural Radioactive Background Suppression in ^{76}Ge Neutrinoless Double-β Decay Experiments

Nicholas W. Ruof

Chair of the Supervisory Committee:
Title of Chair Jason Detwiler
Department of Chair

The observation of neutrino oscillations showed that neutrinos have mass and provides direct evidence that the Standard Model of particle physics is an incomplete theory of the universe at the fundamental scale. As a neutral fermion, the neutrino is the only known particle in the Standard Model that could have a Majorana mass. A particle with a Majorana mass is indistinguishable from its anti-particle and gives the possibility for lepton number flavor violating reactions to occur. The observation of a Majorana neutrino would demonstrate lepton number flavor violation of two, which is necessary to support the baryogenesis through leptogenesis model; a compelling theory that offers an explanation for the preferred production of matter over anti-matter in the early universe. The most practical way to discover a Majorana neutrino is through the observation of neutrinoless double-β decay ($0\nu\beta\beta$). $0\nu\beta\beta$ decay is a process where a nucleus that prefers to undergo double-β decay over single β decay emits two electrons and no neutrinos. Current experiments have set the largest lower half-life limits for $0\nu\beta\beta$ decay on the order of 10^{26} years. The next generation ^{76}Ge experiment, LEGEND-1000, plans to be sensitive to half-lifes on the order of 10^{28} years. To reach these half-life sensitivities much research and development has been done on current generation, LEGEND-200, and previous generation, Majorana Demonstrator and GERDA, ^{76}Ge experiments to determine the optimal technology and data analysis methods for LEGEND-1000. This

work will discuss pulse shape analysis contributions to the MAJORANA DEMONSTRATOR's final result half-life sensitivity of 8.3×10^{25} years and silicon photomultiplier characterization results relevant for understanding the efficiency of the LEGEND style liquid argon veto.

TABLE OF CONTENTS

LIST OF FIGURES

Figure Number Page

LIST OF TABLES

GLOSSARY

PMNS: Pontecorvo-Maki-Nakagawa-Sakata

C: Charge

CP: Charge-Parity

CMB: Cosmic Microwave Background

$2\nu\beta\beta$: Two Neutrino Double Beta Decay

2νECEC: Two Neutrino Double Electron Capture

$0\nu\beta\beta$: Neutrinoless Double Beta Decay

EDF: Energy Density Functional Theory

IBM: Interacting Boson Model

NSM: Nuclear Shell Model

$Q_{\beta\beta}$: Q-value of neutrinoless double beta decay

ROI: Region of Interest

QRPA: Quasi-Particle Random-Phase Approximation

SURF: Sanford Underground Research Facility

HPGE: High Purity Germanium Detector

GERDA: Germanium Detector Array

LNGS: INFN Gran Sasso National Laboratory

FWHM: Full Width Half Maximum

BEGE^{TM}: Broad Energy Germanium

PPC: P-type Point Contact

ICPC: Inverted Coaxial Point Contact

LMFE: Low Mass Front End

TRAPENF: Uncalibrated Energy

TRAPENFCAL: Calibrated Energy

TRAPENFCALC: Calibrated Energy with stability correction

FINAL_ENERGY: trapENFCalC with fixed time pickoff correction

AVSE: Multi-site Discrimination Parameter

DCR: Delayed Charge Recovery Parameter

LQ: Late Charge Parameter

BI: Background Index

FEP: Full Energy Peak

DEP: Double Escape Energy Peak

SEP: Single Escape Energy Peak

CC: Compton Continuum

CM: Continuum Mode

MS: Multi-site Sector

LEGEND: Large Enriched Germanium Experiment for Neutrinoless Double $\beta\beta$ Decay

LEGEND-200: LEGEND phase with 200 kg of Germanium Detectors

LEGEND-1000: LEGEND phase with 1000 kg of Germanium Detectors

PEN: Polyethylene Naphthalate

LAR: Liquid Argon

WLS: Wavelength Shifting

SIPM: Silicon Photomultiplier

VUV: Vacuum Ultraviolet

TPB: Tetraphenyl Butadiene

PMMA: Polymethylmethacrylate

PDE: Photon Detection Efficiency

APD: Avalanche Photodiode

SPAD: Single Photon Avalanche Diode

DICT: Direct Cross-Talk

DECT: Delayed Cross-Talk

AP: Afterpulsing

LED: Light Emitting Diode

SIMT: single instruction multiple thread

ACKNOWLEDGMENTS

Pursuing a PhD is a huge challenging commitment and I wouldn't have made it this far without the support I've received from my colleagues, close friends, and family. Jason has been an incredible advisor and mentor in guiding my scientific curiosity and development as a research scientist. Thank you Jason for giving me the opportunity and confidence to build my own experiment and contribute a crucial part to the MAJORANA analysis. When I first joined the group I was welcomed by Julieta Gruszko, Micah Buuck, and Ian Guinn who showed me how everything worked in the lab. I'd like to thank Walter for assisting me on my lab work, especially in the beginning when I had no idea what I was doing, and being an engaging mentor in pushing MAJORANA DEMONSTRATOR to its final major result. This work wouldn't have been possible without the generous support of the CENPA Staff: Tim Van Wechel, David Peterson, Tom Burritt, Gary Holman, and Ida Boeckstiegel. It's been a pleasure to work along side my office mate and close friend in the MAJORANA group, Alex Hostiuc. We really had to push through together the last couple of years to wrap up the Majorana analysis and we made it.

Over summer 2021, I worked at Modern Electron to explore my career options for the future. I'd like to thank the Modern Electron team for giving me the opportunity to work in their computational physics group. I learned so many things about efficient teamwork and leadership and what motivates me to do physics research. Roelof Groenewald was a great mentor in helping me find and work towards my career goals. Collaborating with Kevin Zhu on the computational team was a pleasure and thank you for showing me how the computer science pros do it.

During my PhD I was still involved with the UW music programs, Studio Jazz Ensemble

and Husky Alumni Band, which I definitely needed when things got very stressful. My long time friends in the Husky Trombone section Neal Peck, Charles Tilander, Jorge Castillo, Alex Le, Shanley Sabo, and Sam Sunseri were always there for Saturday home football games and are some of the most memorable times I've had while here at UW. I lived with a great group of roommates from the physics department: Mike Smith, Tyler Blanton, Seth Hirsh, Sean Gasiorowski, Paul Malinowski, and Kevin Zhao from computer science. Our house was always the one that brought everybody in our class together for potlucks, Thanksgiving, and the Super Bowl.

I've been at UW for quite a while, since the beginning of my undergraduate years, and Steve Sharpe who is on my committee has been there all the way. He's the first professor I got to know in the physics department and I wouldn't be here down this career path without his support. I owe it to my high school chemistry teacher Vincent Ward for inspiring my curiosity for the strange things that make the universe work. To my family, Mom, Dad, and my brother Erik, this has been a long journey of love, care, and support and I can't thank you enough for shaping me into the person I've grown up to be.

DEDICATION

For Mom, Dad, Erik, and Gladys

Chapter 1

INTRODUCTION

One of the most thought-provoking questions is where do we come from. It's a profound question that can lead to many different answers, depending on how far back in the universe's history you wish to go. Most, if not all, of the protons at the core of each chemical element that comprises us has existed since a few minutes after the Big Bang, 13.8 billion years ago. At that point the universe was cool enough for quarks and gluons to bind under the strong force and produce baryons, of which the proton is the most stable. However, there is no established mechanism that can predict the number of total number of baryons in the present day observable universe, given the known laws of physics that would have existed in the early universe. In all observed fundamental-particle interactions total lepton number and baryon number are always conserved. Baryon number is the total sum of quarks minus anti-quarks divided by three and lepton number is the total sum of leptons minus the total sum of anti-leptons within one generation. After cosmic inflation ($10^{-32} - 10^{-5}$ s), a mechanism must exist that emerges out of thermal equilibrium in the early universe and violates C and CP symmetry as well as baryon number. Of these symmetries only CP symmetry has been observed to be violated within the Standard Model. This leads to the addition of a heavy right-handed Majorana mass neutrinos to the Standard Model, which initiate the production of a baryon/anti-baryon asymmetry from producing a lepton/anti-lepton asymmetry through C and CP violating decays. With the help of anomalous electroweak processes already within the standard model theory, a lepton/anti-lepton asymmetry can be converted into a baryon/anti-baryon asymmetry since such processes are predicted to conserve baryon number minus lepton number.

The neutrino is the most common fundamental, massive particle in the observable uni-

verse, and arguably the most bizarre. It's mass scale is incredibly tiny, it oscillates between different flavors, and it hardly interacts with other forms of matter. Neutrinos participate in nuclear fusion interactions that power the stars and Type-II supernovae, which are a source for producing elements heavier than iron in the periodic table. Neutrinos also participate in radioactive decay that helps sustain the Earth's molten core. The motion of liquid iron in the core generates the Earth's magnetic field that the planet's surface from cosmic radiation and ejections of high energy charged particles from the sun. Measuring and understanding the neutrino's properties has led us to a greater understanding of the universe's properties we interact with and depend on in our everyday life.

Two of the leading unknowns about neutrinos are their masses and whether they are their own anti-particles or not. Neutrinos are neutrally charged, unlike electrons and protons, so describing their antimatter counterpart is not straightforward. However, if it turns out the neutrino is its own anti-particle, that would have profound implications for how we understand the formation of the matter excess in the early universe. It could also help explain why neutrinos are so light compared to all the other known fundamental particles. A neutrino indistinguishable from its own anti-particle is allowed to have a Majorana mass, a property that allows a neutrino to annihilate with another neutrino just like any other matter/antimatter pair. In the early universe, a heavy Majorana neutrino can disassociate out of thermal equilibrium and decay in such a way to produce the observed matter/antimatter asymmetry in the present observable universe. All of this can be explained through the addition of a heavy Majorana neutrino and is the most attractive explanation because the necessary extension to the Standard Model of particle physics is the most simple. The addition of a heavy Majorana neutrino that exists at the energy scale of the early universe would support many theoretical extensions to the standard model that already predict neutrinos to be Majorana particles.

The discovery of a Majorana neutrino would require the observation of neutrinoless double-β decay, a hypothetical process where double-β decay occurs in a radioactive isotope that emits two electrons and no neutrinos. The challenge with this observation is that

theoretically predicted half-lifes for this process can be on the order of $10^{26} - 10^{30}$ years and experiment run times to measure half-life limits of those magnitudes can be on the order of a decade. In addition, signals from natural radioactivity can obscure such a rare signal and increase the amount of run time necessary to observe a significant number of events above a certain background level. Therefore, the goal of a neutrinoless double-β decay experiment is to create an apparatus that is large enough to measure long half-life limits and background-free enough to be able to accomplish this within a reasonable time frame; i.e. no more than a decade.

This chapter gives an overview of the predictions and discoveries throughout history that led to everything that is known about the neutrino to date. Then following is a discussion on how a neutrino mass mechanism would work in quantum field theory and how Majorana neutrinos can initiate the matter/antimatter asymmetry production in the early universe. The chapter then closes with an overview of neutrinoless double-β decay and how one would construct an experiment to search for it.

1.1 Brief History on the Neutrino

In the early 20^{th} century, notable scientists including Henri Becquerel, Ernest Rutherford, and Marie Curie discovered and probed the properties of nuclear radioactive decay [1, 2, 3]. Three decay mechanisms were discovered:

- α-decay: An atomic nucleus emits a bound state of two protons and two neutrons, or a helium nucleus, and leaves behind an atom with two less protons and two less neutrons. Mean free path in air is approximately 1 inch.

- β-decay : An atomic nucleus emits a high-energy electron when a neutron is converted into a proton or a high-energy positron when a proton is converted to a neutron. Mean free path is approximately several yards in air and about 1.5 inch into skin.

- γ-decay: After α-decay or β-decay the daughter nucleus can be left in an excited state

and then decay to a lower energy state by emitting a high-energy photon. Mean free path is approximately tens of yards in air. The γ's can usually be stopped by several inches of heavy material like lead or concrete.

It was observed that α-decay and γ-decay produced mono-energetic signatures, however energy measurements of emitted β particles produced a continuous energy spectrum. This is unexpected if you assume a two body decay where the emitted particle's energy is equal to the difference in energy of the initial and final nuclear states. However, this is expected if some additional undetected particle is taking away a fraction of the total energy of the emitted β due to conservation of momentum and conservation of energy. In 1930, Wolfgang Pauli postulated the existence of a light neutral particle that would be emitted in addition to a high-energy electron [4].

Later in 1934, Enrico Fermi proposed his theory of point-like weak interactions and named the light neutral particle the "neutrino" [5]. Fermi's theory also allowed for inverse-β decay:

$$\nu_e + \mathrm{n} \longrightarrow \mathrm{p} + e^-$$
$$\overline{\nu}_e + \mathrm{p} \longrightarrow \mathrm{n} + e^+$$

Inverse-β decay provided a way for physicists to measure the cross-section of a process that involved the capture of a neutrino. Inverse-β decay was proposed by Hans Bethe and Rudolf Peierls in 1934 and they calculated the reaction cross-section to be less than 10^{-44} cm^2, thus concluding that "It is therefore absolutely impossible to observe processes of this kind with neutrinos created in nuclear transformations"[6]. In 1956, neutrinos were first observed in the Savannah River Experiment by Frederick Reines and Clyde L. Cowan Jr. They measured the inverse-β decay cross-section from nuclear reactor neutrinos incident on proton targets in water [7]. It was not known at the time, but Reines and Cowan discovered what would be called the electron anti-neutrino.

Weak nuclear reactions were further probed after the discovery of the neutrino. In 1956, Chien-Shiung Wu discovered that decays of polarized ^{60}Co atoms preferentially emitted β

particles opposite the nuclear spin, indicating the weak force is maximally parity violating [8]. Later in 1957, Goldhaber et al. determined the helicity of the neutrino to be left-handed by measuring the photon's helicity and neutrino's momentum in the decay of ^{152m}Eu [9]. Helicity refers to the projection of a particle's spin onto its momentum. A right-handed particle is one where the projected spin is in the same direction as the momentum and a left-handed particle is where the projected spin is in the opposite direction of the momentum. ^{152m}Eu decays via electron capture to an electron neutrino and an excited state of ^{152}Sm, notated as ^{152}Sm*. Since ^{152m}Eu and ^{152}Sm both have angular momentum $J = 0$, if the decay products are constrained to be back-to-back, then the emitted γ-ray will have the same helicity as the emitted neutrino, see Fig. 1.1.

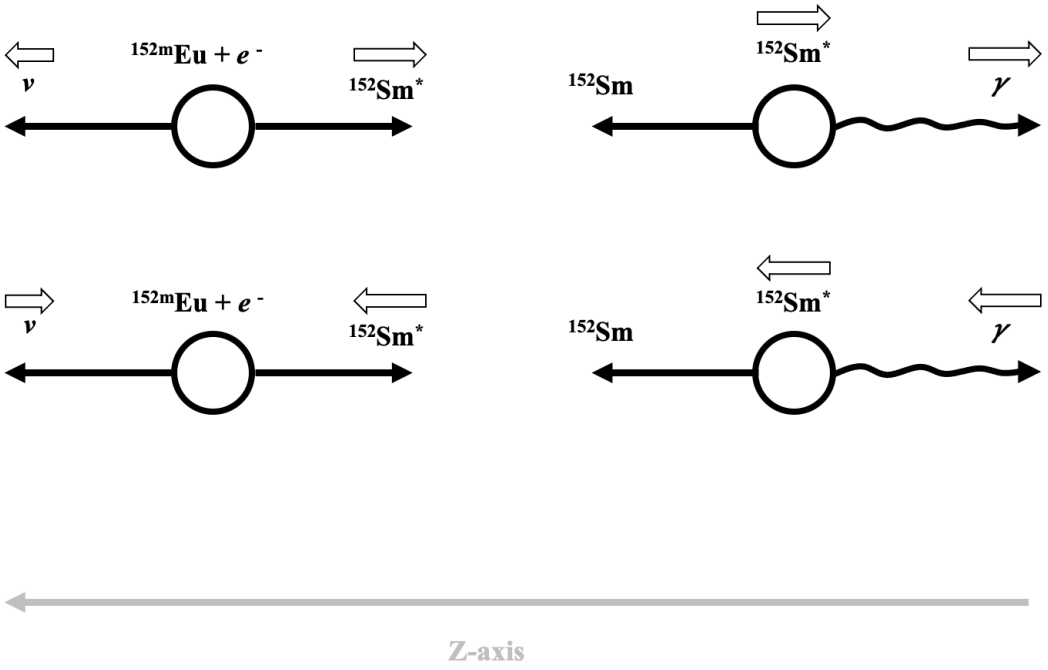

Figure 1.1: ^{152m}Eu ($J = 0$) decays to ^{152}Sm* ($J = 1$) through electron capture and ^{152}Sm* de-excites to ^{152}Sm ($J = 0$) by emitting a 960 keV γ-ray. If the γ-ray is emitted back-to-back with the neutrino, the two particles will have the same helicity. Solid arrows indicate momentum direction and hollow arrows indicate spin direction and magnitude.

In the experiment, back-to-back neutrino and γ-ray configurations are selected by allowing the γ-ray to be absorbed and re-emitted by a Sm_3O_2 scatterer into a Na-I detector. This preferentially selects emitted γ-rays from ^{152m}Sm parent nuclei moving towards the scatterer due to increased energy from the Doppler shift. The Eu_2O_3 source is placed inside of a magnet with the ability to switch its polarization to preferentially select the γ-ray helicity. It was found that the experiment detected more photons from a negative helicity γ-ray consistent with a left-handed neutrino.

In 1970 a similar experiment found that antineutrinos are only observed to be right-handed [10, 11]. These observations seemed to confirm the hypothesis that neutrinos were massless, which was considered by Abdus Salam and Lev Landau in 1957 as the simplest case for maximally parity-violating weak-interactions [12, 13]. In general, mass terms in the standard model theory couple left-handed and right-handed chiral fields, which is forbidden under gauge transformations of the electroweak symmetry group. This was resolved by introducing spontaneous electroweak symmetry breaking through the Higgs Mechanism in 1964 [14, 15, 16]. The Higgs Boson was first observed by ATLAS and CMS at the Large Hadron Collider in 2012 [17, 18]. Charged leptons and quarks then obtain a mass through the coupling of the left-handed and right-handed chiral states to the nonzero Higgs vacuum expectation value. However, if the neutrino is only left-handed and the anti-neutrino is only right-handed there is no corresponding field with opposite handedness to produce a neutrino mass in the Standard Model.

Electron neutrinos were the only neutrinos known to exist until in 1962 at the Brookhaven National Lab's Alternating Gradient Synchrotron (AGS) the muon neutrino was discovered [19]. Pions decay via the muon channel with nearly 100% branching ratio and the resulting neutrinos from this process only produced muons via inverse-μ decay, suggesting that each lepton had a unique neutrino partner with the same flavor. The τ lepton was discovered in the mid 1970's and the τ neutrino was later first observed by the DONUT collaboration in 2000 [20, 21].

As a main sequence star, the majority of the sun's energy is produced by thermonuclear

fusion through the proton-proton chain and is comprised of several branches that contribute to the fusion of hydrogen into helium. For the proton-proton branch III process, the decay of ^{8}B produces $\sim$ 14 MeV high energy neutrinos that would be detectable from terrestrial experiments and serve as a direct test of the Standard Solar Model [22]. Neutrinos were and are currently the only way to observe nuclear reactions inside a star's core due to their extremely small interaction cross-section. From 1965 to 1967 at the Homestake Mine in Lead, South Dakota, Ray Davis led the construction of the Homestake Solar Neutrino Observatory that would measure this solar neutrino flux from the inverse-β decay reaction.

$$\nu_e + {}^{37}\mathrm{Cl} \longrightarrow {}^{37}\mathrm{Ar} + e^-$$

This experiment consisted of 100,000 gallons of tetrachloroethylene C_2Cl_4 that served as the solar neutrino target and the resulting ^{37}Ar was extracted and counted using proportional counters. The experiment observed the solar electron neutrino flux to be significantly lower than the solar model prediction, nearly a factor of three times less [23]. This indicated two possibilities: the Standard Solar Model did not correctly reproduce the neutrino flux from the Sun or some fraction of neutrinos were somehow going undetected. If the Standard Solar Model was correct, then neutrinos could have been avoiding detection by changing flavor (e, μ, τ) while traveling through space-time.

The first theoretical model of neutrino flavor oscillation was developed by Maki Ziro, Nakagawa, and Sakata Shoichi in 1962 based on Bruno Pontecorvo's first conception of the phenomenon in 1957 [24]. This work established a two-neutrino-flavor mixing model, which was later extended to a three neutrino flavors model analogous to the CKM matrix parameterization formulated in 1984 [25, 26]. In a two-neutrino-flavor mixing model, the neutrino is emitted in a flavor state from weak currents, but propagates through space-time as a superposition of two neutrino mass eigenstates ν_1 and ν_2,

$$\begin{bmatrix} \nu_e \\ \nu_\mu \end{bmatrix} = \begin{bmatrix} \cos(\theta) & -\sin(\theta) \\ \sin(\theta) & \cos(\theta) \end{bmatrix} \begin{bmatrix} \nu_1 \\ \nu_2 \end{bmatrix} . \tag{1.1}$$

Neutrino flavor oscillation results from the interference in the mass eigenstate phases evolving at different rates through time. This occurs theoretically when applying the free-propagation Hamiltonian to the mass eigenstates and the probability of oscillation becomes a function of the mixing angle θ and the mass difference $|m_2 - m_1| = \Delta m$ between the states,

$$P_{\nu_e \to \nu_e} = |\langle \nu_e | \nu_e(L) \rangle|^2 = 1 - \sin^2(2\theta) \sin^2 \left(\frac{\Delta m^2 L}{4E} \right) . \tag{1.2}$$

L is the distance traveled and E is the total neutrino energy.

The deficit of ^{8}B solar neutrinos was confirmed in 1989 by Kamiokande-II, and later seen with low energy neutrinos from the GALLEX and SAGE experiments in the early 1990's [27, 28, 29]. The first indication of possible neutrino oscillation came from the Super Kamiokande experiment, which observed the ν_μ flux from cosmic rays to vary with zenith angle with respect to the ν_e flux [30]. Muon neutrino deficits were then later confirmed by the K2K long baseline accelerator neutrino experiment by measuring a muon neutrino deficit from a controlled accelerator beamline [31]. The solar neutrino deficit wasn't solved until 2001 when the Sudbury Neutrino Observatory (SNO) observed the flavor transformation of ^{8}B solar neutrinos by comparing charged-current, neutral current, and elastic scattering interactions [32]. This confirmed that Super Kamiokande observed ν_μ oscillation.

$$\nu_e + d \longrightarrow p + p + e^- \qquad \text{(CC)} \tag{1.3}$$

$$\nu_x + d \longrightarrow p + n + \nu_x \qquad \text{(NC)} \tag{1.4}$$

$$\nu_x + e^- \longrightarrow \nu_x + e^- \qquad \text{(ES)} \tag{1.5}$$

Neutral current (NC) and elastic scattering (ES) measurements are sensitive to all neutrino flavors, and the number of events occurring from these interactions were observed to agree with the predicted neutrino flux from the Standard Solar Model. NC interactions occur with all neutrinos through the Z^0 boson, while ES interactions occur with all neutrinos through the Z^0 boson and additionally with the W^- for electron neutrinos. Charged-current (CC)

interactions produced a deficit that agreed with previous experiments and confirmed that solar electron neutrinos had transformed into muon and tau flavors, thus going undetected. The observation of neutrino oscillation demonstrated that neutrinos have mass and lepton flavor number is only conserved when the ratio of distance traveled to total energy is small, which is satisfied in most particle physics experiments.

1.2 Neutrino Mass

The three known electroweak neutrino flavor states can be expressed in the mass basis using the Pontecorvo-Maki-Nakagawa-Sakata (PMNS) Matrix, with the conventional decomposition in Eq. 1.6

$$U = \begin{bmatrix} 1 & 0 & 0 \\ 0 & c_{23} & s_{23} \\ 0 & -s_{23} & c_{23} \end{bmatrix} \begin{bmatrix} c_{13} & 0 & s_{13}e^{-i\delta} \\ 0 & 1 & 0 \\ -s_{13}e^{i\delta} & 0 & c_{13} \end{bmatrix} \begin{bmatrix} c_{12} & s_{12} & 0 \\ -s_{12} & c_{12} & 0 \\ 0 & 0 & 1 \end{bmatrix} \begin{bmatrix} e^{i\alpha_1/2} & 0 & 0 \\ 0 & e^{i\alpha_2/2} & 0 \\ 0 & 0 & 1 \end{bmatrix} \tag{1.6}$$

The c_{ij} and s_{ij} are the cosines and sines of the mixing angle between mass eigenstate i and mass eigenstate j. δ is a CP violating phase and α_1 and α_2 are phase factors that become physically meaningful if the neutrino is a Majorana particle. Table 1.1 shows the current known values from neutrino oscillation experiments.

The current unresolved parameters are the sign of Δm_{31} and the values of δ, α_1, and α_2. Since the value of Δm_{31} is not precisely known, this gives two possible orderings for the neutrinos masses, see Fig. 1.2. Global analyses combining data from recent neutrino experiments seems to slightly prefer the normal ordering, but more research must be done to demonstrate that this is the case [34]. δ, the CP-violating phase, describes the difference in probabilities for neutrino oscillation and anti-neutrino oscillation. $\delta = 0, \pi$ gives oscillation probabilities that are the same for neutrinos and anti-neutrinos where as other values give unequal probabilities. The latest 3σ confidence intervals for the parameter, made by the T2K collaboration, are $\delta = [-3.14, -0.03]$ for the normal ordering and $\delta = [-2.54, -0.32]$ for the inverted ordering [35]. The Majorana phases α_1 and α_2 are entirely unknown and can only

	Normal Ordering	Inverted Ordering
$\sin^2(\theta_{12})$	$0.307^{+0.013}_{-0.012}$	$0.307^{+0.013}_{-0.012}$
$\sin^2(\theta_{23})$	0.546 ± 0.021	0.539 ± 0.022
$\sin^2(\theta_{13})/10^{-2}$	2.20 ± 0.07	2.20 ± 0.07
$\frac{\Delta m^2_{21}}{10^{-5}\text{eV}^2}$	7.53 ± 0.18	7.53 ± 0.18
$\frac{\Delta m^2_{3l}}{10^{-3}\text{eV}^2}$	$+2.453 \pm 0.033$	-2.536 ± 0.034

Table 1.1: Measured parameters in the PMNS matrix from neutrino oscillation experiments. For normal ordering $\Delta m^2_{3l} = \Delta m^2_{31} > 0$ and for the inverted ordering $\Delta m^2_{3l} = \Delta m^2_{32} < 0$ as shown in Fig. 1.2. The sign of Δm^2_{21} is positive is known from the MSW effect. Data from the Particle Data Group [33].

be inferred from the observation of lepton number violating processes such as neutrinoless double-β decay, 1.4.

Neutrinos are unique in that they are the only known fundamental, neutral fermions. This gives the option for neutrinos to have different kinds of mass. In general, a spin-1/2 fermion can be described by the following Lagrangian, excluding standard model interactions other than the Higgs Mechanism

$$\mathscr{L} = \overline{\psi}(i \overleftrightarrow{\partial\!\!\!/} - m)\psi \,, \tag{1.7}$$

where $\overleftrightarrow{\partial}_\mu = \frac{\overrightarrow{\partial}_\mu - \overleftarrow{\partial}_\mu}{2}$. $\overrightarrow{\partial}_\mu$ is applied to the right and $\overleftarrow{\partial}_\mu$ is applied to the left. For a massive spin-1/2 fermion, the quantity ψ is a 4-dimensional object composed of two 2-component spinors, also called a *bispinor*. 2-component spinors are the simplest nontrivial representations of the Lorentz group and are the fundamental quantities for constructing the Lagrangian [36]. A bispinor can be broken down into it's chiral components ((1/2, 0) and (0, 1/2)), which transform differently under a Lorentz boost. These are noted as right-handed

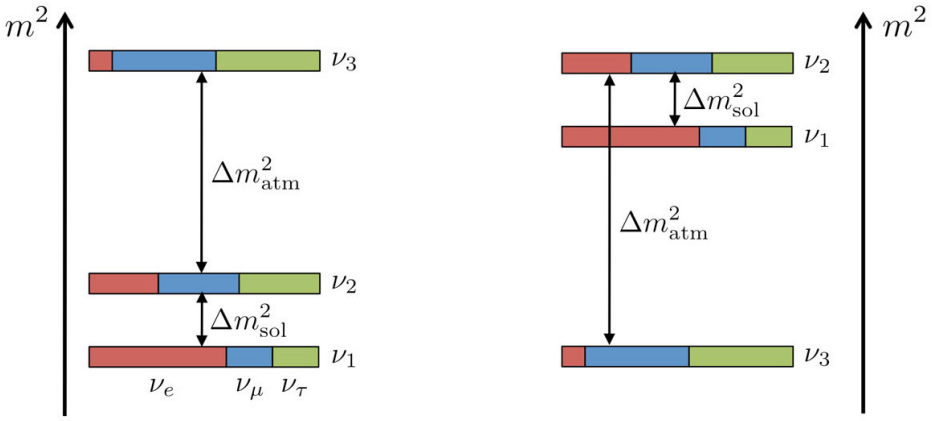

Figure 1.2: Given the known mass differences between the neutrino energy states, there are two possible orderings for the neutrino masses: Normal Ordering (left) and Inverted Ordering (right). *Image Credit: JUNO Collaboration*

and left-handed chiral components of ψ,

$$\mathscr{L} = (\overline{\psi_R} + \overline{\psi_L})(i \overleftrightarrow{\partial\!\!\!/} - m)(\psi_R + \psi_L) \tag{1.8}$$

$$= \overline{\psi_R} i \overleftrightarrow{\partial\!\!\!/} \psi_R + \overline{\psi_L} i \overleftrightarrow{\partial\!\!\!/} \psi_L - m(\overline{\psi_R}\psi_L + \overline{\psi_L}\psi_R)\,. \tag{1.9}$$

Solving the Euler-Lagrange equations yields the following field solutions,

$$i\partial\!\!\!/\psi_R = m\psi_L \tag{1.10}$$

$$i\partial\!\!\!/\psi_L = m\psi_R\,. \tag{1.11}$$

In the Lagrangian the chiral fields are coupled by a mass term, therefore the space-time evolutions of the chiral fields are related by the mass m. If the mass is zero then ψ can be described by a single chiral field, or *Weyl spinor*, like in the case of the massless neutrino. In Eq. 1.9, a mass term that couples a left-handed chiral component with a right-handed chiral component that are independent from each other is called a *Dirac mass*. Dirac masses are given to the charged fermions in the Standard Model through Yukawa couplings to the Higgs field.

In 1937 Ettore Majorana proposed an alternative theory in which a massive spin-1/2 fermion can be described by a single spinor instead of a bispinor [37]. In order for this to be the case the left-handed and right-handed chiral components of the fermion field must be dependent on each other, and thus can be expressed through one instead of two field equations. This is achieved by setting $\psi_R = C\overline{\psi_L}^T$, where C represents charge conjugation,

$$\psi = \psi_L + C\overline{\psi_L}^T \tag{1.12}$$

$$i\partial\!\!\!/\psi_L = mC\overline{\psi_L}^T . \tag{1.13}$$

In the case of Eq. 1.12, the charge conjugation of ψ results in ψ, which demonstrates that for a field described by the Majorana relation particle and anti-particle are indistinguishable. Only neutral fermions can be described by such a relation otherwise charge conservation, or the $U(1)$ symmetry within electroweak interactions, would be violated. When a mass term couples a chiral field with its charge conjugate this is called a *Majorana mass*.

In principle, a neutrino can have both a Dirac mass and a Majorana mass, given that a right handed neutrino exists to produce the Dirac mass. A Dirac mass would be produced by the Higgs mechanism whereas a Majorana mass must come from beyond-standard-model processes because the lowest dimension Lagrangian term that can produce a Majorana mass is non-renormalizable. Accounting for only one generation, a neutrino mass in the Lagrangian can be expressed as

$$\mathscr{L}_{\text{mass}} = -m_D\overline{\nu_R}\nu_L + \frac{1}{2}m_L\nu_L^T C^\dagger \nu_L + \frac{1}{2}m_R\nu_R^T C^\dagger \nu_R + \text{H.c.}\,. \tag{1.14}$$

where H.c. represents the Hermitian conjugate. At the electroweak symmetry-breaking scale the Dirac mass terms can be expressed in terms of the Higgs field coupling the left-handed lepton doublet with the right-handed neutrino singlet:

$$\mathscr{L}_{\text{mass}} = -y^\nu\left(\overline{\nu_R}\tilde{\Phi}^\dagger L_L + \overline{L_L}\tilde{\Phi}\nu_R\right) + \frac{1}{2}m_R\left(\nu_R^T C^\dagger \nu_R + \overline{\nu}_R^\dagger C\nu_R^*\right) . \tag{1.15}$$

It is common to set m_L to zero since a non-zero value would leave a Higgs interaction with the lepton doublet that violates hypercharge conservation. To avoid this one must construct

a dimension 5 element in the mass Lagrangian, which is non-renormalizable. The Dirac mass of the neutrino would be related by a Yukawa coupling constant and the Higgs vacuum expectation value.

$$m_D = \frac{y^\nu v}{\sqrt{2}} \tag{1.16}$$

The Dirac mass of the neutrino comes out in a similar form to the Dirac masses induced for the other leptons, which is odd considering the neutrino is observed to have a mass many orders of magnitude smaller, see Fig 1.3. The current upper limit for the effective neutrino mass from tritium β-decay is set by KATRIN at less than 0.8 eV [38]. For a Dirac neutrino, this requires a coupling constant that is approximately six orders of magnitude less than their flavored lepton partners, which seems unnatural given there is no obvious physical motivation for why the Yukawa coupling constants would be different. Another possibility is that the Yukawa coupling constants for the neutrinos are the same as their lepton partners, but the masses are effectively suppressed at the electroweak scale due to the presence of heavy right-handed Majorana neutrinos at the grand unified energy scale. This is often referred to as the Type-I seesaw mechanism. For this scenario, the neutrino mass Lagrangian can be expressed in matrix form as follows:

$$\mathscr{L}_{\text{mass}} = \frac{1}{2} N_L^T C^\dagger M N_L + \text{H.c.} \tag{1.17}$$

$$M = \begin{bmatrix} 0 & m_D \\ m_D & m_R \end{bmatrix}, \qquad N = \begin{bmatrix} \nu_L \\ C\overline{\nu_R}^T \end{bmatrix}. \tag{1.18}$$

The left term in Eq. 1.18 represents the mass matrix for the Type-I seesaw mechanism if $m_D \ll m_R$. If we assume the Yukawa couplings to the Higgs to be of similar magnitude for neutrinos as it is for the other leptons, then m_D is a Dirac mass that is on the order of the electroweak symmetry breaking scale. m_R is the mass for a very massive right-handed Majorana neutrino. It's important to note that m_D and m_R are 3×3 block diagonal matrices when considering three generations of neutrinos.

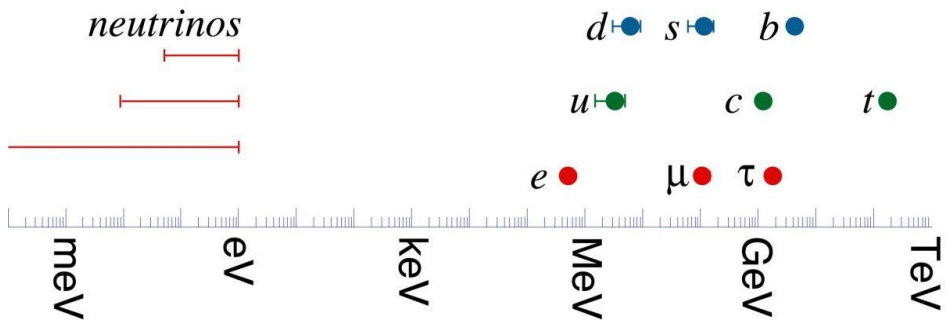

Figure 1.3: The masses of all the fundamental fermions, including the limits on the neutrino masses. *Image Credit: Hitoshi Murayama*

The description of a neutrino's mass is interesting here because there are multiple ways for generating a mass term when expressing a neutrino as the sum of its individual chiral fields. The physical particle masses and states can be deduced by expressing the neutrino mass Lagrangian as a sum of independent mass states. This is just an eigenvalue problem for the mass matrix M in Eq. 1.18 when considering one neutrino flavor,

$$m_\nu \simeq \frac{m_D^2}{m_R}, \quad m_{\mathcal{N}} \simeq m_R \tag{1.19}$$

$$\nu = \left(\nu_L + C\overline{\nu_L}^T\right) - \frac{m_D}{m_R}\left(\nu_R + C\overline{\nu_R}^T\right), \quad \mathcal{N} = \left(\nu_R + C\overline{\nu_R}^T\right) + \frac{m_D}{m_R}\left(\nu_L + C\overline{\nu_L}^T\right) \tag{1.20}$$

$$\mathscr{L}_{\text{mass}} = \frac{1}{2}\left(\frac{m_D^2}{m_R}\right)\overline{\nu}\nu - \frac{1}{2}m_R\overline{\mathcal{N}}\mathcal{N} + \text{H.c.}\,. \tag{1.21}$$

Eq. 1.19 show the eigenvalues, Eq. 1.20 show the independent eigenstates, and Eq. 1.21 is a reformulation of the neutrino mass Lagrangian in the eigenstate basis. In the Type-I seesaw mechanism, the mass of the light neutrino is inversely related to the mass of the heavy Majorana neutrino, which would give the neutrino a very small mass in comparison to the other leptons at the electroweak scale. This would also impose a small Majorana mass on the light neutrino because in this scenario the light neutrino is primarily composed of the

left-handed neutrino and its charge conjugate.

1.3 Baryogenesis from Leptogenesis

After cosmic inflation, the universe undergoes reheating where particles are thermalized from the oscillations and decay of the inflaton field [39]. Once the universe cools to below the grand unified scale at $T \sim 10^{15}$ GeV it is dominated by leptons, photons, quark-gluon plasma, and electroweak processes. A history of the evolution of the universe is shown in Fig. 1.4. However if the universe is in equilibrium throughout the electroweak epoch then a baryon asymmetry cannot form, resulting in matter and antimatter total annihilation. This is the problem of *baryogenesis*. What physics allows for the creation of a non-zero baryon density? The baryon density is measured by fitting the ΛCDM model to the power spectral density of the *cosmic microwave background* (CMB) radiation or by measuring the primordial abundance of deuterium and applying calculations inferred from Big Bang Nucleosynthesis [40, 41]. The baryon asymmetry is then $\eta_b/\eta\gamma = 6.0 \times 10^{-10}$, where η_b is the number density of baryons and η_γ is the number density of photons. The number density of photons is calculated from the black-body spectrum of the CMB. The baryon-to-photon ratio indicates that for every baryon in the observable universe there are approximately 10 billion photons, which leaves the open question of how does this baryon asymmetry get produced in the early universe?

For baryogenesis to occur sometime in the universe's history there are three conditions that must be satisfied [43]:

- Baryon Number, total number of baryons minus total number of anti-baryons, must be violated
- C-symmetry and CP-symmetry must be violated
- Interactions must occur out of thermal equilibrium

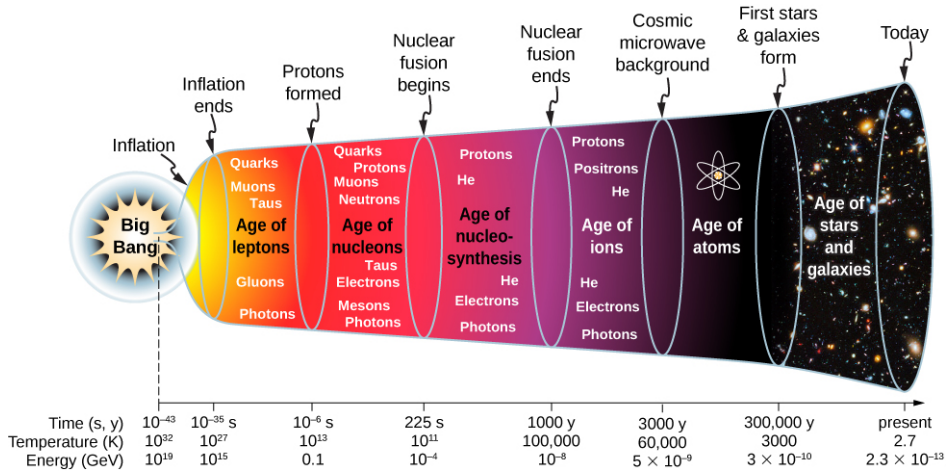

Figure 1.4: A graphic showing the evolution of the universe broken down by various epochs via their associated energy scales and physics. Fig. from ref. [42].

There are many ways baryogenesis can occur, however one of the simplest mechanisms is through *leptogenesis* from the decays of massive right-handed Majorana neutrinos before the electroweak phase transition [44]. A minimal extension of the Standard Model, by adding a mass ordering of heavy right-handed Majorana neutrinos, would explain the small effective mass of the neutrinos at the electroweak scale and provide an explanation for the observed matter-antimatter asymmetry in the observable universe.

If we assume a heavy neutrino mass ordering that scales like the generations of the massive leptons, and set the heaviest neutrino mass to the grand unified scale, then we have a neutrino mass ordering where $M_1 \ll M_2, M_3$ and $M_3 \sim 10^{15}$ GeV. In this case it is the lightest heavy neutrino, which propagates out of thermal equilibrium due to it not interacting with Standard Model processes present in the electroweak epoch, and is responsible for producing the initial lepton/anti-lepton asymmetry. The lepton/anti-lepton asymmetry arises from the CP-asymmetry in the decays of Fig. 1.5b and Fig. 1.5c with respect to the tree-level decay in Fig. 1.5a. The higher order corrections in Fig. 1.5b and Fig. 1.5c can contain irremovable phases in the Yukawa couplings that allows for CP violation [45]. From this model the

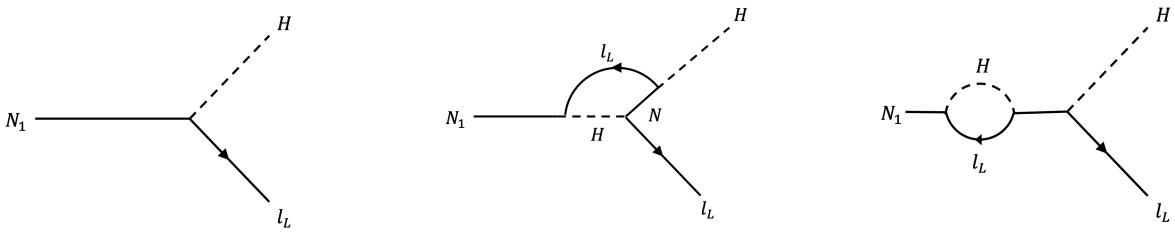

Figure 1.5: The decays of the lightest Majorana right-handed neutrino responsible for leptogenesis during the electroweak epoch phase of the universe's history. The interference between (a), and (b) and (c) violates C symmetry and CP symmetry in the decay of the lightest right-handed neutrino N_1 to Higgs lepton pairs when the Yukawa couplings have irremovable phases [45]. H is the standard Higgs doublet and l_L is a left-handed lepton.

achieved baryon asymmetry η_B can be expressed in terms of the CP-asymmetry ϵ_1, and sphaeleron conversion efficiency c_s, and baryon, lepton, and photon densities n_B, n_L, and n_γ.

$$\eta_B = \frac{n_B - n_{\overline{B}}}{n_\gamma} \simeq -c_s \frac{n_L - n_{\overline{L}}}{n_\gamma} \equiv -\frac{c_s}{f} N_{B-L} \tag{1.22}$$

$$= \frac{3}{4}\frac{c_s}{f}\epsilon_1 \kappa_f \simeq 10^{-2}\epsilon_1 \kappa_f \tag{1.23}$$

The sphaleron conversion efficiency goes as $B_{final} = c_s(B-L)$, $L_{final} = (c_s - 1)(B-L)$ to conserve $B-L$, f is the fraction of photons produced at leptogenesis up until recombination, N_{B-L} is the total $B-L$ asymmetry at the time of leptogenesis, and κ_f is the washout factor calculated from solving Boltzmann equations for the out-of-equilibrium decay process [46]. A sphaleron is a time-independent solution to the electroweak field equations already included the Standard Model and is represented as a saddle-point in the electroweak potential. Interactions can occur at sphalerons that violate lepton number and baryon number, but conserve $B-L$ and such interactions are predicted to occur in thermal equilibrium at

the critical temperature of the electroweak phase transition. The CP-asymmetry factor is calculated using the decay rates from the interactions in Fig. 1.5a, Fig. 1.5b, and Fig. 1.5c:

$$\epsilon_1 = \frac{\Gamma_{Nl} - \Gamma_{N\bar{l}}}{\Gamma_{Nl} + \Gamma_{N\bar{l}}} \,. \tag{1.24}$$

To produce the observed $\eta_B \sim 10^{-10}$ one needs $\epsilon_1 - 5 \sim 10^{-8}$ [45]. Values of ϵ_1 and κ_f can be expressed in terms of M_1, the effective neutrino mass $\widetilde{m_1}$, and the absolute neutrino mass scale $\overline{m}$ to give a lower limit on the lowest heavy Majorana neutrino mass and an upper limit on the absolute neutrino mass scale for a given $\overline{m}$ to successfully produce the observed baryon asymmetry. A full analysis from [46] provides a parameter space for possible M_1 values vs $\widetilde{m_1}$, Fig. 1.6.

The lower bound of M_1 for $\widetilde{m_1} < 10^{-3}$ eV turns out to be sensitive to the abundance of N_1, which effects the baryon asymmetry. Removing this sensitivity and inferring from the CP-asymmetry and washout rate bounds, this gives a neutrino mass scale range for successful leptogenesis by heavy right-handed Majorana neutrinos:

$$10^{-3}\,\text{eV} < m_i < 0.1\,\text{eV} \,. \tag{1.25}$$

Therefore a measurement of m_β from neutrino mass experiments, a non-zero $m_{\beta\beta}$ from neutrinoless double-β decay experiments, and the measurement of $\sum_i m_i$ from cosmology consistent with Eq. 1.25, the sum of neutrino masses, would strongly support this baryogenesis from leptogenesis model.

1.4 Neutrinoless Double-β Decay

Double-β decay ($2\nu\beta\beta$) is the process by which an atomic nucleus undergoes two β-decays simultaneously and was first directly observed in ^{82}Se in 1987 [47]. Half-lifes for $2\nu\beta\beta$ range from $10^{19} - 10^{21}$ years, while the longest half-life observed to date is for the related reaction 2νECEC, 1.8×10^{22} years from Xenon1T [48]. $2\nu\beta\beta$ occurs dominantly when the single β-decay is energetically forbidden due to nuclear pairing forces. Some even-even

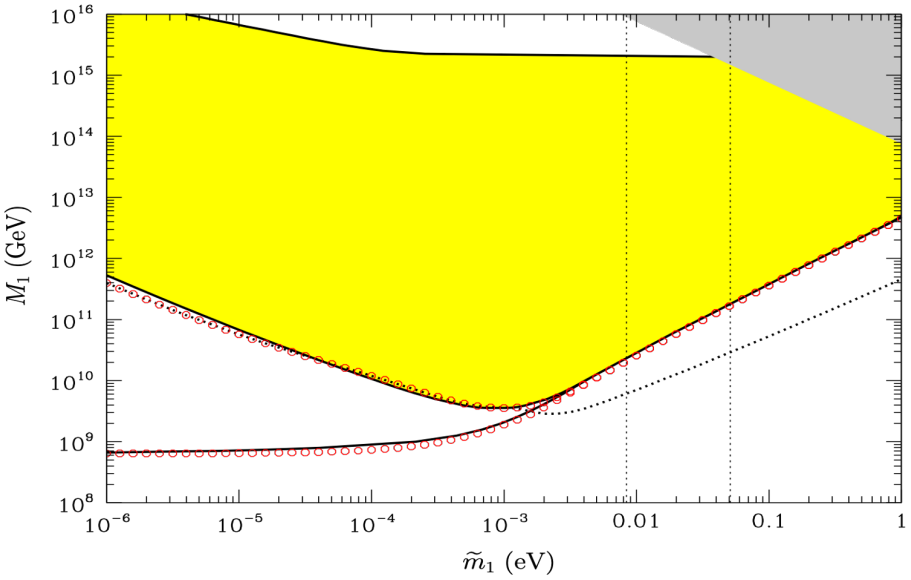

Figure 1.6: The parameter space for possible heavy neutrino masses, M_1, and effective neutrino masses $\widetilde{m_1}$ for successful leptogenesis. The dotted line corresponds to $m_1 = 0$ and $\eta_B = \eta_B^{\rm CMB} \sim 6 \times 10^{-10}$. The red dots and solid lines compare analytical and numerical results respectively. The yellow region is the allowed parameter space for given lightest right-handed neutrino mass and lightest effective neutrino mass. The parameter boundary that sits below the yellow region signifies the boundary where the lepton asymmetry depends on the abundance of N_1. The gray triangle is excluded by theory. Fig. from ref. [46].

nuclei can be more bound than their odd-odd neighbors, but less bound than their even-even neighbors, see Fig. 1.7, and can decay by emitting two β's and two electron anti-neutrinos. If the neutrino has an effective Majorana mass then there is a double-β decay mode where no electron anti-neutrinos are emitted from the decay called *neutrinoless double-β decay* ($0\nu\beta\beta$), see Fig. 1.8. In principle any $\Delta L = 2$ process that produces $0\nu\beta\beta$ decay will generate a Majorana neutrino mass contribution by the Schetcher-Valle theorem [50], however it could be negligibly small. Lepton number violating processes that produce $0\nu\beta\beta$ decay typically give the neutrino a Majorana mass so light neutrino exchange, Fig. 1.8b,

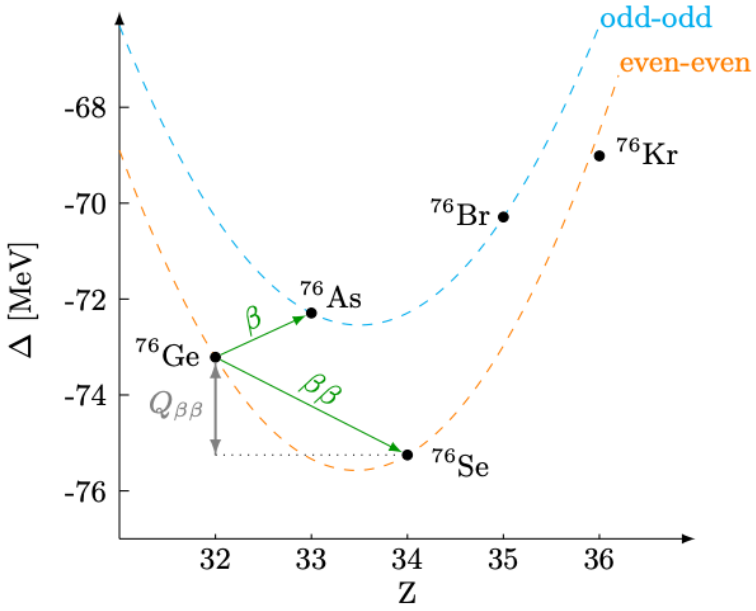

Figure 1.7: Mass excess $\Delta = M_f - M_i$ as a function of the atomic number Z for isotopes with total nucleons $A = 76$. The ^{76}Ge single β-decay to ^{76}As is energetically forbidden so instead the leading order decay process is a double-β decay to ^{76}Se. $Q_{\beta\beta}$= Δ - $2m_{e^-}$ and is the summed energy of the two emitted β's. Fig. from ref. [49].

is at least present and usually also dominates. In light neutrino exchange the presence of a Majorana mass allows the two neutrinos to virtually annihilate and would constitute a lepton number violation of $\Delta L = 2$. The decay rate through light-neutrino exchange can be expressed through the effective majorana mass, nuclear matrix elements, and phase space factor for a specific isotope,

$$T_{1/2}^{-1} = G_{01} g_A^4 \left(M_{\text{long}}^{0\nu} + M_{\text{short}}^{0\nu} \right)^2 \frac{m_{\beta\beta}^2}{m_e^2} \tag{1.26}$$

$$m_{\beta\beta} = \left| m_1 c_{12}^2 c_{13}^2 + m_2 s_{12}^2 c_{13}^2 e^{i\alpha_{21}} + m_3 s_{13}^2 e^{i(\alpha_{31} - \delta)} \right| . \tag{1.27}$$

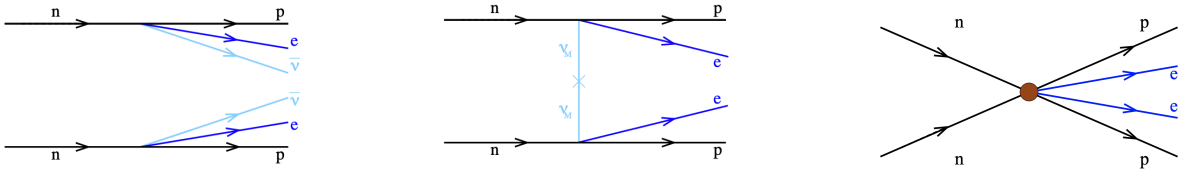

Figure 1.8: Feynman diagrams for double-β decay (a) and neutrinoless double-β decay long range (b) for the light neutrino exchange model and short range contribution (c). Fig. from ref. [51].

$m_{\beta\beta}$ is the *effective Majorana mass* from the leptonic part of Fig. 1.8b, G_{01} is the phase space factor from Fermi's Golden Rule, g_A is the axial vector coupling constant, and $M^{0\nu}_{\text{long}}$ and $M^{0\nu}_{\text{short}}$ are the long and short range nuclear matrix elements, described below. The Majorana phases in the PMNS matrix have a physical effect on $m_{\beta\beta}$ and thus the $0\nu\beta\beta$ decay half-life ($T_{1/2}$).

Since $0\nu\beta\beta$ decay takes place within an atomic nucleus, nuclear structure factors must be accounted for and this is done through the calculation of *nuclear matrix elements*. Nuclear matrix elements account for the transition of initial to final nuclear states through many-body interactions and can be challenging to estimate precisely, especially without much guidance from experimental results. The nuclear matrix element for light neutrino exchange can be broken down into a long range interaction and a short range interaction, M_{long} and M_{short}.

$$M_{\text{long}} = \frac{1.2A^{1/3}\text{fm}}{g_A^2} \left\langle 0_f^+ \right| \sum_{n,m} \tau_m^- \tau_n^- \left[H_F^\nu(r)\mathbb{1} + H_{GT}^\nu(r)\boldsymbol{\sigma}_n \cdot \boldsymbol{\sigma}_m + H_T^\nu(r) S_{nm} \right] \left| 0_i^+ \right\rangle \tag{1.28}$$

$$M_{\text{short}} = \frac{1.2A^{1/3}\text{fm}}{g_A^2} \left\langle 0_f^+ \right| \sum_{n,m} \tau_m^- \tau_n^- \mathbb{1} \left[\frac{2}{\pi} \int j_0(qr) h_S q^2 dq \right] \left| 0_i^+ \right\rangle \tag{1.29}$$

Eq. 1.28 and Eq. 1.29 are the decompositions of the nuclear matrix elements expressed as

state transitions through nuclear structure factors. H^{ν}_{F}, H^{ν}_{GT}, and H^{ν}_{T} are the Fermi, Gamow-Teller, and Tensor structure factors. τ^{-}_{m} and τ^{-}_{n} are the nuclear isospin operators and $\boldsymbol{\sigma}_n$ and $\boldsymbol{\sigma}_m$ are the spin operators, while $S_{mn} = 3(\hat{r} \cdot \boldsymbol{\sigma}_n)(\hat{r} \cdot \boldsymbol{\sigma}_m) - \boldsymbol{\sigma}_n \cdot \boldsymbol{\sigma}_m$, and $r = |\boldsymbol{r}_n - \boldsymbol{r}_m|$ is the distance between nucleons n and m. A is the number of nucleons and $\left\langle 0^{+}_{i} \right|$ and $\left| 0^{+}_{f} \right\rangle$ are the initial and final nuclear state, respectively. h_S is the neutrino potential within the nucleus. There are several common methods for evaluating the nuclear matrix elements, all of which offer a method for approximating the many-body interactions. A list of the most common methods is provided bellow:

- **Energy Density Functional Theory (EDF)**: An energy functional of local and semi-local densities such as number density, spin density, current density etc. are minimized to obtain ground state energies and densities. The resulting wave functions have no physical interpretation outside of producing the correct ground state energies and densities. This can be formulated as a mean field theory and transitions between nuclear states are governed by the probability of density deformations.

- **Nuclear Shell Model (NSM)**: Constrains the full Hilbert space of nucleon states to the "valence space" near the Fermi surface and assumes states far away from the surface contribute negligibly to low energy nuclear transitions. An effective Hamiltonian is usually created from a subset of active nucleons that can only occupy a limited set of states since most of the core nucleons are assumed frozen at lower energy states. Many body states are linear combinations of orthogonal Slater determinants. A Slater determinant is a way of creating an anti-symmetric wavefunction that describes a system of multiple fermions.

- **Interacting Boson Model (IBM)**: Nucleon pairs are treated as interacting bosons. The number of degree of freedoms in the nucleus is usually half of the number of total nucleons. More shells are used than the nuclear shell model, however there are fewer correlations. The effective operators are usually determined by fits to data rather than

by mappings from the shell model.

- **Quasi-Particle Random-Phase Approximation (QRPA)**: An extension of the general random-phase approximation (RPA) that takes into account charge-changing and nuclear boson pairing. In RPA the ground state of a quantum multi-body problem is described by a Slater determinant and nearby states are described by excitations to the Slater determinants. For QRPA, occupied orbitals are described as protons and neutrons, which incorporates charge-changing. To include boson pairing, the orbitals are described by Hartree-Fock-Bogoliubov (HFB) quasiparticle vacuum instead of the Hartree-Fock state and the nearby Slater determinants with nearby quasiparticle vacua.

- **"ab initio" Methods**: The degrees of freedom for all nucleons are taken into account. A nuclear potential is derived from an effective field theory matching of a $\Delta L = 2$ process. The nuclear matrix elements are calculated from the potential using a variational Monte-Carlo. Precision and calculations for heavier nuclei are limited due to computing power, but recent advancements have extended these principles to heaver nuclei [52].

Current nuclear matrix element calculations for these methods are shown in Fig. 1.9a and Fig. 1.9b. In principle, higher dimensional terms can contribute to $T_{1/2}^{-1}$, as indicated by an effective field theory formulation of $0\nu\beta\beta$ [53, 49].

$$T_{1/2}^{-1} = G_{01} g_A^4 (M_{\text{light}}^{0\nu})^2 \frac{m_{\beta\beta}}{m_e^2} + \frac{m_N^2}{m_e^2} \tilde{G} \tilde{g}^4 \tilde{M}^2 \left(\frac{v}{\tilde{\Lambda}}\right)^6 + \frac{m_N^4}{m_e^2 v^2} \tilde{G}' \tilde{g}'^4 \tilde{M}'^2 \left(\frac{v}{\tilde{\Lambda}'}\right)^{10} + \cdots \tag{1.30}$$

The second and third terms are contributions from dimension-7 and dimension-9, respectively. For extensions beyond the standard model extra terms are expected, which can interfere with each other and with light neutrino exchange.

For $2\nu\beta\beta$ decay and $0\nu\beta\beta$ decay the measurable quantities are the energy and momenta of the two emitted electrons, see Fig. 1.10. $2\nu\beta\beta$ decay is a five body decay into two electrons and two anti-neutrinos and thus produces a spectrum of energies, while $0\nu\beta\beta$

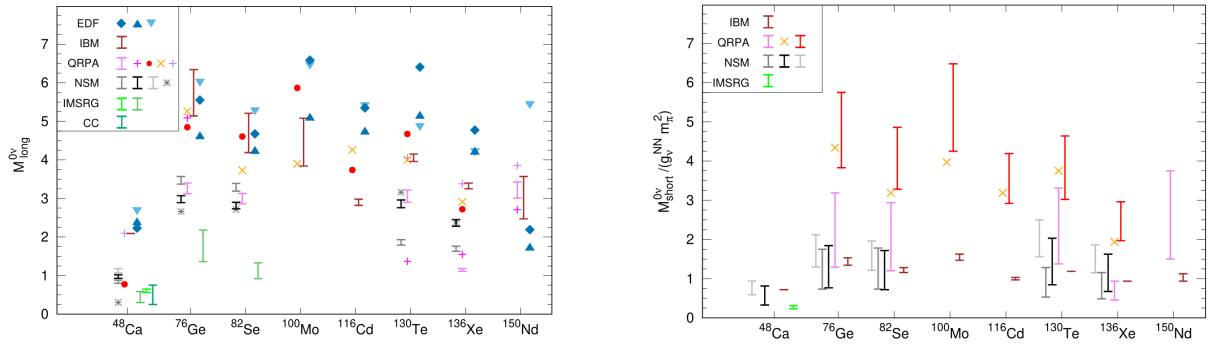

(a) (b)

Figure 1.9: Nuclear matrix element calculations for long (a) and short(b) range light neutrino exchange. m_π is the mass of the pion and g_ν^{NN} is a coupling constant for the nucleon nucleon interaction in the leading order contact term to light neutrino exchange. Fig. from ref. [49].

decay is a three body decay where the sum of the electron energies is equal to a Q-value, $Q_{\beta\beta} = M_f - M_i - 2m_{e^-}$. The nuclear recoil is small due to the large mass difference between the electrons and nuclei, but will induce some minimal spread about the observed $Q_{\beta\beta}$. However, this spread is orders of magnitude smaller than the best detector resolutions and is usually neglected. The only way to distinguish $0\nu\beta\beta$ decay from $2\nu\beta\beta$ decay is to measure the total summed energy of the two emitted electrons. All $0\nu\beta\beta$ decay experiments are searching for a peaked excess at $Q_{\beta\beta}$ with at least a 3σ deviation from an expected background level.

The sensitivity of a $0\nu\beta\beta$ decay experiment can be captured by a heuristic counting analysis in which two variables effect the discovery potential for $0\nu\beta\beta$ decay: the "sensitive exposure", $\mathcal{E}$, and the "sensitive background", $\mathcal{B}$ [55]. $\mathcal{E}$ is the product of the active double-β decay isotope mass, the time the experiment was running (livetime), and the detection efficiency. $\mathcal{B}$ represents the number of background events in the $Q_{\beta\beta}$*region of interest* (ROI) after all background reduction analysis cuts, divided by the sensitive exposure. These two

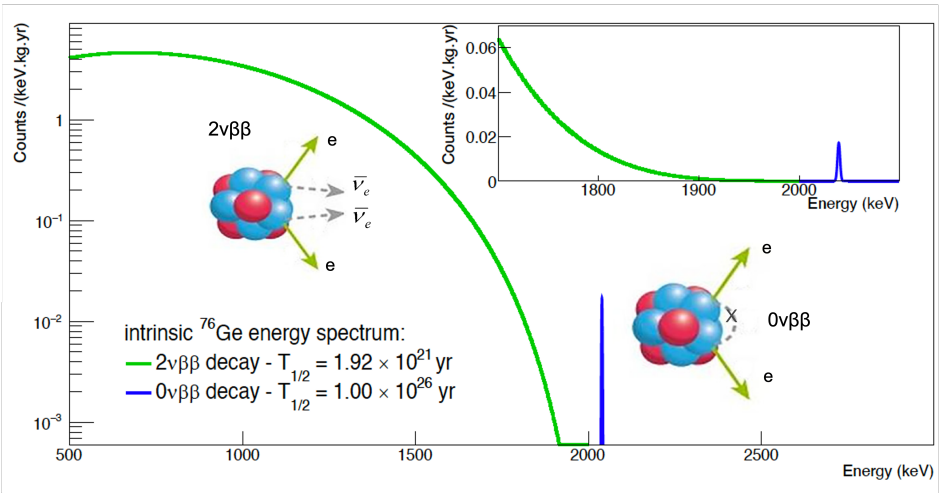

Figure 1.10: The resulting theoretical spectrum from counting the number of events based on the summed energy of the two emitted electrons for a double-β decay isotope. The scaling shows what a background free result would look like for a hypothetical $0\nu\beta\beta$ decay half-life at 10^{26} years. The inset shows a close up of an energy region including $Q_{\beta\beta}$. Fig. from ref. [54].

properties can be used to give the number of signal and background events in an experiment.

$$N_{0\nu\beta\beta} = \frac{\ln 2 \cdot N_A \cdot \mathcal{E}}{m_a \cdot T_{1/2}}, \qquad B = \mathcal{B} \cdot \mathcal{E} \tag{1.31}$$

N_A is Avogadro's number and m_a is the molar mass of the active isotope. Since $0\nu\beta\beta$ decay is still yet to be observed, common metrics to evaluate an experiment's capability of discovering $0\nu\beta\beta$ are the half-life discovery sensitivity and the median exclusion sensitivity. The discovery sensitivity is the value of $T_{1/2}$ for which an experiment with a given sensitive exposure and total background counts has a 50% chance of measuring a signal above background B with a significance of at least 3σ [55].

$$T_{1/2} = \ln(2)\frac{N_A \mathcal{E}}{m_a S_{3\sigma}(B)} \tag{1.32}$$

$S_{3\sigma}(B)$ is the Poisson signal expectation at which 50% of the measurements in an ensemble of identical experiments would report a 3σ positive fluctuation above B. $S_{3\sigma}(B)$ is found by

solving $\mathrm{CDF}_{\mathrm{Poisson}}(C_{3\sigma}|B) = 3\sigma$ and $\overline{\mathrm{CDF}}_{\mathrm{Poisson}}(C_{3\sigma}|S_{3\sigma}+B) = 50\%$; $S_{3\sigma}(B) \propto \sqrt{B}$ when B is large. The discovery sensitivity is drawn as a function of sensitive exposure for different projected background indexes, see Fig. 1.11.

The exclusion sensitivity is the median lower limit that an experiment would place on $T_{1/2}$, in the absence of a signal, given its sensitive exposure and sensitive background.

$$T_{1/2} > \ln(2)\frac{N_A\mathcal{E}}{m_a S_{UL}(B)} \tag{1.33}$$

Here $S_{UL}(B)$ is the upper limit on the number of $0\nu\beta\beta$ signal events in the absence of a signal, usually taken at the 90% confidence level. The upper limit $S_{UL}(B)$ can be determined by several different methods. A standard one to use is the Feldman-Cousins Confidence Intervals, which provides an upper limit given a Poisson distribution with an expected background and observed number of counts in the ROI [56]. This type of confidence interval and sensitivity are frequentist and are determined by the outcomes of a set of hypothetical identical experiments. One can also define Bayesian confidence intervals by assessing the inherent probability of measuring a signal above an expected background rate.

In a Bayesian treatment, the discovery probability of $0\nu\beta\beta$ decay can be estimated by combining the discovery sensitivity with the prior probability distribution of different $m_{\beta\beta}$ values.

$$\mathrm{DP} = \int_0^\infty \left(\frac{dP}{dm_{\beta\beta}}\right) \overline{\mathrm{CDF}}_{\mathrm{Poisson}}(C_{3\sigma}|S(m_{\beta\beta})+B)\, dm_{\beta\beta} \tag{1.34}$$

The probability density can be constructed from a Markov-chain Monte Carlo sampling of a marginal posterior distribution from a fit to the known and unknown neutrino oscillation and phase parameters [55]. The mass observables are logarithmic priors and phases are flat priors in the range $[0, 2\pi]$. Allowed regions for $m_{\beta\beta}$ assuming light left-handed neutrino exchange are shown in Fig. 1.12. In next generation one tonne scale experiments, it is found that the discovery probability for a Majorana neutrino in the inverted ordering is nearly 100% where as for the normal ordering the discovery probability is as high as 50%. Discovery probabilities are shown in Fig. 1.13.

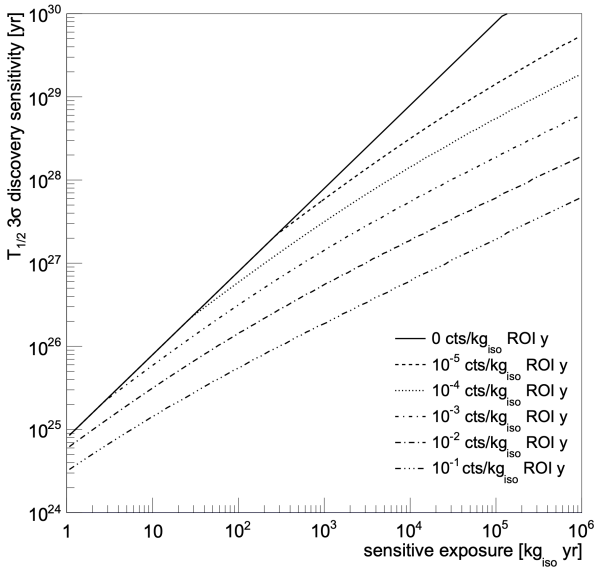

Figure 1.11: Discovery sensitivity for a ^{76}Ge experiment as a function of sensitive exposure for various background indexes. For reference, the current best background indexes are on the order of 10^{-3} and 10^{-4} cts / $\mathrm{kg_{iso}}$ ROI yr. Fig. from ref. [55].

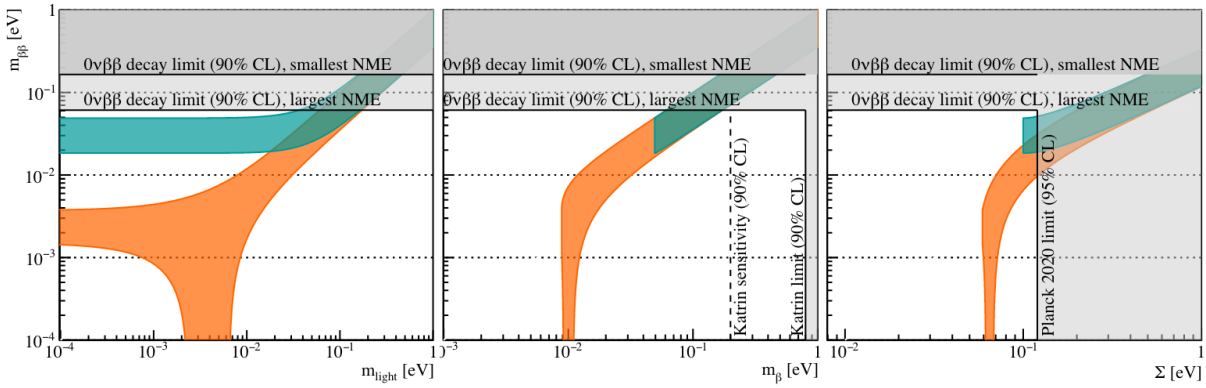

Figure 1.12: The allowed regions for $m_{\beta\beta}$ as a function of m_{light} the lightest neutrino mass, m_β the effective kinematic neutrino mass, and Σ the sum of neutrino masses. Orange indicates the allowed for the normal mass ordering and blue indicates the allowed region for the inverted mass ordering. Gray is excluded by experiments. Fig. from ref. [49].

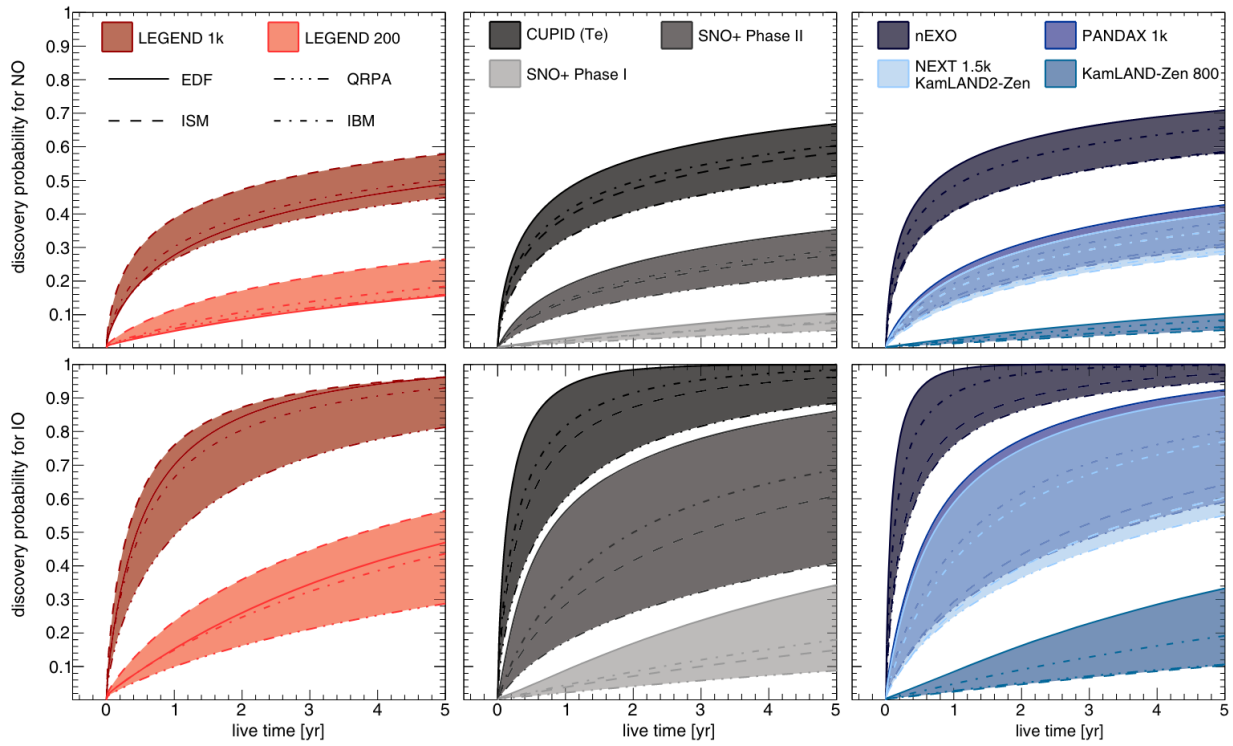

Figure 1.13: The discovery probability as a function of livetime for a collection of next-generation experiments using different double-β decay isotopes. From left to right ^{76}Ge, ^{130}Te, and ^{136}Xe. The bounds represent the variation in nuclear matrix element results. The uniform prior probability on $\log \Sigma$ for the discovery probability here is the sum of neutrino masses, Σ, instead of $m_{lightest}$ and gives the higher discovery probability for the normal ordering. The upper plots are for the normal mass ordering and the lower plots are for the inverted mass ordering. Next generation experiments have 100% chance of discovery for the inverted ordering and up to 50% chance of discovery for the normal ordering. Fig. from ref. [49].

Chapter 2

THE MAJORANA DEMONSTRATOR

The MAJORANA DEMONSTRATOR is an experiment used to search for $0\nu\beta\beta$ decay in ^{76}Ge located at the 4850 ft level at the Sanford Underground Research Facility(SURF) in Lead, South Dakota. The experiment consists of modular arrays of *high-purity Ge* (HPGe) detectors operated in a vacuum cryostat surrounded by layers of passive-shielding and an active cosmic-ray muon veto. The experiment recently concluded enriched data-taking for the $0\nu\beta\beta$ decay analysis in March 2021. Along with the Germanium Detector Array (GERDA) at INFN Gran Sasso National Laboratory (LNGS), the MAJORANA DEMONSTRATOR is an experiment to demonstrate the feasibility of operating a tonne scale HPGe experiment to reach half-life sensitivities greater than 10^{28} years, or $m_{\beta\beta}$ sensitivities less than ~ 17 meV, with a background goal of less than 1.0×10^{-5} cts/(keV $\cdot$ kg $\cdot$ yr). The operation goals of the MAJORANA DEMONSTRATOR are as follows:

- Reach a background index of less than 3 cts / (FWHM-t-y), or approximately 2×10^{-3} cts / (keV·kg·yr), using a 4 keV ROI around the 2039 keV $Q_{\beta\beta}$for ^{76}Ge with a total exposure of at least 65 kg-yrs

- Set competitive half-life limits on $0\nu\beta\beta$ in comparison to other leading searches such as KamLAND-Zen and GERDA[57, 58].

- Search for additional physics beyond the standard model. This has included dark matter searches, trinucleon decay, lightly ionizing particles, and $2\nu\beta\beta$ decay to excited states [59, 60, 61, 62].

This chapter serves as an overview of the MAJORANA DEMONSTRATOR experiment

with a focus on the analysis that led to the final $0\nu\beta\beta$ decay half-life limit result [63].

2.1 HPGe Detectors

^{76}Ge is the double-β decay isotope inside the MAJORANA DEMONSTRATOR. The main advantage of using ^{76}Ge is that the isotope can be used as the source of double-β decay material and at the same time be the material the detectors are made out of. Additionally, Ge has a low mean ionization energy at 2.9 eV, thus many electron-hole pairs are produced per energy deposition. This produces excellent energy resolutions on the single to few keV level due to negligible recombination and efficienct charge collection. On the contrary, ^{76}Ge has a low natural abundance of $\sim$ 7.8%, therefore in order to use this isotope to reach competitive half life limits for $0\nu\beta\beta$ decay a HPGe detector must be enriched with ^{76}Ge. Isotopic enrichment occurs at the Electrochemical Plant in Zelenogorsk, Russia in the large centrifuge facility, where GeO_2 is processed to have greater than 87% ^{76}Ge [64]. The $^{76}GeO_2$ is stored under concrete, steel, and soil and then transported by land and ship to Oak Ridge to limit the exposure of the material to cosmic-ray neutrons. The germanium ore is reduced to germanium semi-metal through a reduction furnace and zone refined to reach a specific impurity level and resistivity. The metal is then melted, a seed crystal is introduced, and is pulled very slowly in a Czochralski crystal puller to form a crystal boule, which is then machined and etched with nitric and hydrofluoric acid solutions.

A HPGe detector essentially functions as a p-i-n diode made out of a Ge crystal. The bulk Ge crystal chosen for $0\nu\beta\beta$ experiments is slightly p-type. There are two contacts: one Lithium diffused n^+ outer contact (1-2 mm thick) and one Boron implanted p^+ contact ($\sim 1\mu$m thick). The two contacts are separated by the bulk Ge and a passivated surface of amorphous Ge ($\sim 0.1\mu$m thick). Establishing a voltage difference of several thousand volts from n^+ contact to p^+ contact gives a reverse biased diode that is fully depleted. Since the band gap of Ge is low at 0.67 eV, a HPGe detector must be run at close to liquid nitrogen temperature to suppress leakage currents between the two contacts. When an energy deposition occurs in the detector many electron-hole pairs are produced as a result of

impact ionization. The electrons drift towards the n^+ contact and holes drift towards the p^+ contact. These two currents make up the raw signals measured from the detector before any electronics signal processing. The total current produced by a moving charge in the vicinity of an electrode contact is described by the Shockley-Ramo Theorem [65, 66].

$$I(t) = q\mathbf{v}(\mathbf{x}(t)) \cdot \mathbf{E}_\omega(\mathbf{x}(t)) \tag{2.1}$$

q is the moving charge, $\mathbf{v}$ is the instantaneous velocity, and $\mathbf{E}_\omega$ is the weighted electric field. The weighting potential is defined as the electric potential when setting the p^+ contact to 1V and grounding all other contacts. The weighted electric field is $\mathbf{E}_\omega(\mathbf{x}(t)) = -\nabla\phi_\omega(\mathbf{x}(t))$.

There are several geometries of HPGe detectors that have been used in the MAJORANA DEMONSTRATOR: *Broad Energy Ge* detector (BEGe^{TM}), *P-type Point Contact* detector (PPC), and *Inverted Coaxial Point Contact* detector (ICPC). All of these designs operate in the same manner, but have different contact and passivated surface geometries, see Fig. 2.1.

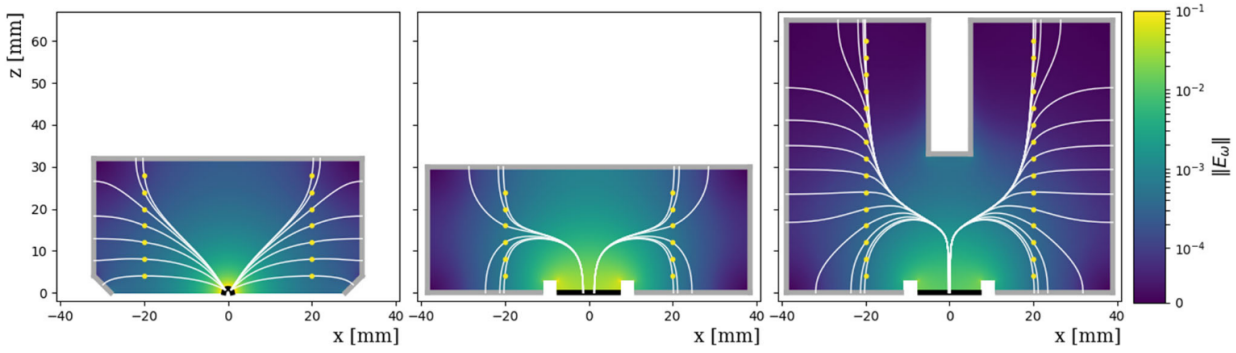

Figure 2.1: Geometries of several HPGe detectors, from left to right: PPC, BEGe^{TM}, and Inverted Coaxial. The Inverted Coaxial detector shown here as a BEGe style p^+ contact, but they can also have a PPC style p^+ contact. For each detector the weighting potential is shown and charge collection trajectories for various energy deposition locations. The gray boundaries indicate the n^+ contact and the p^+ contacts are shown in black. Fig. from ref. [67].

A set of detectors are assembled into strings and a module is composed of several detector strings under vacuum. A total of two modules was used in the experiment. The strings' structural components are made out of copper electroformed on-site underground for maximum radio-purity. Electroformed copper is also used for the high voltage bias contact, and for the thermal contact to the LN reservoir. The insulating components are made out of a low background NXT-85 Teflon™ and Vespel®. For the electronics readout, each detector has a *low mass front end* (LMFE) [68] on the p^+ contact, see Fig 2.3. This serves as the first stage of amplification and is close to the detector to minimize electronics noise and maximize bandwidth. The purpose of the first stage is to convert the current pulses from the detector into a voltage signal that measures the total charge collected, see Fig. 2.4. Those signals are further amplified by second stages that are outside of the cryostat. The second stage shapes the signal to match the dynamic range and impedance of the digitizer inputs. The two stages impose a 70 μs decay time constant for the waveform, which is ideal for the event rates experienced in background and calibration data. The output of the second stages is divided into a high gain with less dynamic range and a low gain with more dynamic range. Each high and low gain is read out by a 14 bit 100 MHz sampling rate digitizer made for the GRETINA experiment [69] with a custom FPGA programming for the MAJORANA DEMONSTRATOR. Connecting the second stage to the digitizers are high-purity, low mass signal cables made by Axon [68].

2.2 Shielding

Background originating from natural radioactivity must be suppressed in some way to be sensitive to $0\nu\beta\beta$ half-lifes greater than 10^{26} years. The majority of background that has the potential to contaminate the ROI are the daughter isotopes in the decay chains of ^{238}U and ^{232}Th, see Fig. 2.5a and Fig. 2.5b. The MAJORANA DEMONSTRATOR has several lines of defense when it comes to background suppression: active and passive shielding around the active isotope, pulse-shape analysis based background rejection applied to HPGe waveforms, use and maintenance of ultra-clean materials, and the HPGe's intrinsic high energy

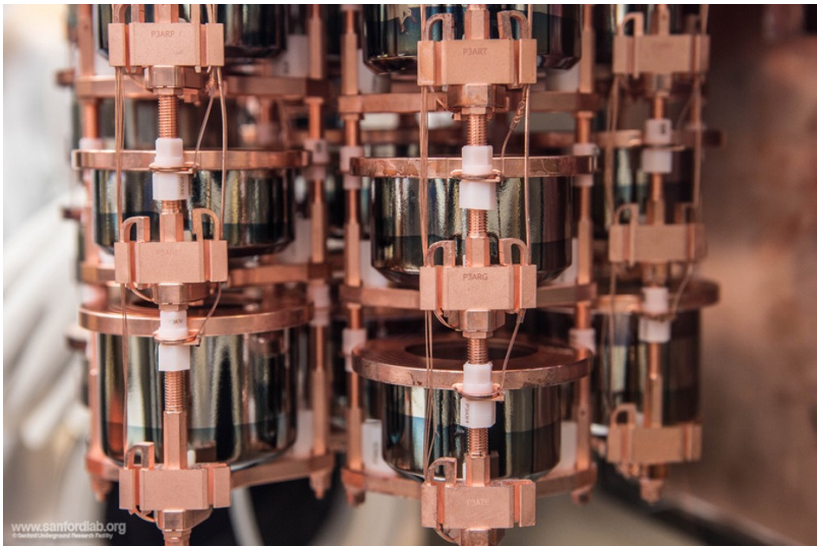

Figure 2.2: Several strings of HPGe detectors from one of the modules in the MAJORANA DEMONSTRATOR. Each detector has a high voltage bias ring on the top and a low mass front end readout connected to the p^+ contact on the opposite end. Fig. from ref. [70].

resolution. The experiment and shielding were constructed in a class-1000 clean room with instrumentation to carefully monitor environment variables. The vacuum hardware, cryogenic hardware, second stage electronics, and calibration hardware are located external to the shielding. A cross arm connects these elements to the two cryostats inside of the passive shielding. The shielding in the MAJORANA DEMONSTRATOR from inside to out is as follows:

- **Copper Shields**: A 5 cm thick inner copper shield surrounding the two detector modules made out of underground electroformed copper. A 5 cm thick outer copper shield surrounding the inner copper shield made of Oxygen-Free High Thermal Conductivity (OHFC) copper. A thin copper shield is located inside each module to block infrared radiation. The inner and outer copper shield is more radio-pure than the surrounding lead and also shields low energy bremsstrahlung production from the lead.

- **Lead Shield**: A 45 cm thick stack of 4120 lead bricks, weighing approximately 108,100

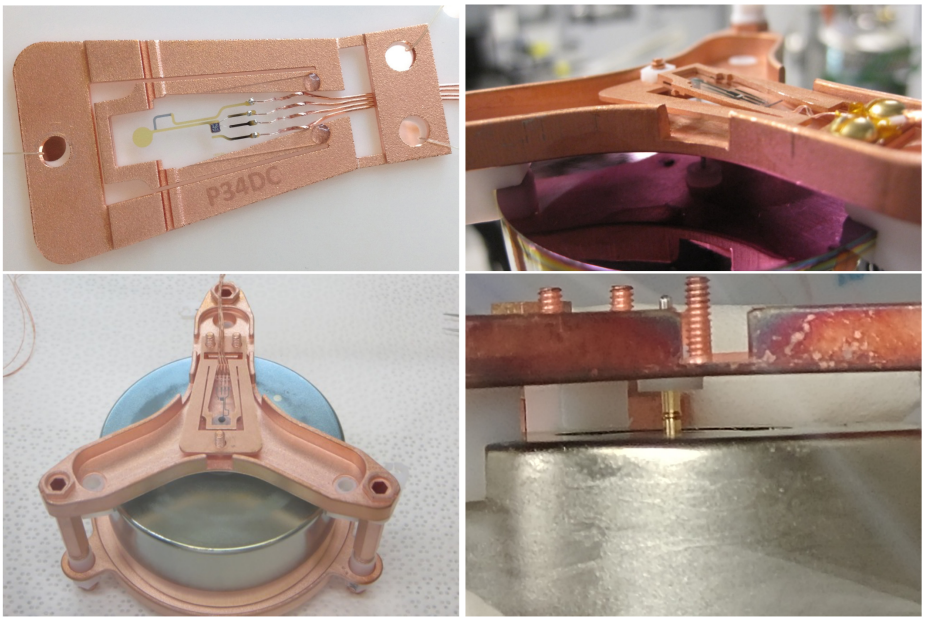

Figure 2.3: (Top left) An LMFE mount in a spring clip. (Top right) LMFE in the spring clip mounted on a pin that's touching the detector p^+ contact surrounded by the passivated surface. (Bottom left) An LMFE mounted on a detector, wide view. (Bottom Right) Side view of the contact pin. Fig. from ref. [68].

lb. This is more than the weight of a Boeing 737-800 after a transcontinental flight with all luggage and passengers disembarked. This is used to shield γ-ray photons from the surrounding rock cavern.

- **Radon Purge**: A sealed aluminum box which is continuously purged with nitrogen gas to remove the interior of radon gas.

- **Muon Veto**: A set of scintillating acrylic panels instrumented with photomultiplier tubes are used as an active muon veto. Cosmic-ray induced muons penetrate through the entire shielding and cause the veto panels to scintillate simultaneously.

- **Polyethylene Shield**: A set of high density polyethylene panels to reduce the energy

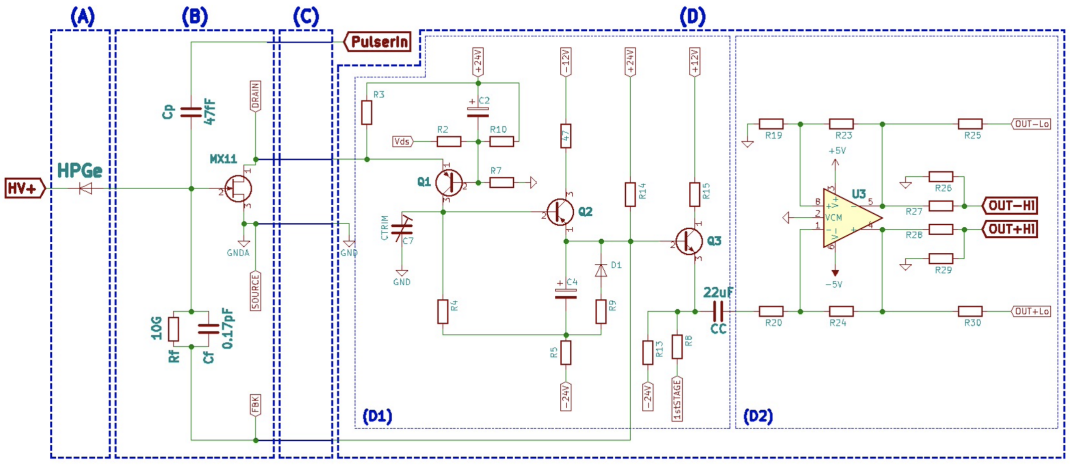

Figure 2.4: A simplified schematic of the readout electronics used for the detectors in the MAJORANA DEMONSTRATOR. (A) is the HPGe detector, (B) is the LMFE charge amplification, (C) are the cables, and (D) is the second stage amplifier. The final stage outputs two dynamic ranges with a high gain and a low gain. This whole readout serves the purpose of converting the small current pulses produced by the detectors into charge-collected waveforms from which to measure the energy of each event. Fig. from ref. [68].

of incident neutrons from the surround environment. 5 cm think of borated polyethylene and 25 cm thick of pure polyethylene.

- **4850 ft level**: The experiment is under 4850 ft of rock to reduce the incident cosmic-ray muon flux

A full schematic of the MAJORANA DEMONSTRATOR is shown in Fig. 2.6.

2.3 Operation

Operation of the DEMONSTRATOR began with module one in July 2015 consisting of 20 enriched PPC detectors (16.8 kg) and 9 natural isotopic abundance BEGe^{TM} detectors (5.4 kg). Module two began operation in August 2015 with 15 enriched PPC detectors (12.9 kg)

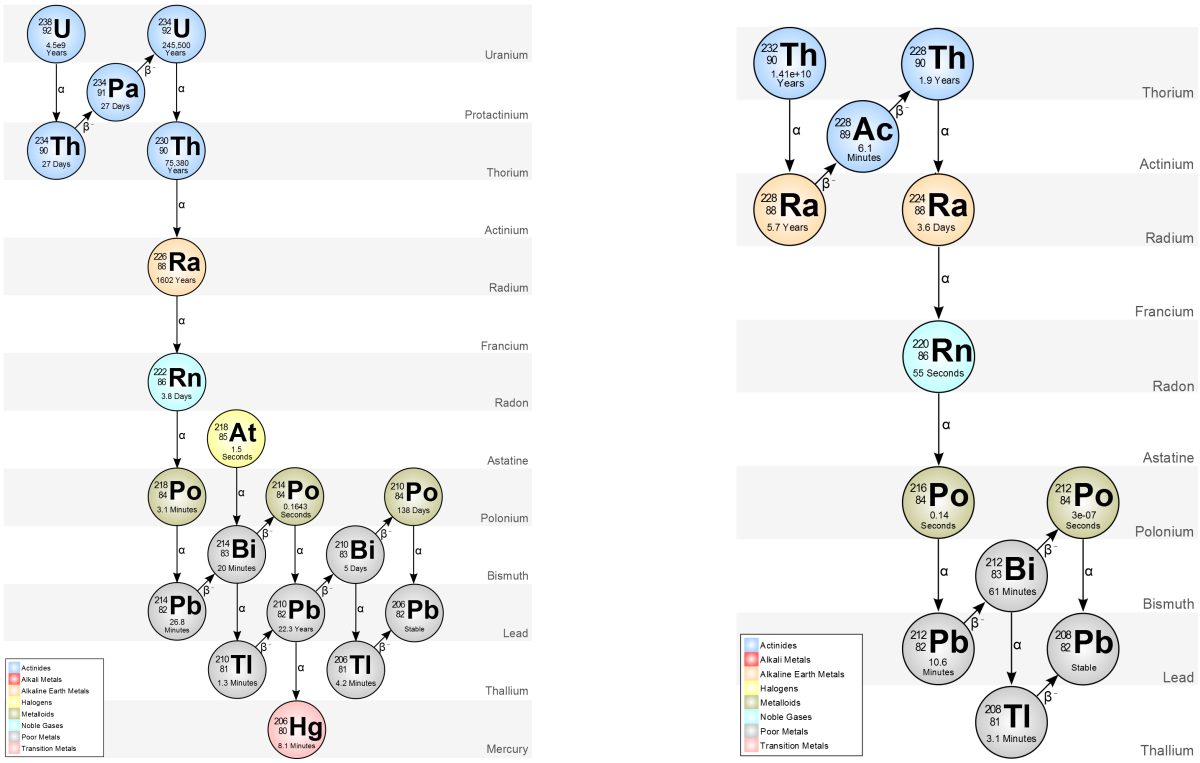

(a) (b)

Figure 2.5: The decay chains of ^{238}U and ^{232}Th. The decay of ^{214}Bi and ^{208}Tl are the dominate sources of background in the ROI from these two decay chains. *Image Credit: Wikipedia*

and 14 natural BEGe^{TM} detectors (8.8 kg). In November 2019, module two was removed from the shield and upgraded with improved cables and connectors and several PPC detectors were replaced with ICPC detectors. Module two restarted operation with 9 enriched PPC detectors (7.4 kg), 6 enriched ICPC detectors (6.7 kg), and 14 natural BEGe^{TM} detectors (8.8 kg). March 2021 marked the end of enriched data-taking and all enriched detectors were removed and sent to LNGS to be used in LEGEND-200. A time line of the collected exposure is shown in Fig. 2.7.

The data from the experiment is taken in segments of one hour long runs while detectors

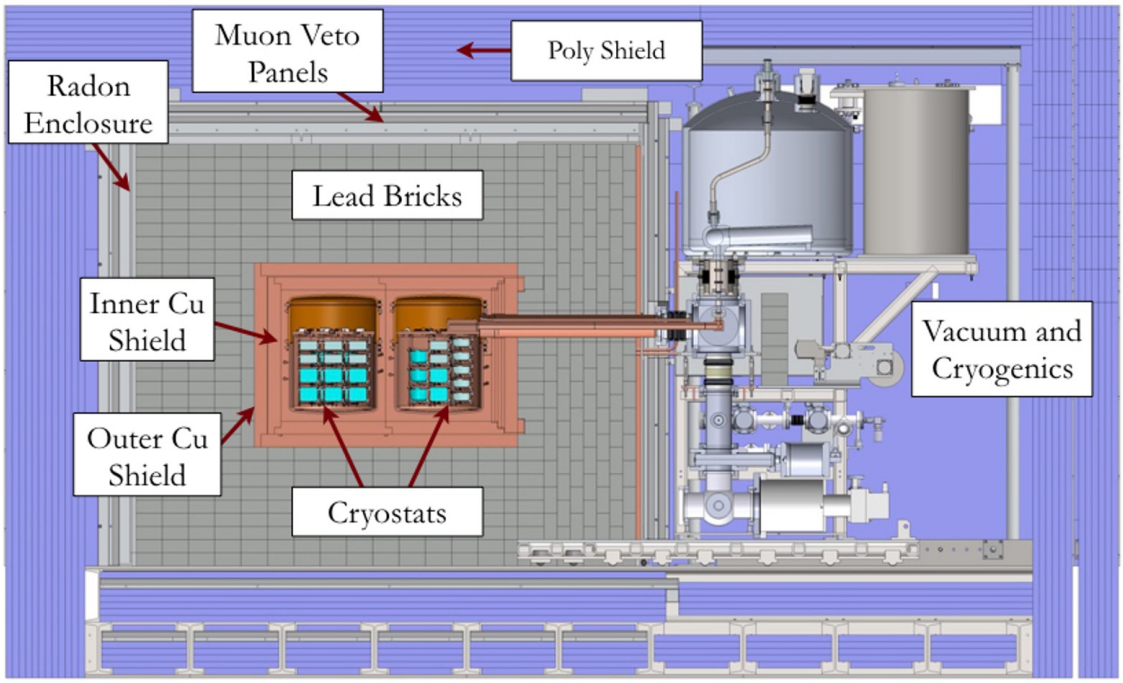

Figure 2.6: A full drawing of the MAJORANA DEMONSTRATOR with the detector modules located slightly left of center. *Image Credit:* MAJORANA *Collaboration*

are operational. The collaboration adopted a "statistical blindness" scheme in which 75% of the background data is not viewable until all analysis schemes are implemented and all key parameters and their uncertainties are finalized. The data cycles correspond to 31 hours of open data followed by 93 hours of blind data. There are two main types of data-taking modes: physics and calibration. Physics data is used for the $0\nu\beta\beta$ decay search and other beyond Standard Model physics, while the calibration data is used to calibrate the event energies and pulse-shape parameters. A standard calibration occurs weekly and lasts for a few hours. Bi-monthly longer calibrations were done to get enough statistics to tune the multi-site pulse shape parameter. The standard calibration is performed by inserting a line source of ^{228}Th that wraps around each module and is retracted when the calibration period ends, see Fig. 2.8. Other calibration sources were used during certain periods such as ^{56}Co, ^{222}Rn, and ^{60}Co to support external research regarding the main analysis or background

modeling.

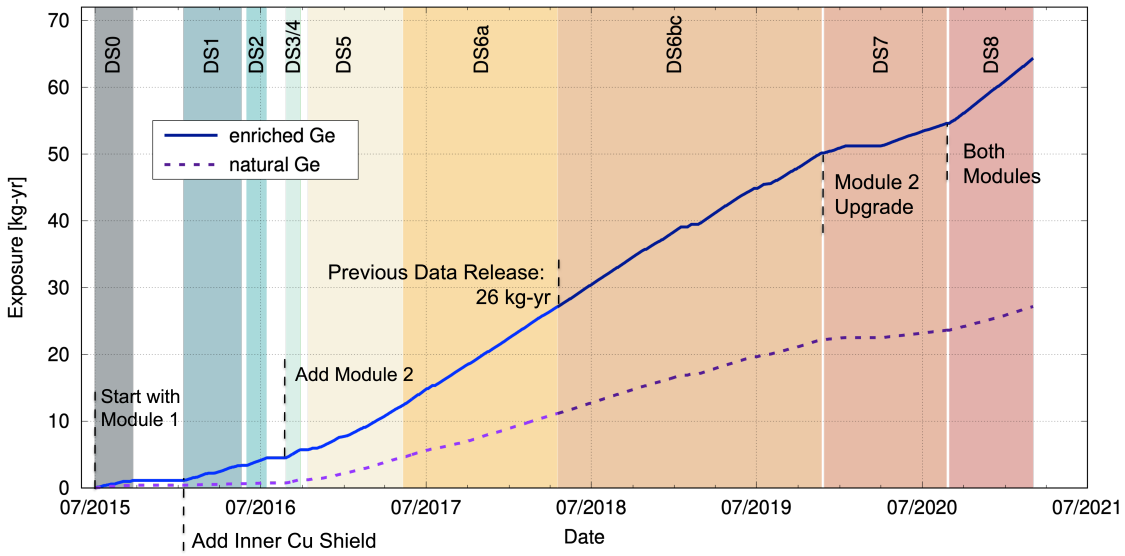

Figure 2.7: A full timeline of enriched data-taking. This diagram shows the accumulative exposure for enriched and natural detectors as well as certain milestones for the experiment as a function of time. By March 2021 all enriched data-taking was stopped and all enriched PPC detectors were shipped to LNGS to be used in LEGEND-200. *Image Credit:* MAJORANA *Collaboration*

2.4 Analysis

There are two main goals of the analysis with regards to the search for $0\nu\beta\beta$ decay and they are measuring the energy of each waveform event precisely and reducing background events further through pulse-shape analysis. Waveforms from all detectors are organized into events with 4 μs time windows. Each waveform has a few features that are removed before analysis is applied. A nonlinearity feature from the digitizers is removed as discussed in [71]. Baselines are removed by subtracting the average of the first 100 samples of the waveform. A pole-zero deconvolution is applied to remove the exponential response from the electronics

Figure 2.8: One of the detector modules outside of the shielding. The ^{228}Th source is inserted into and retracted from a plastic tube that wraps around the module. Fig. from ref. [70].

and charge trapping [72]. Removing these waveform features increases the energy resolution and was instrumental for demonstrating a world leading energy resolution. Improving the resolution also increases the half-life sensitivity by shrinking the ROI and thus lowering the background.

2.4.1 Energy

The total charge collected on the charge-sensitive pre-amp feedback capacitor is related to the maximum voltage drop across it, $V_{\max} = Q/C$, where the capacitance is constant. Given a detector response that is approximately linear, the energy of a waveform can be estimated by the maximum height. However in high resolution spectroscopy, there are several optimal pulse-shaping techniques which lead to significantly better energy resolutions [73]. In the MAJORANA analysis, the uncalibrated energy is estimated by using an optimal trapezoidal filter. Each pole-zero corrected waveform is convolved with an impulse function to give a trapezoid waveform with shaping parameters (rise time, flat time, fall time) that optimize

the energy signal-to-noise ratio,

$$s(t) = \int_{-\infty}^{\infty} v(t-t')h(t')dt' \,. \tag{2.2}$$

$v(t)$ is the input waveform signal, $h(t)$ is the impulse function, and $s(t)$ is the output trapezoidal waveform whose amplitude provides and estimate of the uncalibrated energy. A symmetric trapezoidal filter has a rise time and fall time that are the same while an asymmetric trapezoidal filter has a rise time and fall time that are different. To correct for charge trapping due to detector, impurities the pole-zero time constant is adjusted for each individual detector.

$$\frac{1}{\tau_{\mathrm{PZ}}} = \frac{1}{\tau_{\mathrm{RC}}} - \frac{1}{\tau_{\mathrm{ct}}} \tag{2.3}$$

The charge trapping time constant τ_{ct} is varied to maximize resolution [72]. The start time of each waveform is calculated by a leading-edge algorithm that uses an asymmetric trapezoidal filter (when rise time and fall time are not the same). The offline uncalibrated energy is then the amplitude of the trapezoidal filter a fixed time away from the start of the waveform, see Fig. 2.9. To calibrate the raw energy, several background energy peaks with known energy from a ^{228}Th calibration energy spectrum are fit with a peak shape function and the raw energies are converted into calibrated energies through a linear transformation. The energy peaks used are the 238 keV, 583 keV, 727 keV, and 2614.5 keV peaks. The linear transformation is

$$E(\mathrm{keV}) = \mathrm{slope} \times E(ADC) + \mathrm{offset} \,. \tag{2.4}$$

The peak shape function contains several components: a gaussian peak plus low energy tail, and a background with a step and quadratic energy dependence,

$$R(E) = \frac{1-f}{\sqrt{2\pi\sigma^2}} \exp\left(\frac{(E-\mu)^2}{2\sigma^2}\right) + \frac{f}{2\gamma} \exp\left(\frac{\sigma^2}{2\gamma^2} + \frac{E-\mu}{\gamma}\right) \mathrm{erfc}\left(\frac{\sigma}{\sqrt{2}\gamma} + \frac{E-\mu}{2\sigma}\right) \tag{2.5}$$

$$B(E) = \frac{H_s}{2} \mathrm{erfc}\left(\frac{E-\mu}{\sqrt{2}\sigma}\right) + \frac{3q}{2}\left(E^2 - \frac{1}{3}\right) + mE + b \,. \tag{2.6}$$

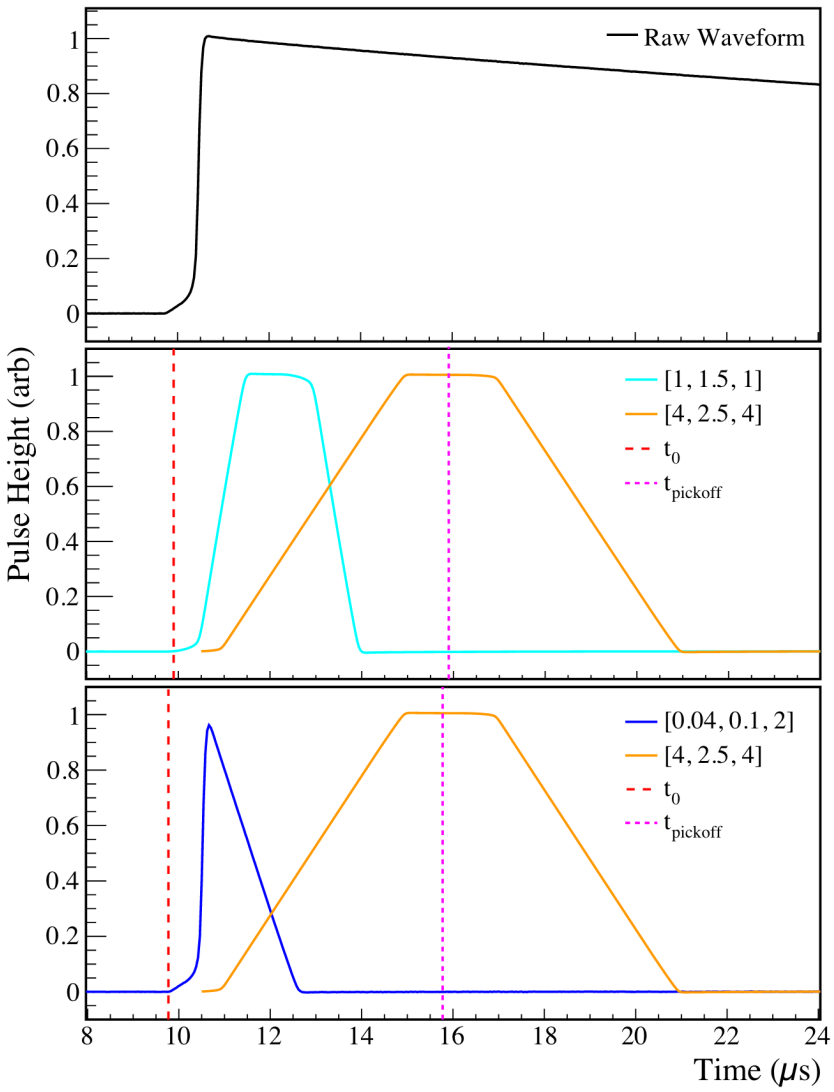

Figure 2.9: Top: a normalized raw waveform. Middle: Symmetric leading-edge filtered waveform and energy trapezoidal-filtered waveform. Bottom: asymmetry leading-edge (blue) waveform and energy (orange) trapezoidal-filtered waveform. The filters are labeled as [*rise*, *flat*, *fall*] in μs. The red dashed line indicates the start time t_0 of the waveform and the pink dashed line indicates the energy pickoff time. Fig. from ref. [72].

μ is the mean of the Gaussian, σ is the standard deviation of the Gaussian, f is the fraction of the amplitude that's taken up by the low energy tail, γ is the decay constant of the tail exponential, H_s is the height of the step background as a fraction of the peak amplitude, b is the flat portion of the background, m is the linear proportionality constant of the background, and q is the quadratic constant for the background. The step contribution to the background shape comes from the forward scattering of γ-rays before depositing the remaining energy into the HPGe detector. A fit to the ^{208}Tl γ energy peak is shown in Fig. 2.10. Additional corrections are made to energy to improve the linearity. All calibrations in a dataset are combined together, for high statistics, and a quadratic is fit to the energy deviation vs energy of the 18 most prominent peaks above 200 keV to correct for differences with the known literature values.

The energy resolution, for a particular energy, is given by the full width at half maximum (FWHM) of the energy peak. The FWHM is comprised of three components: the electronics noise (Γ_n), the Fano noise (Γ_F), and extra broadening from incomplete charge collection (Γ_q), $\text{FWHM}_E(E) = \sqrt{\Gamma_n^2 + \Gamma_F^2 E + \Gamma_q^2 E^2}$ [74]. A germanium detector has two possible energy deposition mechanisms, ionization of electron-hole pairs and phonons from lattice vibrations. Since the phonon excitation energy is less than that for electron-hole pairs, many more phonons are generated than charge-carriers, which reduces the observed variance in charge-carriers relative to what is expected from poisson statistics [75]. The Fano noise is the poisson statistics variance scaled by the detector material's intrinsic Fano factor, the ratio of observed variance over the expected poisson variance. The full calibration energy spectrum and $\text{FWHM}_E(E)$ are shown in Fig. 2.11.

2.4.2 Multi-site Discrimination

A more detailed explanation of multi-site discrimination is included in section 3, but a quick overview is shown here for completeness when describing the overall analysis for the MAJORANA DEMONSTRATOR. PPC detectors have a particular advantage in that waveforms from γ-rays that scatter multiple times within one detector can be designated as background

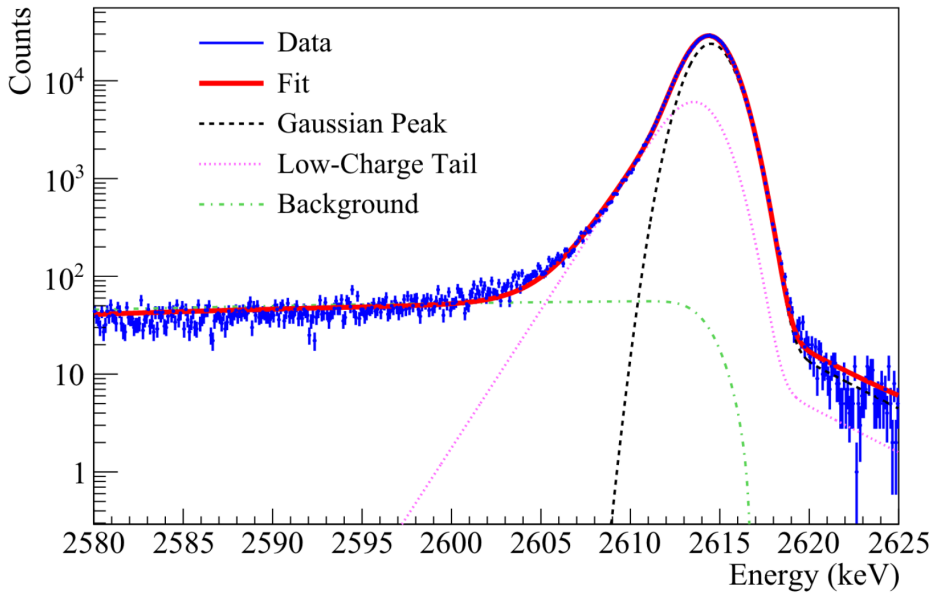

Figure 2.10: A fit of the peak shape from Eq. 2.5 and the background function from Eq. 2.6 to the 2614.5 keV γ peak from ^{208}Tl. The background function is shown in green and the individual terms of the peak shape is shown in black and magenta. The red line is the sum of the peak shape and background function. Fig. from ref. [74].

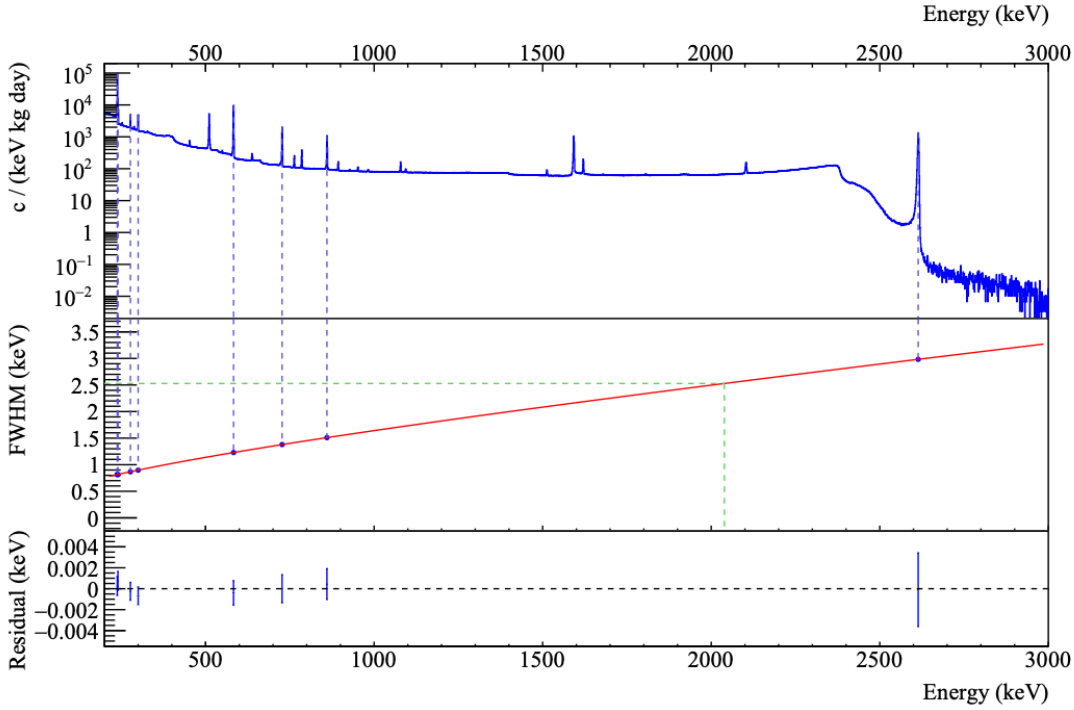

Figure 2.11: Top: the combined energy spectrum for all calibrations in DS0−DS6a for MAJORANA analysis result from 2019. The vertical lines are the γ lines used in the final energy calibration in each data set. Center is the exposure-weighted energy resolution for each energy peak used in the calibration fit. The green lines indicate the exposure-weighted average resolution of 2.53 keV at $Q_{\beta\beta}$, 2039 keV. Bottom: the fit residuals for the FWHM. Fig. from ref. [74].

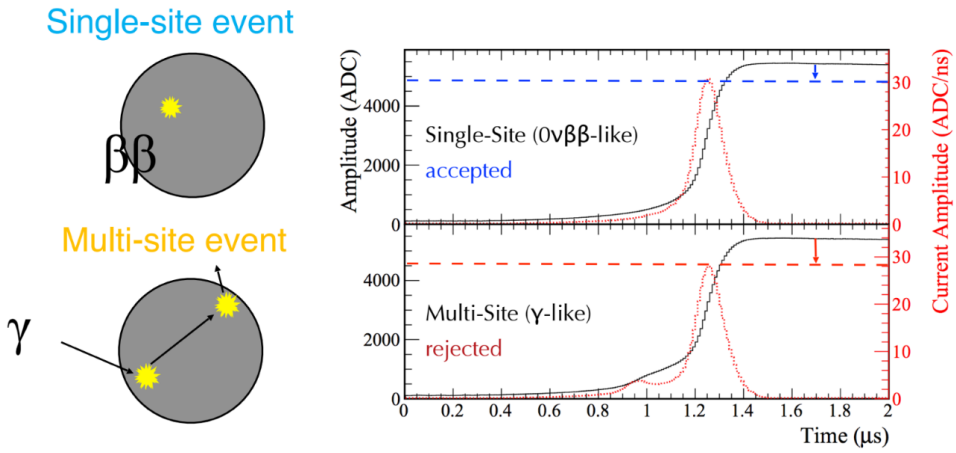

Figure 2.12: (left) Simplified diagram of a $\beta\beta$-like energy deposition (top) as opposed to a scattered γ background deposition in multiple locations (bottom). (right) The resulting waveforms and currents from a single-site deposition (top) and a multi-site deposition (bottom) both with the same total energy. The identifying feature of a multi-site event is the lower maximum current amplitude compared to the maximum current amplitude of a single-site waveform of the same energy.

through pulse-shape analysis. The dominant source for compton scattered γ-rays is the decay of ^{208}Tl in Fig. 2.5b, which has a full energy deposition of 2614.5 keV. Since the magnitude of the weighting potential is localized at the p^+ contact, events that deposit their energy at different equipotential surfaces within the detector will have different drift-times to full charge collection. This is beneficial because $0\nu\beta\beta$ events are expected to deposit their full energy within a single localized region, so any events that can be identified as having an energy deposition that spans multiple locations in a single detector can be removed as background, see Fig. 2.12. When comparing a single-site waveform with a multi-site waveform of the same energy, the maximum current amplitude, the maximum of the derative of the waveform, is lower for the multi-site waveform and is the distinguishing feature for identifying a multi-site background event.

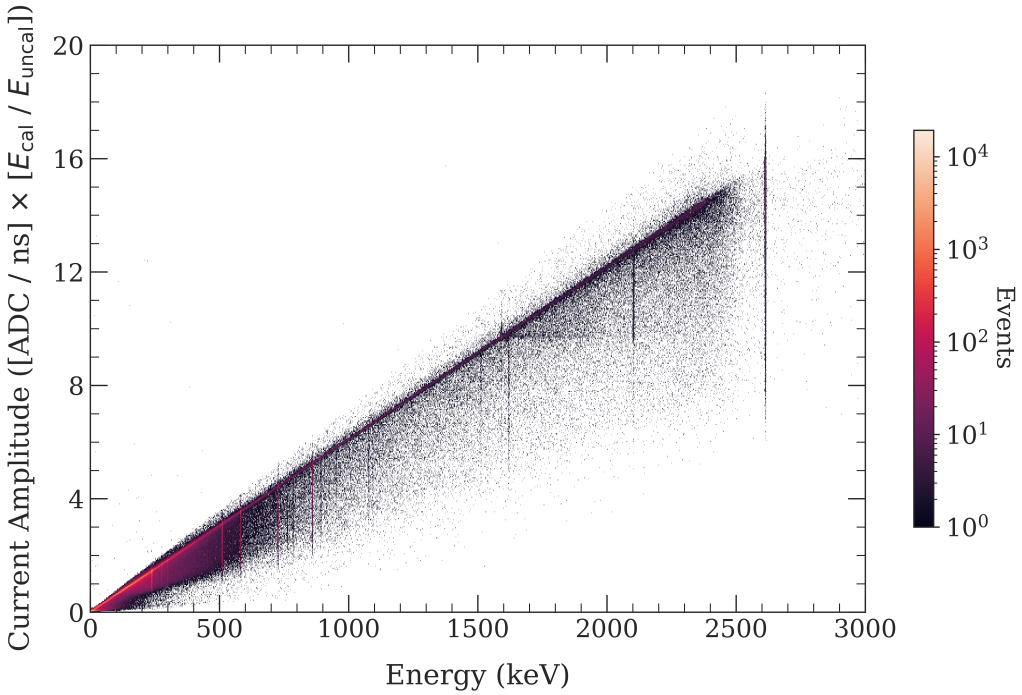

Figure 2.13: The initial spectrum of maximum current amplitude vs energy, for a single detector that is analyzed to produce a multi-site cut. Events that show degraded current amplitude below the continuum slope are multi-site events.

The *multi-site discrimination* parameter (AvsE) is tuned by accepting 90% of excess events above the ^{208}Tl γ compton continuum in a known single-site event population during a ^{228}Th calibration. This is the 1592.5 keV *double-escape peak* (DEP) of from ^{208}Tl. In order to tune AvsE, more statistics are necessary than are collected in the weekly calibrations, and hence AvsE is tuned by analyzing bi-monthly "long calibrations". The AvsE cut is designed by analyzing the current amplitude vs energy spectrum, see Fig. 2.13. All energy-dependence, width energy-dependence, and drift-time dependence is removed and the cut is scaled to accept 90% of excess events above the continuum at the DEP.

The AvsE parameter is defined as the following equation where all events with AvsE

> -1 are accepted as single-site:

$$\text{AvsE} \equiv -\frac{A \cdot E_{\text{cal}}/E_{\text{uncal}} - \text{quad}(E_{\text{cal}}, a, b, c) - \exp(E_{\text{cal}}, d, \tau)}{\text{FWHM}_{\text{A}}(\text{E}_{\text{cal}}) \cdot \text{s}} \tag{2.7}$$

The quadratic and exponential functions are empirically fit to remove the energy-dependence of the maximum current amplitude. $\text{FWHM}_A(E) = \sqrt{a_0^2 + (a_1 E)^2 + (a_2^2 E^2)^2 + (a_3^3 E^3)^2}$ is an empirically fit function to remove the width-energy dependence, which is calculated by measuring the changing width of multiple DEPs with energy for each detector in a ^{56}Co calibration. s is the scale factor to scale the AvsE cut value to -1. The maximum current estimator A is the slope of a linear fit to a small range of the waveform, which serves as an approximation of the time derivative. The DEP sits on top of a compton continuum background so the AvsE distribution of this background must be subtracted first before calculating the acceptance (side-band subtraction). The side-band energy windows are 1570$-$1580 keV and 1600$-$1610 keV. The signal acceptance and and signal acceptance statistical uncertainty are then

$$\epsilon = \frac{N_c - \tau B_c}{N - \tau B} \tag{2.8}$$

$$\left(\frac{\sigma_\epsilon}{\epsilon}\right)^2 = \frac{N + \tau^2 B}{(N - \tau B)^2} + \frac{N_c + \tau^2 B_c}{(N_c - \tau B_c)^2} - 2\frac{N_c + \tau^2 B_c}{(N - \tau B)(N_c - \tau B_c)}\,. \tag{2.9}$$

N is the number of total events in the DEP region, B is the total number of events in the side-band regions, N_c and B_c are what's cut for both regions and τ is the ratio of the DEP energy window size to side-band regions size [76]. The AvsE DEP acceptance is evaluated for each detector individually and the total acceptance is the exposure weighted averaged. AvsE for the energy window around the DEP has some drift-time dependence., due to a correlation with the maximum current A and the drift-time. Single-site events closer to the point contact will have a shorter time to charge collection than DEP events which are most likely to occur towards the corners of the detectors. This causes a multi-site parameter to cut asymmetrically across all drift-times. This is shown in Fig. 3.10. Drift-time is defined as the difference between the 90% rise-time of a waveform and the initial t_0 as determined

in Fig. 2.10 from an asymmetric trapezoidal filter. To remove the drift-time dependence a rotation is done in AvsE vs drift-time space on the side-band subtracted DEP to align the principle components with the axes.

$$\text{AvsE}_{corr} = [(\Delta t - \overline{\Delta t}_{dep})\sin(\theta) + (A_{corr} - \overline{A}_{dep})\cos(\theta) + \overline{A}_{dep}] \times (-1/s) \tag{2.10}$$

How much the drift-time correction effects the AvsE cut depends on the spread in drift-times for a particular detector. The final tuned AvsE spectrum for a single detector in one long calibration is shown in Fig. 2.14.

2.4.3 Delayed Charge Recovery

Additional sources of background that concern the MAJORANA DEMONSTRATOR include the various decay chains for radon isotopes, in particular ^{222}Rn as shown in Fig. 2.5a. Deposits of ^{222}Rn on the PPC detector passivated surface can produce 5.304 MeV α's, from the decay of ^{210}Po. This creates degraded charge depositions inside the detector that can occur within the $Q_{\beta\beta}$ ROI [77]. ^{222}Rn plates out on the detector surfaces, especially during assembly, and the decay of ^{210}Po, supported by ^{210}Pb gives a constant α rate throughout the experiment's lifetime. A 5.304 MeV α has a penetration depth in germanium of about 20 μm and therefore does not produce background signals when incident on the lithiated dead-layer, however a 5.304 MeV α has enough energy to penetrate the thin passivated layer and deposit energy within the germanium crystal. PPC detectors are vulnerable to α backgrounds due to their large passivated surface compared to some other HPGe designs.

Charge depositions near the passivated surface have drastically reduced charge mobility, giving waveforms that have a tail with a slow rise component relative to bulk-like signal events, Fig. 2.15. The passivated surface appears to contain strong trapping sites that re-release charge on a slow time scale. This is the characteristic signal for a degraded α deposition through the passivated surface. The *delayed charge recovery* parameter (DCR) uses the pole-zero corrected waveform slope in addition to some energy dependent corrections to produce a cut that removes α events with a signal acceptance greater than 98%. It is

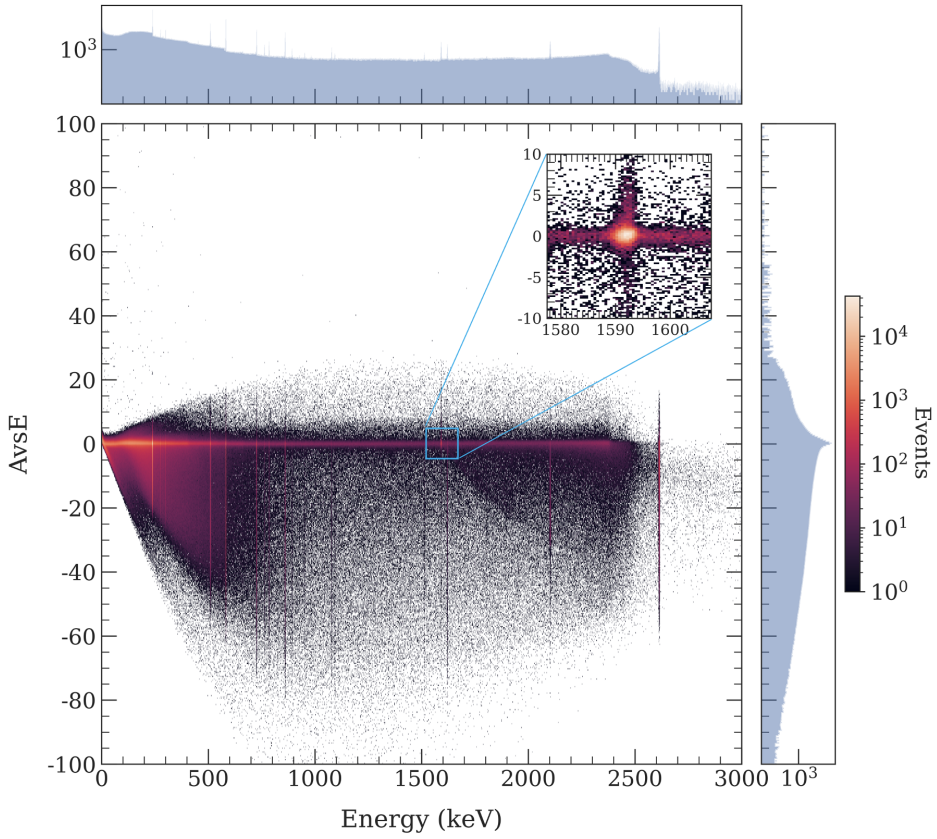

Figure 2.14: AvsE vs Energy after all corrections have been applied for one detector in one long calibration. Note the DEP at 1592.5 keV in the inset plot which has very little spread below AvsE= 0 indicating that this energy peak is predominantly made of single-site events.

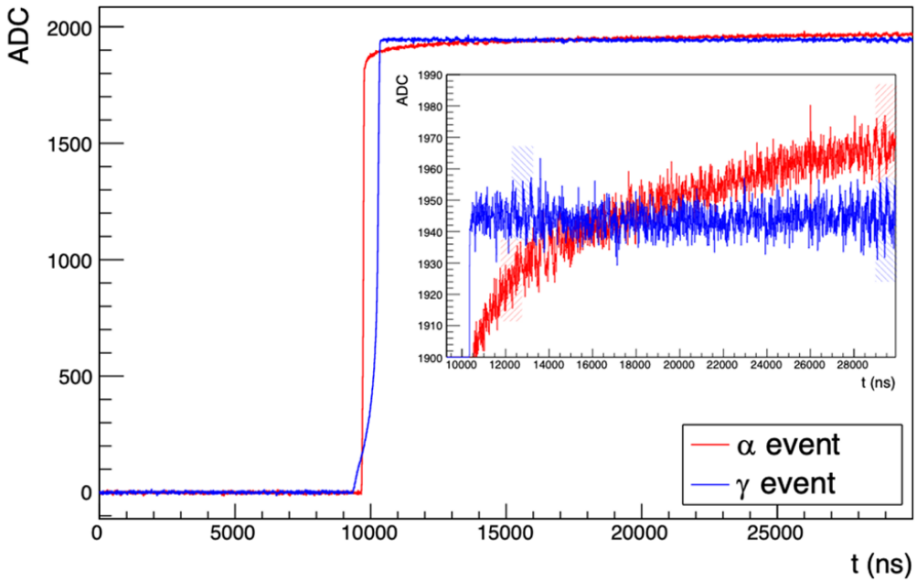

Figure 2.15: An example of an α energy deposition and bulk γ deposition. The inset plot shows a close up near the top of the rising edge. The distinguishing feature that's used to differentiate these two events are the slopes computed from the shaded blue regions and shaded red regions. Fig. from ref. [77].

computed as

$$\mathrm{DCR} = \frac{\delta - \alpha E}{\beta E + \gamma}\,, \tag{2.11}$$

where δ, the waveform slope, is scaled by an energy dependent mean, $\mu = \alpha E$, and an energy dependent width, $\sigma = \beta E + \gamma$. α, β, and γ are tuned to give a DCR distribution that is Gaussian in shape with a zero mean and unit standard deviation. These parameters are fit per detector for each set of calibration runs and the DCR cut is set to have a nominal signal acceptance of 99% in the energy window 2028 keV$-$2050 keV around $Q_{\beta\beta}$; DCR<2.326 passes the cut. α depositions are not dominant in calibration data so DCR is tuned to a high signal acceptance, while α rejection efficiency in background is estimated from detector characterization work [77]. DCR also has a drift-time correction to remove the drift-time dependence on the DCR parameter. The slope estimation δ has some dependence on the

drift-time since events that occur farther from the point contact will have slower times to charge collection than events near the point contact. The drift-time dependence is removed by re-scaling DCR:

$$\mathrm{DCR}_{\mathrm{corr}} = \frac{1}{\sigma_c}\left[(\mathrm{DCR} - \mu_{\mathrm{DCR}}) - \frac{t_{\mathrm{drift}} - \mu_{\mathrm{drift}}}{m} - \mu_c\right]. \tag{2.12}$$

DCR is centered by μ_{DCR}, the drift-time dependence is then projected onto an axis perpendicular to DCR, and then DCR is scaled by subtracting a μ_c and scaled by σ_c to create a new normalized Gaussian-like distribution, $\mathrm{DCR}_{\mathrm{corr}}$. The DCR acceptance rate is calculated by the ratio of total passed events over total events with Poisson errors for the efficiency window 2028 keV - 2050 keV after the AvsE multi-site cut,

$$\epsilon = \frac{N_c}{N} \tag{2.13}$$

$$\sigma = \sqrt{\frac{\epsilon(1-\epsilon)}{N}}\,. \tag{2.14}$$

The DCR signal acceptance is computed for each detector individually and the total signal acceptance is the exposure weighted average.

2.4.4 High AvsE

In addition to the AvsE and DCR cuts there is another AvsE cut, AvsE<9, used to remove events that originate from a small volume around the point contact. Since the charge collection is the fastest near the point contact, multi-site events with at least one event near the point contact and α particles that deposit near the point contact evade the previoulsy mentioned AvsE and DCR cuts. A high AvsE cut effectively is a volumetric cut around the p-type point contact where the weighting potential is highly nonlinear. This also effectively removes exposure, but since the α background rate in this region is large enough, a high AvsE signal acceptance of 98% is expected to increase the half-life sensitivity of the experiment. The high AvsE signal acceptance is calculated for all the detectors together after applying a

multi-site cut using Eq. 2.8, see Fig. 2.16a shows the AvsE vs DCR distributions for a 2350 - 5000 keV window where α's are more dominant and Fig. 2.16b shows the same distribution for the background estimation window excluding the ROI around $Q_{\beta\beta}$. Inferring from Fig. 2.16a, where the α background is dominant, the background events in the upper-left region in Fig. 2.16b is attributed to α depositions near or on the point contact.

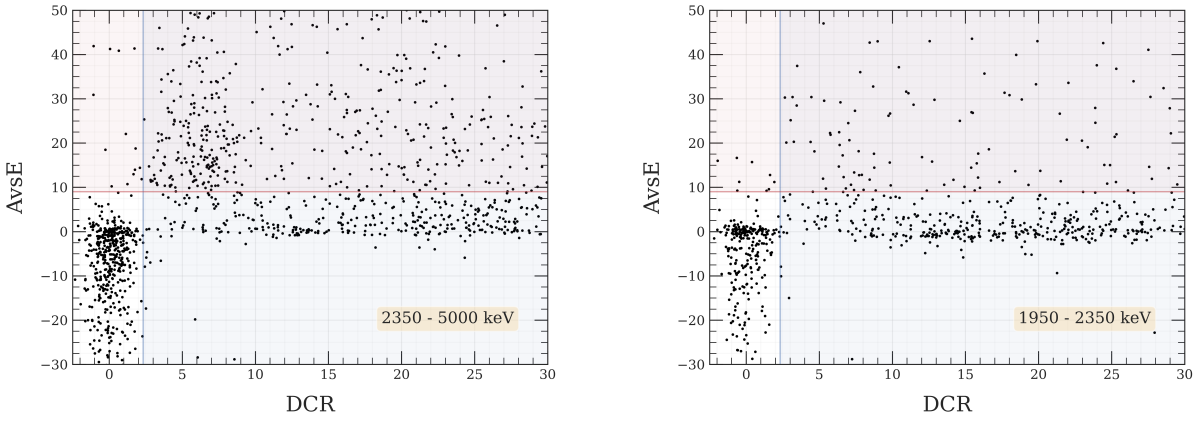

(a) (b)

Figure 2.16: The AvsE vs DCR distribution for background physics data in the full enriched data-taking range for (a) the 2350-5000 keV energy range and (b) the 1950 - 2350 keV background estimation window. The red shaded regions indicate all events cut by the AvsE $<$ 9 cut and the blue shaded regions indicate all events cut by the DCR $<$ 2.326 cut. The region in the upper left corner is attributed to α depositions near the point contact that pass the DCR cut and potential multi-site events where one of the site depositions is near the point contact.

2.4.5 Late Charge

In between the detector bulk and the lithiated dead-layer of the n^+ contact is a transition region where the charge mobility is significantly lower than the detector bulk. Backgrounds

such as high energy β's and multi-site energy depositions both have the possibility of depositing energy in the transition layer, while at the same time evading the other analysis cut parameters. To identify such events, a *late charge* (LQ) parameter is measured by calculating the area above a pole-zero corrected waveform starting at the 80% rise-time point, removing a drift-time dependence, and then scaling to mean zero, unit standard deviation:

$$\mathrm{LQ} = \frac{\mathrm{LQ80} - \mathrm{offset} - \mathrm{slope} \times \Delta t}{\sigma} \,. \tag{2.15}$$

Here, LQ80 is the integral above the waveform (offset$-$slope$\times\Delta t$) is the drift-time dependent mean, and σ is the standard deviation of the distribution. An example of a late charge waveform in comparison to a single-site bulk waveform is shown in Fig. 2.17.

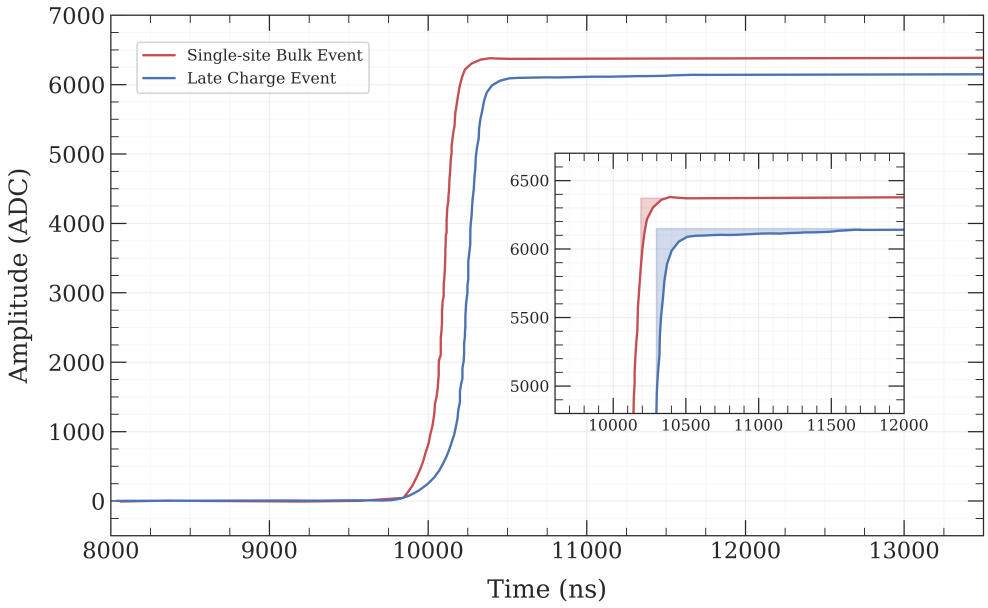

Figure 2.17: Comparison of a single-site bulk event in red and a late charge event in blue. Late Charge uses the area above the waveform after 80% of the charge is collected to cut events with slow charge collection.

The LQ parameter is tuned during the ^{228}Th calibrations where the cut is set at 5σ away

from the mean to give a high signal acceptance of greater than 99%. LQ < 5 events pass the cut and represents a cut that excludes the detector volume which comprises the transition layer. Incidentally, the LQ parameter has some overlap with AvsE and DCR, since both AvsE and DCR detect waveform shapes that also effect the area above the waveform, see Fig. 2.18. The LQ parameter in some cases will identify waveforms with delayed charge collection and in some cases will identify multi-site events where one of the events is near the point contact. The LQ parameter will also identify multi-site events where one of the energy depositions is small and far from the point contact, which are missed by AvsE.

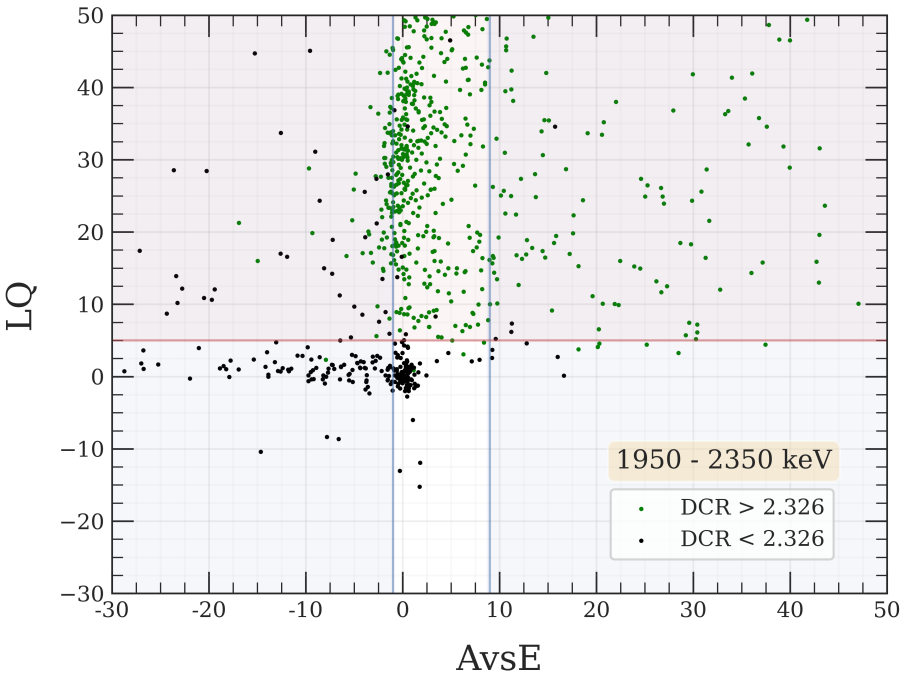

Figure 2.18: LQ vs AvsE events in the 1950−2350 keV background estimation window. The blue region indicate events cut by AvsE and the red region indicate events cut by LQ. Green points indicate events that are cut by DCR. This shows the high correlation of LQ with DCR, high correlation with the high AvsE cut, and some correlation with the multi-site AvsE cut.

2.4.6 Data Cleaning

Before an analysis can be done on the physics background data, imperfections that produce a significant error in estimating any one of the analysis parameters are removed. This is done by examining the open calibration and physics data to infer what run ranges in the open and blind data might be unstable. There are four main levels of data cleaning: run-level data quality, event-level data quality, waveform-level data cleaning, and run-level channel selection.

Run-level data quality assesses the quality of data during the time the data is taken. The run-level data quality rankings are used to identify run ranges that have low background, high background, parts of the experiment disassembled, are transition periods when the calibration source is inserted or retracted, or are periods of disruptive work or testing. Runs that are designated as low background and have at least one module operational are used in the $0\nu\beta\beta$ decay analysis under the good runs list. Event-level data quality remove liquid nitrogen fill periods and muon veto periods.

Waveform-level data cleaning identifies individual waveforms that have anomalies due to electronics noise, pile-up, digitization errors etc. This includes waveforms with large positive/negative spikes, early or late trigger positions, positive or negative saturation, and two or more single energy depositions that happen in the same waveform time-window. The waveform data cleaning efficiency is equal to the fraction of waveforms remaining in the physics data and is found to be 0.999 ± 0.001 for the entire data-taking period.

The run-level channel selection identifies detector instabilities based on criteria from the analysis parameters (Energy, AvsE, and DCR) as well as criteria from run selection. Run selection primarily identifies detectors that are not operational for certain run range periods. All analysis parameters have criteria where the parameter was impossible to tune or is unstable for some period of time. An in-depth description of the AvsE criteria and stability studies are discussed in Ch. 3.

2.4.7 Exposure and Deadtime

The exposure of a $0\nu\beta\beta$ decay experiment is the product of the active isotope mass with the livetime. The active isotope mass is

$$N = \frac{N_A M_D f_{76}}{M_{Ge}} \,. \tag{2.16}$$

N_A is Avogadro's number, M_D is the total detector mass, f_{76} is the isotopic fraction of ^{76}Ge, and M_{Ge} is the atomic weight of the enriched material. The total active mass of the detector is estimated by measuring the thickness of the dead-layer on the outer edge of each detector. This is typically done with a ^{133}Ba source, which produces two low-energy γ peaks where the detected peak intensity ratio is sensitive to the dead-layer thickness. Additional work within the MAJORANA collaboration has been done to characterize dead-layer thicknesses from charge diffusion models [78, 79]. The isotopic fraction of germanium samples can be measured using mass spectrometry.

The live-time is the total time of an experiment for which it was recording data (subtracting the dead-time from the total run-time). The run-time is calculated by reading the digitizer trigger times at the beginning and end of each run with a 10 ns sampling period. During the run-time each detector channel is not sensitive to $0\nu\beta\beta$ decay events during the whole run-time due to experiment dead-time. Dead-time can originate from the hardware, pulser, liquid nitrogen fills, and muon veto.

- Hardware Deadtime: For brief periods of time the hardware is unable to trigger and record an event. To calculate the deadtime a pulser with a known frequency is injected into each channel. The deadtime is estimated from measuring the expected number of pulser events compared with the total number of actual pulser events found in the channel:

  $$D_{ij,hardware} = R_{ij}(1 - N_{found,ij}/N_{expected,ij}) \,. \tag{2.17}$$

  i sums over channel and j sums over run. R is the run-time and N are the number of pulser events.

- Pulser Deadtime: The pulser input signal is a square wave with a period of 8.388608 seconds. The pulser deadtime originates from a retrigger deadtime of 62 μs or 100 μs depending on if multi-sampling is enabled (waveform rising edge contains more samples than the other parts of the waveform). This measures the delay time for each output pulse given an input pulse to the pulser.

$$D_{ij,pulser} = N_{found,ij} D_{retrigger,ij} \tag{2.18}$$

- LN Fill Deadtime: The automatic LN fill system is known to produce large amounts of micro-phonic noise while a fill is taking place. Veto periods are assigned for the experiment with LN fill start and stop times from the LN control hardware. In early datasets this was set to a constant 20 minute veto period.

- Muon Veto Dead-time: The muon veto dead-time originates from the time lost during a veto of a muon event passing through the experiment, detected by the muon veto panels. Muons passing through the MAJORANA DEMONSTRATOR are highly ionizing and generate showers of charge carriers that obscure searches for low background physics. Each muon event contributes to 1 second or less of dead-time.

For a single channel the live-time is

$$L = (R - D_{LN} - D_{veto}) \times (1 - \frac{D_{hardware}}{R} - \frac{N_p D_p}{R}) \tag{2.19}$$

This equation accounts for the overlap of LN fill and muon veto dead-time with the hardware and pulser dead-time (N_p is the number of pulses and D_p is the pulser dead-time). The exposure is then the product of the active detector mass, m_i, and live-time, $L_{i,j}$ summed

over channel and run number,

$$E = \sum_{i,j}^{chan,run} m_i L_{i,j} \tag{2.20}$$

$$\sigma^k_{exp} = m_k(L_{HG,k} + L_{LG,k})\sqrt{\left(\frac{\sigma_{m_k}}{m_k}\right)^2 + \frac{\sigma^2_{HG,k} + \sigma^2_{LG,k}}{(L_{HG,k} + L_{LG,k})^2}}\,. \tag{2.21}$$

L is the live-time which is displayed for both high gain and low gain channels, m is the active mass, and the σ's are the uncertainties on each. High gain channels are used by default, but if an analysis selects a high gain channel as unstable in the data cleaning then a low gain channel will be used if it is not marked as unstable. The full exposure uncertainty is then the linear sum of Eq. 2.21 over the detector index k.

2.5 Results

Combining all of the data quality and analysis parameter cuts over a total active exposure of 64.5 ± 0.93 kg yr results in the final energy spectrum for background physics events from the MAJORANA DEMONSTRATOR, see Fig. 2.19 and Fig. 2.20. The spectrum shows clearly the broad $2\nu\beta\beta$ energy spectrum from ^{76}Ge and remaining background counts in the background estimation window. The background estimation window (1950−2350 keV) is an energy window with a flat background that surrounds the ROI. It serves as a region to estimate the number of expected counts to fall within the ROI and as a metric for the background suppression magnitude of the experiment. 10 keV regions around the 2103 keV ^{208}Tl single escape peak, 2118 keV and 2204 keV ^{214}Bi γ-rays and a 4 keV ROI around 2039 keV are excluded from the background estimation window. Incorporating all the signal acceptances, the lower half-life limit is then defined by

$$T_{1/2} > \ln(2)\frac{NT\epsilon_{det}\epsilon_{res}}{S}\,. \tag{2.22}$$

N is the molar mass of the active isotope and T is the live-time, ϵ_{det} is the total signal detection efficiency after all analysis cuts are applied, ϵ_{res} is the ROI containment efficiency,

and S is the upper limit on signal counts based on the observed data.

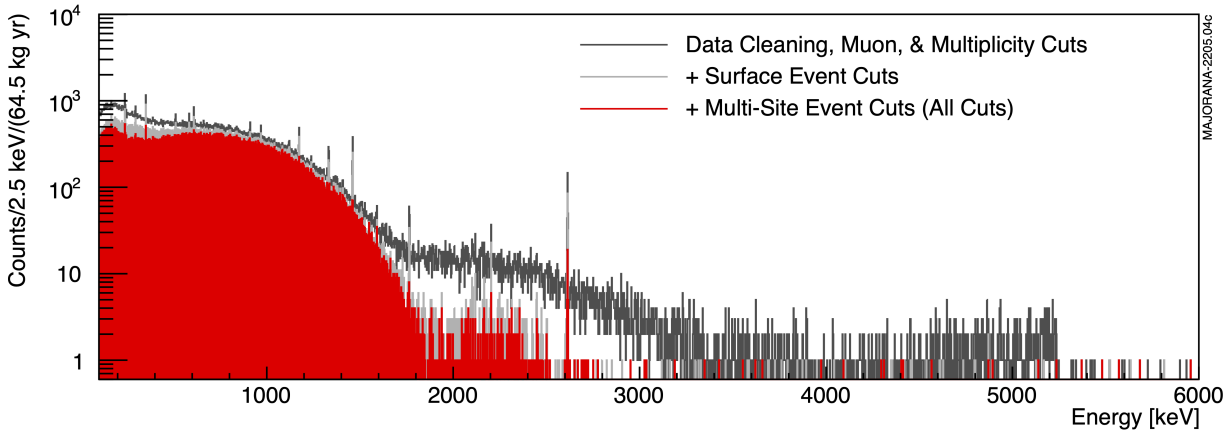

Figure 2.19: Energy of events remaining in the full background spectrum after several levels of data cleaning and analysis cuts. Multiplicity cuts remove γ events that scatter in multiple detectors simultaneously, Surface Event Cuts include DCR and LQ, and Multi-Site Event Cuts include the AvsE multi-site cut and high AvsE cut. Energies below 2000 keV are dominated by the $2\nu\beta\beta$ spectrum. Fig. from ref. [63].

ϵ_{det} is calculated from combining all of the analysis parameter efficiencies including the containment efficiency, ϵ_{cont}, which estimates the percentage of signal-like events that deposit their entire energy within the HPGe detectors, Table 2.1. Some fraction of $0\nu\beta\beta$ decay energy depositions will lose energy due to bremsstrahlung, X-rays, or electrons escaping the active volume of the detector. The fraction of $0\nu\beta\beta$ decay events that deposit all of their energy inside each active detector volume is calculated from simulating millions of $0\nu\beta\beta$ decay events in a GEANT4 based model of the MAJORANA DEMONSTRATOR. ϵ_{res} is the ROI efficiency and measures the probability of a signal event falling with in the ROI.

The *background index* (BI) is measured by counting the number of events that fall within the background estimation window after all analysis cuts, Fig. 2.20. The background is taken to be a flat distribution background, suggested from simulation, and is used to estimate the

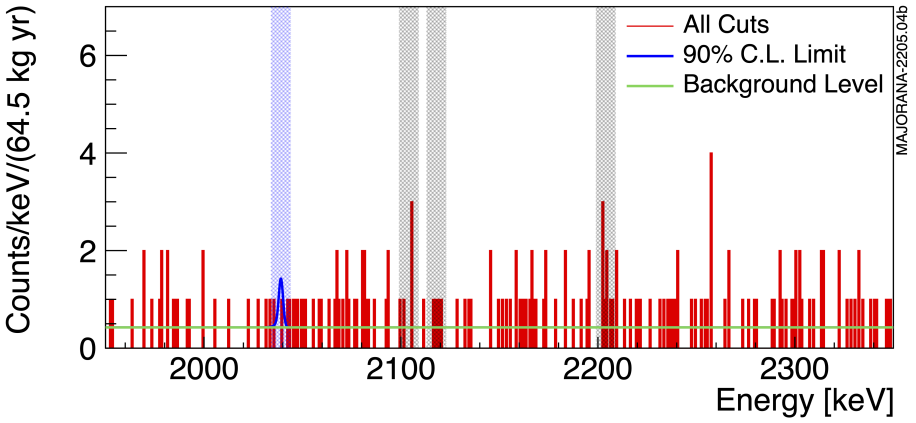

Figure 2.20: Remaing events in the background estimation window. 10 keV windows shown in gray exclude known energy peaks from the flat background estimation. The blue region highlights the 4 keV ROI and includes the 90% confidence level limit. Fig. from ref. [63].

average expected number of background counts within the ROI to calculate the half-life limit. The background index achieved for each dataset is shown in Table 2.2.

The lower half-life limit is calculated by performing a frequentist profile likelihood analysis on the strength of a possible $0\nu\beta\beta$ decay signal $\mathcal{S} = 1/T_{1/2}$[80]. The likelihood is defined assuming a Gaussian distribution for the signal and a flat distribution for the background and is indexed for each dataset i.

$$\mathcal{L}_i(\mathcal{D}_i|\mathcal{S}, \mathrm{BI}_i, \theta_i) = \prod_{j=1}^{N_i^{\mathrm{obs}}} \frac{1}{\mu_i^B + \mu_i^S} \left[\mu_i^B \frac{1}{\Delta E} + \mu_i^S \frac{1}{\sqrt{2\pi}\sigma_i} \exp\left(\frac{-(E - Q_{\beta\beta} - \delta_i)^2}{2\sigma_i^2} \right) \right] \tag{2.23}$$

$$\mu_i^S = \ln(2)(N_A/ma)\epsilon_i \mathcal{E}_i \mathcal{S} \tag{2.24}$$

$$\mu_i^B = \mathcal{E}_i \mathrm{BI}_i \Delta E \tag{2.25}$$

μ_i^S is the expected number of $0\nu\beta\beta$ events with $S = 1/T_{1/2}$, ϵ_i the total efficiency, and $\mathcal{E}_i$ the exposure. μ_i^B is the measured number of background counts in the background estimation

	PPCs	ICPCs
Total Exposure	67.94 kg yr	3.12 kg yr
Active Exposure	61.64 ± 0.89 kg yr	2.82 ± 0.04 kg yr
FWHM@2039 keV	2.52 ± 0.08 keV	2.55 ± 0.09 keV
^{76}Ge Enrichment	$87.4 \pm 0.5\%$	$88.0 \pm 1.0\%$
PSD Eff.	$86.1 \pm 3.9\%$	$81.0^{+5.3}_{-7.3}\%$
Data Cleaning	$99.9 \pm 0.1\%$	$99.9 \pm 0.1\%$
Low AvsE Cut	$89.9^{+3.3}_{-3.2}\%$	$85.2^{+4.2}_{-5.9}\%$
DCR Cut	$98.5 \pm 0.7\%$	$97.9 \pm 1.1\%$
High AvsE Cut	$97.9 \pm 1.0\%$	$97.8 \pm 1.4\%$
Late Charge Cut	$99.3 \pm 0.7\%$	$99.5^{+0.5}_{-0.9}\%$
Containment Eff.	$90.8 \pm 1.3\%$	$91.9 \pm 0.8\%$
ROI Peak Eff.	$86.3 \pm 1.1\%$	$86.9 \pm 1.2\%$

Table 2.1: A summary of all exposures and analysis parameter efficiencies for the full enriched data-taking period split between PPC and ICPC detectors. ϵ_{cont} is the containment efficiency and ϵ_{res} is the ROI efficiency.

window with energy window width ΔE and background index BI_i. In Eq. 2.23 E_j are the individual event energies, δ_i are systematic offsets for the energies, $\sigma_i = \mathrm{FWHM}_i/2\sqrt{2\ln(2)}$ is the energy resolution at $Q_{\beta\beta}$, and $\theta_i = \{\epsilon_i, \sigma_i, \delta_i\}$. The full likelihood is constructed by multiplying the likelihood for each dataset weighted by the signal plus background Poisson distribution,

$$\mathcal{L}_i(\boldsymbol{\mathcal{D}}|\mathcal{S}, \mathbf{BI}, \boldsymbol{\theta}) = \prod_i \left[\frac{e^{-(\mu_i^S + \mu_i^B)}(\mu_i^S + \mu_i^B)^{N_i^{\mathrm{obs}}}}{N_i^{\mathrm{obs}_i}!} \times \mathcal{L}_i(\mathcal{D}_i|\mathcal{S}, \mathrm{BI}_i, \theta_i) \right] . \tag{2.26}$$

A two-sided test statistics is made by using the profile likelihood ratio $\lambda(S)$ [81],

$$t_{\mathcal{S}} = -2\ln[\lambda(\mathcal{S})] = -2\ln\left[\frac{\mathcal{L}(\mathcal{S}, \widehat{\widehat{\mathbf{BI}}}, \hat{\hat{\boldsymbol{\theta}}})}{\mathcal{L}(\hat{\mathcal{S}}, \widehat{\mathbf{BI}}, \hat{\boldsymbol{\theta}})} \right] . \tag{2.27}$$

The numerator includes values of the background index and θ which maximize the likelihood for a fixed signal $\mathcal{S}$, $\hat{\theta}$, and $\hat{\hat{\theta}}$, respectively The denominator is the absolute maximum

Data set	Window cts	BI $\times 10^{-3}$ cts/(keV kg yr)	ROI (keV)	ROI BG (cts)
DS0	11	$27.20^{+9.06}_{-7.41}$	3.75	0.11
DS1	4	$4.92^{+2.89}_{-2.07}$	3.79	0.04
DS2	1	$2.48^{+3.37}_{-1.73}$	3.75	0.000
DS3	0	< 2.73	3.75	0.000
DS4	0	< 10.21	3.53	0.000
DS5a	9	$9.20^{+3.42}_{-2.74}$	4.08	0.1
DS5b	0	< 1.49	3.77	0.0
DS5c	5	$6.41^{+3.31}_{-2.46}$	3.70	0.05
DS6a	29	$5.46^{+1.08}_{-0.95}$	3.63	0.29
DS6b	29	$8.24^{+1.63}_{-1.44}$	3.62	0.29
DS6c	20	$4.19^{+1.01}_{-0.87}$	3.62	0.20
DS7	17	$10.56^{+2.78}_{-2.36}$	4.04	0.19
DS8P	24	$9.54^{+2.09}_{-1.82}$	3.46	0.23
DS8I	4	$3.94^{+2.31}_{-1.66}$	3.57	0.04
Total	153	$6.59^{+0.56}_{-0.53}$	3.57	1.52

Table 2.2: The set of background counts and background indexes achieved for each dataset during the enriched data-taking period. Window is the background estimation window of 360 keV region inside 1950 keV - 2350 keV with known peaks and ROI excluded. DS0 is a high background period. that included one module and a partially built shielding.

likelihood. The confidence intervals are constructed by monte-carlo sampling different realizations of the experiment from the signal acceptances and uncertainties for a given S. This determines the probability distribution of $t_{\mathcal{S}}$, $f(t_{\mathcal{S}}|\mathcal{S}_j)$, for each value of $\mathcal{S}$ and finds $t_c(\mathcal{S})$ for which 90% of the monte-carlo trials give $t_{\mathcal{S}} < t_c(\mathcal{S})$. This is calculated using

$$p_{\mathcal{S}_j} = \int_{t_{\rm obs}}^{\infty} f(t_{\mathcal{S}}|\mathcal{S}_j)\, d(t_{\mathcal{S}_|}) \,. \tag{2.28}$$

$t_{\rm obs}$ is the value of the test statistics observed by the MAJORANA DEMONSTRATOR data for $\mathcal{S}_j$. The 90% confidence level is given by all $\mathcal{S}_j$ with $p_{\mathcal{S}_i} > 0.1$. The lower half-life limit is defined as the threshold point where $p_{\mathcal{S}_i} > 0.1$ and the half-life sensitivity is defined as

the median of the p-value distribution at the threshold crossing, see Fig. 2.21. A Bayesian method for determining the half-life limit is also described in the supplemental material of [80].

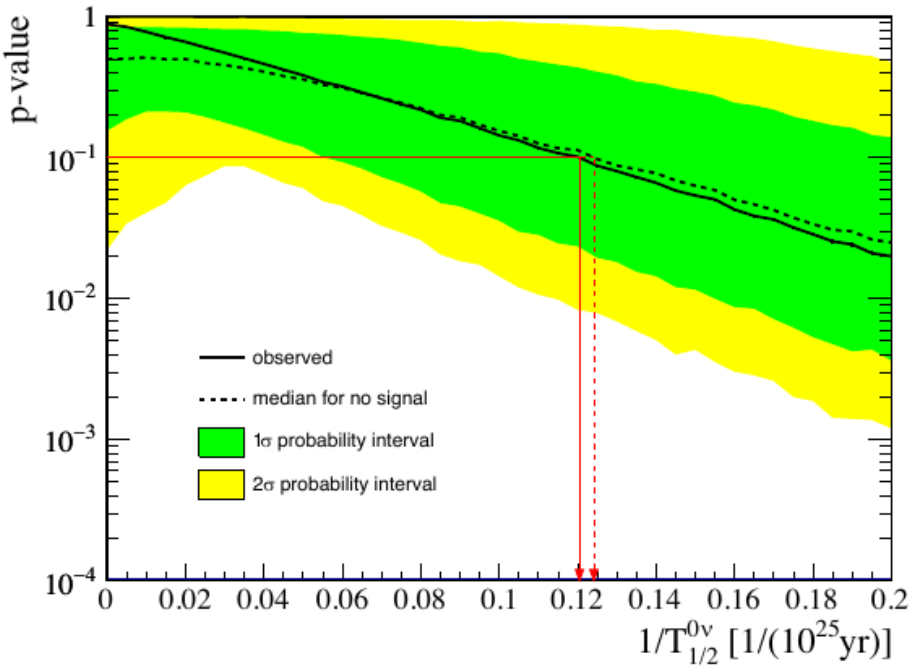

Figure 2.21: A monte-carlo sampling of the p-value from Eq. 2.28 for a range of signal values. The solid black line indicates the p-value using the observed data from the MAJORANA DEMONSTRATOR. The dashed black line indicates the median of the probability distribution with 1σ intervals in green and 2σ intervals in yellow. The solid red line indicates the half-life limit at the 90% confidence level and the dashed red line indicates the half-life sensitivity. *Image Credit:* MAJORANA *Collaboration*

The MAJORANA DEMONSTRATOR concluded enriched data-taking with a lower half-life limit of 8.3×10^{25} yrs and a half-life sensitivity of 8.1×10^{25} yrs, which corresponds to a $m_{\beta\beta}$ upper limit of $113 - 269$ meV under the light neutrino exchange model and a range of Ge nuclear matrix element values [82, 83, 84, 85, 86, 87, 88, 89, 90, 91, 92, 93], see Fig. 2.22. The MAJORANA DEMONSTRATOR reached a background index of $6.59^{+0.56}_{-0.53} \times 10^{-3}$

cts / (keV kg yr) with a total sensitive exposure of 64.5 ± 0.93 kg yrs. The MAJORANA DEMONSTRATOR has concluded enriched data-taking in preparation for the next phase of HPGe $0\nu\beta\beta$ search experiments, LEGEND-200, however the DEMONSTRATOR is continuing the operation of natural Ge detectors for more background modeling studies and beyond Standard Model physics searches.

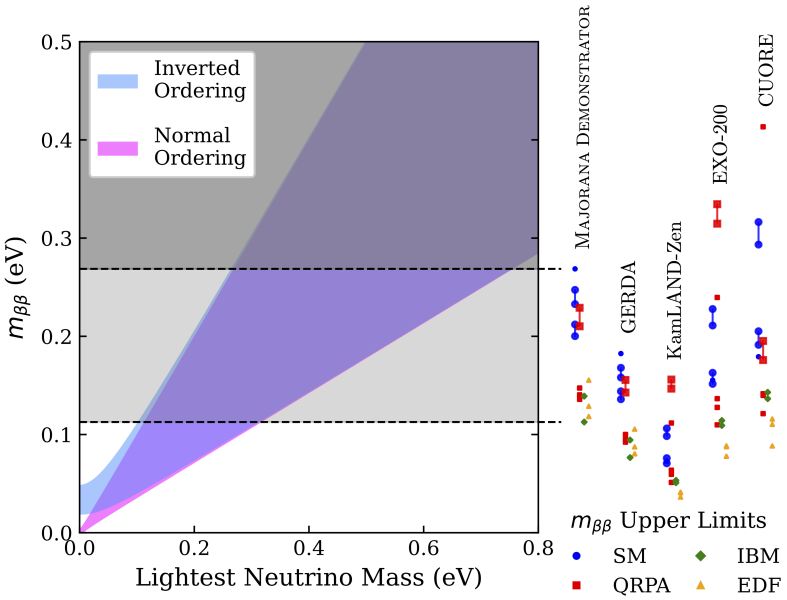

Figure 2.22: The final MAJORANA DEMONSTRATOR results and other experimental results on the $m_{\beta\beta}$ exclusion region in relation to the allowed region for the inverted neutrino mass ordering and normal neutrino mass ordering. The light gray region between the horizontal dashed lines are the $m_{\beta\beta}$ limits for the MAJORANA DEMONSTRATOR result and the dark gray region is the excluded region for the MAJORANA DEMONSTRATOR result. Each experimental regions are specified with various choices of nuclear matrix element calculation methods: shell model, interacting boson model, QRPA, and energy density functional. *Image Credit:* MAJORANA *Collaboration*

Chapter 3

MULTI-SITE DISCRIMINATION

The energy deposition of a $0\nu\beta\beta$ decay event would occur as an isolated event at a localized position in the bulk of an enriched HPGe detector. A single ^{76}Ge nucleus would emit two electrons with a summed energy of 2039 keV. Some of that energy can escape detection in the form of bremsstrahlung, X-rays, or electrons escaping the active detector volume. The probability of a $0\nu\beta\beta$ decay event to deposit the full $Q_{\beta\beta}$ is approximately 90% for the detectors in the MAJORANA DEMONSTRATOR. When a $0\nu\beta\beta$ decay like event deposits its full energy then this creates one energy deposition and is referred to as a single-site event.

Events can also contain multiple energy depositions in a detector from an initial source, in particular the scattering of γ-ray photons. This can sometimes happen for $0\nu\beta\beta$ decay like events since the mean free path of bremsstrahlung at $Q_{\beta\beta}$ is sufficiently large. A dominant γ-ray background is the 2614.5 keV γ-ray emitted from ^{208}Tl in the ^{232}Th chain from near-detector components, which results in energy depositions from multiple scattered electrons, separated spatially by as much as $\sim$ 1 cm or more. These types of events are referred to as multi-site events and can be registered as such with a minimum energy deposition separation distance of about 1 mm.

PPC HPGe detectors have the capability to differentiate these two classes of events due to the geometry of the point contact. Because the point contact is small relative to the detector active volume the magnitude of the weighting potential is very small throughout the bulk of the detector and very large near the point contact. Therefore, most of the induced charge at the point contact from an ionizing event will be created when the charge-carriers reach the immediate vicinity of the point contact. This property gives waveforms with very fast rise-

times in comparison to their drift-times, which allows one to observe a current signal that is multi-peaked. When an event deposits energy at multiple locations in one detector the multi-peaked current signal from the entire event will produce a waveform with a degraded maximum current in relation to a single-site event of the same energy; this primarily happens when the energy depositions are at different distances from the point contact. This feature of PPC HPGe detectors can be used to further reduce backgrounds in the ROI through rejection via pulse-shape analysis of the detector waveforms.

The simplest way to construct a multi-site discrimination parameter is to take the maximum current of a waveform and divide by it's energy (A/E) and then tune a cut value to accept about 90% of the excess events in the ^{208}Tl double escape peak energy window [94]. A/E tends to be the most simple and stable parameter for implementing a multi-site background cut, however it does not precisely account for the energy dependence of "A", but rather assumes a linear approximation. The energy dependence is important because even though a cut can be tuned at one energy using a double escape peak from calibration source γ-rays, the acceptance that really affects the experiment's sensitivity is the acceptance at $Q_{\beta\beta}$. A precisely tuned and understood energy dependence also allows analyses projects other than $0\nu\beta\beta$ decay searches to use a multi-site cut in other energy ranges. The MAJORANA collaboration has thus been pursuing a high-precision multi-site discrimination parameter, AvsE, that aims to provide a multi-site cut that is viable across a large energy range ($<$ 100 - 3000 keV) [76].

The work summarized in this chapter represents the author's own research into improvements for AvsE to better characterize the energy dependencies more precisely, and to correct for additional dependencies from detector response properties. Removing dependencies to AvsE that are extraneous to multi-site identification is an avenue of research to improve pulse-shape discrimination capabilities for tonne-scale germanium experiments where the background levels are more stringent. This chapter will first review how HPGe detectors are used for γ-ray spectroscopy and how it relates to the detection and identification of single-site and multi-site events. A full description of how the multi-site discrimination parameter,

AvsE, is calculated and how it contributes to the overall efficiency, ϵ, for the experimental half-life sensitivity is then discussed. This chapter concludes with the AvsE performance results in the MAJORANA DEMONSTRATOR and conclusions from the analysis overall.

3.1 Spectroscopy in HPGe Detectors

One of the dominant backgrounds in the MAJORANA DEMONSTRATOR, particularly in the ROI, is the 2614.5 keV γ background when ^{208}Tl β-decays to ^{208}Pb. This background originates from the ^{232}Th decay chain, Fig. 2.5b; ^{232}Th is a naturally occurring radioisotope found in the earth's crust. Though a large fraction of this background is blocked externally by the lead shielding, module components can still possess trace amounts of radioisotopes from this decay chain. There are three types of electromagnetic interactions that a γ-ray can undergo inside a HPGe detector and those are photoelectric absorption, compton scattering, and pair production, see Fig. 3.1. Photoelectric absorption is when the full energy of the incoming γ-ray is absorbed and an electron is ejected with energy equal to $E_{e^-} = E_\gamma - E_b$, where E_b is binding energy of the e^-. On average an electron-hole pair takes 2.9 eV to produce, several orders of magnitude smaller than an incoming γ-ray from ^{208}Tl. When the full energy of an incident γ-ray is collected by the detector either directly through one photoelectric absorption or photoelectric absorption after multiple compton scatters is referred to as the *full energy peak* (FEP). Compton scattering is when a γ-ray deposits some, but not all of it's energy into ejecting an electron, Eq. 3.1. The scattered γ-ray can interact with the detector again or escape the detector entirely. In Compton scattering, the energy of an ejected electron by an incoming photon is given by

$$E_{e^-} = E_\gamma \left[\frac{(E_\gamma/m_{e^-})(1-\cos(\theta))}{1+(E_\gamma/m_{e^-})(1-\cos(\theta))} \right] . \tag{3.1}$$

E_γ is the energy of the incident γ-ray, θ is the angle between the momentum vectors of the electron and γ-ray, and m_{e^-} is the mass of the electron. Pair production is when a γ-ray has enough energy to convert into one electron and one positron. The positron will typically annihilate with a valence band electron and produce two 511 keV γ-rays. If both γ-rays

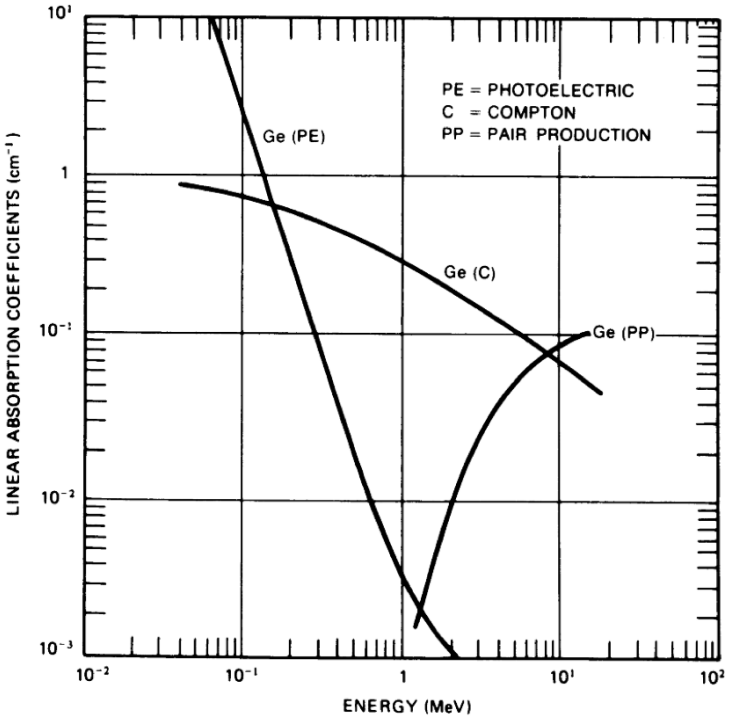

Figure 3.1: A measurement of the linear absorption coefficient for photon interactions in a HPGe detector broken down by interaction type: photoelectric absorption Ge (PE), Compton scatter Ge (C), and pair production Ge (PP). From *ORTEC's Overview of Semiconductor Photon Detectors*

escape the detector then this is detected as the *double escape energy peak* (DEP), where the remaining electron energy is $E_{e^-} = E_\gamma - 2m_{e^-}$. If only one γ-ray escapes the detector while the other deposits its energy through photoelectric absorption this is detected as the *single escape energy peak* (SEP), where the remaining electron energy is $E_{e^-} = E_\gamma - m_{e^-}$. In the MAJORANA DEMONSTRATOR, calibration runs use a ^{228}Th source to calibrate the energy measurements and to tune the pulse-shape parameters on the ^{208}Tl background, Fig. 3.2.

The ^{208}Tl γ-ray can interact with any of the mechanisms show in Fig. 3.1, which can involve one or more energy depositions within a detector. For the PPC HPGe design it is possible to distinguish between single-site energy depositions and multi-site energy deposi-

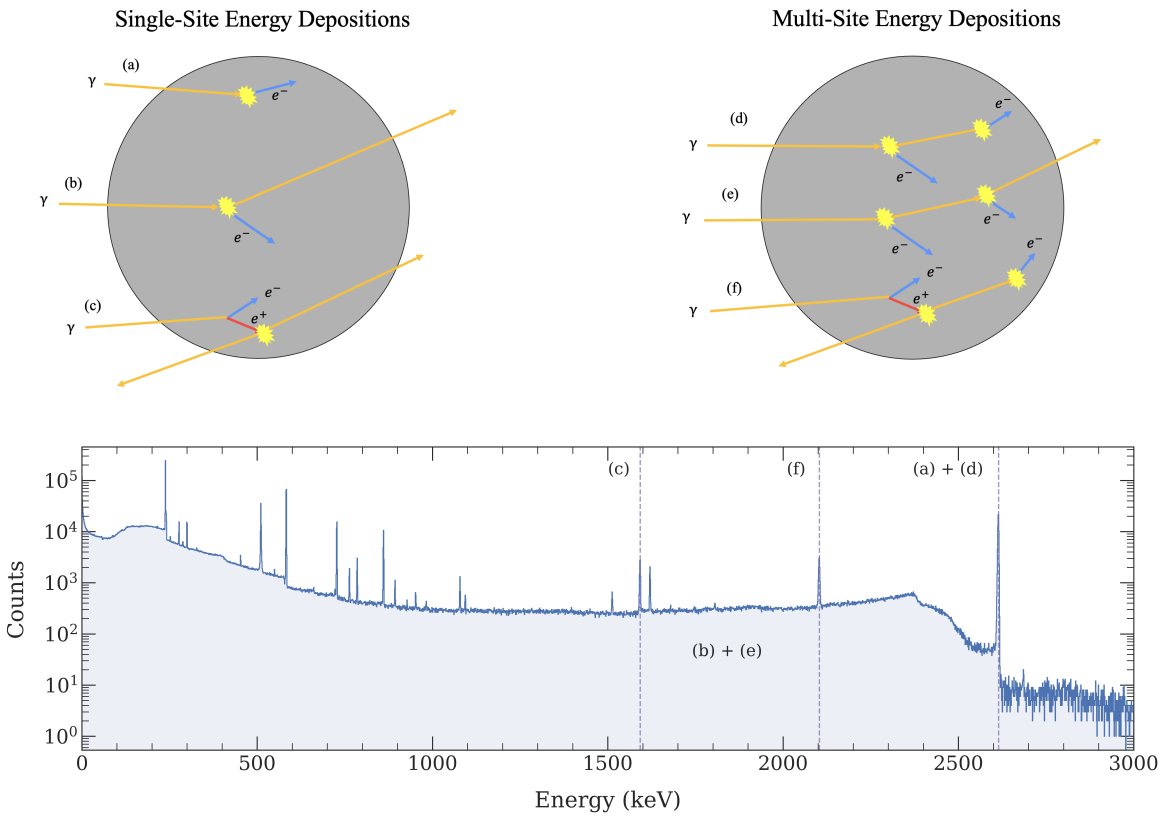

Figure 3.2: A diagram and ^{228}Th calibration spectrum showing the various possible ways a ^{208}Tl γ-ray can deposit its energy into a HPGe detector: (a) photoelectric absorption, (b) compton scattering continuum with one energy deposition, (c) double escape peak (DEP) (d) photoelectric absorption with one or more Compton scatters, (e) Compton scattering continuum with more than one energy deposition, and (f) single escape peak (SEP). Note: other ^{208}Tl energy peaks and other backgrounds are present at lower energies.

tions by measuring the detector output current. The magnitude of the weighting potential is concentrated enough near the point contact that the charge drift-time depends on how far the energy deposition is from the point contact. Drift-time differences are typically 1 μs or less. In the MAJORANA DEMONSTRATOR the smallest isochrone distance that can be resolved is 1 mm, which is an order of magnitude smaller than the compton scattering mean

free path of a few centimeters. The weighting potential and drift-time isochrones are shown in Fig 3.3. The waveforms of events like (a) and (d) from Fig. 3.2 are shown in Fig. 2.12.

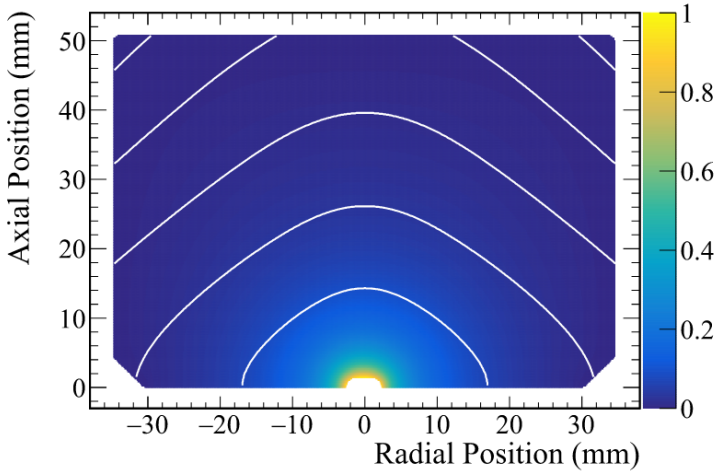

Figure 3.3: A vertical cross-section of a PPC HPGe design. The color-grading is the magnitude of the weighting potential and the solid white lines are the isochrones of equal drift-time spaced out 200 ns apart relative to the point contact. Fig. from ref. [76].

When a γ-ray deposits its energy on multiple isochrones this degrades the current amplitude in comparison to the same γ-ray event if it were to deposit its energy in only one location. In a multi-site deposition the energy of the event is spread over multiple drift-times, leaving regions of the charge cloud to travel slower relative to other regions, thus reducing the maximum current generated from the event. In a search for $0\nu\beta\beta$, the degraded maximum current can be used to identify multi-site energy depositions as background since a $0\nu\beta\beta$ event is inherently a single-site energy deposition. This is done by measuring the maximum current (A) vs Energy (E) in a ^{228}Th calibration run, Fig. 3.4. The current is in principle the first time derivative of the charge collected waveform and this can be calculated in several ways. The MAJORANA analysis approximates the current by fitting lines to a rolling time window of 100 ns across the entire waveform to determine the slope in each interval and the maximum slope is the maximum current (A). There are several key components and

properties that make up the A vs E distribution:

- **Full Energy Peak (FEP)**: Located at 2614.5 keV and is comprised of majority multi-site energy depositions, but includes some single-site depositions.

- **Continuum Mode (CM)**: This region is the mode of the single-site A value with respect to energy. The continuum mode is virtually linear, but has some nonlinear energy dependence at low energy due to a breakdown in the calculation of the maximum current amplitude for low signal-to-noise waveforms and at high energy due to space charge effects. At high energy the impact ionization becomes more non-local and the width of the continuum mode comes from "A" depending on the ionization track spacial orientations and charge cloud repulsions.

- **Multi-site Sector (MS)**: Below the compton mode are the current degradations due to multi-site energy depositions. The current degradation is proportional to the isochron distance between each deposition in a multi-site event. The width of the multi-site sector increases with energy, this is due to the variance in space charge repulsion when more charge carriers are present.

- **Single Escape Peak (SEP)**: Located at 2103.5 keV and is comprised of roughly 90% multi-site events. Single-site Compton continuum events can fall within this energy window. Single escape peak events typically occur near the edges of the detector, which allows one 511 keV γ-photon to easily escape and one 511 keV γ-photon to be easily absorbed.

- **Double Escape Peak (DEP)**: Located at 1592.5 keV and is comprised of roughly 90% single-site events, as indicated by the very little variance in the current amplitude. Multi-site compton continuum events and other low energy interactions can fall around this energy. DEP events typically occur near the corners of the detector, which allows both 511 keV γ-photons to easily escape. The DEP also exhibits a high energy tail:

when one or both 511 keV γ-photons Compton scatter in the lithiated dead layer extra energy is deposited into the detector, but due to slow charge collection these events can still appear single-site. Pair-produced γ-photons can also scatter in the detector bulk, which leaves a horizontal tail in the A vs E distribution.

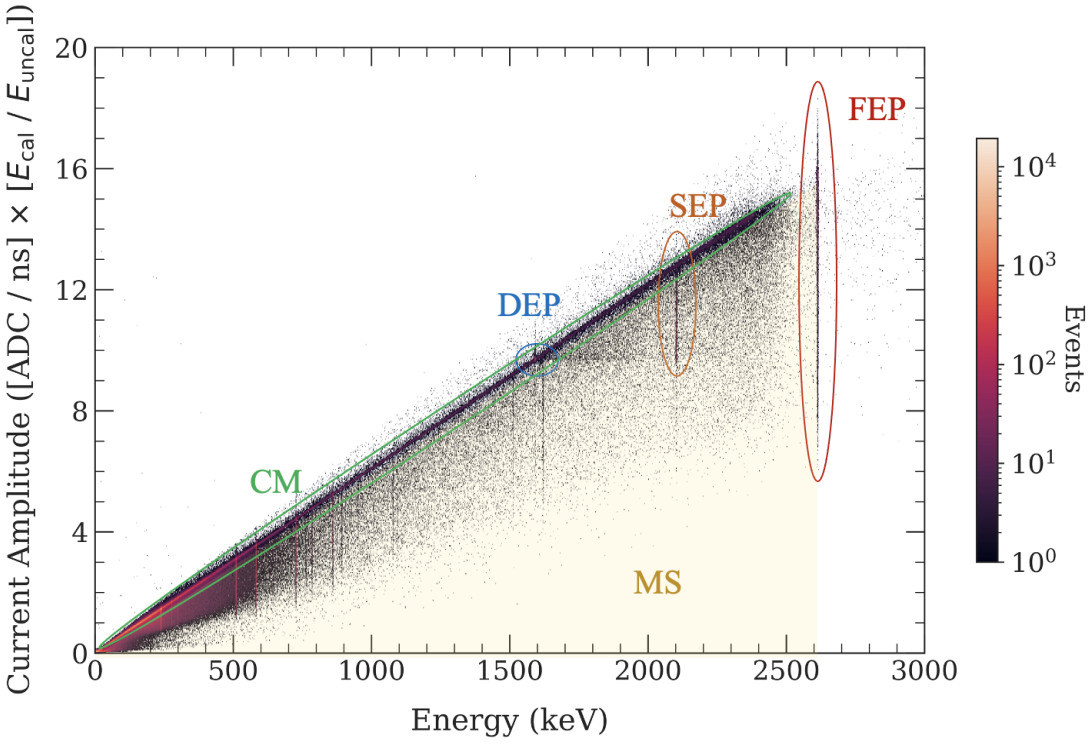

Figure 3.4: Current amplitude vs Energy for a single detector in a ^{228}Th calibration with key features labeled based on the interaction with a 2614.5 keV ^{208}Tl γ-photon: Full Energy Peak (FEP), Single Escape Peak (SEP), Double Escape Peak (DEP), Continuum Mode (CM), and Multi-site sector (MS).

To develop a flat cut that removes multi-site background in a $0\nu\beta\beta$ search, the A vs E distribution must be transformed in such a way to remove all of the dependencies with energy and drift-time; and a single-site event population must be used as a reference to determine

where to set the cut boundary. Setting the multi-site event cut boundary is non-trivial because the true single-site and multi-site event populations overlap with each other.

3.2 The AvsE Parameter

An ideal multi-site parameter is a parameter with no dependencies outside of multi-site dependence and is tuned to accept single-site events with an optimal signal acceptance. The A vs E distribution has several dependencies that are analyzed to produce a flat and uniform multi-site discrimination cut across all detectors: energy dependence, width-energy dependence, drift-time dependence, and a detector scale factor dependence for where to set the multi-site cut boundary.

3.2.1 Energy Dependence

The maximum current amplitude of a signal pulse within a HPGe detector rises as the energy deposition increases and in an ideal detector this relationship is linear. However, non-linearity can arise from several factors:

- **Spatial Energy Dependence**: higher energy depositions tend to have longer range, which broadens out the impact ionization spatially within the detector.

- **Space Charge Effects**: higher energy depositions tend to produce many charge carriers that interact with each other, causing deformation in the charge clouds before reaching the detector electrodes

- **Response of the Electronics**: the readout electronics response can produce non-linearities separate from the detector response.

The energy dependence is clearly visible in Fig. 3.4; as energy increases so does the current amplitude. Higher energy depositions induce a concave-down curvature to the A vs E distribution because the resulting ionization from the depositions decrease in localization. And

when a signal is less localized the maximum current amplitude decreases since the charge carriers are spread over multiple drift-time isochrones. The concave curvature is small and the energy dependence can be approximated by a Taylor expansion out to second order, see Fig. 3.5a. This is done by isolating the continuum mode and doing a weighted least-squares fit to the set of points that represent the center of a gaussian in "A" for various energy slices. All prominent peaks are removed before the fit and each mode is the center of a gaussian fit to the peak in 50 keV energy slices. Subtracting the second order polynomial removes the vast majority of the energy dependence, however it leaves undesired residuals, which can have an impact on the evaluation of an AvsE cut in different energy regions. The fit is less constrained at higher energies due to larger uncertainties on the mode, and the nonlinearity at low energy forces the quadratic to not intersect the origin. After subtracting the quadratic energy dependence, the modes of the continuum are re-calculated and then fit again with another quadratic above 1000 keV and an exponential below 1000 keV, see Fig. 3.5b. The exponential was chosen for the low energy region because it was the simplest function that described the data empirically. Performing the additional quadratic and exponential energy dependence subtraction results in the "A corrected" distribution,

$$A_{\text{corrected}} = A(E_{\text{cal}}/E_{\text{uncal}}) - \text{quad}(E_{\text{cal}}, a, b, c) - \exp(E_{\text{cal}}, d, \tau)\,. \tag{3.2}$$

The quadratic function combines the main energy dependence correction with the residual second order polynomial correction.

3.2.2 Width-Energy Dependence

Since the ^{228}Th decay chain only produces one prominent DEP observable with HPGe detectors, it is not possible to assess the signal acceptance of single-site event populations at different energies. This is important because even though the signal acceptance is tuned based on the ^{208}Tl DEP events, the signal acceptance that is ultimately important is the signal acceptance at $Q_{\beta\beta}$. Another calibration source that can be used to produce multiple DEPs is ^{56}Co. ^{56}Co decays to ^{56}Fe either through electron capture or β^+ emission and sev-

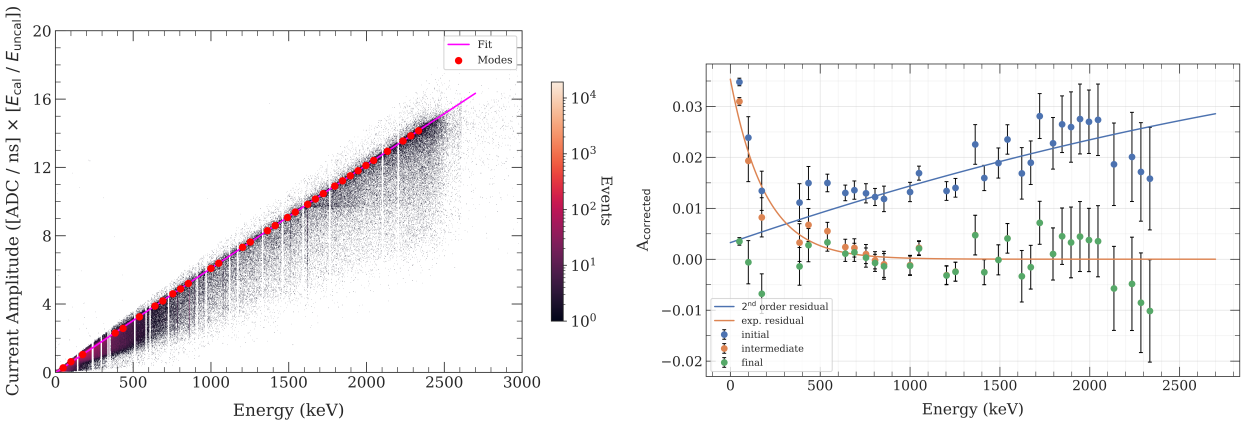

(a) (b)

Figure 3.5: (a) A vs E distribution with prominent peaks removed and a second order polynomial fit to the continuum mode. The second order polynomial is a fit to the modes of the "A" distribution for events in 50 keV energy slices as determined by mean of a gaussian. (b) Subtracting the energy dependence and re-calculating the modes, leaves residuals that are corrected with an additional second order polynomial fit above 1000 keV and an exponential at less than 1000 keV. The green points represent the final location of the continuum mode after the full energy dependence correction.

eral prominent γ transitions can be produced (2598.5 keV, 3010 keV, 3202 keV, 3253.5 keV, 3273 keV, 3451 keV), Fig. 3.6. ^{56}Co is not used as the regular calibration source because it's half-life is short (77 days).

The signal acceptance at each ^{56}Co DEP is calculated using Eq. 2.8 with a 10 keV signal window and two 10 keV side-band subtraction windows, one on either side of each peak. The side-band subtraction takes the average $A_{corrected}$ histogram between the two side-band windows subtracts it from the DEP $A_{corrected}$ histogram, leaving the number of excess events remaining from the DEP. $A_{corrected}$ is then scaled so that 90% of events pass the cut where, AvsE > -1, at the 1576.5 keV DEP. Section 3.2.4 describes why this is the chosen metric for

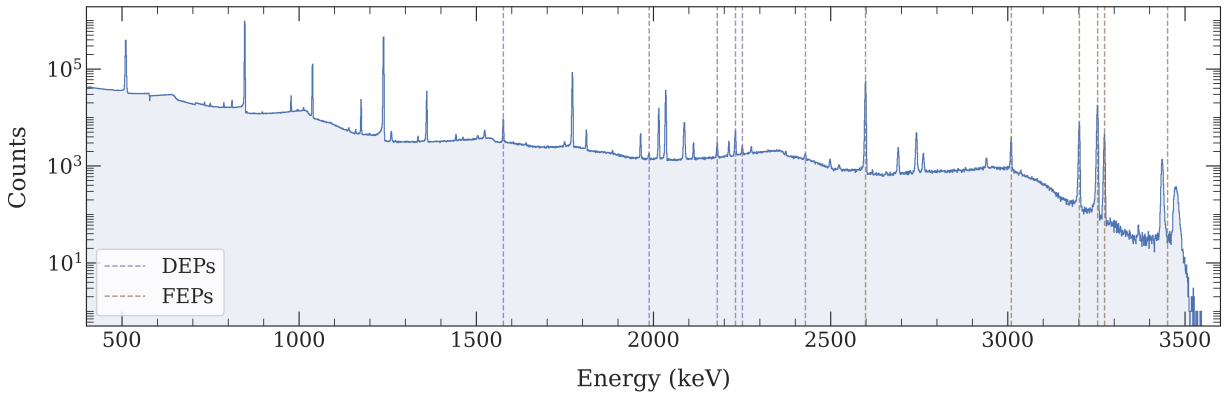

Figure 3.6: ^{56}Co calibration source spectrum. FEPs are in brown and DEPs are in purple. Energies approaching 3500 keV are distorted due to reaching the maximum range of the digitizer.

the multi-site cut. Measuring the AvsE signal acceptance across all prominent ^{56}Co DEPs shows a degradation of the signal acceptance with increasing energy, Fig 3.7. In a $0\nu\beta\beta$ search, where the DEP acceptance is tuned at the 1592.5 keV ^{208}Tl DEP, the acceptance at $Q_{\beta\beta}$ would be $\sim 5\%$ lower, Fig. 3.19.

The signal acceptance degradation indicates that the width of the AvsE distribution is growing with increasing energy. When the AvsE distribution is wider at certain energies more events are cut compared to the energy for where the cut value is set. There are two factors that contribute to the width-energy dependence: space charge effects varying the shape of collected charge carriers and the energy dependence of bremsstrahlung production. Higher energy depositions in the detector will produce more charge carriers within the detectors through more impact ionization. Due to space charge effects, the variance of the AvsE distribution mode increases for larger amounts of charge carriers produced. Bremsstrahlung is the process where an electron decelerates in the vicinity of an atomic nucleus and emits radiation. At low energies the mean free path of bremsstrahlung radiation is negligible and is immediately re-absorbed through photoelectric absorption, however bremsstrahlung photons

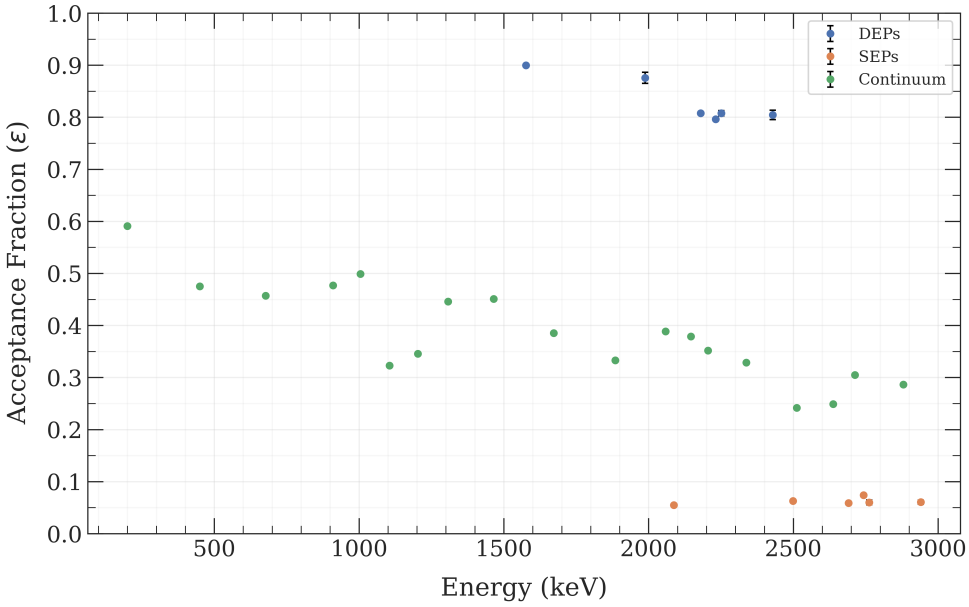

Figure 3.7: Signal acceptance fraction across the DEPs and SEPs of ^{56}Co and the Compton continuum from the compton scatter of the ^{56}Co FEPs. When tuning the 1576.5 keV DEP to 0.9 signal acceptance fraction the DEP signal acceptance fraction degrades with increasing energy.

are more likely to generate multi-site events with increasing energy. The fraction of multi-site events per energy window increases with increasing energy.

The width-energy dependence of AvsE due to space charge effects can be removed by scaling the $A_{corrected}$ distribution by an energy dependent function. Establishing such a function requires the width of single-site event populations to be known for as many energies as possible. This is done by measuring the width of simulated $2\nu\beta\beta$ and $0\nu\beta\beta$ events in $A_{corrected}$, in addition to the measured widths of DEPs from calibration data, and fitting an empirical width function,

$$\mathrm{FWHM}_A(E) = \sqrt{a_0^2 + (a_1 E)^2 + (a_2^2 E^2)^2 + (a_3^3 E^3)^2}\,. \tag{3.3}$$

The width function is treated as the FWHM of the sum of gaussian distributions with variances that depend on energy to some polynomial order. Including extra terms gives coefficients a_n that rapidly decrease at fourth order and beyond, so the last term considered is the third order polynomial contribution to the width. The FWHM is calculated by fitting a Pseudo-Voigt function to the side-band subtracted DEP AvsE peaks from data and the DEP AvsE peaks from simulation. A Pseudo-Voigt profile is the weighted sum of a Gaussian and a Lorentzian,

$$V_p(x) = \eta \cdot G(x;\mu,\sigma) + (1-\eta)\cdot L(x;x_0,\gamma)\,, \quad 0 < \eta < 1\,. \tag{3.4}$$

$\text{FWHM}_{gauss} = 2\sigma\sqrt{2\ln(2)}$ and $\text{FWHM}_{lorentz} = 2\gamma$, however the FWHM of the Pseudo-Voigt profile is non-analytical. Typical weightings for DEP peaks are 70% Gaussian and 30% Lorentzian. The side-band subtracted DEP peaks of ^{56}Co are shown in Fig. 3.8. The weighted Gaussian plus Lorentzian was chosen because it accurately captured the FWHM of the higher statistics side-band subtracted DEPs when using a fit range that includes a majority of the peak.

The same profile is fit to the AvsE peaks of simulated $2\nu\beta\beta$ events and simulated $0\nu\beta\beta$ events. Since all double-β decay events are single-site in nature, there is no need to side-band subtract the average background events. The Pseudo-Voigt profile is fit to 25 keV energy slices of the $2\nu\beta\beta$ energy spectrum and a 10 keV window around $Q_{\beta\beta}$ for the $0\nu\beta\beta$ events and the detailed simulations were used to derive the functional form of $\text{FWHM}_A(E)$. The full fit of Eq. 3.3 for a single detector is shown in Fig. 3.9. Each detector's events should be simulated with the electronics response of that detector and since this is still an on-going research project, only two detectors within the MAJORANA DEMONSTRATOR have fully characterized electronics response functions so far. So instead, detector width functions are fit using the DEP widths from a single special ^{56}Co calibration run period and constraining the fit using the width of the low energy Compton continuum. This will cause the signal acceptance to be slightly larger than the optimal value for energies less than 500 keV, however this is tolerable since multi-site discrimination is not precise below 500 keV. Scaling the $\text{A}_{\text{corrected}}$

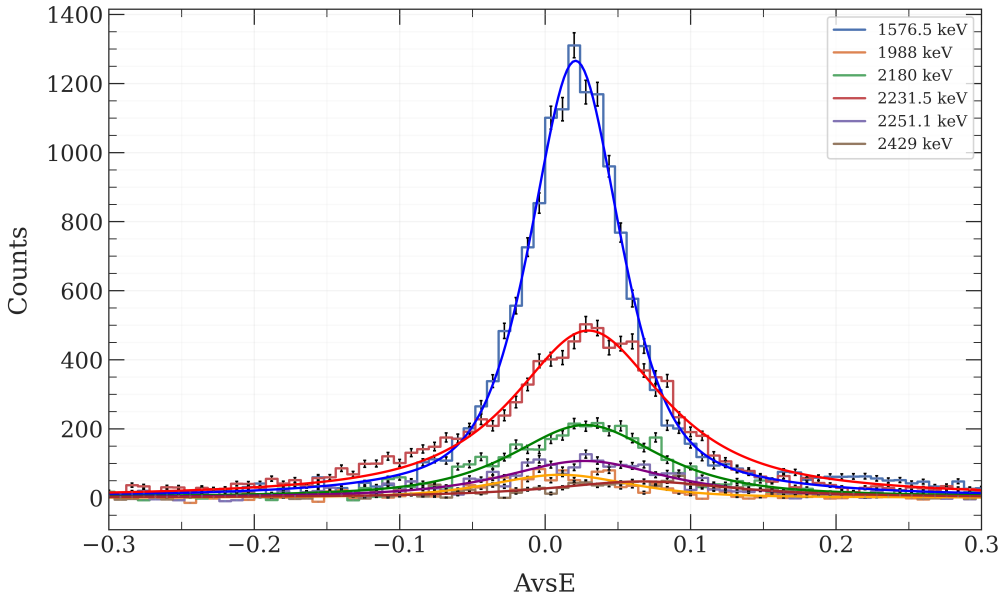

Figure 3.8: Side-band subtracted DEP peaks in a ^{56}Co calibration. Each DEP is fit with a Pseudo-Voigt profile to determine the FWHM.

by the width-energy dependence function in Eq. 3.3, gives $\mathrm{A}_{\mathrm{width\,corr.}}$, Eq. 3.5.

$$A_{\mathrm{width\,corr.}} = \frac{A(E_{\mathrm{cal}}/E_{\mathrm{uncal}}) - \mathrm{quad}(E_{\mathrm{cal}}, a, b, c) - \exp(E_{\mathrm{cal}}, d, \tau)}{\mathrm{FWHM}_A(E_{\mathrm{cal}})} \tag{3.5}$$

3.2.3 Drift-time Dependence

Since the maximum current amplitude is related to the time it takes for charge to be fully collected from an energy deposition in the germanium detector bulk, a correlation between the $\mathrm{A}_{\mathrm{width\,corr.}}$ parameter and drift-time is expected. A single-site energy deposition that occurs in one part of the detector can have a different current amplitude than the same energy deposition at a different distance from the point contact. In this case a degradation in current amplitude comes from two contributions: multi-site nature of the event and how long it took for the charge to collect. The drift-time is measured as the difference in a

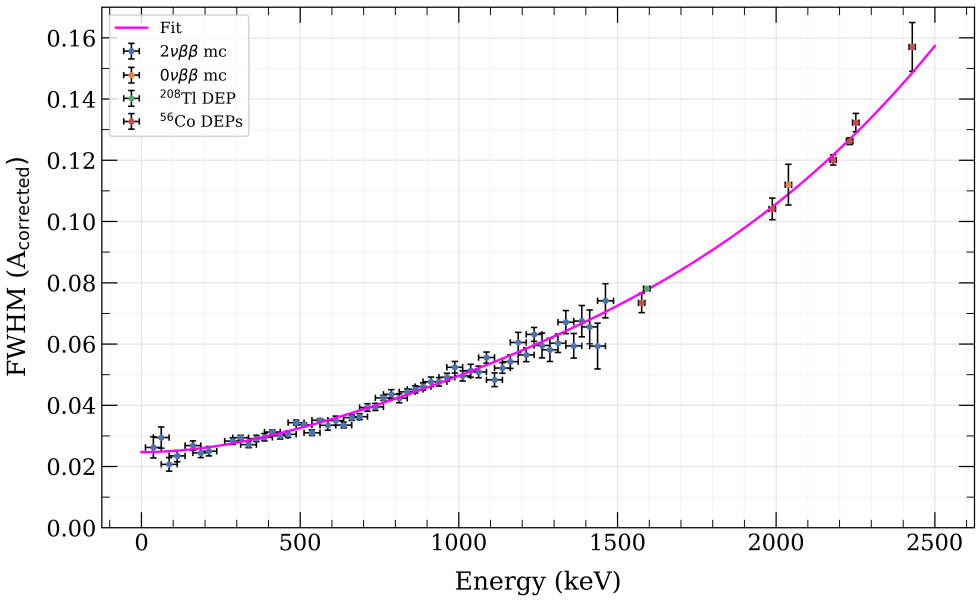

Figure 3.9: A weighted least-squares fit of Eq. 3.3 to the FWHM of various single-site DEP peaks in $A_{\text{corrected}}$. The FWHM for each peak is the FWHM of a Pseudo-Voigt profile.

waveform's 90% rise-time and the initial rise-time above baseline as determined from an asymmetric trapezoidal filter as shown previously in Fig. 2.9.

The drift-time dependence of $A_{\text{width corr.}}$ is shown in Fig. 3.10. The slope of the drift-time dependence is related to the magnitude of the weighted electric field inside the detector bulk. Higher electric field strengths will produce steeper slopes, while lower electric field strengths will produce slopes that are more flat. A nonlinear region below a drift-time of about 600 ns in PPC detectors comes from the high weighted electric field near the point contact. Due to the nonlinear increase in the magnitude of the weighted electric field, the maximum current amplitude of the single-site events also increases nonlinearly. The drift-time dependence is removed by rotating the linear fit in Fig. 3.10 about the average drift-time and average

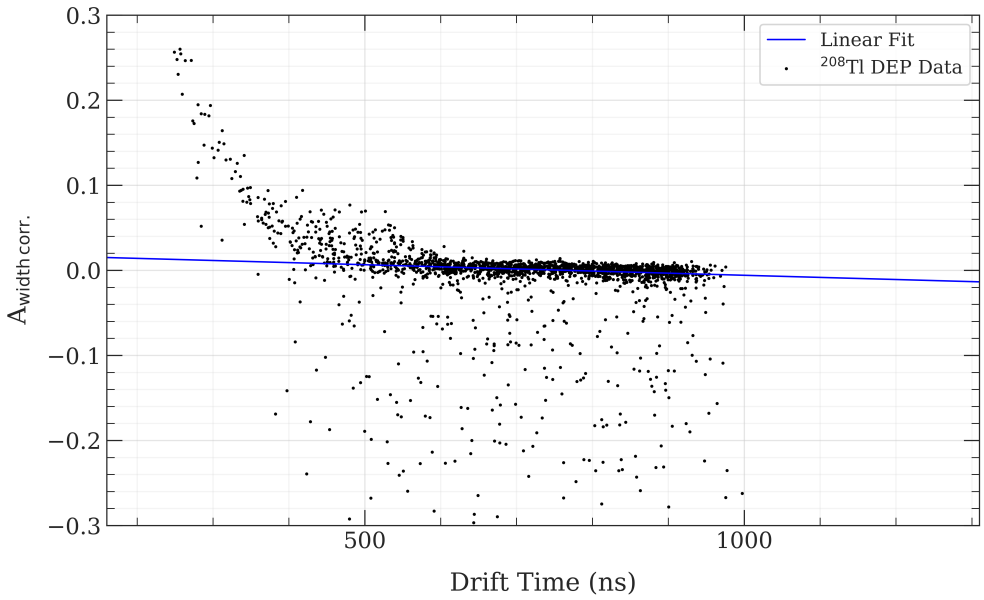

Figure 3.10: The drift-time of ^{208}Tl DEP events vs $A_{\text{width corr.}}$ for one PPC detector. The drift-time here is defined as the time to the 90% rise-time of a waveform from the initial rise-time above baseline as determined from an asymmetric trapezoidal filter. AvsE has a linear dependence with drift-time and some non-linearity towards 200 ns drift-time which corresponds to events within the DEP energy window that deposit near the point contact.

$A_{\text{width corr.}}$ point.

$$A_{\text{drift corr.}} = (\Delta t - \overline{\Delta t_{dep}})\sin(\theta) + (A_{\text{width corr.}} - \overline{A}_{\text{width corr. dep}})\cos(\theta) + \overline{A}_{\text{width corr. dep}} \quad (3.6)$$

3.2.4 AvsE Cut Values

With the energy dependence, width-energy dependence, and drift-time dependence removed, the multi-site parameter is now fairly uniform across all detectors, all energies, and all drift-times and over time throughout a dataset. This means that the multi-site parameter, at least within uncertainty, is mostly dependent on the multi-site nature of a particular energy

deposition event. However, setting what the multi-site cut boundary should be is non-trivial. This is mainly due to the ^{208}Tl DEP not being a pure sample of single-site events. The DEP energy window also includes Bremsstralung, multi-site compton scattering events, and X-ray fluorescence.

A natural choice in choosing a multi-site cut value is to solve for the value that maximizes the discovery sensitivity of the experiment. A multi-site cut will remove background, which is beneficial, while at the same time will lower signal acceptance, which is not beneficial. The discovery sensitivity, given by Eq. 1.32, determines how large of a half-life limit an experiment is predicted to achieve and the analysis cut thresholds can be optimized for the maximum discovery sensitivity. The portion of the discovery sensitivity that's effected by the multi-site parameter is the signal acceptance fraction incorporated in the exposure and the $S_{3\sigma}(B)$ term. With these pieces a figure of merit that approximates the discovery sensitivity can be maximized to obtain the optimal multi-site cut value,

$$\text{F.O.M.} = \frac{\epsilon_{\text{DEP}}}{S_{3\sigma}(B)}\,, \quad S_{3\sigma}(B) \approx n_{cl}\sqrt{B}\left(1 + \frac{0.2}{\sqrt{\text{B} + 1/2}}\right) + \ln(2)\,, \quad B = 2.5 \times \epsilon_{\text{CC}}\,. \tag{3.7}$$

ϵ_{DEP} is the DEP acceptance, ϵ_{CC} is the $Q_{\beta\beta}$ Compton continuum acceptance, n_{cl} is the confidence level which is set to 3 for a 3σ discovery sensitivity, and B is the expected number of background counts in the ROI. $B = 2.5 \times \epsilon_{CC}$ is used to assume a background count of one with an $\epsilon_{CC} = 0.4$, which is the observed number of counts and ϵ_{CC} reported previously in the 2019 MAJORANA result [74]. The optimization is done by varying the signal acceptance fraction of the ^{208}Tl DEP peak on a large subset of the open data, see Fig. 3.11. The precision of the AvsE signal acceptance is approximately ± 0.03 so differences of a few percent in signal acceptance are not significant. The signal acceptance chosen for the multi-site parameter is 90%, which approximately maximizes within uncertainty the discovery sensitivity figure of merit. This also corroborates a 90% signal acceptance used in the previous AvsE analysis, which determined that 90% of events within the DEP are single-site from Monte-Carlo simulations from the previous AvsE analysis [76]. The AvsE multi-site cut parameter is then scaled to have 90% signal acceptance when all events with

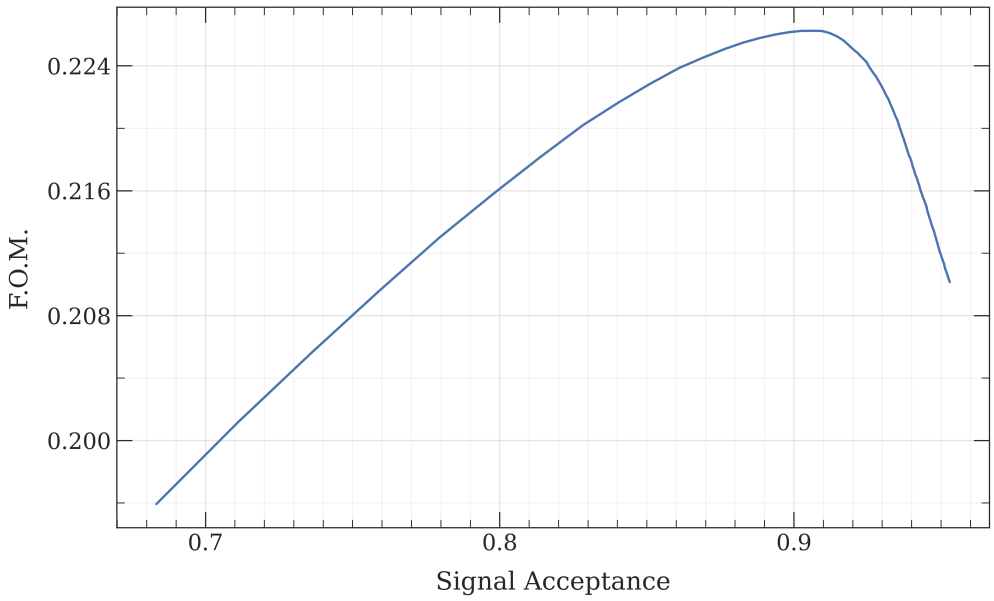

Figure 3.11: Varying the signal acceptance of the ^{208}Tl DEP peak to solve for the maximum of the figure of merit in Eq. 3.7. The uncertainty on the signal acceptance is approximately ± 0.03 so the signal acceptance fraction that is chosen to give the maximum discovery sensitivity is a signal acceptance value of 0.9

AvsE > -1 pass the cut,

$$\text{AvsE} = -\frac{\text{A}_{\text{drift corr.}}}{s} \,. \tag{3.8}$$

This is defined as the multi-site cut.

AvsE is a reliable multi-site cut parameter for all events that occur within the detector bulk. For energy depositions that occur close to the point contact, the weighting potential is very non-linear and drift-time is significantly shorter than for events that deposit in the rest of the detector. This allows for multi-site events with at least one event near the point contact to pass the AvsE cut. A high AvsE cut would remove these types of multi-site events and would also remove degraded alphas near the point contact which escape the DCR cut. A caveat however is the high AvsE cut would effectively remove all events which deposit energy

near the point contact, therefore acting as a volumetric cut of the active detector material. Performing a F.O.M. optimization for the high AvsE cut shows that for the ^{208}Tl background, the cut only decreases the F.O.M., so that the maximum corresponds to not applying a high AvsE cut at all. The main advantage of the high AvsE cut is to remove degraded surface α's near the point contact, which rarely occur in the calibration data. Selecting a high AvsE < 9, before the F.O.M. drops considerably, removes $\sim$7% of events in the background estimation window in open data while decreasing the overall signal acceptance in calibration data by $\sim$2%, Fig. 3.12. In the full dataset there are the nine events that are removed only by the high AvsE cut, see Fig. 2.16b. This gives a slight increase to the discovery sensitivity and a overall reduction in the number of counts in the background estimation window.

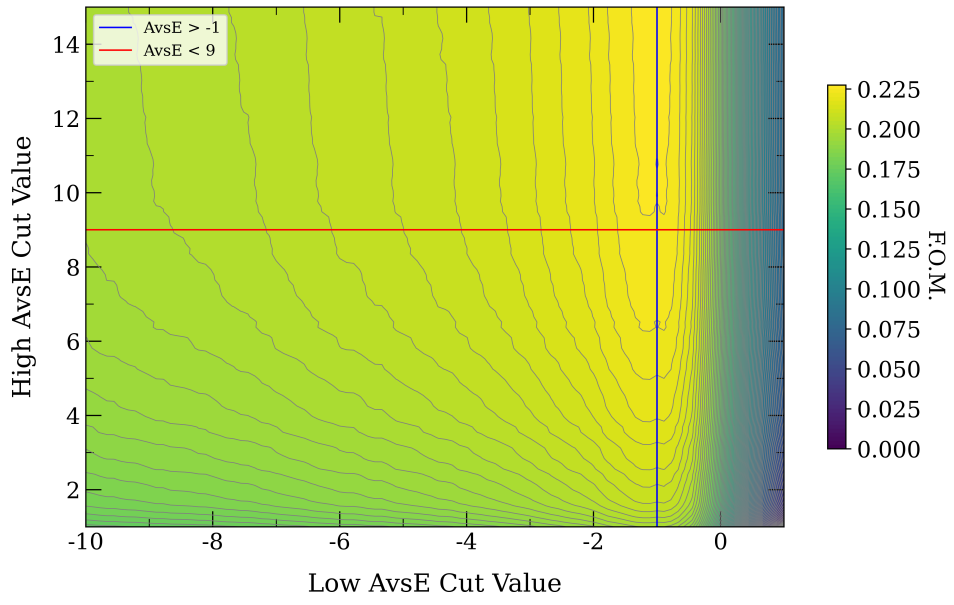

Figure 3.12: F.O.M. calculated for various AvsE cut values. The blue and red lines indicate the cut boundaries for approximately optimal discovery sensitivity.

3.3 AvsE Data Cleaning

For all data the AvsE parameter is tuned during each long calibration of the dataset and the tuned parameters are used until the next long calibration where AvsE is re-tuned. The first long calibration of a dataset also applies to the first run up to the first long calibration. Between long calibrations the AvsE parameter can drift in the open short calibrations and physics data leaving residuals which compromise the signal acceptance for that series of runs. In the full MAJORANA analysis AvsE is the most unstable parameter because of its infrequent tuning compared to energy calibration and DCR, and due to its sensitivity to the rising edge shape of the waveforms. In addition, the AvsE energy dependences are difficult to correct between long calibrations since the fit to the energy dependence is nonlinear. Any deviations from the energy dependence due to gain instabilities produce complicated residuals that are nearly impossible to correct for. Some data periods were corrected by re-fitting the second order and linear term in the quadratic energy dependence for detectors with large AvsE energy dependence drift among short calibrations.

Unstable periods by detector are then selected as "veto-only"; a veto-only detector will only be used for the multiplicity cut to remove physics events that deposit energy in multiple detectors. This is referred to as *channel selection* in the MAJORANA analysis. The criteria to remove unstable periods are chosen to preserve the optimal DEP acceptance within a certain threshold. A veto-only period for a detector channel begins when the DEP AvsE peak drifts by more than one FWHM since the previous tuned long calibration, and ends when the peak is within the FWHM. For all detector channels for all calibrations, A vs E, AvsE vs E , DEP and SEP AvsE peaks are examined by eye to remove unstable periods. This was chosen to maximize exposure as a primary goal was to try and reduce the amount of channel selection from the 2019 MAJORANA result. Automated methods made it difficult to control the amount of exposure lost through channel selection. Examples of calibration data with run periods selected as veto-only are shown in Fig. 3.13a and Fig. 3.13b. [74].

For the full MAJORANA dataset, channel selection removed 16% of the available expo-

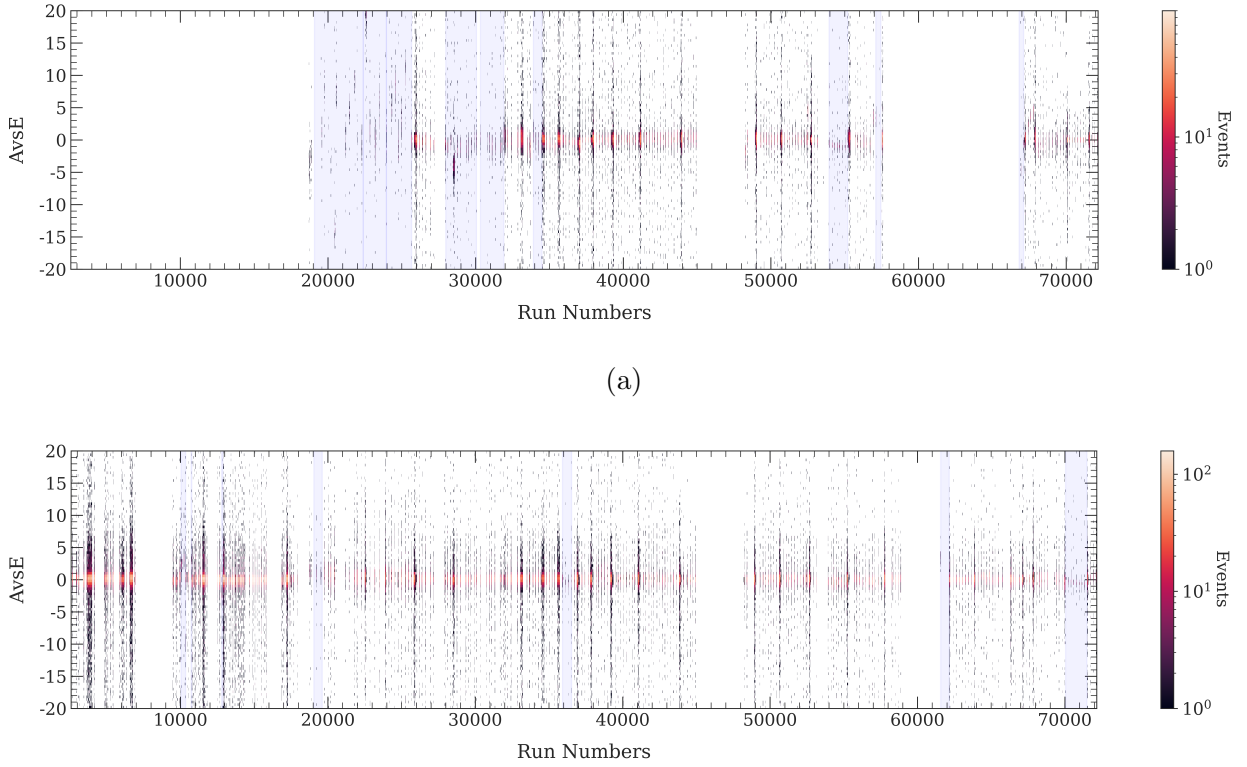

Figure 3.13: 10 keV energy windows around the DEP peak vs run number for calibration data. The blue shaded regions are unstable periods where the run range is selected as veto-only. Panel (a) shows is a more unstable enriched detector, and panel (b) shows a fairly stable enriched detector.

sure for the $0\nu\beta\beta$ decay analysis, of which roughly half of the loss comes from AvsE, see Fig. 3.14. Over half of the exposure loss comes from two enriched detectors, one with unstable current gain observable on the time scale of hours and another with consistently poor SEP acceptance, which only affects the data quality for AvsE and none of the other analysis parameters. These effects can arise from a non-uniform impurity gradient distorting the current amplitude degradation.

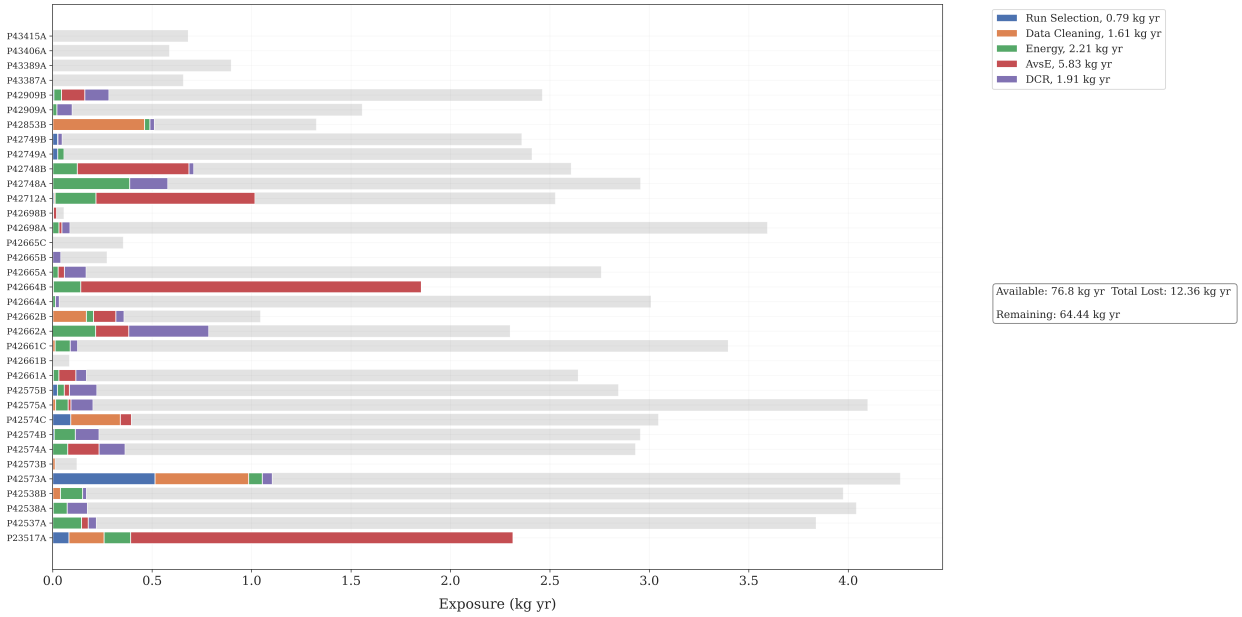

Figure 3.14: The exposure loss broken down by detector serial numbers on the y-axis and channel selection criteria in the legend. The gray bars represent the remaining exposure to be used in the $0\nu\beta\beta$ analysis. Run selection removes detector data due to detector operations/malfunctions, and data cleaning removes detector data based on unphysical waveform features, waveform triggering issues, and waveform pile up events.

3.4 Multi-site Cut Signal Acceptance and Systematic Uncertainties

The contribution to the detection efficiency from AvsE is the AvsE signal acceptance at $Q_{\beta\beta}$ and its uncertainty. This includes the multi-site cut signal acceptance and the high AvsE cut signal acceptance after the multi-site cut is applied. Both of these cuts have statistical and systematic uncertainties, which assesses the precision and accuracy of each transformation applied to calculate the AvsE parameter. The methods for calculating the signal acceptance and systematics are shown in this section while the results are tabulated in Sec. 3.6. Four ICPC detectors were deployed in the last dataset of enriched data-taking and are treated as a separate dataset with an A/E analysis, described in Appendix A.

3.4.1 Signal Acceptance and Statistical Uncertainty

The multi-site cut efficiency is calculated by measuring the number of events that pass the AvsE > -1 cut in the DEP energy window for all long calibrations combined. This also includes a background subtraction to remove the AvsE background from the Compton continuum. The AvsE side-band energy windows, 1570−1580 keV and 1600−1610 keV, are averaged together and subtracted from the AvsE events in the DEP energy window, 1587.5−1597.5 keV, to get the number of excess events attributed to the DEP. An AvsE > -1 cut is applied to calculate the fraction of events remaining in the DEP energy window and the statistical uncertainty to the signal acceptance:

$$\epsilon = \frac{N_c - \tau B_c}{N - \tau B} \tag{3.9}$$

$$\left(\frac{\sigma_\epsilon}{\epsilon}\right)^2 = \frac{N + \tau^2 B}{(N - \tau B)^2} + \frac{N_c + \tau^2 B_c}{(N_c - \tau B_c)^2} - 2\frac{N_c + \tau^2 B_c}{(N - \tau B)(N_c - \tau B_c)}\,. \tag{3.10}$$

N_c and B_c are the number of events cut in the signal region and background region respectively, τ is the ratio of DEP energy window size to the background energy window size, and N and B are the total counts in the signal and background regions. The AvsE acceptance, for the full MAJORANA dataset and all enriched detectors, is taken to be the exposured weighted average acceptance for all enriched detectors, see Fig. 3.15. The acceptance results for all enriched detectors are shown in Table 3.1. The CC energy window is 1989 − 2089 keV.

DEP	SEP	CC
89.91% ± 1.20%	6.34% ± 0.83%	43.13% ± 1.13%

Table 3.1: AvsE multi-site cut acceptance for the DEP, SEP, and ROI CC for all enriched PPC detectors.

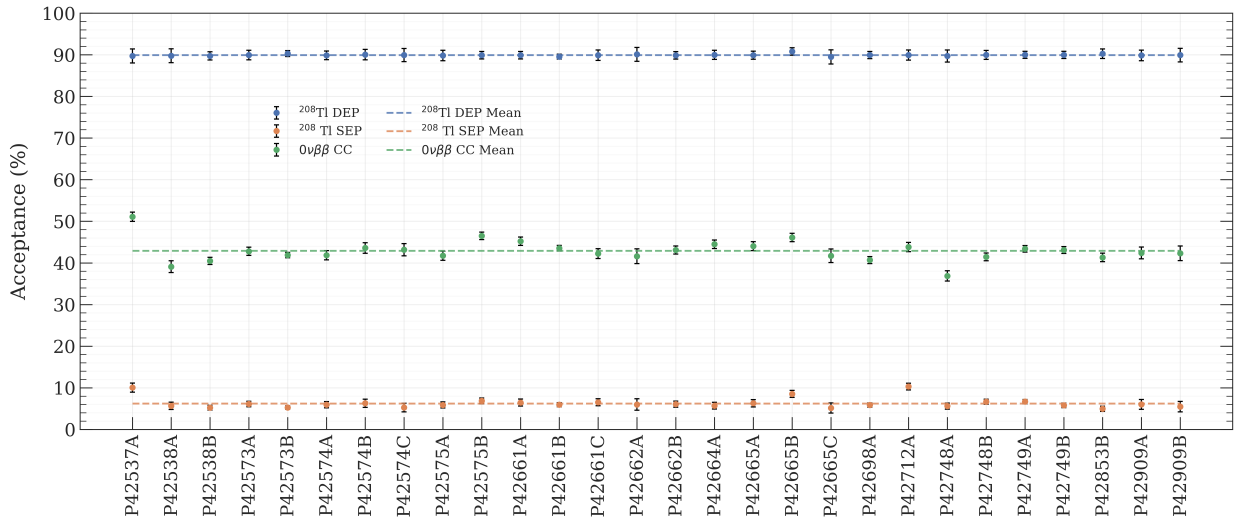

Figure 3.15: The DEP, SEP, and CC acceptance by enriched detector. The weighted average acceptance is shown with the dashed horitonzal lines. The ICPC detectors are treated with a different analysis and are not shown here.

3.4.2 $Q_{\beta\beta}$ Energy Dependence

The energy dependence and width-energy dependence corrections together transform the A vs E distribution so that a uniform multi-site cut can be applied equally at all energies. The energy dependent correction removes the dependence in the mode of the distribution and the width-energy dependent correction removes the dependence in the width of the distribution. The $Q_{\beta\beta}$ energy dependence systematic assesses the precision of the energy dependence between the ^{208}Tl DEP and a 100 keV energy window centered around $Q_{\beta\beta}$. The systematic takes the two mode locations for each detector within all long calibrations in a dataset and varies the AvsE cut value by the difference in these AvsE mode values. The mode values are calculated from a gaussian fit to peaks of the distribution. This is done by detector and for each combined set of long calibrations in each dataset. The distributions used to calculate the systematic for one detector are shown in Fig. 3.16.

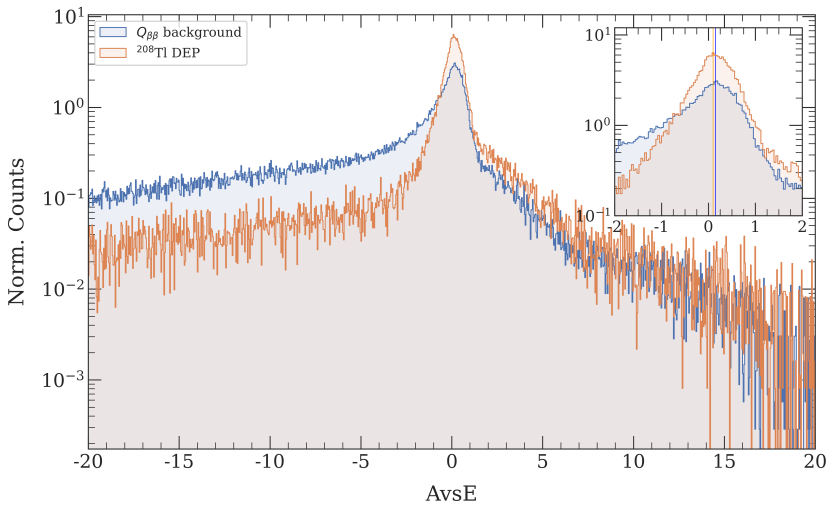

Figure 3.16: AvsE spectrum for the DEP energy window $1587.5 - 1597.5$ keV in orange and $Q_{\beta\beta}$ energy window $1989 - 2089$ keV in blue for one detector in long calibration data. The $Q_{\beta\beta}$ systematic is the change in acceptance when varying the AvsE cut between the modes of these two distributions. The inset plot shows a close up two distribution peaks. The systematic is calculated by detector and then averaged. The DEP is not side-band subtracted since the modes of the distributions are being compared and not the signal acceptances.

3.4.3 $2\nu\beta\beta$ Energy Dependence Systematic Uncertainty

The $2\nu\beta\beta$ energy dependence systematic is an additional assessment of the precision of the energy dependence correction. This systematic tests how precisely the energy dependence is corrected in the physics data, for which the $Q_{\beta\beta}$ acceptance systematic doesn't account. There may be some correlations between this systematic and the $Q_{\beta\beta}$ acceptance systematic, however when conducting a blind analysis there are insufficient statistics in the background to measure this effect, and both systematics are taken as independent to be conservative. The $2\nu\beta\beta$ energy dependence systematic is measured by computing the difference in the DEP mode from calibration and the 950-1400 keV energy window mode from the $2\nu\beta\beta$

background. The AvsE cut is then varied by the difference in the two modes to estimate the deviation in the signal acceptance. All detectors are combined for this analysis to achieve enough statistics. A visual for the enriched data-taking period is shown in Fig. 3.17.

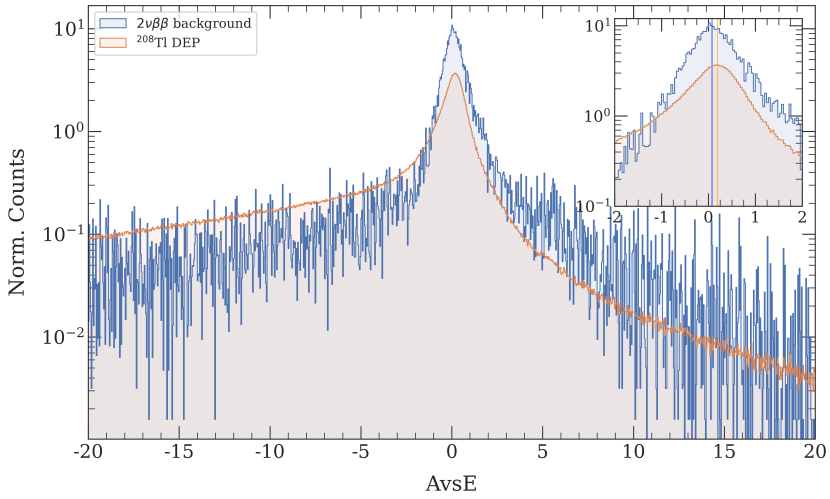

Figure 3.17: The $2\nu\beta\beta$ energy window shown in blue and the ^{208}Tl DEP window from long calibrations shown in orange for the entire dataset. A difference in the peak locations in shown in the inset. The AvsE cut value is then varied by this difference for each detector to calculate the change in acceptance from this systematic. The DEP is not side-band subtracted since the modes of the distributions are being compared and not the signal acceptances

3.4.4 $0\nu\beta\beta$ Acceptance Systematic Uncertainty

The signal acceptance is evaluated at the DEP, since it is an energy peak known to contain a majority of single-site energy depositions. The signal acceptance that is relevant for a $0\nu\beta\beta$ decay search is the acceptance at $Q_{\beta\beta}$. The width-energy dependence has been corrected to reduce the drop in acceptance at higher energies, however there is still some

difference leftover that contributes to the systematics. Another contribution to the $0\nu\beta\beta$ acceptance is the difference in acceptance between the DEP acceptance, the DEP acceptance from simulations, and the true $0\nu\beta\beta$ acceptance from simulations. These differences arise from the different spatial distributions of DEP vs $0\nu\beta\beta$ decay events within a detector and the different fraction of multi-site events produced by bremsstrahlung. $0\nu\beta\beta$ decay events would happen uniformily throughout the detector bulk, while DEP events are concentrated more towards the detector corners. Tuning to the DEP population induces a slight bias for single-site waveforms with longer drift-times. Though $0\nu\beta\beta$ is a single-site event and most events are contained very close to $Q_{\beta\beta}$ there are several phenomena that can change how these events are measured: radiative energy loss, leakage current, bremsstrahlung, and near point contact depositions. Simulations are done in a GEANT4 based software package and expected waveforms are generated by using an HPGe electronics response model [95]. Only two PPC detector electronics response models are available and the average results between the two are used for calculating the systematic. The simulation data was re-used from the previous AvsE analysis paper [76]. The two dominating components of the $0\nu\beta\beta$ acceptance systematic are the difference between the observed DEP acceptance and the simulated $0\nu\beta\beta$ acceptance, and the predicted drop in acceptance at $Q_{\beta\beta}$ after applying the width-energy dependent correction.

The $0\nu\beta\beta$ acceptance is calculated by tuning AvsE to a simulated ^{228}Th source spectrum and then applying the AvsE transformation to a set of simulated $0\nu\beta\beta$ decay events. The simulated $0\nu\beta\beta$ current amplitude vs energy spectrum is shown in Fig. 3.18. Most $0\nu\beta\beta$ decay events are single-site and contained within the ROI, however there are a small fraction of events that have incomplete charge collection, bremsstrahlung production, or near point contact depositions that change these two measurable quantities. The calculated $0\nu\beta\beta$ acceptance is 91.81%. This acceptance serves as the upper bound for the $0\nu\beta\beta$ acceptance systematic. The lower bound comes from fitting a second order polynomial to the ^{56}Co DEP peak acceptances from the ^{56}Co calibration data, Fig. 3.19. This predicts an acceptance at $Q_{\beta\beta}$ of 87.43% and serves as the lower bound of the $0\nu\beta\beta$ acceptance systematic.

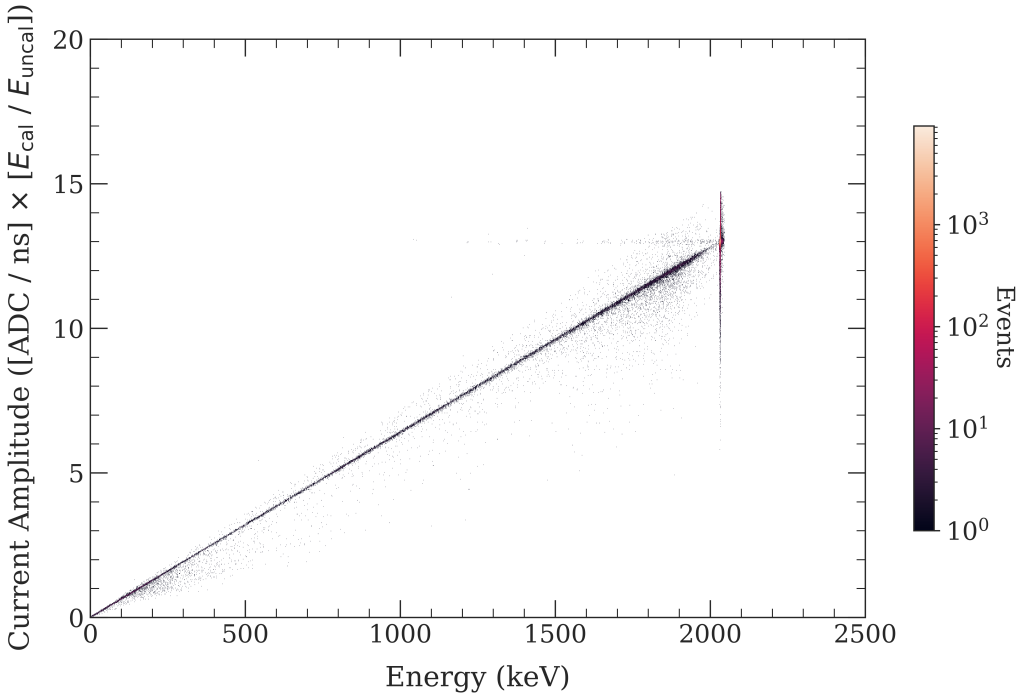

Figure 3.18: Current amplitude vs Energy for a sample of simulated $0\nu\beta\beta$ events in an enriched HPGe detector.

3.4.5 Signal Acceptance Stability Systematic Uncertainty

The signal acceptance is tuned by analyzing only the long calibration periods, therefore the signal acceptance is prone to change in the short calibration periods. The measured signal acceptance at each short calibration gives a sampling of how stable the signal acceptance is throughout the full dataset. The stability systematic is the difference of a weighted flat line fit to the short calibration signal acceptances and the DEP acceptance in Table 3.1. The standard deviation of all the short calibration DEP acceptances is then added in quadrature, see Fig. 3.20.

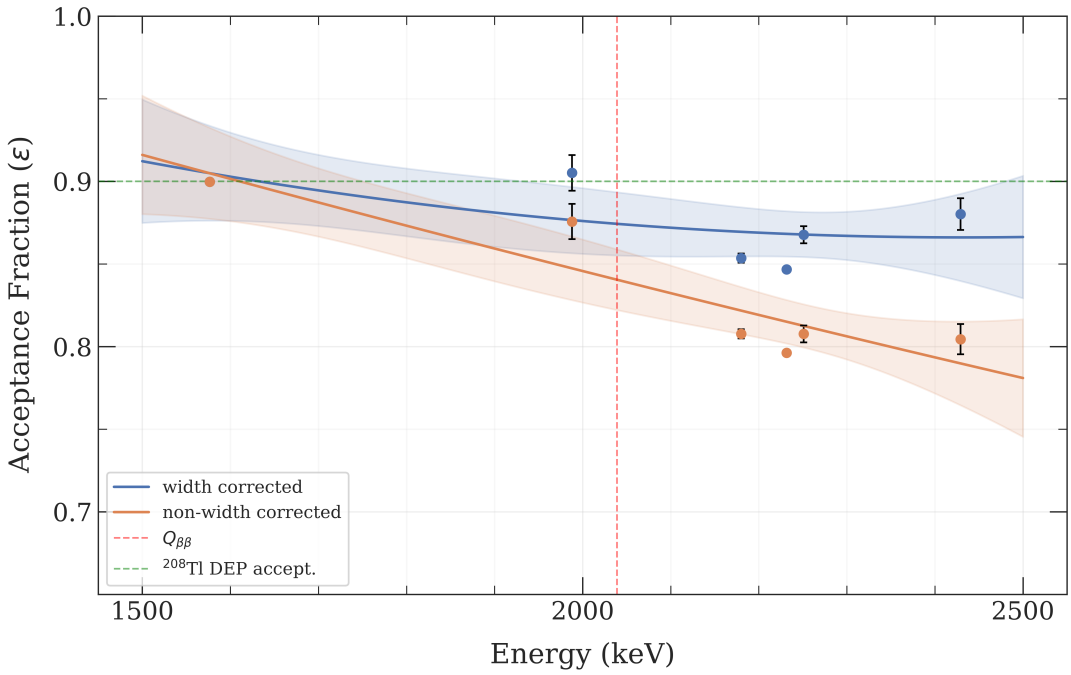

Figure 3.19: The acceptances of each of the ^{56}Co DEP peaks fit to a second order polynomial for with and without a width-energy dependent correction. The shaded regions are the fit 1-σ confidence bands and the dotted lines show for reference the ^{208}Tl DEP acceptance and $Q_{\beta\beta}$ energy. The lower bound of the $0\nu\beta\beta$ acceptance systematic is the difference between the green line and the the blue line where the dotted orange intersects.

3.4.6 Width Correction Systematic Uncertainty

The width function in Fig. 3.8 is fit for every detector using the ^{56}Co peak widths and the CM widths at low energy; the simulated $2\nu\beta\beta$ widths are only available for two detector response models. All enriched detectors operational during the ^{56}Co calibration period have specially fit width-energy dependencies. Those that were not operational dure the ^{56}Co calibration use the average width-energy dependence, Fig. 3.21. The width correction uncertainty is calculated by varying the width-energy dependent correction for each detector about the

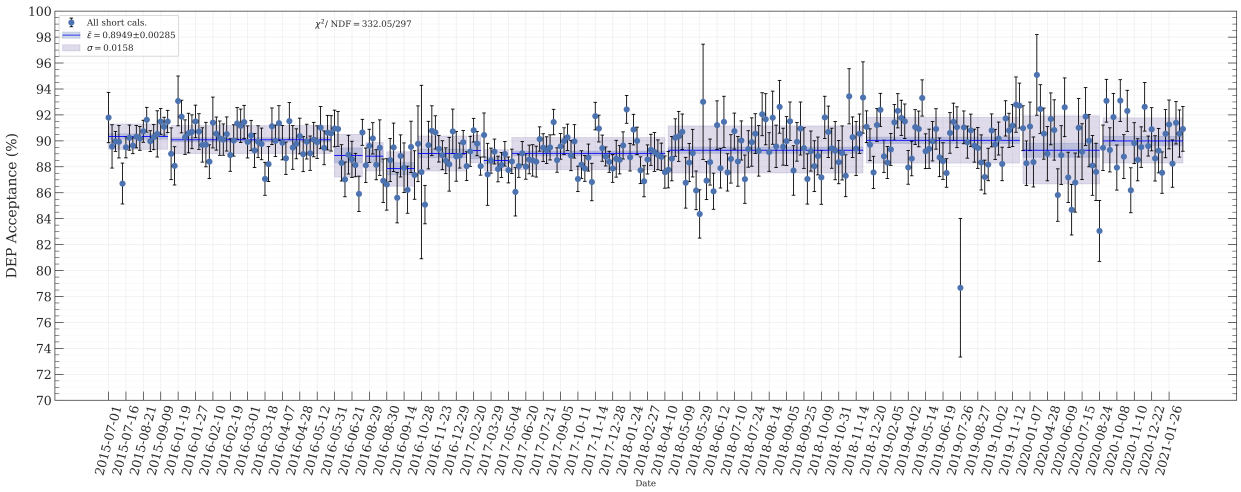

Figure 3.20: The DEP acceptance for each short calibration, evaluated using Eq. 3.9 and Eq. 3.10. The solid blue flat line is the weighted average of all the points and the shaded purple region is the standard deviation. The fit is performed for each dataset individually.

1-σ confidence interval and calculating the signal acceptance. This is done using all long calibrations combined. Detectors that use the average width-energy dependent function are varied by the average 1-σ confidence interval. Another contribution to the AvsE width is the $\cos(\theta)$ term in Eq. 3.5, which is also varied by its statistical uncertainty per detector. The variance between the width-energy dependent function and $\cos(\theta)$ that gives the maximum uncertainty is used.

3.5 High AvsE Signal Acceptance and Systematic Uncertainties

Evaluating the high AvsE cut signal acceptance uses the same criteria for the multi-site AvsE cut. Eq. 3.9 and Eq. 3.10 are used with the cut defined at AvsE < 9. Before evaluating the signal acceptance of the high AvsE cut, the low AvsE cut is applied to the data so that the overall AvsE signal acceptance is the product of the two signal acceptances. Since the high AvsE cut is not tuned for each detector and is instead a global cut value assigned to all detectors, the high AvsE signal acceptance is calculated for all enriched detectors and all

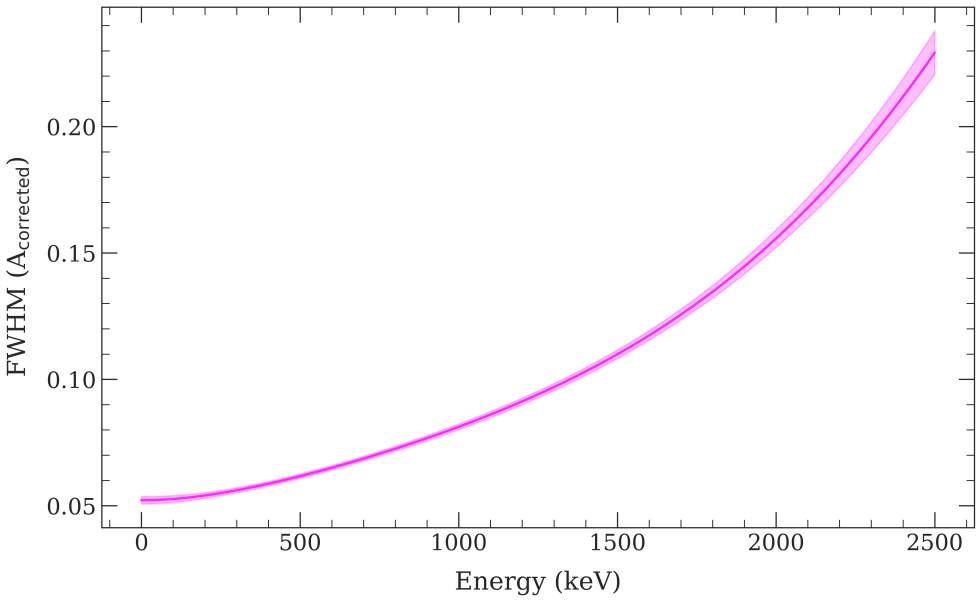

Figure 3.21: The average width function and 1-σ confidence interval for all detectors. The low energy portion is higher than in Fig. 3.8 since these fits use the low energy CC modes. This will slightly raise the acceptance and is the only way to constrain the fits without resorting to simulation.

long calibrations combined within each dataset, Table 3.2.

DEP	SEP	CC
98.05% ± 0.08%	96.54% ± 0.45%	97.67% ± 0.05%

Table 3.2: High AvsE cut acceptance for the DEP, SEP, and ROI CC for all enriched PPC detectors.

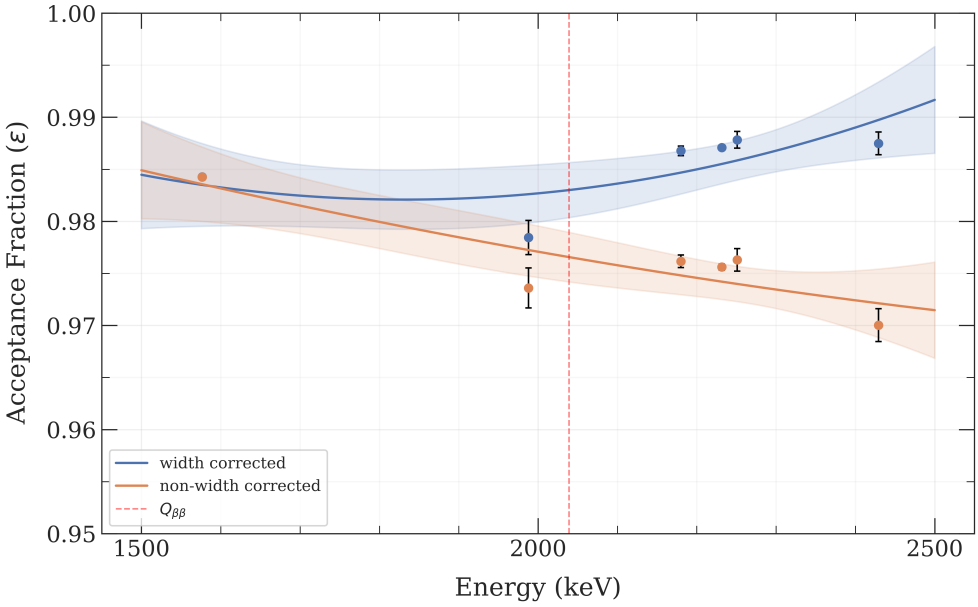

Figure 3.22: The acceptances of each of the ^{56}Co DEP peaks fit to a second order polynomial for with and without a width-energy dependent correction for a high AvsE cut. The shaded regions are the fit 1-σ confidence bands and the dotted line shows the $Q_{\beta\beta}$ energy. The systematic is the difference between the calibrated high cut signal acceptance and the projected signal acceptance at $Q_{\beta\beta}$ for the width-corrected AvsE.

3.5.1 $0\nu\beta\beta$ Acceptance Systematic Uncertainty

The high AvsE cut is still prone to signal acceptance degradation at higher energies above the DEP, similar to the multi-site cut. This is measured by calculating the signal acceptance in the ^{56}Co DEP peaks for AvsE < 9 cut and estimating the acceptance energy dependence with a second order polynomial, Fig. 3.22. There is a dependence present after the width-energy dependence correction is applied, but small in comparison to the multi-site cut.

3.5.2 $2\nu\beta\beta$ Acceptance Systematic Uncertainty

The $2\nu\beta\beta$ acceptance tests how similar the acceptance at the DEP is to another single-site population in the energy range 950−1400 keV. For the high AvsE cut these two signal acceptances should be roughly the same within a certain precision. A DCR cut is first applied here to remove the degraded α events in the background data. The systematic is then the difference in the high AvsE signal acceptance between the DEP AvsE spectrum and $2\nu\beta\beta$ AvsE spectrum after a multi-site cut in both and DCR cut in the $2\nu\beta\beta$ background.

3.5.3 Signal Acceptance Stability

The high AvsE stability is evaluated by monitoring the signal acceptance at the DEP for a high AvsE cut for all short calibrations, see Fig. 3.23. The systematic is the same as in section 3.4.5.

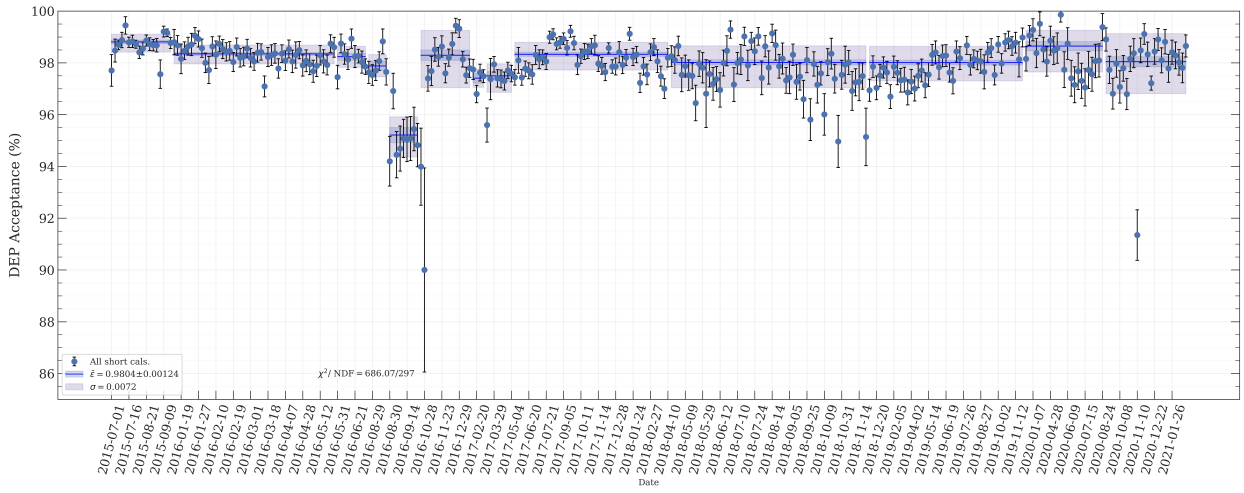

Figure 3.23: The DEP acceptance for each short calibration, evaluated using Eq. 3.9 and Eq. 3.10 with a high AvsE cut. The solid blue flat lines are the weighted average per dataset and the shaded purple region is the standard deviation. The fit is performed for each dataset individually.

3.6 Results

Each of the signal acceptance and systematics are evaluated by dataset. Datasets within the full-enriched data-taking time period signify changes to the configuration of the MAJORANA DEMONSTRATOR. This could be upgrades, shielding changes, or detector/channel replacement. The multi-site efficiency and high AvsE efficiency used in the calculation of the efficiency for the half-life sensitivity is the exposure weighted average of the nominal signal acceptances and uncertainties from all datasets. The multi-site cut efficiency is $0.8991^{+0.0326}_{-0.0324}$ and the high AvsE cut efficiency is 0.9795 ± 0.0106. The signal acceptances and uncertainties by dataset are broken down in Tables 3.3−3.6. Combining with the DS8 ICPC dataset results, as shown in Appendix A, this gives a multi-site cut efficiency of $0.8971^{+0.0330}_{-0.0335}$ and a high cut efficiency of 0.9793 ± 0.0106.

Dataset	DEP efficiency and systematics (enriched detectors)
DS0	$0.8985 \pm 0.0073(\text{stat})\ ^{+0.0039}_{-0.0028}(\text{roi})\ ^{+0.0072}_{-0.0077}(2\nu\beta\beta)\ ^{+0.019}_{-0.0149}(0\nu\beta\beta) \pm 0.0108(\text{stab})\ ^{+0.0149}_{+0.0131}(\text{width})$
DS1	$0.8993 \pm 0.0092(\text{stat})\ ^{+0.004}_{-0.0015}(\text{roi})\ ^{+0.0044}_{-0.005}(2\nu\beta\beta)\ ^{+0.019}_{-0.0162}(0\nu\beta\beta) \pm 0.0109(\text{stab})\ ^{+0.0145}_{+0.0131}(\text{width})$
DS2	$0.8991 \pm 0.0133(\text{stat})\ ^{+0.0032}_{-0.0046}(\text{roi})\ ^{+0.0068}_{-0.0074}(2\nu\beta\beta)\ ^{+0.019}_{-0.0158}(0\nu\beta\beta) \pm 0.0196(\text{stab})\ ^{+0.0167}_{+0.0143}(\text{width})$
DS3	$0.8992 \pm 0.0144(\text{stat})\ ^{+0.0046}_{-0.0176}(\text{roi})\ ^{+0.0106}_{-0.0132}(2\nu\beta\beta)\ ^{+0.019}_{-0.0159}(0\nu\beta\beta) \pm 0.0158(\text{stab})\ ^{+0.0226}_{+0.0205}(\text{width})$
DS4	$0.9015 \pm 0.0139(\text{stat})\ ^{-0.0102}_{-0.0199}(\text{roi})\ ^{+0.0054}_{-0.0073}(2\nu\beta\beta)\ ^{+0.0191}_{-0.0195}(0\nu\beta\beta) \pm 0.0268(\text{stab})\ ^{+0.0089}_{+0.0078}(\text{width})$
DS5a	$0.8996 \pm 0.0235(\text{stat})\ ^{-0.0019}_{-0.024}(\text{roi})\ ^{+0.0054}_{-0.0049}(2\nu\beta\beta)\ ^{+0.019}_{-0.0165}(0\nu\beta\beta) \pm 0.0164(\text{stab})\ ^{+0.0142}_{+0.0114}(\text{width})$
DS5b	$0.8996 \pm 0.0235(\text{stat})\ ^{-0.0019}_{-0.024}(\text{roi})\ ^{+0.0033}_{-0.0027}(2\nu\beta\beta)\ ^{+0.019}_{-0.0165}(0\nu\beta\beta) \pm 0.0121(\text{stab})\ ^{+0.0142}_{+0.0114}(\text{width})$
DS5c	$0.8996 \pm 0.0235(\text{stat})\ ^{-0.0019}_{-0.024}(\text{roi})\ ^{+0.0033}_{-0.0025}(2\nu\beta\beta)\ ^{+0.019}_{-0.0165}(0\nu\beta\beta) \pm 0.0165(\text{stab})\ ^{+0.0142}_{+0.0114}(\text{width})$
DS6a	$0.8994 \pm 0.0089(\text{stat})\ ^{-0.0009}_{-0.0093}(\text{roi})\ ^{+0.0068}_{-0.0086}(2\nu\beta\beta)\ ^{+0.019}_{-0.0162}(0\nu\beta\beta) \pm 0.0155(\text{stab})\ ^{+0.0138}_{+0.0114}(\text{width})$
DS6b	$0.899 \pm 0.0097(\text{stat})\ ^{-0.0004}_{-0.0091}(\text{roi})\ ^{+0.0066}_{-0.0068}(2\nu\beta\beta)\ ^{+0.019}_{-0.0156}(0\nu\beta\beta) \pm 0.0189(\text{stab})\ ^{+0.0117}_{+0.0099}(\text{width})$
DS6c	$0.8978 \pm 0.0088(\text{stat})\ ^{+0.0004}_{-0.0075}(\text{roi})\ ^{+0.006}_{-0.0064}(2\nu\beta\beta)\ ^{+0.019}_{-0.0138}(0\nu\beta\beta) \pm 0.0178(\text{stab})\ ^{+0.0117}_{+0.0097}(\text{width})$
DS7	$0.9002 \pm 0.0159(\text{stat})\ ^{+0.0019}_{-0.0258}(\text{roi})\ ^{+0.0089}_{-0.0098}(2\nu\beta\beta)\ ^{+0.019}_{-0.0176}(0\nu\beta\beta) \pm 0.0271(\text{stab})\ ^{+0.014}_{+0.0117}(\text{width})$
DS8	$0.8998 \pm 0.0147(\text{stat})\ ^{+0.0062}_{-0.0058}(\text{roi})\ ^{+0.007}_{-0.0074}(2\nu\beta\beta)\ ^{+0.019}_{-0.0169}(0\nu\beta\beta) \pm 0.0174(\text{stab})\ ^{+0.015}_{+0.0131}(\text{width})$
DS8 (ICPC)	$0.8520 \pm 0.0221(\text{stat})\ ^{-0.0031}_{-0.0306}(\text{roi})\ ^{+0.0112}_{-0.0309}\ (2\nu\beta\beta)\ ^{+0.0338}_{-0.0338}\ (0\nu\beta\beta) \pm 0.0031(\text{stab})$

Table 3.3: Efficiency and systematics for the multi-site AvsE cut for all PPC enriched detectors by dataset

Dataset	DEP eff. (all)	DEP eff. (natural)	DEP eff. (enriched)
DS0	$0.8987\ ^{+0.0311}_{-0.0314}$	$0.8993\ ^{+0.0681}_{-0.0717}$	$0.8985\ ^{+0.0286}_{-0.0251}$
DS1	$0.8995\ ^{+0.0277}_{-0.0251}$	$0.9009\ ^{+0.0473}_{-0.0466}$	$0.8993\ ^{+0.0284}_{-0.0257}$
DS2	$0.8996\ ^{+0.0335}_{-0.0315}$	$0.904\ ^{+0.0397}_{-0.0417}$	$0.8991\ ^{+0.0354}_{-0.033}$
DS3	$0.8991\ ^{+0.0348}_{-0.0365}$	$0.8988\ ^{+0.0334}_{-0.0336}$	$0.8992\ ^{+0.0382}_{-0.0402}$
DS4	$0.9002\ ^{+0.0401}_{-0.0452}$	$0.8992\ ^{+0.0493}_{-0.0544}$	$0.9015\ ^{+0.0386}_{-0.0424}$
DS5a	$0.8984\ ^{+0.0347}_{-0.0372}$	$0.8971\ ^{+0.0359}_{-0.0349}$	$0.8996\ ^{+0.0376}_{-0.0427}$
DS5b	$0.8984\ ^{+0.0317}_{-0.0345}$	$0.8971\ ^{+0.0317}_{-0.0305}$	$0.8996\ ^{+0.0357}_{-0.0411}$
DS5c	$0.8984\ ^{+0.0329}_{-0.0356}$	$0.8971\ ^{+0.0324}_{-0.0312}$	$0.8996\ ^{+0.0375}_{-0.0426}$
DS6a	$0.8992\ ^{+0.0266}_{-0.026}$	$0.8991\ ^{+0.0284}_{-0.0277}$	$0.8994\ ^{+0.0303}_{-0.0295}$
DS6b	$0.8989\ ^{+0.0276}_{-0.0265}$	$0.8989\ ^{+0.0315}_{-0.0306}$	$0.899\ ^{+0.0315}_{-0.0304}$
DS6c	$0.8983\ ^{+0.0261}_{-0.0238}$	$0.899\ ^{+0.0277}_{-0.0266}$	$0.8978\ ^{+0.0305}_{-0.0279}$
DS7	$0.8999\ ^{+0.0401}_{-0.0455}$	$0.8992\ ^{+0.0757}_{-0.076}$	$0.9002\ ^{+0.0404}_{-0.0469}$
DS8	$0.898\ ^{+0.031}_{-0.0297}$	$0.8957\ ^{+0.0365}_{-0.0371}$	$0.8998\ ^{+0.0345}_{-0.0326}$
DS8 (ICPC)	-	-	$0.8520^{+0.0421}_{-0.0594}$

Table 3.4: Efficiency and uncertainties (statistical and systematic uncertainties combined) for the multi-site AvsE cut by dataset and for all detectors.

In the background estimation window the multi-site AvsE cut removes $\sim$ 27% of the remaining events and the high AvsE cut removes $\sim$ 23% of the remaining events. Overall AvsE is responsible for about a $\sim$ 60% background reduction in the background estimation window after DCR and LQ cuts are applied. $\sim$ 34% of events are cut by both AvsE and DCR and $\sim$ 30% are cut by both AvsE and LQ. In the 10 keV window centered at $Q_{\beta\beta}$ the multi-site cut is responsible for removing four events that pass all other cuts, including one event at 2039.34 keV. The events in the background estimation window and cut overlap matrix are shown in Fig. 3.24 and Fig. 3.25, respectively.

3.7 Summary

The AvsE multi-site parameter has proven to be an effective, yet complicated, analysis cut in removing multi-site backgrounds from the ROI and background estimation window.

Dataset	DEP efficiency and systematics
DS0	0.9877 ± 0.0005(stat) ± 0.0019($2\nu\beta\beta$) ± 0.0035(stab)
DS1	0.982 ± 0.0007(stat) ± 0.0001($2\nu\beta\beta$) ± 0.0038(stab)
DS2	0.9826 ± 0.001(stat) ± 0.0149($2\nu\beta\beta$) ± 0.0041(stab)
DS3	0.9782 ± 0.0011(stat) ± 0.0138($2\nu\beta\beta$) ± 0.0043(stab)
DS4	0.9767 ± 0.0018(stat) ± 0.0082($2\nu\beta\beta$) ± 0.0265(stab)
DS5a	0.9781 ± 0.0016(stat) ± 0.0055($2\nu\beta\beta$) ± 0.0116(stab)
DS5b	0.9781 ± 0.0016(stat) ± 0.0128($2\nu\beta\beta$) ± 0.0053(stab)
DS5c	0.9781 ± 0.0016(stat) ± 0.014($2\nu\beta\beta$) ± 0.0068(stab)
DS6a	0.9802 ± 0.0005(stat) ± 0.0043($2\nu\beta\beta$) ± 0.0059(stab)
DS6b	0.9772 ± 0.0006(stat) ± 0.0024($2\nu\beta\beta$) ± 0.0082(stab)
DS6c	0.9784 ± 0.0006(stat) ± 0.0087($2\nu\beta\beta$) ± 0.0068(stab)
DS7	0.9829 ± 0.001(stat) ± 0.0028($2\nu\beta\beta$) ± 0.0082(stab)
DS8	0.9797 ± 0.0009(stat) ± 0.012($2\nu\beta\beta$) ± 0.0116(stab)
DS8 (ICPC)	0.9781 ± 0.0015(stat) ± 0.0077($2\nu\beta\beta$) ± 0.0118(stab)

Table 3.5: Efficiency and systematics for the high AvsE cut for all enriched detectors by dataset after the application of a multi-site cut.

From recent work within the MAJORANA Collaboration, additional detector response corrections have been incorporated into the latest rendition of AvsE through the correction of width-energy dependence and drift-time energy dependence. When comparing the MAJORANA Collaboration official result reported in 2019 [74], the new AvsE parameter suggests that the signal acceptance at $Q_{\beta\beta}$ was less than the signal acceptance at the DEP, but within uncertainties. This is inferred from the width-energy dependence discovered in the signal acceptance of AvsE.

Though AvsE precisely tunes for all of these dependencies with respect to other parameters, part if not all of this advantage is negated by the parameter's instability. AvsE is an unstable parameter for two reasons: it is tuned for bi-monthly long calibrations and not weekly short calibrations, and the energy dependence is non-linear and produces non-linear instabilities. The non-linear instabilities are difficult to correct for in the short calibrations

Dataset	DEP eff. (all)	DEP eff. (natural)	DEP eff. (enriched)
DS0	$0.9872^{+0.0034}_{-0.0034}$	$0.9859^{+0.006}_{-0.006}$	$0.9877^{+0.004}_{-0.004}$
DS1	$0.9821^{+0.0041}_{-0.0041}$	$0.9842^{+0.0158}_{-0.0298}$	$0.982^{+0.0039}_{-0.0039}$
DS2	$0.9827^{+0.0146}_{-0.0146}$	$0.9835^{+0.0165}_{-0.0206}$	$0.9826^{+0.0154}_{-0.0154}$
DS3	$0.98^{+0.014}_{-0.014}$	$0.9864^{+0.0136}_{-0.0144}$	$0.9782^{+0.0145}_{-0.0145}$
DS4	$0.9811^{+0.0177}_{-0.0177}$	$0.9851^{+0.0149}_{-0.0156}$	$0.9767^{+0.0233}_{-0.0278}$
DS5a	$0.9821^{+0.0107}_{-0.0107}$	$0.9869^{+0.0129}_{-0.0129}$	$0.9781^{+0.0129}_{-0.0129}$
DS5b	$0.9821^{+0.0172}_{-0.0172}$	$0.9869^{+0.0131}_{-0.0221}$	$0.9781^{+0.0139}_{-0.0139}$
DS5c	$0.9821^{+0.0166}_{-0.0166}$	$0.9869^{+0.0056}_{-0.0056}$	$0.9781^{+0.0157}_{-0.0157}$
DS6a	$0.9833^{+0.0085}_{-0.0085}$	$0.9886^{+0.0114}_{-0.0119}$	$0.9802^{+0.0073}_{-0.0073}$
DS6b	$0.982^{+0.0082}_{-0.0082}$	$0.9892^{+0.0082}_{-0.0082}$	$0.9772^{+0.0085}_{-0.0085}$
DS6c	$0.9829^{+0.0128}_{-0.0128}$	$0.9895^{+0.0059}_{-0.0059}$	$0.9784^{+0.0111}_{-0.0111}$
DS7	$0.9835^{+0.0069}_{-0.0069}$	$0.9846^{+0.0103}_{-0.0103}$	$0.9829^{+0.0087}_{-0.0087}$
DS8	$0.9833^{+0.0167}_{-0.0168}$	$0.9885^{+0.0057}_{-0.0057}$	$0.9797^{+0.0167}_{-0.0167}$
DS8 (ICPC)	-	-	0.9781 ± 0.0142

Table 3.6: Efficiency and uncertainties (statistical and systematic uncertainties combined) for the high AvsE cut by dataset and for all detectors after the application of a multi-site cut.

due to limited statistics and resulted in $\sim$ 2 kg yr of exposure lost in the analysis. Further research in stabilizing AvsE in the short calibration run periods has the most potential for improving the parameter's performance, with the goal of reducing the stability systematic and increasing the exposure at the same time. Another direction of further research is tuning an AvsE parameter for the ICPC detectors. This requires investigating each of the dependencies in the max current amplitude "A" change when the active mass of the detector becomes larger and the electrode configuration is modified.

Research into AvsE has demonstrated that there is a trade-off in exposure vs signal acceptance uncertainty. When combined with the entire analysis this affects the trade-off of half-life sensitivity vs half-life uncertainty. Traditionally A/E allows for more exposure at the expense of larger uncertainty and AvsE has less uncertainty at the expense of lower

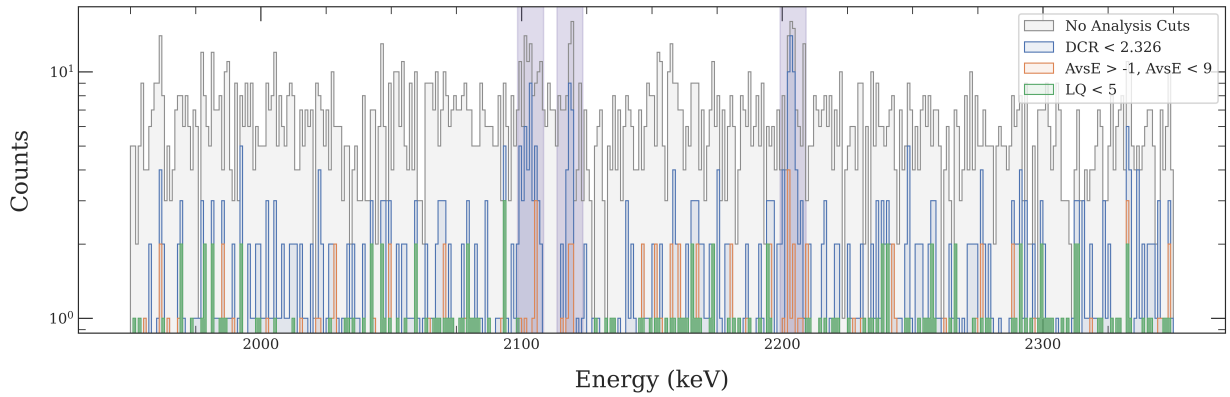

Figure 3.24: Events remaining in the background estimation window after applying different analysis cuts in sequence. The difference in the blue and orange shows the impact of applying the multi-site and high AvsE cut, which removes about 60% of the events. Adding the LQ cut reduces the background to the green spectrum. The purple vertical bands indicate the 10 keV energy windows around known energy peaks.

exposure. Choosing A/E or AvsE comes down to the requirements for and optimization of a particular analysis. However, for future tonne-scale ^{76}Ge experiments it may be important to search for a multi-site parameter that breaks this trade-off by increasing exposure and increasing stability at the same time.

For ^{76}Ge experiments searching for $0\nu\beta\beta$ decay, A/E may be sufficient given its superior stability and simpler energy dependence. Due to the instability of AvsE, a quadratic energy dependence may not have much of an advantage, if at all, for removing events in the background averaging window. AvsE does present the advantage that it can be used at lower energy in other rare physics searches or background model fitting, but there is no evidence so far that establishes whether AvsE out-performs A/E in any significant way for a $0\nu\beta\beta$ search. While $0\nu\beta\beta$ decay searches remain in "discovery mode" with half-life limits dominated by statistics, minor systematic uncertainties will have only a minor impact on experimental sensitivities. In this case, A/E with a width-energy dependence correction and

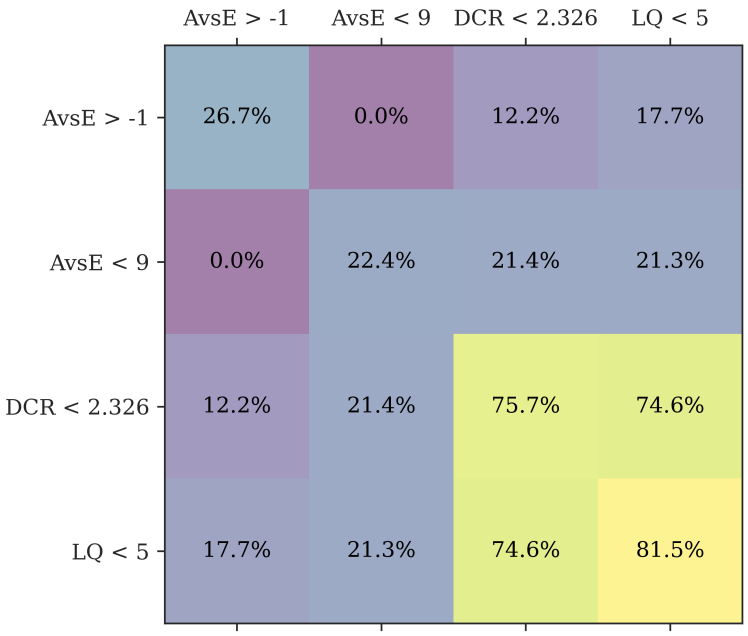

Figure 3.25: Correlation matrix showing the percentage of events cut with different pairwise combinations of analysis cut parameters. The diagonal represents the percentage of events cut when using one analysis cut before all cuts are applied.

a drift-time correction will probably out perform AvsE by retaining exposure at the cost of a modest increase in signal acceptance uncertainty. However, given the more stringent background level requirements for LEGEND-1000 there is still room to search for more effective multi-site discrimination parameters.

Chapter 4

LARGE ENRICHED GERMANIUM EXPERIMENT FOR NEUTRINOLESS $\beta\beta$ DECAY

Neutrinoless double-β decay experiments run in multiple phases, where each iteration of the experiment determines the feasibility of the next. The MAJORANA DEMONSTRATOR and GERDA were experiments used to test different technologies for operating a HPGe experiment at the tonne scale. Results from both experiments have determined that a larger HPGe experiment could be built to raise $0\nu\beta\beta$ half-life limits up several orders of magnitude within the next few decades [96]. The next phase in HPGe $0\nu\beta\beta$ experiments is the Large Enriched Germanium Experiment for Neutrinoless $\beta\beta$ Decay (LEGEND). LEGEND will operate in two phases: one with 200 kg of HPGe detectors (LEGEND-200) using the GERDA infrastructure at LNGS, and a subsequent phase with 1000 kg of HPGe detectors (LEGEND-1000), with possible locations at SNOLAB or at LNGS, see Fig. 4.1a and Fig. 4.1b. LEGEND-200 commissioning data-taking has been on going since the Fall of 2021 and the collaboration plans to begin data-taking with the full experiment before the end of 2022. LEGEND-1000 is in the conceptional design phase and could begin data-taking sometime within the next decade.

The goal of LEGEND-200 is to reach a half-life sensitivity of 10^{27} years in five years of operation with a background index of 2×10^{-4} cts / (keV kg yr) and the goal of LEGEND-1000 is to reach a half-life sensitivity of 10^{28} years in ten years of operation with a background index of less than 1×10^{-5} cts / (keV kg yr) [96]. This chapter will give a brief overview of LEGEND with a focus on the liquid argon veto. GERDA was able to achieve the lowest background level within the ROI for any experiment with a liquid argon veto even when prior backgrounds without its implementation in the analysis produced a higher background

level than the MAJORANA DEMONSTRATOR [97]. These showed that the use of a liquid argon veto for future ^{76}Ge experiments is essential for background suppression. Though the GERDA liquid argon veto is effective, there are still several areas for improving the detection efficiency and this motivates the next chapter on silicon photomultiplier characterization.

4.1 LEGEND-200

LEGEND-200 is the next leading phase of ^{76}Ge $0\nu\beta\beta$ decay experiments and the preceding phase to LEGEND-1000. LEGEND-200 is the combination of technologies from the MAJORANA DEMONSTRATOR and GERDA that is expected to have the highest background suppression. The experiment is using the low background cables and connectors from MAJORANA and the Liquid Argon Veto, with higher purity liquid argon, in the GERDA infrastructure. LEGEND-200 will use the existing 70 kg of enriched detectors from the MAJORANA DEMONSTRATOR and GERDA as well as 130 kg of newly produced *inverted coaxial point contact* detectors (ICPC) to have a total of 200 kg of active isotope.

ICPC detectors are HPGe detectors with a p^+ point contact and an outer layer n^+ contact like the other BEGe and PPC detector designs used in the MAJORANA DEMONSTRATOR and GERDA, see Fig. 4.2. The p^+ point contact and n^+ contact are separated by a groove, which contains a passivated surface of amorphous germanium. The ICPC detector design uses an inverted coaxial geometry to ensure the detector can be fully depleted when reversed biased up to 5 kV. The main advantage of deploying ICPCs is the average active mass per detector is approximately two times that of the typical BEGe or PPC, while maintaining a 2.5 keV or less resolution at $Q_{\beta\beta}$and excellent single-site/multi-site discrimination. This means that in order to achieve a targeted active mass for a germanium detector experiment one would need fewer detectors if the mass per detector is larger. Having fewer detector units is beneficial because this will reduce the total number of cables and harnesses needed for the experiment. Due to the germanium processing discussed in section 2.1, the germanium is the most radiopure material in the experiment. When scaling up a ^{76}Ge experiment it is the most beneficial to increase the relative mass of the germanium more than the relative mass

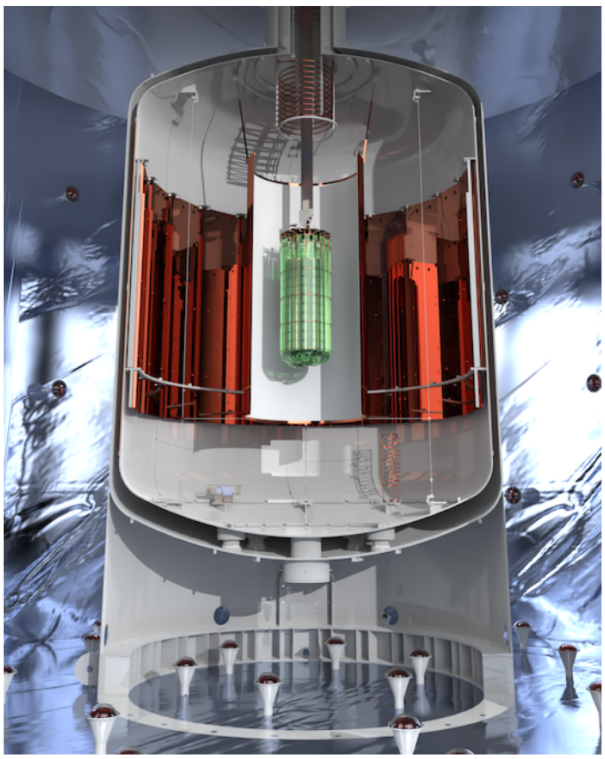

(a)

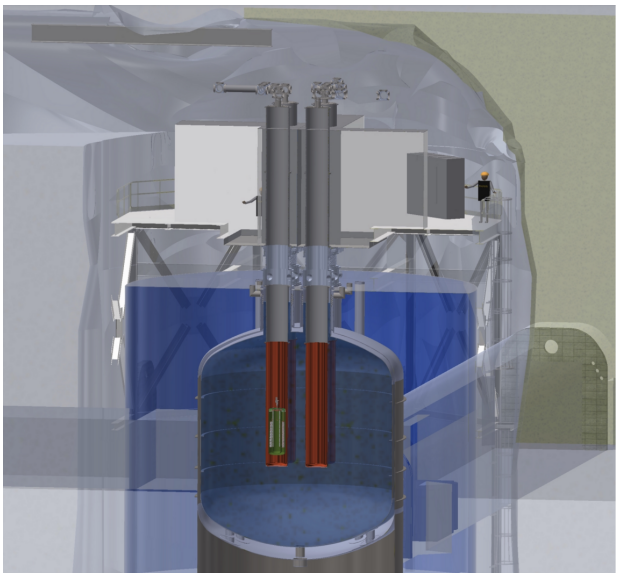

(b)

Figure 4.1: A schematic of LEGEND-200 (a) and LEGEND-1000 (b). The detectors are submersed in liquid argon and surrounded by wavelength shifting fibers to veto liquid argon scintillation against HPGe detector signals. The liquid argon also serves as a cryogenic bath to maintain the detectors at 87 K. Outside of the detector array are copper panels to block radioactivity from the cryostat walls. Outside the inner vessel is a Cherenkov water detector for vetoing cosmic ray muons. LEGEND-1000 has similar design concepts as LEGEND-200, the main difference being that LEGEND-1000 has a total of four copper vessels to insert detector/fiber arrays into and are filled with underground sourced argon to limit radioactivity originating from cosmogenic activation. Fig. (a) from ref. [96] and Fig. (b) *Image Credit: https://legend-exp.org*

of the inactive components of the experiment.

A new addition to LEGEND-200 is the use of detector base-plates made out of polyethylene naphthalate (PEN). PEN is a radiopure, scintillating material that shifts liquid argon scintillation light peaked at 128 nm to visible light [98]. This is beneficial because LEGEND uses photosensitive devices that have peak efficiency in the visible spectrum. The PEN material has an efficiency of 30% (5000 photons per MeV) with a bulk absorption length of 60 mm at 450 nm over a time constant of 25.5 ns [99]. Due to the liquid argon veto, increasing the number of active material components within the experiment will increase the number of signal events registered as background. The liquid argon veto is described in detail in section 4.3. In this case the baseplates will re-emitt scintillated light originating from any radioactivity present in near detector components and if simultaneous signals are also detected in a HPGe detector then the event can be identified as background.

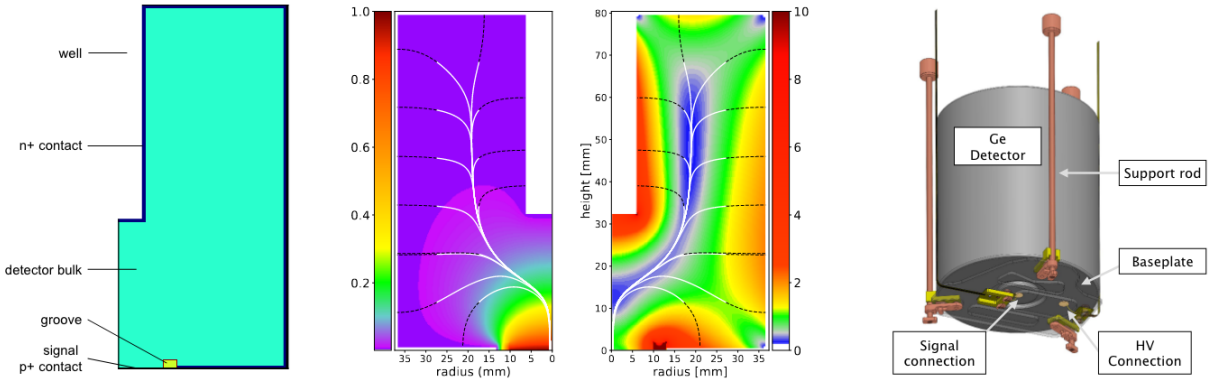

Figure 4.2: (Left) The ICPC detector features. (Middle-left): ICPC weighting potential with hole drift paths in white and electron drift paths in black. (Middle-right) The electric field magnitude where the minimum is at 200 V / cm. ICPC conceptual drawing with LEGEND-1000 front end electronics. Fig. from ref. [96]

4.2 LEGEND-1000

LEGEND-1000 is the superseding phase to LEGEND-200 and plans to use a total detector mass of 1000 kg. The experiment plans to manufacture 870 kg of new detectors and reuse 130 kg of existing detectors from LEGEND-200. With a projected 75% detector yield from the starting material and recycling 50 kg from existing small detectors this amounts to a procurement of 1100 kg of enriched ^{76}Ge. This gives a detector layout of 400 ICPC detectors in four separate liquid argon cryostats with an average mass of 2.6 kg enriched with ^{76}Ge to more than 90%. With more stringent radiopurity requirements to meet a lower background level, LEGEND-1000 includes new front-end electronics designs and the use of underground sourced liquid argon. For LEGEND-200 it is sufficient for all detectors to use the MAJORANA DEMONSTRATOR and GERDA front end electronics, however for LEGEND-1000 it is necessary to have near detector electronics that are more radiopure and have a higher bandwidth due to the longer cable paths from detector to signal digitizer. This is done by adopting a CMOS ASIC-based front-end electronics design and lower-background Kapton flex cables, currently under development at Lawrence Berkeley National Laboratory and Technical University of Munich. The ASIC design also allows for less plastic mass at the signal cable and high voltage cable bonding points.

The liquid argon in LEGEND-200 is sourced from the atmosphere, which contains a significant concentration of radioactive argon isotopes produced from cosmic-ray neutrons. In particular, ^{42}Ar decays to ^{42}K which later decays by emitting a high energy β that can create background events within the ROI. LEGEND-200 shields these β's by surrounding the detectors in a nylon mini-shroud. To increase the radiopurity close to the detectors in LEGEND-1000, the nylon mini-shrouds are removed and the concentration of cosmogenic isotopes in the liquid argon is reduced by sourcing the liquid argon from underground.

4.3 Liquid Argon Veto

$0\nu\beta\beta$ is intrinsically a single-site event that can only originate from the ^{76}Ge inside the HPGe detectors. γ-rays present in the ^{238}U and ^{232}Th decay chains can scatter through multiple locations within the experiment. Events with multiple energy depositions can be removed through multi-site discrimination, detector multiplicity, and with the GERDA infrastructure a *liquid argon veto* (LAr). The LAr veto is a type of active background suppression where background events are removed in the data post processing phase by identifying germanium detector signals that occur simultaneously with liquid argon scintillation signals. This is also referred to in general as an *anti-coincidence cut*. All events that are anti-coincident with detected liquid argon scintillation pass the cut. LAr reaches a temperature of 87 K and is chemically inert, which allows HPGe detectors to operate successfully when directly submerged. The LAr also acts as a passive shield for radiation coming from far detector components due to the attenuation length of liquid argon to MeV scale γ-rays.

The LAr-Veto works by collecting scintillation light with *wavelength shifting fibers* (WLS) that guide the light towards *silicon photomultiplier* (SiPM) detectors, Fig. 4.3. PEN plastic baseplates near the detectors also emit wavelength- shifted light from radioactive background which can also reach the SiPM arrays. LAr scintillation peaks in the vacuum ultraviolet (VUV) spectrum and is shifted by the fibers to the visible spectrum to better match the spectral response of the SiPMs.

4.3.1 Liquid Argon Scintillation

Noble elements, such as argon and xenon, are used in a variety of neutrino and dark matter experiments due to their scintillation properties from excitation and ionizing energy depositions. In the GERDA infrastructure, liquid argon scintillates from ionizing radiation, most commonly from emitted γ-rays in the ^{238}U and ^{232}Th decay chains. LAr scintillation is emitted through the production and decay of Argon excimers. In the case of LAr, an excimer is formed by the chemical bond of a ground state Argon atom with an excited state argon

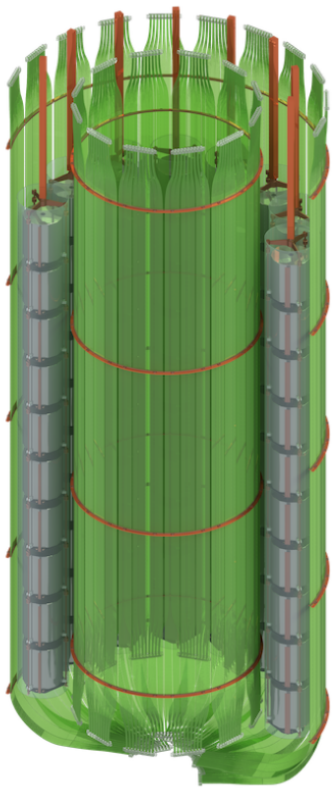

Figure 4.3: One module of detectors and wavelength shifting fibers that is submerged in liquid argon. LAr scintillation light is collected through the wavelength shifting fibers and guided to arrays of SiPMs. The detectors are surrounded by a nylon mini-shroud to shield against β's from radioactive background in the liquid argon. The mini-shroud will be removed for LEGEND-1000 modules due to the usage of lower background underground sourced argon. Fig. from ref. [96].

atom. There are two ways this can happen either through the excitation of a ground state argon atom through an inelastic collision or through the ionization of a ground state argon atom and recombination with a free electron, see Fig. 4.4. An Argon excimer will decay to two unbound ground state Argon atoms and emit a VUV photon, with the emission spectrum peaked at 128 nm, see Fig. 4.5a. The scintillated photons peaked at 128 nm are not

absorbed by atomic argon, so liquid argon is transparent to its own scintillation.

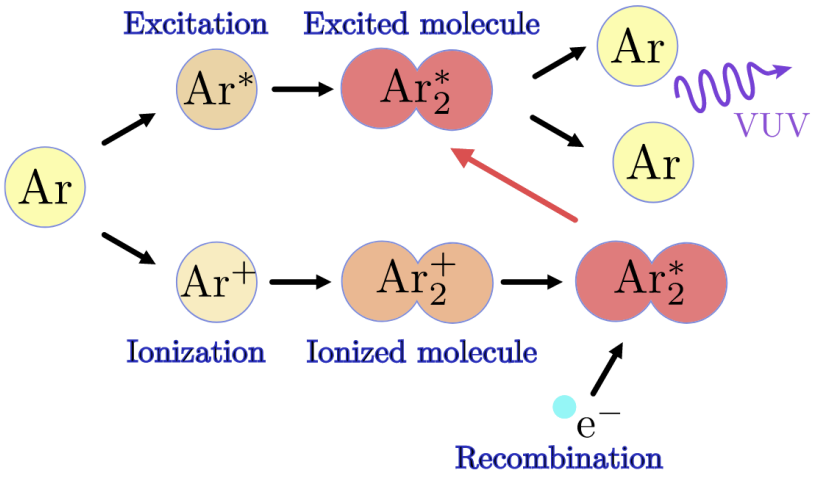

Figure 4.4: A diagram showing the mechanism for LAr scintillation. There are two main path ways for producing an Ar excimer, through excitation or through ionization and recombination with an electron. The short-lived excimer state will then decay back to two ground state argon atoms along with a VUV photon. The photon emission spectrum is narrowly peaked at 128 nm. Fig. from ref. [100].

The average number of ions produced in LAr can be estimated from the total energy deposition divided by the average energy expended per each ion produced,

$$N_{ion} = \frac{E}{W_{ion}}\,. \tag{4.1}$$

The measured value of W_{ion} for LAr is 23.6 eV [101]. For each ion produced there is an average number of argon excimers produced, with a measured value in LAr of $N_{ex}/N_{ion} = 0.21$ [102]. Assuming the liquid argon to be 100% pure and all ions and excimers produced result in scintillation, the maximum number of photons per energy deposition can be estimated by substituting Eq. 4.1 into Eq. 4.2 to give

$$N_\gamma = N_{ion} + N_{ex} \tag{4.2}$$

$$W_\gamma = W_{ion}\left(1 + \frac{N_{ex}}{N_{ion}}\right)^{-1}. \tag{4.3}$$

Substituting in the measured values results in $W_\gamma = 19.5\,\text{eV}$ and a maximum LAr scintillation yield of $\sim 51,000$ photons/MeV. LAr scintillation yields in experiments typically range in the tens of thousands of photons/MeV below the ideal scintillation yield due to the presence of impurities and reduction factors for different types of background [103]. The decay time of the Argon excimer depends on whether the excimer ends up in the singlet ($^1\Sigma_u^+$) or triplet ($^3\Sigma_u^+$) excited state. The $^1\Sigma_u^+$ state has a decay time in the nanosecond scale, while the $^3\Sigma_u^+$ state has a decay time in the microsecond scale [104]. Fig. 4.5b shows an example of what detected LAr scintillation looks like for a γ-ray background and for a neutron background.

Introducing impurities into the LAr has a significant effect on the scintillation light yield and can be observed by measuring changes to the triplet state decay time. Because of the longer lifetime, the triplet state has a higher probability of colliding with impurities that de-excite the Ar excimer states without emitting any scintillation, for example with nitrogen [105]. Scintillation can also be absorbed and re-emitted, thus reducing the attenuation length of the scintillation light through LAr. This occurs with oxygen, where it can be excited through the absorption of LAr scintillation and subsequently de-excited through the emission of infrared radiation [106]. The LEGEND Liquid Argon Monitoring Apparatus (LLAMA) has reported a LAr attenuation length for LEGEND0-200, due to scattering and absorption, to be 50 ± 4 cm [107].

Small concentrations of Xenon can be dissolved into liquid argon to enhance the light collection efficiency. After an Ar excimer is produced, it can transfer its energy to produce a Xenon excimer which then de-excites and emits a higher wavelength VUV photon with an emission spectrum peaked at 175 nm. LAr has a higher attenuation length to Xenon scintillation than its own scintillation, so adding small concentrations of Xenon can result in a higher light collection efficiency for a liquid argon veto [108]. The liquid Xenon freezing point is higher than the temperature of liquid Argon so Xenon concentrations are typically limited to $10-1000$ ppm or else the Xenon will condense. Alternative designs to LEGEND-

1000 have been considered for the use of Xe-doped liquid argon and could improve the light collection efficiency by a factor of 2 over the current design [109].

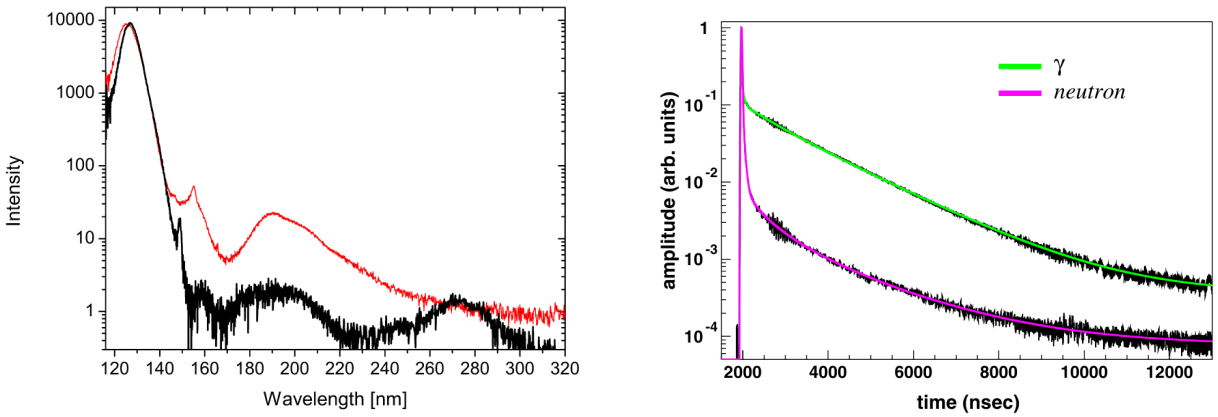

(a) (b)

Figure 4.5: LAr scintillation spectrum (a), where black is liquid and red is gas, and liquid argon scintillation signal with a fast and slow component for incoming γ-rays and incoming neutrons. Fig. from ref. [110, 104].

4.3.2 Light Collection

The LAr scintillation light is collected by wavelength shifting the VUV photons to the visible spectrum and guiding the resulting light through optical fibers to several SiPM arrays. When entering the fibers, VUV photons first interact with a 1μm layer of tetraphenyl butadiene (TPB) that has been applied as an external coating through a vacuum-evaporation process. TPB is an organic chemical compound that fluoresces under the illumination of ultraviolet light. The absorption of a VUV photon brings a TPB molecule from the fundamental electronic state, S_0, to one of the vibrational levels of the first singlet electronic state, S_1 [111]. Part of the absorbed energy is lost to vibrational relaxation and a decay from the S_1 state back down to the S_0 state results in the emission of a longer wavelength photon within

picoseconds to nanoseconds of the original absorption (fluorescence). Phosphorescence can also occur where the S_1 state moves to the first excited triplet state, T_1, through intersystem crossing and then decays to the ground state. This type of transition is typically "forbidden", but can occur through spin-orbit coupling and has a transition time on the order of microseconds. TPB absorbs ultraviolet light and emits visible light peaked around 430 nm; the absorption spectrum and emission spectrum of TPB is shown in Fig. 4.6. TPB has a wide range of possible wavelength shifting efficiencies, which depends on how the TPB is coated onto the fibers, but could have efficiencies of at least 40-50% for liquid argon scintillation and possibly near or higher than 100% [112]. There is also some evidence that TPB coating could degrade or displace off of the fibers into the liquid argon over time [113].

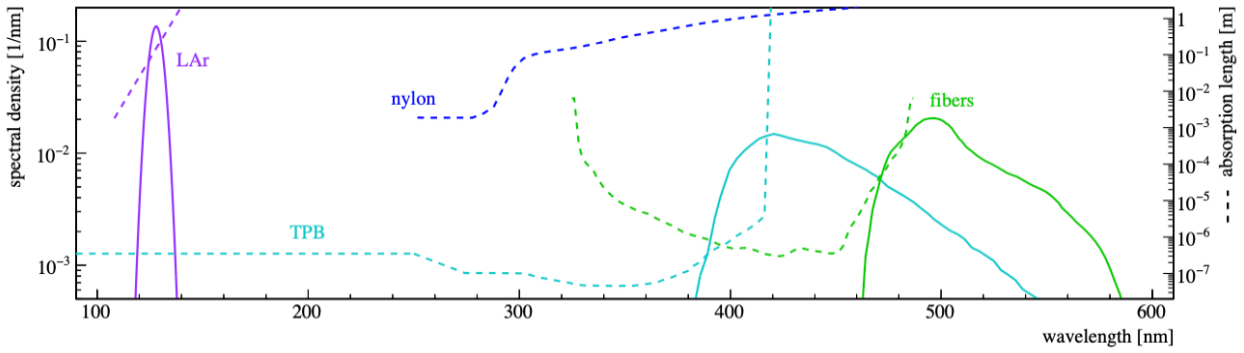

Figure 4.6: A plot showing the LAr scintillation emission spectrum, TPB emission spectrum, and WLS fiber emission spectrum (solid lines) along with their respective absorption lengths (dashed lines). Fig. from ref. [114].

The optical fibers used in LEGEND are BCF-91A wavelength shifting (WLS) fibers produced by Saint-Gobain Crystals. Blue photons, emitted from the TPB, are wavelength shifted to the green part of the visible spectrum with a peak wavelength of 494 nm. The WLS fibers have a polystyrene core doped with fluorescent compounds to produce the desired scintillation and two layers of polymethylmethacrylate (PMMA) cladding [115]. The PMMA cladding has an index of refraction less than the polystyrene core to contain photons within

the fiber by total internal reflection. The additional wavelength shifting from the fiber core is necessary to improve the transport of photons toward the SiPM arrays. Each fiber has a cross-sectional radius of 1 mm.

The detection of photons that have traversed to the ends of the fibers, occurs at the SiPM arrays. SiPMs are solid-state photosensitive detectors that can resolve the arrival times of single photon energy depositions, typically on the nanosecond time scale. The LAr-Veto cuts events where SiPM photon signals and germanium detector signals occur simultaneously within roughly a 10 μs time window. LEGEND-200 uses KETEK PM33100T 3 $\times$ 3 mm SiPMs with each array containing nine SiPMs connected in parallel, see Fig. 4.7. The base material of the array is made of a high radiopurity synthetic fused silica and two sputtered aluminum traces connect all SiPMs in parallel [107]. The outer barrel contains 20 arrays and the inner barrel contains 9 arrays with each SiPM coupled to nine individual fibers.

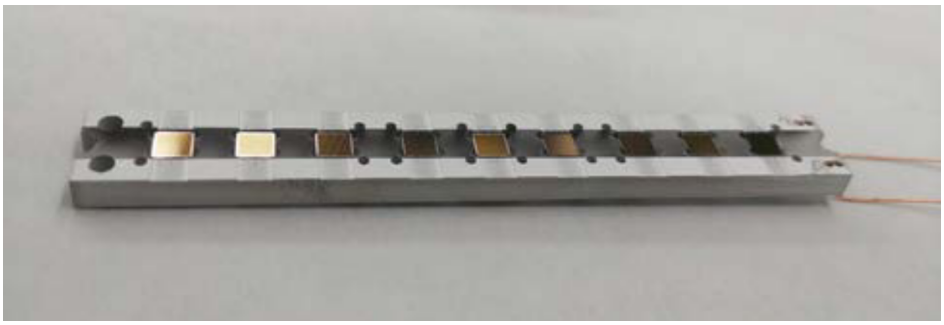

Figure 4.7: One array containing nine SiPMs. Two sputtered aluminum traces connect the SiPMs in parallel. The base material of the array case is made out of a high radiopurity fused silica. Each SiPM has nine fibers directly mounted onto the SiPM active area. Fig. from ref. [107].

4.3.3 LAr-Veto Performance

The LAr-Veto in GERDA proved to be very effective as both a passive shield from far detector components and an active shield for near detector components. After pulse shape

discrimination cuts from the HPGe detectors, the LAr-Veto cut reduces the GERDA background to a world leading background level around $Q_{\beta\beta}$ of 5.2×10^{-4} cts / (keV kg yr) [58]. A histogram of the GERDA background after sequential analysis cuts is shown in Fig. 4.8 for the collaboration's 2019 analysis.

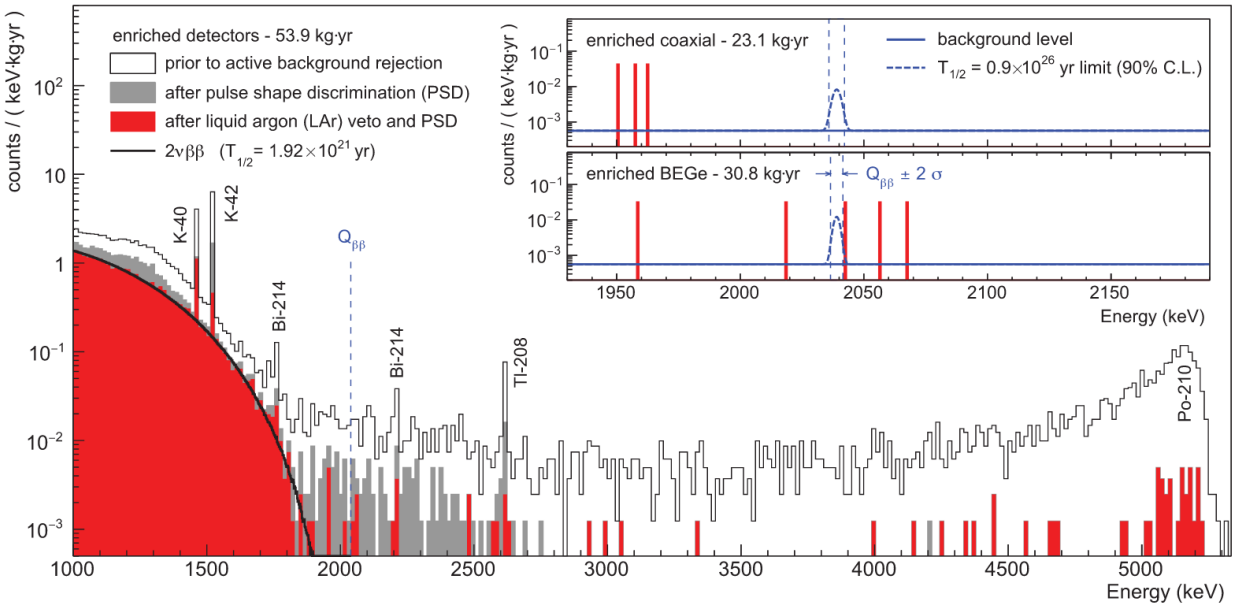

Figure 4.8: The GERDA background level, in 2019, showing all events before cuts, all events after pulse shape analysis cuts, and LAr-Veto cut in additional to all previous cuts. The inset plot shows the background estimation window for BEGe and Coaxial detectors separately with the half-life lower limit. Fig. from ref. [97].

Similar to pulse shape analysis cuts, the LAr-Veto factors into the half-life sensitivity by lowering the sensitive background given a certain signal acceptance. Due to random coincidences and the detection of correlated signals among SiPM channels, the LAr-Veto will occasionally remove data that are not actual coincidences with a germanium detector signal. The signal acceptance of the LAr-Veto in GERDA is estimated to be $\sim 98\%$ from measuring the rate of ^{39}Ar decay signals detected within a $< 10\,\mu$s window [114]. The rejection efficiency can also be measured from the ^{39}Ar background. β's originating from

this decay have a short path length in LAr and emit bremsstrahlung radiation. Sometimes either type of radiation can also produce signals in the germanium detectors, but because signal's origin is from the LAr most events within a 200 - 400 keV window are in principle anti-coincidence candidate events. The LAr-Veto in GERDA is able to reject about 50% of these events [114].

Though the LAr-Veto has proven to be an effective tool for reducing background, studies have shown the light collection yield could be several orders of magnitude lower than the expected LAr scintillation yield. From test stand research done within the GERDA collaboration the light collection yield could be as low as 50 photoelectrons/MeV [116]. This also matches the total light yield of the LAr-Veto when multiplying the expected efficiencies of the LAr-Veto components together, see Fig. 4.9. The detected light yield is expected to improve in LEGEND-200 with purified LAr. In the background projection for LEGEND-200 and LEGEND-1000, photon detection probability maps are generated from optical monte-carlo simulations to estimate the efficiency of the LAr-Veto, Fig. 4.10. The simulations incorporate all of the optical efficiencies, optical properties, and shadowing from detector components. The LEGEND collaboration is in the process of measuring the efficiency of each of the LAr-Veto components to understand the LAr-Veto efficiency and search for improvements that can be made to the design.

4.4 Backgrounds

The background rate projected for LEGEND-200 is about 2.5 times lower than the background rate achieved by GERDA, the lowest background rate at $Q_{\beta\beta}$ achieved by any $0\nu\beta\beta$ experiment to date. This is accomplished by using the larger mass ICPC detectors, MAJORANA DEMONSTRATOR low noise electronics and clean materials, scintillating PEN plastics, and higher purity liquid argon. LEGEND-1000 aims to reduce the background rate further by a factor of 30. This is to be achieved by using underground-sourced liquid argon and lower background electronics. The background sources of concern for LEGEND are as follows:

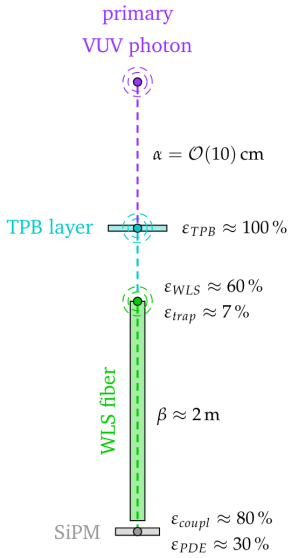

Figure 4.9: A one dimensional representation of the material that scintillation photons pass through in order to be detected as scintillation light. The overall light collection efficiency is of $\mathcal{O}(0.1\%)$. α is the attenuation length, ϵ_{TPB} is the TPB quantum efficiency, ϵ_{WLS} is the wavelength shifting efficiency, ϵ_{trap} is the fiber trapping efficiency, ϵ_{coupl} is the percentage of photons that make it to the SiPM from the fiber, and ϵ_{PDE} is the photon detection efficiency of the SiPM. This does not include shadowing, reflections, and optical coverage. Fig. from ref. [114].

- **^{238}U and ^{232}Th Decay Chains:** These backgrounds are naturally occurring and are present, to some extent, in all manufactured parts of the experiment. ^{208}Tl from the ^{232}Th decay chain and ^{214}Bi from the ^{238}U decay chain both emit γ rays with energies higher than the 2039 keV $Q_{\beta\beta}$for ^{76}Ge. Compton scattering from these γ rays can be contained in one detector, contained in several detectors, or contained between one detector and the liquid argon. Each of these scenarios are effectively rejected by multi-site discrimination, detector multiplicity, and the LAr-Veto, respectively.

- **^{42}K in Liquid Argon:** Liquid Argon is commonly sourced from the atmosphere and is

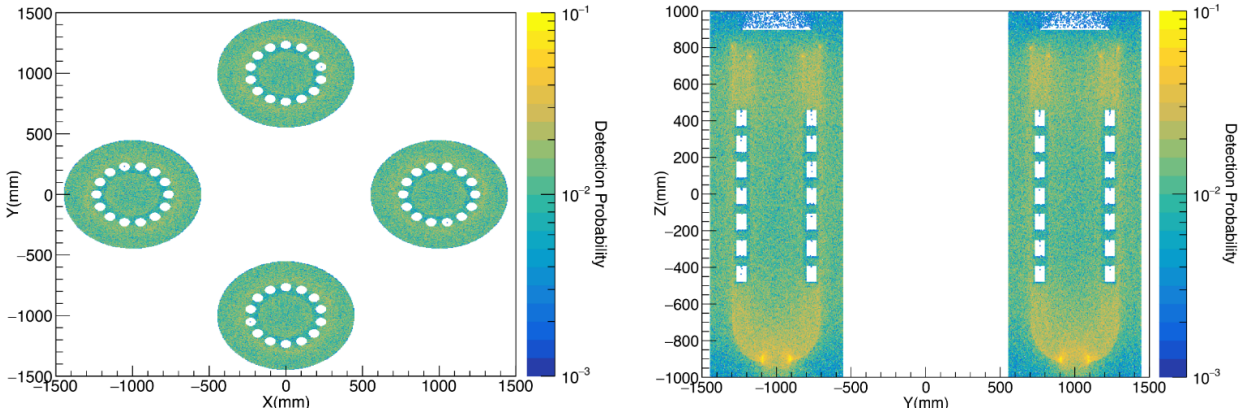

Figure 4.10: Probability of photon detection per location with in a LAr volume containing detector strings. VUV photons are generated uniformly around the volume and propagate through the various components within the experiment geometry to reach the SiPMs. The white spaces in the middle are where the detectors are located. The highest probability of detection occurs when the scintillation is closest to the optical fibers. Fig. from ref. [96]

mostly made up of the stable isotopes ^{40}Ar, ^{36}Ar, and ^{38}Ar. However due to interactions with cosmic rays, trace amounts of radioactive ^{37}Ar, ^{39}Ar, and ^{42}Ar are also present. These radioisotopes are produced from neutron capture on the stable argon isotopes, with ^{42}Ar being produced primarily through spallation cosmic ray nucleon interactions $^{40}\mathrm{Ar}(\alpha,\ 2p)^{42}\mathrm{Ar}$. ^{42}Ar is of particular concern because it decays to a high energy β emitter, ^{42}K, with an end point energy of 3525 keV. High energy β's can deposit energy near $Q_{\beta\beta}$ within the detector lithiated dead-layer and passivated surfaces. In addition, ^{42}Kr are present as ions in the liquid argon and drift towards the high voltage detector components. This is avoided in LEGEND-200 by surrounding the detectors in a nylon mini-shroud, which blocks ^{42}K in a majority of the liquid argon volume from reaching the detector surfaces. For LEGEND-1000, liquid argon surrounding the detectors will be sourced from underground to minimize the presence of argon radioisotopes.

- **α Decays on Detector Surfaces:** Isotopes originating from the decay of ^{222}Rn in the ^{238}U decay chain, can produce α emitters, in particular ^{210}Po that can plate out on detector surfaces during manufacturing and assembly. α's from ^{210}Po, with an energy of 5.304 MeV, can penetrate the passivated surface with a degraded energy deposition. The detector response to α's is not well understood, but has been studied by detector characterization setups within the LEGEND collaboration [117, 77, 118]. Degraded α's can effectively be rejected through delayed charge recovery pulse shape discrimination. The n^+ contact is thick enough to stop α's from depositing energy in the detectors. The detector passivated surface does not scale with detector size so upgrading to larger mass ICPC detectors effectively reduces the detected background from degraded α's.

- **Cosmogenics:** ^{68}Ge and ^{60}Co are produced from the exposure of Ge to cosmic-rays. Both are long lived isotopes on the scale of the experiment run-time and emit radiation that can fall into the ROI. ^{68}Ge decays through electron capture to ^{68}Ga which then can decay to ^{68}Zn through β+-decay with a Q-value of 1899 keV plus a 1077 keV γ. ^{60}Co decays through β-decay with a Q-value of 2823 keV. In the detector manufacturing phase, material is stored underground when possible to minimize cosmogenic activation. The production of ^{77}Ge and ^{77m}Ge can also happen during the experiment's runtime through cosmic-ray induced neutrons bombarding the ^{76}Ge isotope, but this is sufficiently mitigated by placing the experiment deep underground. The SNOLAB reference depth is 6010 meter water equivalent.

From Monte Carlo simulation and material assay studies, the overall anticipated background rate at $Q_{\beta\beta}$ is $9.1^{+4.9}_{-6.3} \times 10^{-6}$ cts / (keV kg yr), consistent with the LEGEND-1000 background goal [96]. Fig. 4.11 shows a comprehensive summary of the background rate from non-negligible sources.

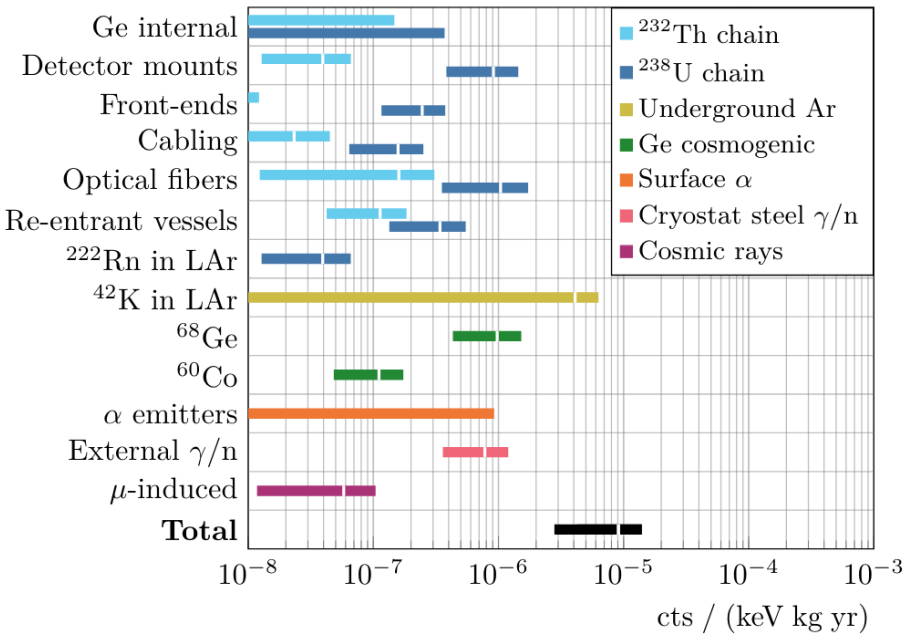

Figure 4.11: Expected non-negligible background contributions for LEGEND-1000. The bands are given as 1-σ uncertainties, where Ge internal and surface α's have only upper bounds provided. Fig. from ref. [96].

4.5 The Future of $0\nu\beta\beta$ Experiments

LEGEND-200 and LEGEND-1000 are the next leading phases for $0\nu\beta\beta$ searches in ^{76}Ge. LEGEND-1000 aims to push the half-life limit for ^{76}Ge to 10^{28} years and obtain an unprecedented background index of 1×10^{-5} cts / (keV kg yr). This will cover the entire parameter space for the existence of a Majorana neutrino in the inverted mass ordering with a 100% discovery probability and up to 50% discovery probability for neutrino masses in the normal ordering [55]. LEGEND will be accompanied by a landscape of $0\nu\beta\beta$ decay experiment searches using different technologies and other double-beta decay isotopes (^{136}Xe, ^{130}Te, ^{100}Mo, and ^{82}Se), each with their own advantages and disadvantages, see Fig. 4.12. All $0\nu\beta\beta$ experiments are renditions of an active mass surrounded by layers of active and passive

shielding, and can be categorized by the different philosophies for increasing the discovery sensitivity for each experiment. The discovery sensitivity will increase when the sensitive exposure increases and will also increase when the background decreases; each experiment employs some combination of the two.

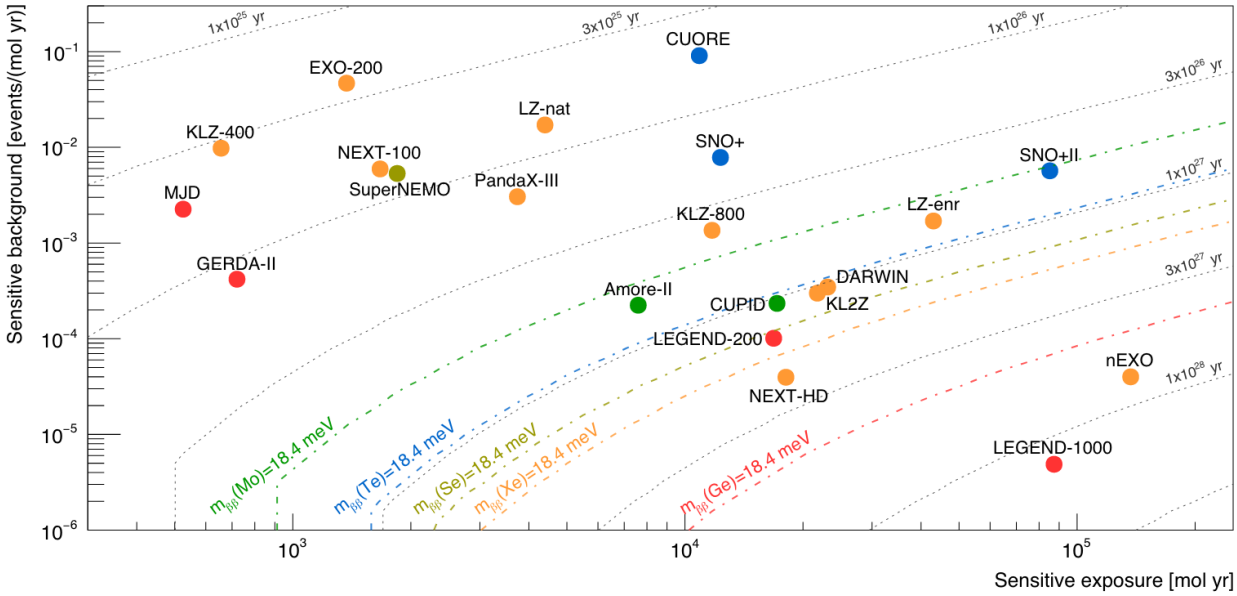

Figure 4.12: The sensitive background vs sensitive exposure for recent and future experiments. The grey dashed lines are discovery sensitivity values for the $0\nu\beta\beta$ half-life and the colored dashed lines are the $m_{\beta\beta}$ lower limits required to test the full inverted ordering for each isotope assuming the largest NME from QRPA calculations. A livetime of 10 yrs is assumed for future experiments. Fig. from ref. [49].

Germanium experiments increase the half-life sensitivity by having the best energy resolution and the lowest backgrounds at $Q_{\beta\beta}$,but face a greater challenge than other techniques of reaching high exposure. Germanium experiments consist of a modular array of detectors and HPGe detectors are challenging and expensive to manufacture. Xenon experiments are intermediate in that ease of scalability is gained for some sacrifice in resolution and higher background rates. However, ^{136}Xe has a low global production rate when compared to the

production rate of ^{76}Ge and ^{130}Te and could be a problem for larger experiments such as nEXO which plans to use 5 tonnes of liquid Xenon. These experiments are monolithic and use several hundred kg of liquid xenon as a time projection chamber or in conjunction with liquid scintillator [119, 120]. Tellurium experiments increase discovery sensitivity by employing the highly naturally abundant active isotope ^{130}Te and having a relatively high energy resolution, but sacrifice in having the highest backgrounds among $0\nu\beta\beta$ experiments. Tellurium experiments use a modular array of TeO_2 crystals as bolometer detectors [121] or Tellurium dissolved in liquid scintillator [122]. Future Molybdenum and Selenium experiments will reduce the background by having a $Q_{\beta\beta}$ that is above the common 2615 keV ^{208}Tl γ background and by employing new background rejection techniques based on crystal scintillation readout or highly pixelated ionization readout. [123, 124].

From now into the next few decades neutrino physics will be thriving with a variety of $0\nu\beta\beta$ experiments. Experiments are projected to search for $0\nu\beta\beta$ decay out to 10^{28} years half-lives. Even though the next-generation of $0\nu\beta\beta$ decay experiments have a foreseen plan to reach larger half-life sensitivities, the future of $0\nu\beta\beta$ decay experiments rests in the current research and development efforts. For LEGEND, searching for ways to make larger active mass detectors with high energy resolution plus understanding the background physics and how to suppress it will dictate the feasibility of tonne-scale ^{76}Ge experiments and beyond. With a lot of research and a bit of luck a discovery or rule-out of the Majorana neutrino could happen before the end of the century.

Chapter 5

SILICON PHOTOMULTIPLIER CHARACTERIZATION

The current best method to achieve the lowest background rate in a germanium $0\nu\beta\beta$ decay experiment is to submerge strings of detectors within a LAr volume. Scintillation in the LAr, caused by partial γ-ray energy depositions from near detector components, will also sometimes be simultaneously detected in a HPGe detector and thus can be disregarded as background.

The readout system in the LEGEND design is a shroud of wavelength shifting fibers coupled to silicon photomultipliers. The fibers convert LAr scintillation to the visible spectrum and provide a large area of coverage to intercept the scintillation photons produced from nearby radioactivity. The silicon photomultipliers are able to detect single photons with up to nanosecond resolution arrival times. This is perfect for an anti-coincidence veto since the arrival time of both a germanium detector signal and SiPM signal(s) must be known to within less than a few μs window.

The background suppression from the LAr veto is an important factor in projecting the background rate for each of the LEGEND phases. The effectiveness of the active veto becomes more important as the experiment acquires more active mass because the background has to be reduced by an order of magnitude or more to increase the discovery sensitivity by an order of magnitude within ten years of operation time. The background suppression from the LAr-Veto is estimated by producing optical photon detection probability maps in a GEANT4 model of the LEGEND design. Radioactive background levels are implemented for the various detector components in the simulation based on their actual assay results and the probability map will determine what fraction of scintillation photons to be vetoed. Current optical simulations use approximate scintillation light yields, LAr attenuation lengths,

fiber WLS efficiencies, and SiPM photon detection efficiencies, since there are few in-situ measurements available to constrain these features experimentally.

This chapter explores one of these properties relevant to LEGEND, in particular the photon detection efficiency of SiPMs at cryogenic temperatures. The SiPMs in LEGEND are operated at 87 K in liquid argon, which is much lower than the typical temperature range in which manufacturers test their devices (-40 to +60 ^{o}C). Work in this chapter and other research work shows that SiPMs can operate at liquid nitrogen temperature (77 K), however properties such as the quantum efficiency and avalanche probability is not precisely known at this temperature [125, 126, 127]. This chapter will go over SiPMs and their relevance to LEGEND. This will be followed by the description of a test stand designed to measure SiPM PDEs at liquid nitrogen temperature, including results that impact how we understand the operation of SiPMs at different temperatures and what it means for the next phases of LEGEND.

5.1 Silicon-based Detectors for Light Collection

A *p-n junction* is the fundamental building block for all semiconductor electronic devices. A semiconductor diode in electronics is essentially the application of a single p-n junction. A p-type and n-type semiconductor are both conductive, but when attached together form a non-conductive region at the junction called a *depletion region*, see Fig. 5.1. The depletion region contains no charge carriers and the potential across the region allows charges to flow in one direction, but not the other. Applying an external bias voltage to a p-n junction can be used to manipulate the width of the depletion region. When the p-doped region is biased higher than the n-doped region the depletion region shrinks allowing forward current to flow through the junction. This is described as applying a *forward bias* to the p-n junction. When the n-doped region is biased higher than the p-doped region the depletion region grows allowing no current to flow through the junction. This is described as applying a *reversed bias* to the p-n junction.

A strong enough reverse bias, depending on the device, can be applied that fully depletes

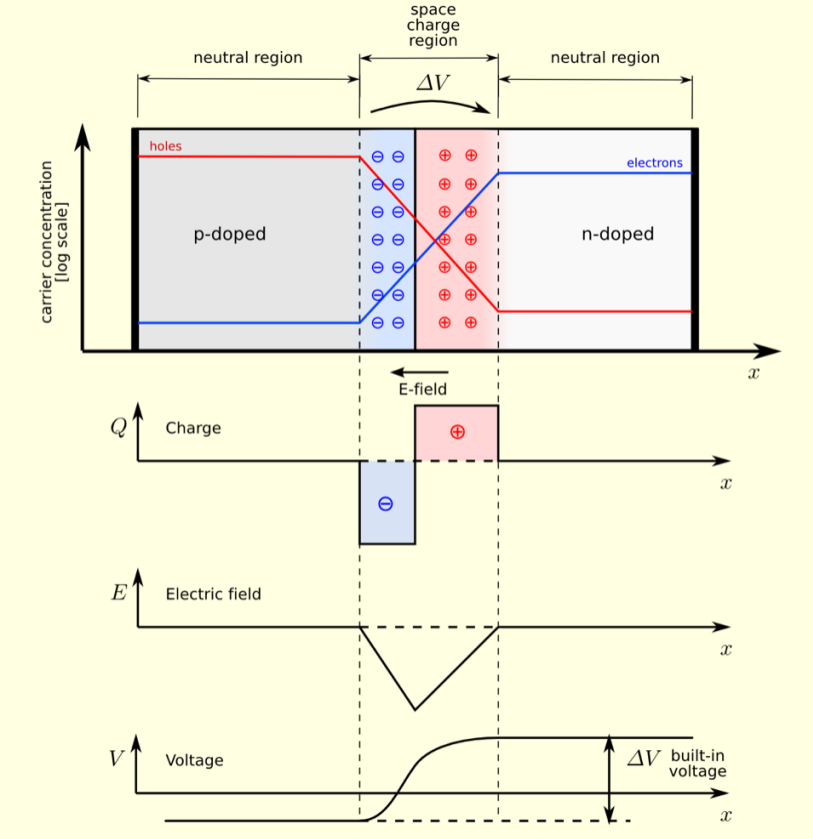

Figure 5.1: A diagram of an unbiased p-n junction along with the charge density, electric field strength, and potential. The red line shows hole concentration and the blue line shows electron concentration. The depletion region creates a potential difference ΔV across the junction. *Image Credit: Wikipedia*

the entire p-n junction of charge carriers. This bias value is called the *breakdown voltage*. Reverse bias voltages at or higher than the breakdown voltage allow current to flow in the reverse direction. At this point electron carriers have enough energy to eject bound electrons into the conduction band and conduction band electrons can then eject more. This is called *avalanche breakdown*. Another process called the Zener effect can lead to electrons with enough energy to tunnel across the junction when the electric field is strong enough in a reversed bias configuration. This happens when the depletion width at breakdown is small

enough to allow for quantum tunneling and is the dominant breakdown process for devices that have a breakdown voltage of 5 V or less [128].

The breakdown voltage of a p-n junction depends on the temperature. For avalanche breakdown, decreasing the temperature decreases the average thermal vibration of charge carriers and thus increases the mean-free path for electrons to induce impact ionization. This lowers the reverse bias voltage necessary to achieve avalanche breakdown.

5.1.1 Photodiode

A photodiode is a diode that is sensitive to light. Photons with enough energy that strike near the depletion region can generate electron hole pairs, which drift according to the electric field in the depletion region generating a current. Photodiodes can be operated in *photovoltaic mode* or *photoconductive mode*, Fig. 5.2. Photovoltaic mode is when the photodiode is operated with a forward bias. Incident photons cause the electric field within the depletion region to increase, which changes the potential across the photodiode to generate a photocurrent. Solar cells are typically operated in photovoltaic mode to convert energy from incident light to a voltage difference across the terminals of the cells. Photoconductive mode is when the photodiode is operated with a reverse bias. Applying a reverse bias essentially reduces the capacitance of the photodiode and allows for faster response times to changing light levels at the expense of a larger dark leakage current and higher electronics noise. Even though the depletion region is wider and thus more sensitive to incident light in photoconductive mode, the dark leakage current noise is usually too high to detect low intensity light signals.

There are two types of photodiodes: a p-n junction photodiode as shown in Fig. 5.3a and a p-i-n junction photodiode as shown in Fig. 5.3b. The p-i-n junction includes an intrinsic semiconductor in between the p-doped and n-doped semiconductor. This increases the depletion region size (decreases capacitance and increases voltage) across the junction improving photodiode response times. The most common photodiode is made out of silicon and has a typical sensitivity for wavelengths between 400 nm and 1000 nm.

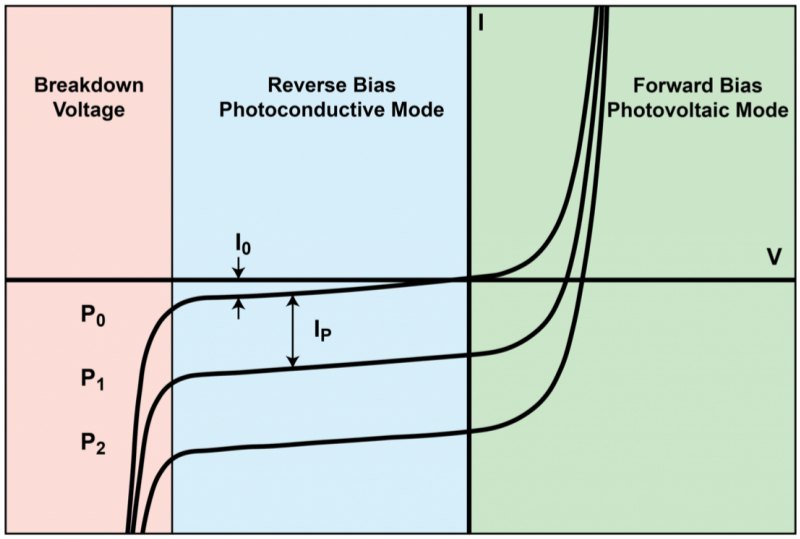

Figure 5.2: Current vs Bias Voltage of a typical photodiode for different incident light levels (P_0, P_1, P_2). P_0 corresponds to no incident light and I_0 is the dark leakage current at P_0. *Image Credit: Wavelength Electronics*

5.1.2 Avalanche Photodiode

An *avalanche photodiode* (APD) is a photodiode that exhibits an internal current gain when operated at a high reverse bias, usually near the breakdown voltage. This is beneficial for low light collection since p-i-n photodiodes typically have a low signal-to-noise ratio when under a high reverse bias. An APD's internal gain is generated from electrons creating additional electron-hole pairs through impact ionization within a high electric field p-doped region. The internal structure is similar to a p-i-n photodiode with a p-doped layer inserted between the n-doped and intrinsic semiconductor, see Fig. 5.4. At a high reverse bias voltage, an APD functions as a linear amplifier. The reverse photocurrent produced is proportional to the number of photons detected by the device.

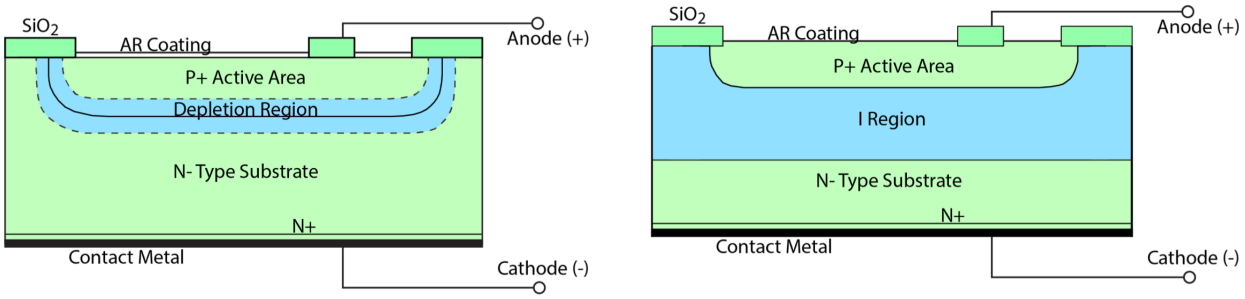

(a) (b)

Figure 5.3: A diagram of a p-n photodiode (a) and p-i-n photodiode (b). Light enters through the anti-reflective coating and generates electron-hole pairs near the depletion region. The intrinsic semiconductor is added between the p-dope and n-doped semiconductor to increase the size of the depletion region and improving photodiode response times. The anode is the side current will enter and the cathode is the side current will leave when the photodiode is forward biased. *Image Credit: Wavelength Electronics*

5.1.3 Single Photon Avalanche Photodiode

A *single photon avalanche diode* (SPAD) is an avalanche photodiode that can be operated in such a way to detect the arrival times of individual photons. This is done by pairing an avalanche photodiode with a RC quenching circuit and operating the device slightly above the breakdown voltage, see Fig. 5.5. Reverse biasing a SPAD above the breakdown voltage causes energy depositions within the device to generate self-sustaining avalanche currents. When an avalanche is triggered, the current from cathode to anode increases (typically a few nanoseconds) until it approaches $I = V_{OV}/(R_q + R_d)$, where the voltage drop across the depletion region is close to the breakdown voltage and the avalanche is terminated. V_{OV} is the applied voltage minus the breakdown voltage, R_q is the quenching resistance, and R_d is the resistance of the avalanche region. The current then decays and the SPAD is recharged after some time $\tau_{recharge} = R_q(C_q + C_d)$. C_q is the capacitance of the quenching circuit and

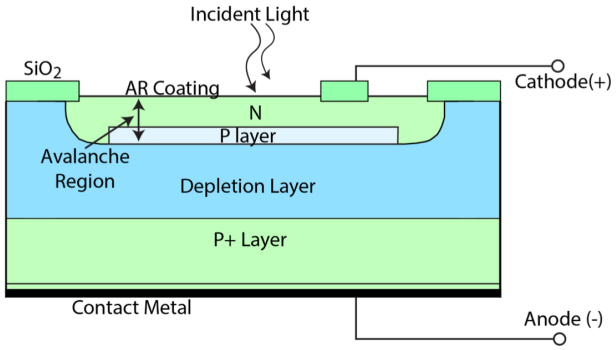

Figure 5.4: A diagram of an avalanche photodiode. The structure is similar to the p-i-n photodiode in Fig. 5.3b, but with an extra p-layer inserted between the n-doped and instrinsic semiconductor. Incident photons deposit near the depletion region and electrons accelerated through the p-layer generate more electron-hole pairs through impact ionization. *Image Credit: Wavelength Electronics*

C_d is the capacitance of the avalanche region. The equivalent circuit of a individual SPAD is shown in Fig. 5.5. Under these conditions, a SPAD functions as a photon counter and is said to be in *Geiger mode*.

5.1.4 Silicon Photomultiplier

A *silicon photomultiplier* is a 2-D array of SPADs connected in parallel. SiPM's are operated in Geiger mode and are optimal for detecting single photons. SiPM's come in various sizes (1 $\times$ 1 mm, 3 $\times$ 3 mm, and 6 $\times$ 6 mm) and various SPAD cell sizes or pixel pitch (15 μm, 25μm, 50 μm, 100 μm). SiPMs are used in a wide range of light sensing applications such as positron emission tomography, LiDAR, detection methods for neutrino and dark matter experiments, and quantum information [130, 131, 132, 133]. They are also an excellent alternative to the more traditionally used photomultiplier tubes: more robust, lower operation voltages (20 V - 70 V), insensitive to high magnetic fields, smaller in size, and cheaper by the unit. Two SiPM samples are shown in Fig. 5.6a and Fig. 5.6b.

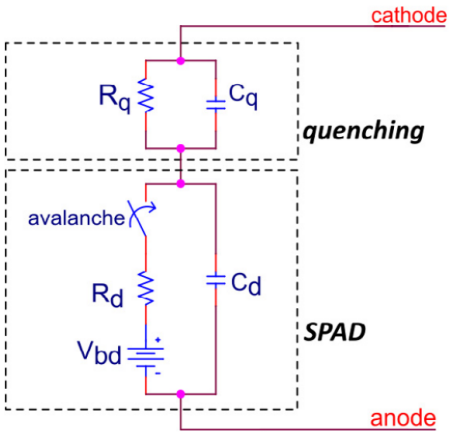

Figure 5.5: Equivalent circuit of a SPAD. The circuit shows the SPAD with a induced avalanche corresponding to the closing of a switch and the RC quenching circuit above. Figure from ref. [129]

5.2 SiPM Properties

When a photon initiates an avalanche within a SPAD, the current through the SiPM rapidly rises and then falls on the time scale of the RC quenching circuit. The total number of charge carriers generated during one sustained avalanche is called the *gain* of the SiPM, Eq. 5.1.

$$G = \frac{Q}{e} = \frac{(C_d + C_q)V_{OV}}{e} \tag{5.1}$$

The total charge Q is given by the total capacitance multiplied by the voltage difference across the device, assuming $R_d \ll R_q$.

Besides incident photons, other phenomena can cause a SPAD within a SiPM to trigger an avalanche. This primarily comes from random thermal excitations near the depletion region and correlated noise between the SPAD cells, see Fig. 5.7.

- **Primary Dark Counts**: A primary dark count is generated from random thermal excitations within the SPAD cell. Under an ambient temperature, the probability of an electron state acquiring an energy above the Fermi-level becomes non-zero and is

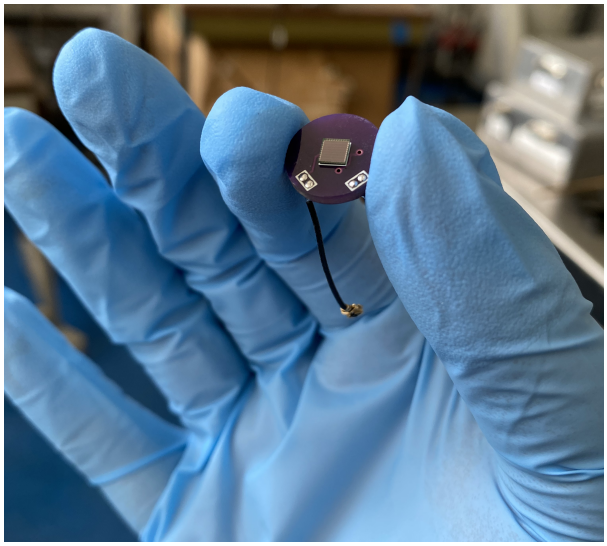

(a)

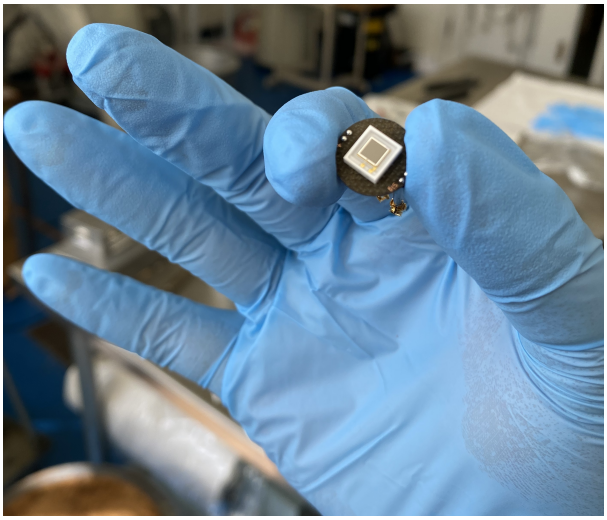

(b)

Figure 5.6: Two 3 × 3 mm SiPMs: one KETEK PM3325-WB-D0 (a) and one Hamamatsu S13360-3050CS (b). The KETEK SiPM has cells with 25 μm pitch and the Hamamatsu SiPM has cells with 50 μm pitch.

sufficient to generate an electron-hole pair. If the electron-hole pair is created near the depletion region then it has the chance to trigger an avalanche. This means under no illumination a SiPM will expend Poisson distributed dark count signals. The SiPM dark count rate will decrease when temperature decreases.

- **Direct Cross-Talk (DiCT)**: Direct cross-talk occurs when a triggered SPAD cell simultaneously triggers one or more neighboring SPAD cells. This happens when secondary photons produced in an avalanche, with some probability, deposit energy near the depletion region of a neighboring cell. The process by which a Poisson distributed parent process creates poisson distributed child processes is described by a Borel distribution.

- **Delayed Cross-Talk (DeCT)**: Delayed cross-talk occurs when a secondary photon generates charge carriers far from the depletion region that diffuse and initiate an avalanche. This type of cross-talk occurs on the nanoseconds to microseconds time scale. Depending on the bandwidth of the readout electronics delayed cross-talk events will be perceived as direct cross-talk.

- **Afterpulsing (AP)**: Charge-carriers in the high electric field region can become trapped and then re-released due to the presence of deep to shallow energy levels near the bandgap. An avalanche may trigger, but some of the charge carriers can become trapped. When the trapped charge carriers are re-released this can trigger another avalanche while the cell is not fully quenched and results in a secondary SiPM waveform that is lower than the single photoelectron level. The afterpulsing probability depends on the number of traps in the high electric field region and the release time in relation to the cell re-charge time.

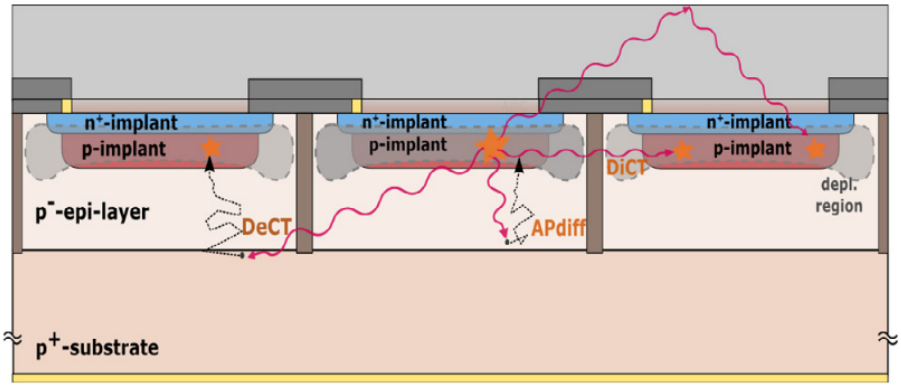

Figure 5.7: A cross-sectional view of neighboring SPAD cells. Stars indicate avalanche triggers, red wavy lines indicate secondary photons, and dotted black lines represent random walk charge carrier diffusion Afterpulses induced by the trapping and re-release of charge carriers is not displayed in this figure. Fig. from ref. [129].

A SiPM's efficiency of detecting individual photons is the *photon detection efficiency* (PDE). The PDE is the product of the *quantum efficiency* (QE), *avalanche probability*(P_T), and *effective fill factor* (FF_{eff}),

$$PDE(V_{OV}, \lambda) = QE(\lambda) \times P_T(V_{OV}, \lambda) \times FF_{eff}(V_{OV}, \lambda)\,. \tag{5.2}$$

The quantum efficiency is the probability for an incoming photon to enter a SPAD cell and produce an electron-hole pair. The avalanche probability is the probability for a generated electron-hole pair to trigger an avalanche. The effective fill factor is the ratio of the number of incident photons landing on an active SiPM component vs an inactive SiPM component. For a uniform light source across the entire device this can be represented as the active area divided by the inactive area of the SiPM. The avalanche probability is dependent on the electric field created from the applied overvoltage and the position where charge carriers are created, which is wavelength dependent.

5.3 Characterization Test Stand

A common approach for measuring the PDE of a SiPM is to compare the total number of photons detected to that of a known calibrated photon detector (usually an APD or photomultiplier tube). This is particularly useful when the light source is not precise in power or wavelength, like a *light emitting diode* (LED) as opposed to a laser light source. For this kind of setup a SiPM, calibrated APD, and a light source are attached with perpendicular lines of sight to an *integrating sphere* shown in Fig. 5.8. An integrating sphere is a hollow sphere made out of a polished white diffuse material such as polytetrafluoroethylene (PTFE), also known as Teflon®, that creates a uniform irradiance on the sphere's inner surface. Ideally the incident photon rate per area received by each port on the integrating sphere is the same. The PDE of the SiPM can be inferred from the ratio of the number of photons per area detected divided by the predicted total incident photon rate per area from the calibrated photon detector.

The SiPM characterization test stand is an integrating sphere suspended inside a dewar

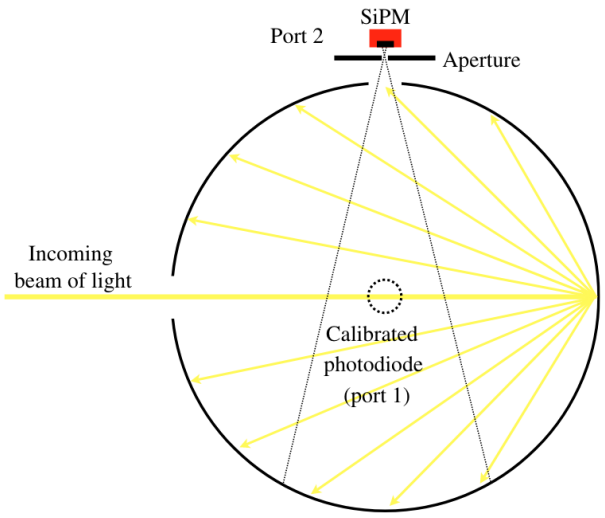

Figure 5.8: A diagram representing a cross-section of an integrating sphere. Incoming light from one port reflects diffusely inside of the integrating sphere to uniformly illuminate the SiPM and calibrated photodiode with the same irradiance. Fig. from ref. [134].

that is inside a dark box, see Fig. 5.9. The dark box is painted with Black 3.0 on the inside to absorb internal ambient light and covered in aluminum foil on the outside to reflect away external ambient light. The dewar can be filled with liquid nitrogen and a copper finger is in thermal contact with the SiPM electronics board to cool down the SiPM to 77 K while at one of the integrating sphere ports. The calibrated photon detector used is a Hamamatsu S5344 APD and the light source is a pulsed green LED with a peak emission at 562.5 nm. A green LED was chosen as a cost effective light source that is within a few tens of nanometers of the wavelength shifting emission spectrum of the scintillating fibers used in LEGEND. The integrating sphere is a Thorlabs IS200-4 with a sphere diameter of 2 inches. A schematic and pictures of the dewar internals is shown in Fig. 5.10. The SiPM and APD signals are both read out by a two-stage pre-amplifier each that is connected to a channel on a CAEN DT5730 digitizer with a 500 MHz sampling rate and 14 bit resolution. Data acquistion is done with the CAEN CoMPASS software and post-processing of the data is done with custom open

source software, https://github.com/nickruof/SiPMStudio.

Figure 5.9: The SiPM characterization test stand. The dewar with the integrating sphere inside is located inside of the dark box which is covered on the outside with aluminum foil. Outside of the dark box are the second stage amplifications of the SiPM and APD and are read out by a CAEN DT5730 digitizer.

The SiPM characterization test stand has four functions: measure dark count behavior at room temperature, measure dark count behavior at liquid nitrogen temperature, measure the PDE at room temperature, and measure the PDE at liquid nitrogen temperature. The pre-amp allows for the option to readout the SiPM signals under a low gain or high gain setting. The SiPM board is connected to a first stage transimpedance amplifier inches away with the additional option of attaching the output signal to a voltage amplifier external to the dark box. Dark count behavior is measured under the high gain setting and pulsed LED illumination is measured under the low gain setting. The APD is always in the high gain

setting, since the internal APD gain is orders of magnitude smaller than the internal SiPM gain.

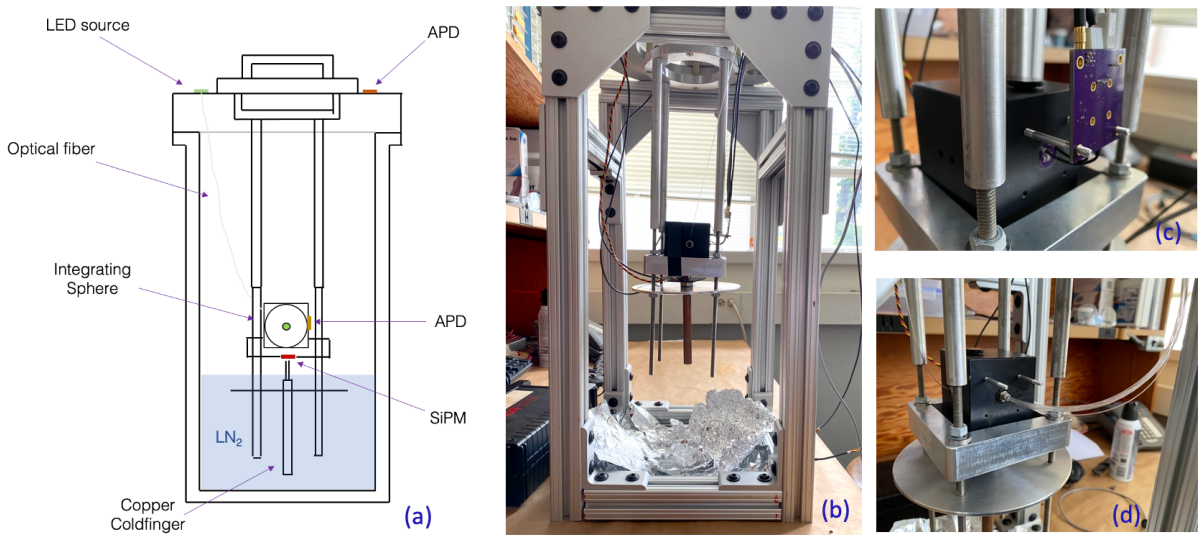

Figure 5.10: a) A cross-sectional view of the dewar inside the dark box. The integrating sphere is suspended down into the dewar with a liquid nitrogen level up to the copper cold finger flange. The SiPM, APD, and LED are connected to the sphere with perpendicular lines of sight to ensure the most even photon rate incident on both of the devices. For the relative PDE measurement the APD is located on the lid and connected to the sphere by a bundle of clear optical fibers. For both measurements the LED is located on the lid of the dewar with one clear optical fiber guiding the light to the integrating sphere. (b) Shows the integrating sphere suspension set-up that is inserted into the dewar. (c) and (d) show the absolute PDE APD configuration with first stage amplification board and the optical fiber bundle for the relative PDE measurement, respectively.

There are two positions the APD can be placed: at one of the integrating sphere apertures or at the lid of the dewar with clear optical fibers running from the lid to one of the integrating sphere ports. Placing the APD at the lid ensures the known responsivity provided

by Hamamatsu is not changed due to temperature effects from the liquid nitrogen or cold boil off gas. G-10 spacers, high-pressure fiberglass laminate, are used as thermal stand-offs from the cold internal component temperatures and keep the lid from icing over. The optical fibers used for the APD lid configuration and the light source are 1 mm, double cladded, PMMA fibers from NanOptics^{TM}. These are used for maximum visible light transmission from end to end. One fiber is used for transmission of the LED light to the integrating sphere and a bundle of 12 fibers are used to transmit light from the integrating sphere to the APD when at the lid.

When the copper cold finger is submerged in liquid nitrogen the temperature of the SiPM board reaches 77 K, which was confirmed with a PT1000 sensor placed between the SiPM board and copper cold finger contact. Other components such as the integrating sphere and optic fibers also become colder. A comparison of the APD signal received from a pulsed LED over a one hour period at room temperature and at liquid nitrogen temperature shows the APD photocurrent to be the same within 141 photons / mm^2, which can be attributed to changes in configurations and optical properities of the fibers and integrating sphere around liquid nitrogen temperature, see Fig. 5.16. More importantly it also suggests that there is no major ice accumulation within the sphere when liquid nitrogen is present. To prevent ice from forming in the integrating sphere, the internals of the dewar are purged with liquid nitrogen boil off gas for more than one hour. A small hole on the integrating sphere allows for nitrogen gas to purge the inside of the sphere. No ice is observed on the dewar internals unless the integrating sphere is lifted out of the dewar after being in close contact with the liquid nitrogen.

5.4 Measurements

The PDE is measured by estimating the total number of photons per area detected on the SiPM divided by the total incident photons per area on the APD:

$$\mathrm{PDE} = \frac{\langle N^{ph}_{\mathrm{SiPM}} \rangle}{\langle N^{ph}_{\mathrm{APD}} \rangle f} \,. \tag{5.3}$$

The number of photons per area is calculated by integrating many waveform signals from LED pulses for both the SiPM and APD and taking the gaussian mean as the mean number of detected photons per pulse. The SiPM operates in Geiger mode where each waveform represents the signal from one avalanche caused by a detected photon or dark count. The number of charge carriers generated in an avalanche is given by the gain and is dependent on the applied overvoltage. The waveforms are normalized in the post-processing analysis so that the integral of a single avalanche waveform corresponds to one ejected photoelectron. The number of photons detected per area is then given by the number of triggers accounting for correlated noise probabilities and integrating sphere form factor. The integrating sphere form factor, f, is the ratio of total photons incident on the SiPM to that on the APD. $f = 1$ means the rate is the same where as $f > 1$ means the SiPM photon rate is higher where as $f < 1$ means the SiPM photon rate is lower. f is estimated by running GPU accelerated optical photon monte-carlo simulations within a triangular mesh model of the integrating sphere. This is discussed in detail in the next chapter. The number of photons detected by the SiPM is given by

$$\langle N^{ph}_{\text{SiPM}} \rangle = \left[\frac{\langle N_{trig} \rangle}{(1 + P_{DiCT})(1 + P_{AP})} - \langle N_D \rangle \right] \frac{1}{A} \,. \tag{5.4}$$

$\langle N^{ph}_{\text{SiPM}} \rangle$ is the mean number of photons detected per LED pulse, $\langle N_{trig.} \rangle$ is the mean number of avalanche triggers per LED pulse, $\langle N_D \rangle$ is the mean number of dark counts, and A is the SiPM area. The gain of a SiPM is determined by computing a weighted average distance between peaks in a *pulse charge spectrum*, where the entries are the integrals of the waveforms. The locations of each peak are given by the fit of a gaussian to each peak. To normalize the charge of each waveform, the zero trigger peak location is subtracted from the charge and then divided by the gain. The integral of a signal avalanche waveform represents $N_{trig.} \approx 1$. SiPM waveforms are shown in Fig. 5.11 and normalized pulse charge spectrums are shown in Fig. 5.12.

The dark count populations, including DiCT and AP, are identified by plotting the time to next pulse from each triggered waveform vs the amplitude of the next pulse, Fig. 5.13.

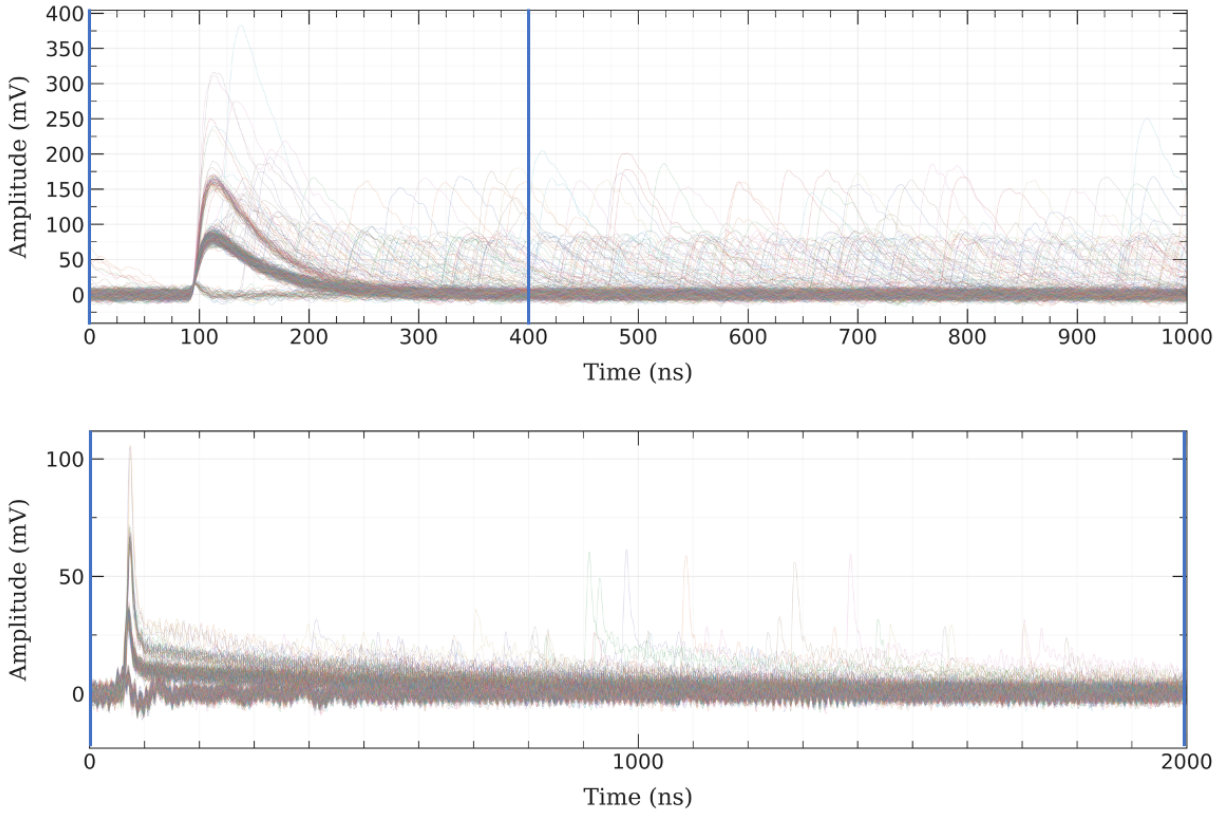

Figure 5.11: Triggered dark count waveforms from the same SiPM when at room temperature (Top) and when at liquid nitrogen temperature (Bottom). The vertical blue lines show the bounds of the integrating window. At liquid nitrogen temperature the quenching resistor resistance increases, which increases the decay time and lowers the maximum current across the SPAD.

DiCT events appear as primary dark counts with an amplitude some integer times greater than a primary dark count. AP events appear as waveforms with amplitudes less than the primary dark count amplitude and occur sometime after a SPAD is not fully recharged. DeCT events are not resolved due to the resolution of the digitizer and achieved signal-to-noise ratio and are contained in the DiCT population. P_{DiCT} is the ratio of triggers greater than 1.5 photoelectrons with the triggers greater than 0.5 photoelectrons. P_{AP} is the ratio

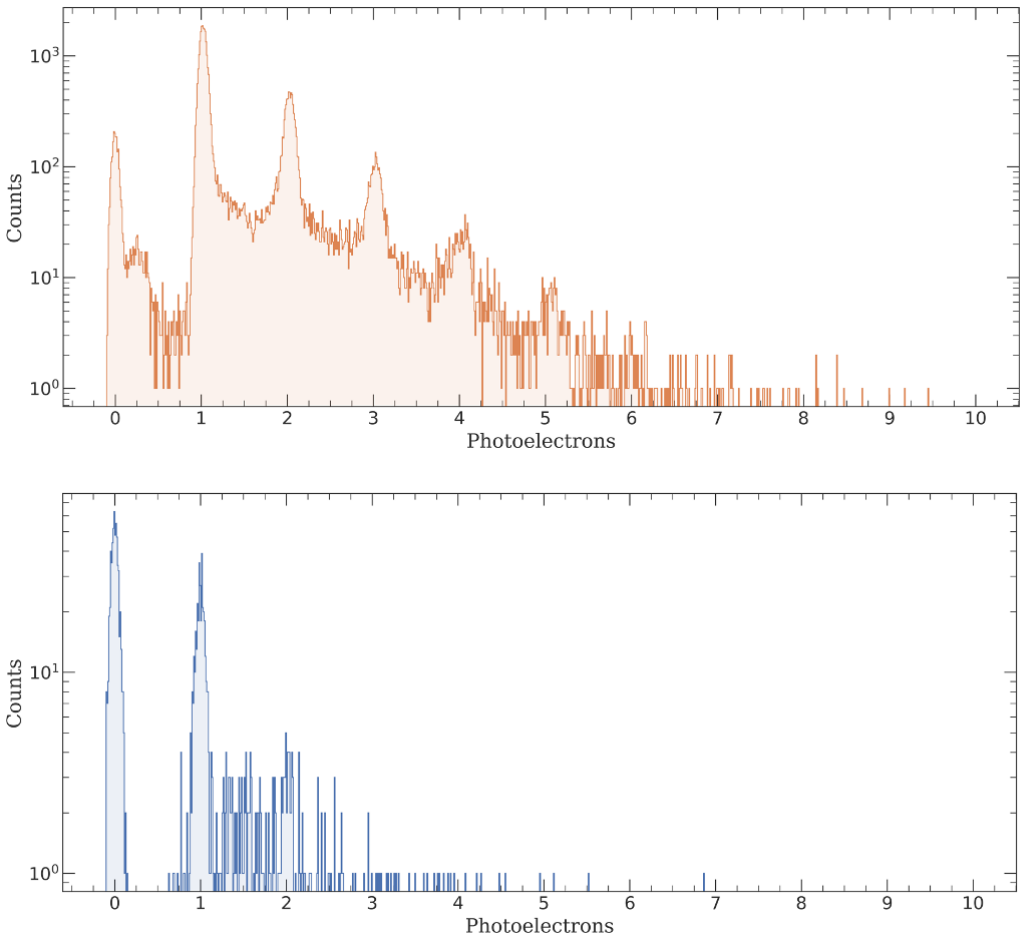

Figure 5.12: Normalized pulse charge spectrum for room temperature (Top) and for liquid nitrogen temperature (Bottom). The dark count rate at liquid nitrogen temperature is on the single Hz level and does not have as many counts for a similar data-taking time.

of afterpulsing waveforms to total number of waveforms. The primary dark count rate is calculated by fitting an exponential to the region that surrounds the primary dark counts and DiCT events in Fig. 5.13. For a set of Poisson distributed dark counts the probability density distribution is given by an exponential where one over the time constant (or average time interval) is the dark count rate [135].

The number of photons received by the APD comes from combining the LED emission

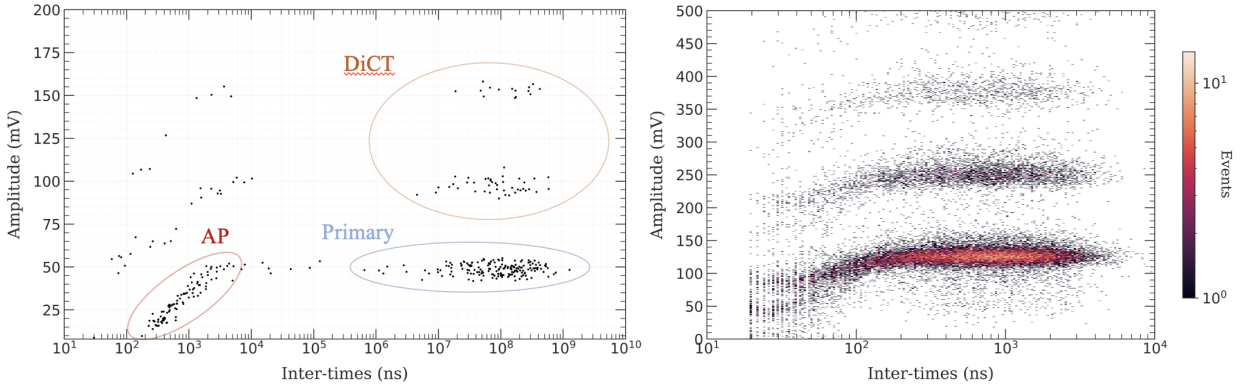

Figure 5.13: Plots of the visible dark count populations for liquid nitrogen temperature (left) and room temperature (right). Room temperature dark counts are dominated by primary dark counts with some DiCT with small amounts of AP. The inter-times are the times to next waveform after a waveform has been triggered on by the digitizer.

spectrum with the APD quantum efficiency and measured gain at the applied bias voltage.

$$\langle N_{APD}^{ph} \rangle = \left(\frac{\langle Q_L \rangle - \langle Q_D \rangle}{A_0} \right) \int \frac{\lambda}{hc} \left[\frac{\rho(\lambda)}{g_{APD} \cdot \eta(\lambda)} \right] d\lambda \tag{5.5}$$

$\langle Q_L \rangle - \langle Q_D \rangle$ is the statistical average photocurrent from the APD for each LED pulse, $\rho(\lambda)$ is the normalized emission spectrum of the LED, $\eta(\lambda)$ is the response of the APD in A/W, g_{APD} is the APD gain, and A_0 is the APD active area. $\eta(\lambda)$ is set by using the known response of a light source peaked at 625 nm and extrapolating based on the provided quantum efficiency curve from the Hamamatsu data-sheet. The APD gain is measured by pulsing the green LED at the APD for various bias voltages. The ratio of the mean integrated signal for a set of pulses at the bias voltage to that at zero bias voltage is the gain. A bias voltage of 150 V with gain of approximately 65 was used for all PDE measurements. The APD responsitivity, LED emission spectrum, and the measured APD gain are shown in Fig. 5.14a and Fig. 5.14b. To measure the incident photon rate on the APD and detected photon rate on the SiPM, the LED light source is pulsed at 1 kHz with a 1 μs pulse width for approximately 15 s. SiPM and APD responses to LED pulses are shown in Fig. 5.15. The room temperature PDE

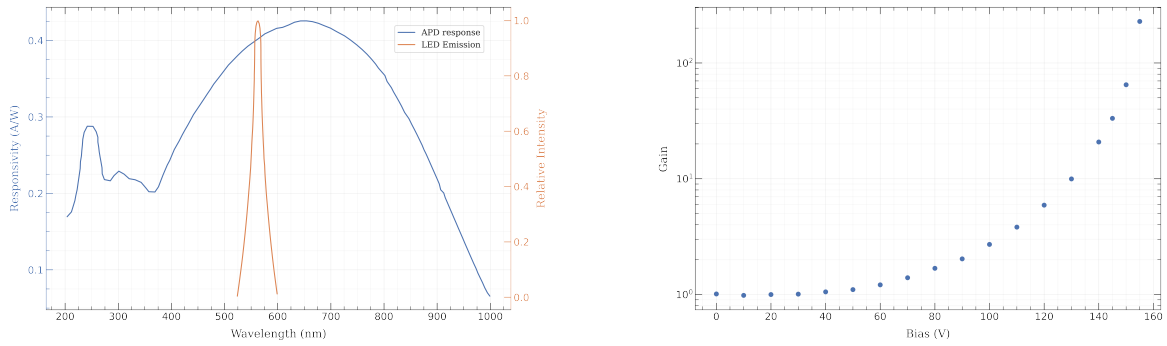

(a) (b)

Figure 5.14: (a) a plot of the APD responsitivity and LED emission spectrum vs wavelength from the manufacturer data-sheets and (b) the measured APD gain vs bias voltage. The APD gain is measured by varying the bias voltage exposed to a pulsed LED light source.

measurement is then Eq. 5.3. The liquid nitrogen PDE measurement is more complicated because of the optic fiber bundle. For the liquid nitrogen PDE, the ratio of the room temperature relative PDE with the liquid nitrogen temperature relative PDE is multiplied by the absolute PDE from room temperature, Eq. 5.6. A relative PDE measurement varies proportionally to an absolute PDE measurement, but does not have the same magnitude. The absolute measurement at room temperature is important because it can confirm the characterization test stand with the applied analysis methods reproduce the documented PDE values quoted by the manufacturers. The PDE at LN temperature is

$$\mathrm{PDE}_{LN} = \mathrm{PDE}_{abs.} \times \frac{\mathrm{PDE}^{rel.}_{ln}}{\mathrm{PDE}^{rel.}_{room}} \,. \tag{5.6}$$

$\mathrm{PDE}_{abs.}$ is the absolute PDE measured at room temperature, $\mathrm{PDE}^{rel.}_{ln}$ is the relative PDE measurement made at LN temperature with the APD receiving light from the fiber bundle, and $\mathrm{PDE}^{rel.}_{room}$ is the same measurement except at room temperature.

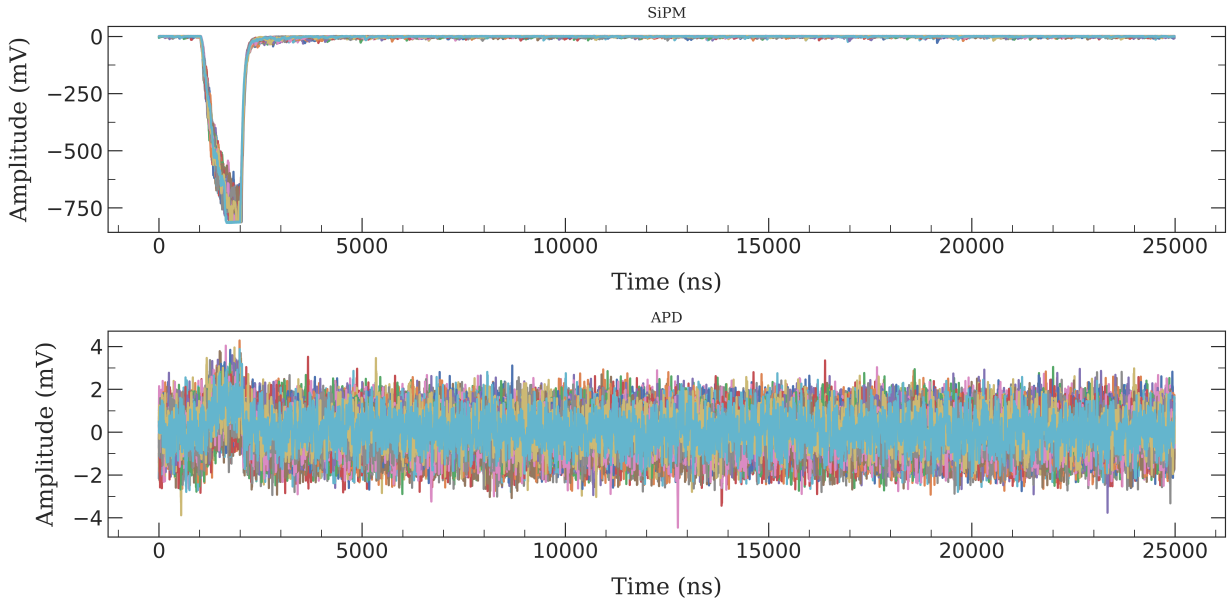

Figure 5.15: Several SiPM and APD waveforms responding to LED pulses. The integrated charges from each waveform are used to determine an average number of photons detected by each device. This is used to determine the SiPM PDE. The flat tops produced in the SiPM signals and the APD signals reconstructing the square wave to pulses from the LED.

5.5 Characterization Results

The following results presented in this section show the measured PDE and dark count behaviors of a KETEK PM3325-WB-D0 SiPM at room temperature and at liquid nitrogen temperature. Room temperature is roughly 72 °F maintained by an air conditioning unit in the laboratory. Given the change in breakdown voltage vs temperature from the data-sheet at 22 mV/K, any fluctuations in breakdown voltage that would change the gain from temperature fluctuations are expected to be negligible. For the PDE measurement, uncertainties are obtained by propagating the uncertainties of the measured quantities in Eq. 5.3, Eq. 5.4, Eq. 5.5, and Eq. 5.6:

$$\sigma^2_{PDE_{LN}} = \left(\frac{PDE_{ln}}{PDE_{room}}\right)^2 \sigma^2_{PDE} + \left(\frac{PDE}{PDE_{room}}\right)^2 \sigma^2_{PDE_{ln}} + \left(PDE \times \frac{PDE_{ln}}{PDE^2_{room}}\right)^2 \sigma^2_{PDE_{room}} \tag{5.7}$$

$$\sigma^2_{PDE} = \left(\frac{1}{N_{APD} f}\right)^2 \sigma^2_{N_{SiPM}} + \left(\frac{N_{SiPM}}{N^2_{APD} f}\right)^2 \sigma^2_{APD} + \left(\frac{N_{SiPM}}{N_{APD} f^2}\right)^2 \sigma^2_f \tag{5.8}$$

$$\sigma^2_{N_{SiPM}} = \frac{1}{A^2}\left[\frac{\sigma^2_{trig}}{(1+P_{DiCT})^2(1+P_{AP})^2} + \frac{N^2_{trig}\sigma^2_{DiCT}}{(1+P_{DiCT})^4(1+P_{AP})^2} + \frac{N^2_{trig}\sigma^2_{AP}}{(1+P_{DiCT})^2(1+P_{AP})^4} + \sigma^2_D\right] \tag{5.9}$$

$$\sigma^2_{APD} = \frac{1}{A^2_o}\left[\frac{\sigma^2_L}{g^2_{APD}}\Phi^2 + \frac{\sigma^2_D}{g^2_{APD}}\Phi^2 + \left(\frac{Q_L - Q_D}{g_{APD}}\right)^2 \sigma^2_\Phi + \left(\frac{Q_L - Q_D}{g^2_{APD}}\right)\Phi^2 \sigma^2_g\right]. \tag{5.10}$$

Φ in Eq. 5.10 is the integral in Eq. 5.5 multiplied by g_{APD}. σ_Φ is a systematic uncertainty from varying the LED response in a 20 nm window and varying the APD response in a 0.01 A/W window. Another systematic, added in quadrature, only in the liquid nitrogen PDE measurement is the difference in photon rate seen by the APD between room temperature and liquid nitrogen temperature measurements. The systematic is the difference in the perceived APD photon rate at room temperature to the perceived APD photon rate at liquid nitrogen

temperature. This accounts for any temperature dependencies in the test stand that aren't accounted for else where. The LED fractional intensity measured by the APD appears to be constant with long term fluctuations of a few hundred photons, see Fig. 5.16. This is not fully explained by the statistical uncertainty in number of photons detected by the APD and must be dominated by instability of the LED intensity. All other uncertainties are statistical. The gain, primary dark count rate, DiCT probability, AP probability, and PDE are shown in Fig. 5.17 - Fig. 5.21 for several overvoltage settings of the KETEK PM3325-WB-D0 SiPM. The breakdown voltage at room temperature is measured to be 24.1 V and at liquid nitrogen temperature to be 20.6 V.

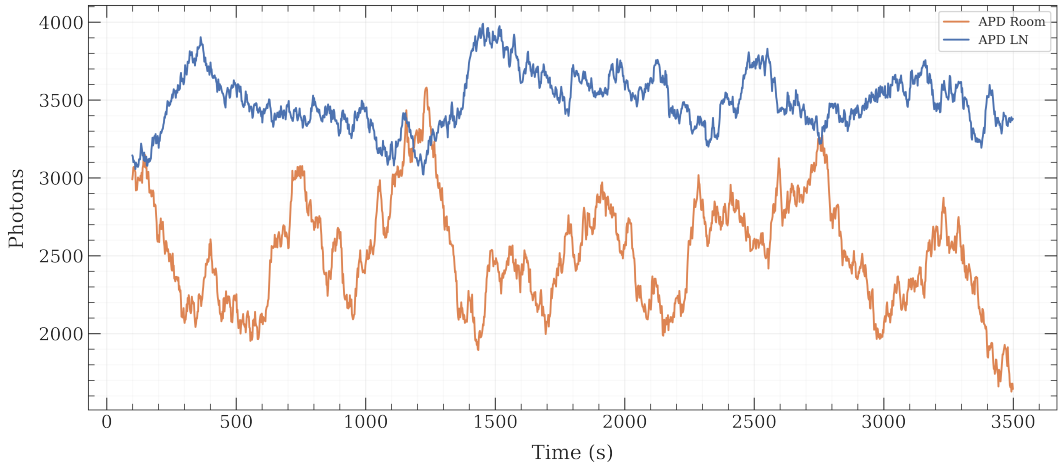

Figure 5.16: LED pulses measured by the APD over one hour for room temperature and liquid nitrogen temperature. The LED is pulsed at 1 Hz and the final plot is a moving average with a window size of 100 seconds to visualize the features occurring over minute time scales.

Measuring the SiPM PDE at room temperature and liquid nitrogen temperature shows that the PDE per overvoltage decreases and the SiPM operating range increases, noted by the smaller curvature, at liquid nitrogen temperature. This suggests non-trivially that a

combination of the quantum efficiency, avalanche probability, and fill factor are changing with temperature for the detected photon spectrum from the LED. From a PDE measurement alone it is not possible to conclusively explain how each component to the PDE is changing, but possible explanations can be hypothesized. The QE of a silicon device is sensitive to temperature due to silicon having an indirect band-gap. In order for a photon to promote an electron into the conduction band and a hole in the valence band a phonon must be absorbed to conserve crystal momentum and since less phonons are present at lower temperatures the QE is expected to decrease. The avalanche probability may also decrease since the mobility of charge carriers tends to decrease with decreasing temperature. Energy in the charge carriers is transferred more easily to impurities instead of other charge carriers at lower temperatures. Recombination probability of electron-hole pairs is lower at lower temperature so the probability of a charge carrier reaching the avalanche region may become higher, but may have a statistically lower probability of generating an avalanche. There is also a slight increase in the silicon band gap, about 10 meV, around liquid nitrogen temperature [136]. The fill factor is not as clear since this depends on how the temperature shrinks the active detector material in relation to the inactive material. If both have similar contraction at low temperature then the fill factor does not effect the PDE in comparison to the other PDE components. A reduction in PDE at liquid nitrogen temperature is possible given the expected qualitative properties of each of the PDE components.

5.6 Summary

A KETEK SiPM has been characterized in our test stand to better understand the properties of SiPMs as relevant for searches for rare fundamental physics. SiPMs in LEGEND are operated in liquid argon at 87 K to detect scintillation from natural radioactive background, which is outside of the temperature range in which manufacturers test their devices. In addition, characterizing SiPMs in very cold environments is considerably more challenging than characterizing them at room temperature. The characterization of SiPMs at liquid nitrogen temperature is important for understanding the background model for future phases of LEG-

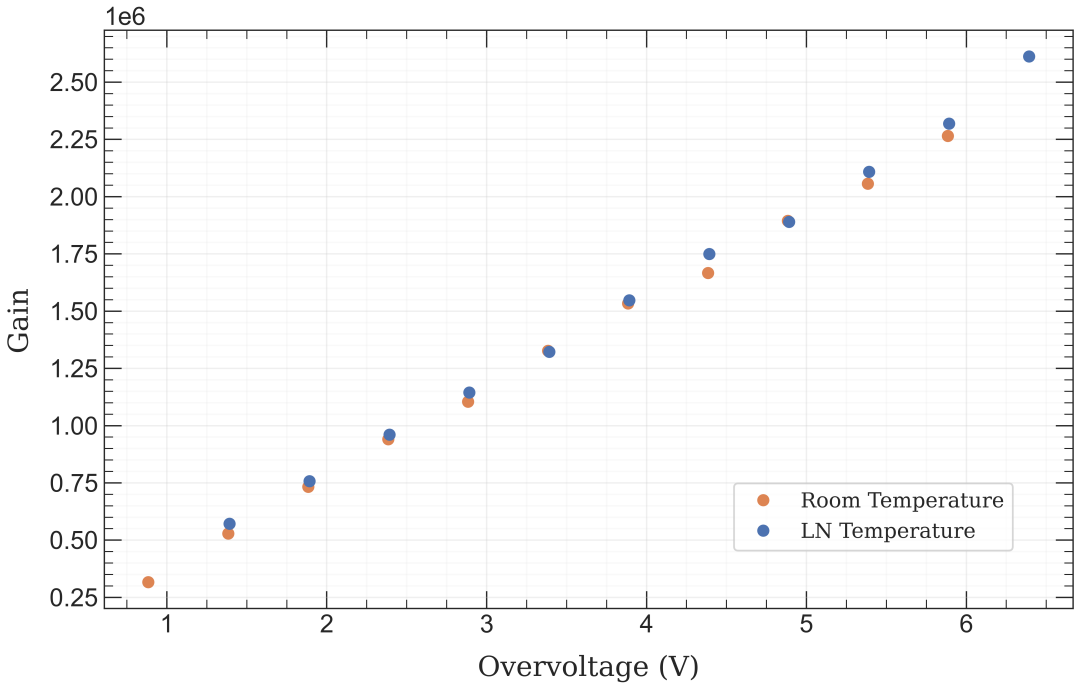

Figure 5.17: Measurement of the gain per overvoltage at room temperature and liquid nitrogen temperature. The gain is the weighted average distance between several peaks in a pulse charge spectrum.

END and possibly could influence alternative design implementations. A measurement of the PDE at liquid nitrogen temperature suggests that the PDE is reduced at colder operating temperatures, however this is accompanied by an increased dynamic range of overvoltages. The measured dark count rate varies insignificantly when compared to the ambient detection rate in the LEGEND cryostat of several hundred Hz. This means LEGEND can presumably operate KETEK SiPMs at the maximum overvoltage that achieves Geiger mode to achieve the maximum photon detection efficiency.

Results from the SiPM test stand show the characteristics of SiPMs at temperatures around liquid argon temperature exhibit interesting behavior that may be worth deeper

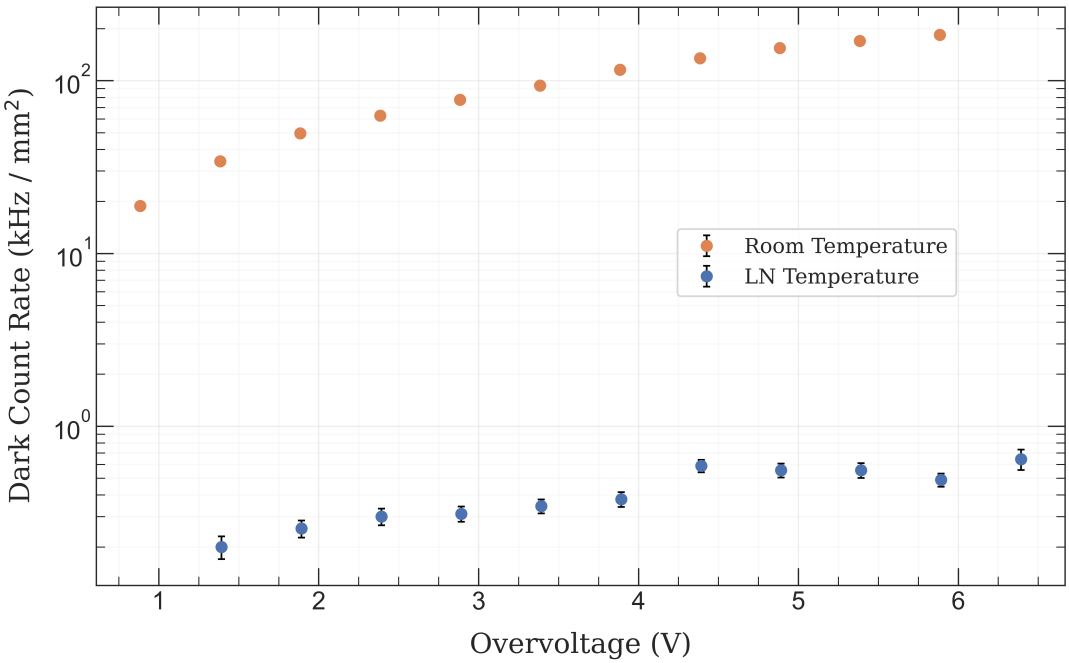

Figure 5.18: The primary dark count rate per SiPM area at room temperature and liquid nitrogen temperature for several overvoltages. The primary dark count rate is measured by fitting an exponential to the inter-time spectrum from the primary dark count regions in Fig. 5.13. The reciprocal of the exponential decay constant is the dark count rate. The uncertainties are from the fit uncertainties on the exponential decay constant.

investigation. Significant improvement can be gained by using more precise light sources that can probe the PDE over narrow band wavelengths. Though the LED emission is within just a few tens of nanometers of the WLS fiber peak emission, it is not clear how the PDE changes per wavelength with temperature. It would also be informative to measure the PDE at liquid argon temperature. Though close to liquid nitrogen temperature at 87K, the temperature dependency of the PDE at cryogenic temperatures has not been explored except recently with VUV SiPMs from the nEXO collaboration [137, 138, 139]. Also it may be interesting

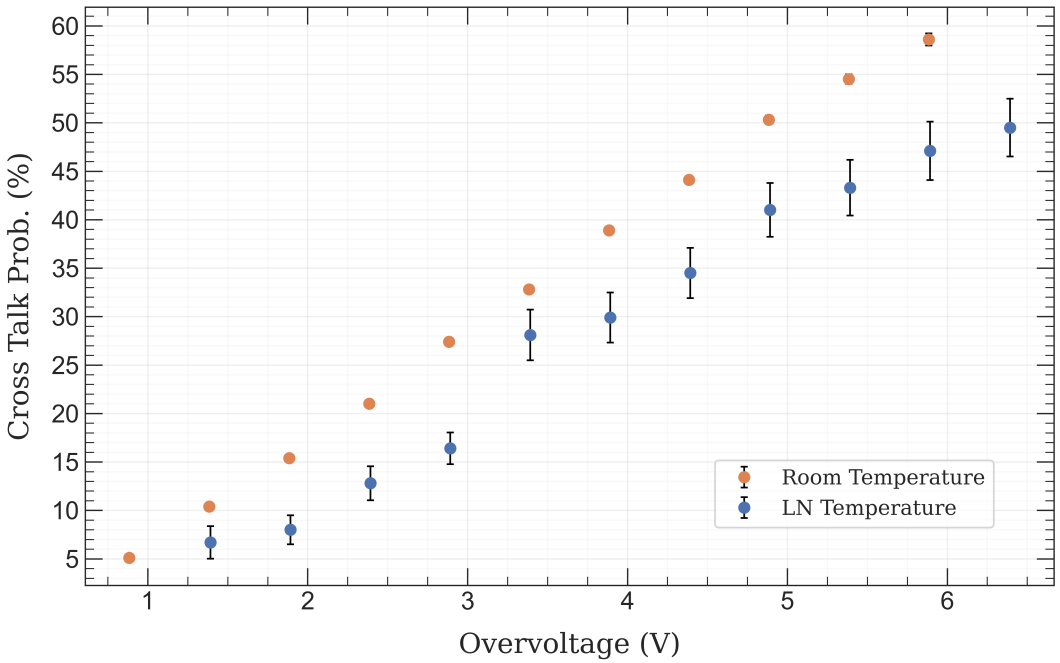

Figure 5.19: Cross-Talk probability at room temperature and liquid nitrogen temperature for several overvoltages. The cross-talk probability is measured by taking the ratio of the number of events greater than 1.5 photoelectrons with the number of events greater than 0.5 photoelectrons. The uncertainties are the propagated poisson statistics errors for the quantities in the ratios.

to pursue the fabrication of SiPMs sensitive to the visible spectrum that are optimized for cryogenic performance, particularly if the impurity concentration is suppressing avalanches at liquid nitrogen temperature. The efficiency of the actual LAr-Veto readout requires an in-situ characterization of the entire SiPM array and would be necessary to accurately estimate an expectation for the background reduction due to the LAr-Veto. However, the SiPM test stand results represent the first steps in understanding the LAr-Veto readout's capabilities.

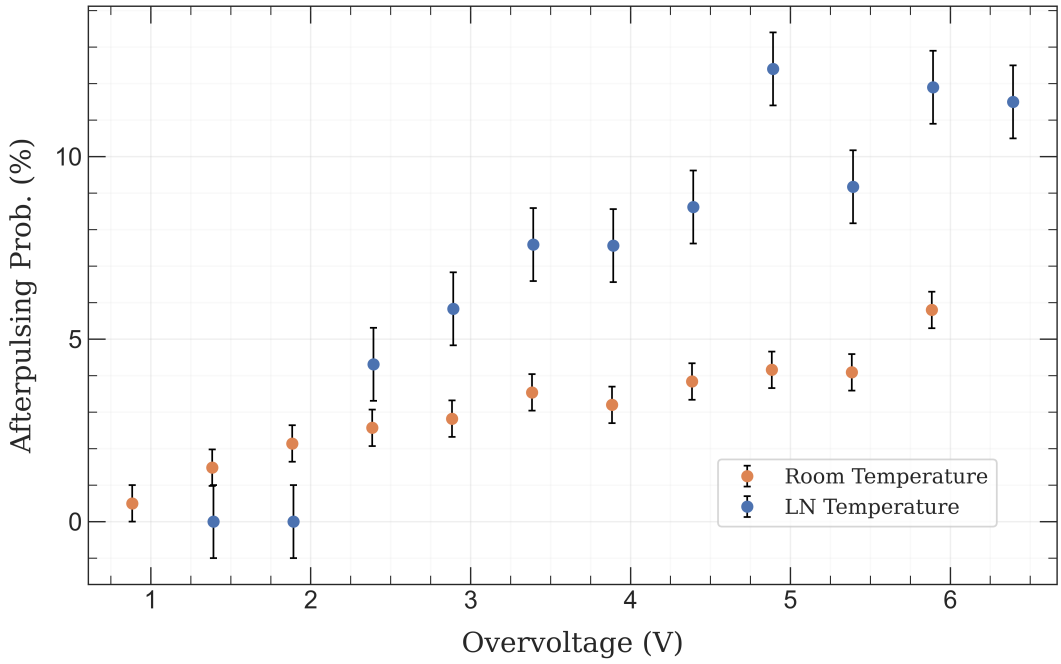

Figure 5.20: Afterpulsing probability at room temperature and liquid nitrogen temperature for several overvoltages. The afterpulsing probability is measured by taking the number of events in the afterpulsing region in Fig. 5.13 divided by the total number of events. The uncertainties are estimated by varying the size of the selected afterpulse region.

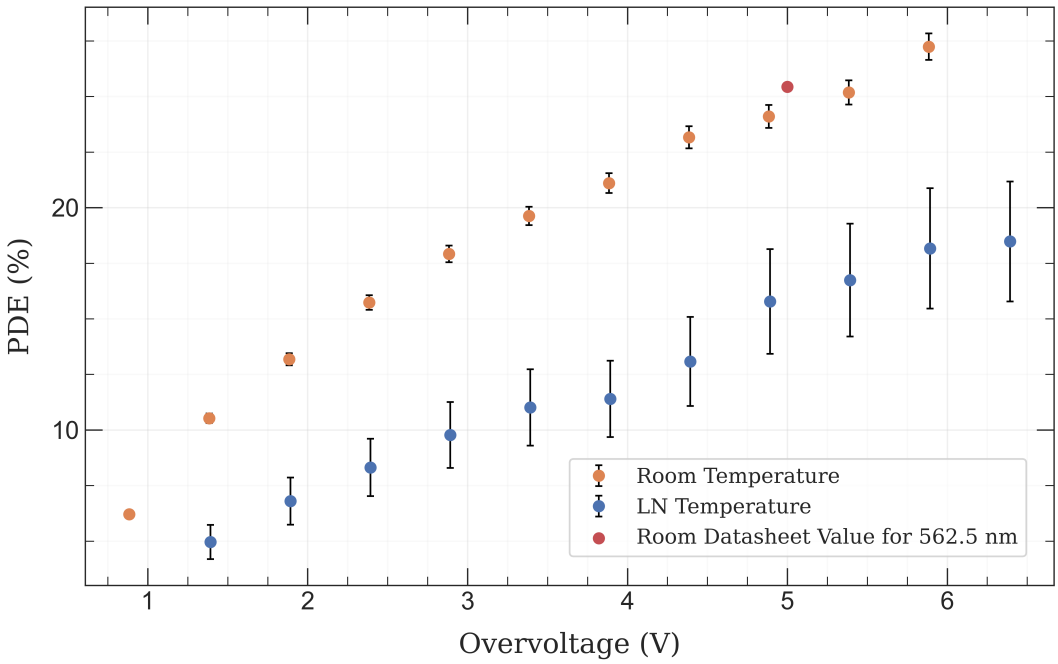

Figure 5.21: The photon detection efficiency measured at room temperature and liquid nitrogen temperature for several bias voltages. The KETEK datasheet PDE for the peak emission wavelength of the LED is the red dot. All contributing uncertainties are shown in Eq. 5.7−Eq. 5.10 in addition to the APD systematic included for the liquid nitrogen PDE measurement.

Chapter 6

GPU-ACCELERATED OPTICAL PHOTON MONTE CARLO

In the SiPM characterization test stand light pulses from a LED are uniformly spread to the SiPM and a calibrated APD through an integrating sphere. An important systematic to understand, given the particular design of the integrating sphere setup, is what's the expected difference in the number of photons seen by the SiPM and APD and how does it effect the PDE. In theory an integrating sphere uniformly spreads the output power of a light source across its spherical surface, but this not exactly true when considering imperfections such as differences in detector device housing, dust and dents on the spherical surface, and parts of the design that violate spherical symmetry. To estimate the incident photon rate expected at the SiPM and APD positions inside the integrating sphere requires an optical photon Monte Carlo simulation. Such a simulation treats visible photons as semi-classical particles that have probabilistic interactions within the simulation geometry. The simulation keeps track of all photons within the geometry and propagates each photon in a straight line to the next interaction site, also known as ray tracing. Computations for ray-tracing photons can be very time consuming when executed on a CPU. A full optical photon Monte Carlo simulation of the LEGEND-1000 geometry using the GEANT4 library currently takes about 2 weeks to complete. Using a GPU for propagating photons, provides the advantage of computing many photon tracks in parallel. Parallelization is not challenging to implement since optical photons do not interact with each other, therefore tracks can be computed on independent GPU threads simultaneously.

The software used to run the simulations is Chroma. Chroma is a python interface that interacts with a CUDA-capable device through the python package PyCUDA to perform the optical photon monte-carlo simulations [140]. The Chroma whitepaper claims that this

methodology can be up to 200 times faster than optical simulations with GEANT4. In the software, geometries are comprised of solids which have three properties: a triangular mesh surface, a bulk material optical property, and a surface material optical property for each triangle. Solids can also be identified as detectors with detection probabilities to collect a certain fraction of absorbed photons as detected.

This chapter describes the basic principles of GPU parallelization and how it applies to Chroma followed by a calculation of the integrating sphere form factor.

6.1 The Graphics Processing Unit (GPU)

A GPU is a device that uses parallel processing to accelerate computational tasks. Marketable GPUs started to emerge when NVIDIA released the "the world's first GPU" GeForce® 256 in 1999. The ability for GPUs to breakdown computationally intensive problems into separate parallel tasks, also known as *single instruction multiple thread* (SIMT), makes them excellent devices for rendering computer graphics. This is in contrast to a CPU, which is intended for fast serial processing, see Fig 6.1. CPUs tend to have higher clock speeds and lower core counts, whereas GPUs have higher core counts and lower clock speeds. Since the first release of CUDA in 2007, software developers have been able to access the parallel computing power of NVIDIA GPUs for other applications. GPUs have played a crucial role in the advancement of video editing, content creation, machine learning as well as physics simulations in the last decade.

A process that is run on a NVIDIA GPU is called a CUDA kernel. From the software perspective a GPU device consists of a grid of *blocks* and each block has a set maximum number of *threads* and set maximum grid dimensions. Choosing the number of thread blocks to run a particular CUDA kernel is a balance between the kernel loading time and the processing time. More thread blocks will typically decrease computation time, but more thread blocks will also increase the overhead time of loading the kernel onto the GPU. On the hardware level, thread blocks will be mapped to the GPU's streaming multiprocessors, see Fig. 6.2. Each streaming multiprocessor divides out the work into groups of synchronized

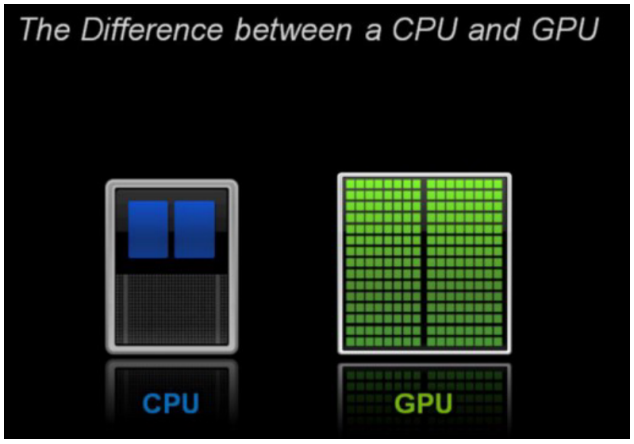

Figure 6.1: A diagrammatic layout of the cores within a CPU and a GPU. A CPU will have fewer cores with higher clock speeds and a GPU will have many cores with lower clock speeds. *Image Credit: Brian Caulfield, NVIDIA Technical Blog*

threads called warps (typically 32 threads per warp). The mapping between thread blocks and warps can effect performance so thread blocks are usually allocated in multiples of 32.

CUDA kernels are written in the C programming language and can be accessed from other programming languages such as python with PyCUDA. A simple example of the usage of a CUDA kernel to add two arrays together is shown in Fig. 6.3. The thread index is given by the block index times the number of threads per block plus the local thread index in the block. Blocks can also be specified in more than one dimension (x, y, and z), however using the x dimension only is the most simple. Each thread will run the CUDA kernel and the for loop splits the array addition into pieces where each piece is a number of elements equal to the total number of threads specified. The kernel is then called at line 33 with one block of 256 threads. This same SIMT principle is used to propagate photons in Chroma. Many photons are propagated simultaneously on batches of threads. Inside the for loop is instead the Monte Carlo, which decides where a photon's trajectory should go for each step.

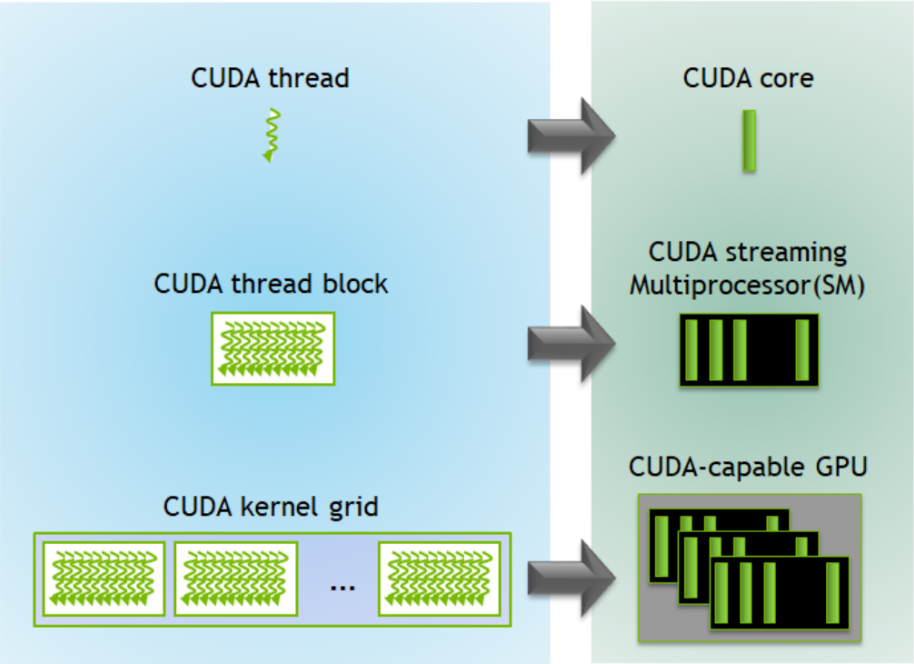

Figure 6.2: A diagram showing the mapping of threads, blocks, and grid to the GPU hardware. A CUDA core can run one warp at a time where a warp consists of 32 synchronized threads. *Image Credit: Pradeep Gupta, NVIDIA Technical Blog*

6.2 Optical Photon Monte Carlo in Chroma

The decisions on how to propagate the photon tracks is done by random number generators that are weighted by wavelength dependent probability distributions. Before the start of each simulation a set of random number generator states are initialized for the user specified thread block configuration to be used on the GPU. On each thread, the random number generator state is sampled when a photon intersects one of the triangles on a solid's mesh. For each step photon track intersections are found by searching through a *bounded volume hierarchy* of the solids in the mesh. A bounded volume hierarchy is a tree structure of enclosed volumes within the entire mesh, see Fig. 6.4. The top node is a volume that encloses the entire mesh and each subsiding child node divides up the mesh into smaller and smaller

```
1  #include <iostream>
2  #include <cmath>
3
4  //-- CUDA Kernel ------------------------------------------------------------
5
6  __global__
7  void add(int n, float *x, float *y)
8  {
9    int index = blockIdx.x * blockDim.x + threadIdx.x;
10   int stride = blockDim.x * gridDim.x;
11   for (int i = index; i < n; i += stride)
12     y[i] = x[i] + y[i];
13 }
14
15 //---------------------------------------------------------------------------
16
17 int main(void)
18 {
19   int N = 1<<20;
20   float *x, *y;
21
22   // Allocate Unified Memory – accessible from CPU or GPU
23   cudaMallocManaged(&x, N*sizeof(float));
24   cudaMallocManaged(&y, N*sizeof(float));
25
26   // initialize x and y arrays on the host
27   for (int i = 0; i < N; i++) {
28     x[i] = 1.0f;
29     y[i] = 2.0f;
30   }
31
32   // Run kernel on 1M elements on the GPU
33   add<<<1, 256>>>(N, x, y);
34
35   // Wait for GPU to finish before accessing on host
36   cudaDeviceSynchronize();
37
38   // Check for errors (all values should be 3.0f)
39   float maxError = 0.0f;
40   for (int i = 0; i < N; i++)
41     maxError = fmax(maxError, fabs(y[i]-3.0f));
42   std::cout << "Max error: " << maxError << std::endl;
43
44   // Free memory
45   cudaFree(x);
46   cudaFree(y);
47
48   return 0;
49 }
```

Figure 6.3: C program with a CUDA kernel that adds two arrays together. The CUDA kernel is executed at line 33 with one block of 256 threads. The kernel runs under SIMT, where all threads run the same operations in the kernel with a specific thread index. The arrays are added in pieces with the same number of elements as number of threads specified. *Credit: Mark Harris, NVIDIA Technical Blog*

volumes. The bounded volume hierarchy is used to search for photon track intersections because it prevents the software from looping over every triangle in the mesh to search for intersections on every step of the simulation.

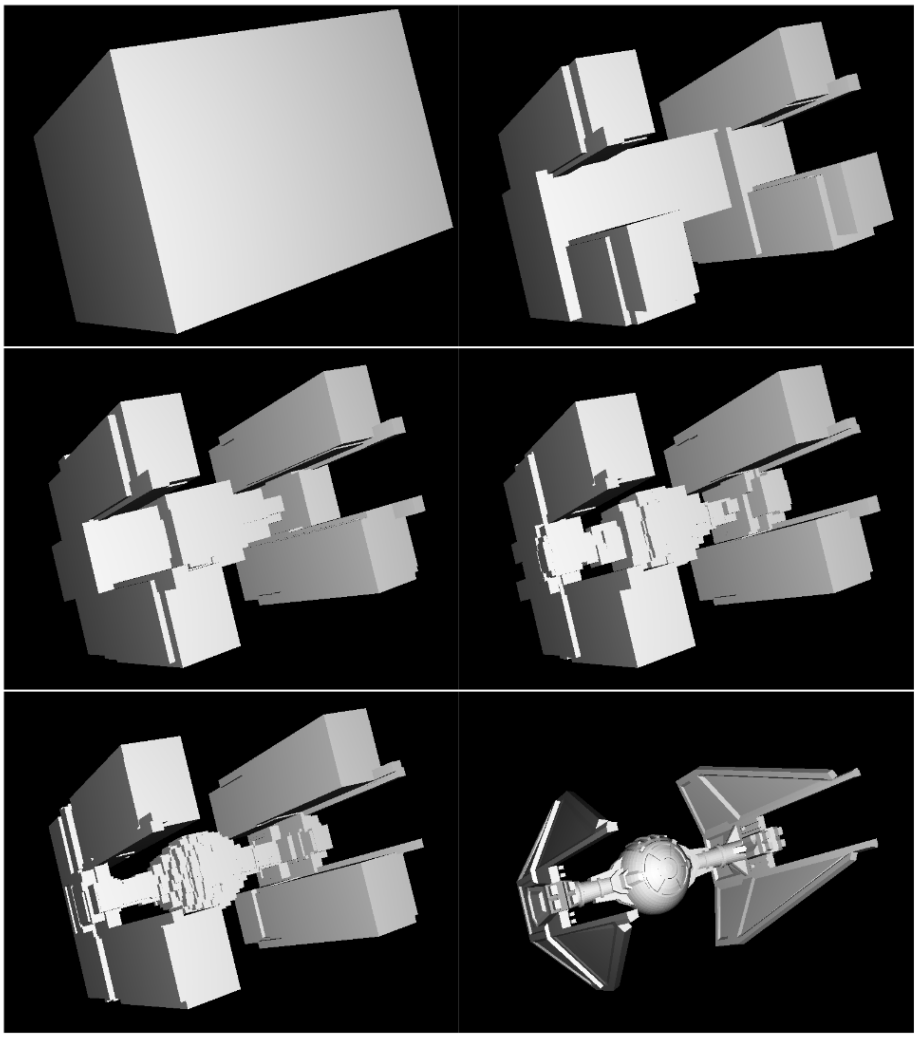

Figure 6.4: A bounded volume hierarchy for the mesh of an Imperial Tie Interceptor. Going from left to right, top to bottom corresponds to moving down the hierarchy tree. When Chroma finds an intersection with a photon track and one of the bounded volumes it moves down the bounded volume hierarchy until the intersected triangle on the mesh is found. Fig. from ref. [140].

The optical properties used in Chroma can be split into bulk material properties and surface properties. A bulk material will have a refractive index, absorption length, and scattering length. A surface will have a detection probability, absorption probability, specular reflection probability, and diffuse reflection probability. Chroma can also simulate fluorescent materials and surfaces with re-emission probabilities, but is not used in this work. Once an interaction between a photon track and a triangle on the mesh is found the weighted random number generators are sampled based on the bulk material optical properties the photon traversed through and the surface optical properties it intersected with, see Fig. 6.5.

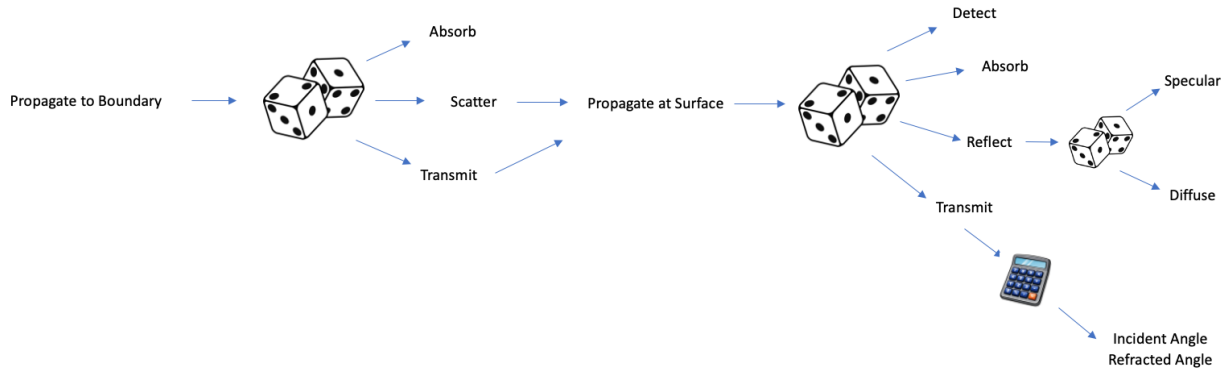

Figure 6.5: A simplified diagram of how Chroma propagates a photon for one step. The dice represent a weighted random number generator based on wavelength dependent optical properties specified by the user. Absorption removes photons from the simulation and detection acts as an absorption in the simulation, but the photon is not lost and instead is stored in memory.

6.3 Photon Propagation in an Integrating Sphere

A triangular mesh of the Thorlabs IS200-4 integrating sphere is made from a CAD model provided by Thorlabs. The CAD model is then converted to a triangular mesh via a `.stl` file in Autodesk Fusion 360® which contains over a million triangles. The computer hardware used is an Intel® Core™ i7-10700k CPU and a GIGABYTE™ GeForce® RTX 2070 Super™ WINDFORCE OC 3X 8G. This CPU and GPU combination was chosen to commercially optimize the computer for *Microsoft Flight Simulator 2020* and the performance is a bit overkill for running the integrating sphere simulation. The SiPM is modeled as a square surface with some thickness, the APD housing is modeled from a Thorlabs CAD model and a circle with some small thickness is used for the active area. The light source is the fiber aperture from the Thorlabs CAD model. Photons in the simulation are spawned just in front of the fiber aperture with wavelengths equal to the LED peak emission wavelength, uniform polarization, and a 10^o divergence angle into the sphere. A sample of ray-traced photon paths and a photon hit map are shown in Fig. 6.6 illustrating how photons are propagating through the integrating sphere geometry. The PTFE has a wavelength dependent reflectance provided by ThorLabs and the surface absorption is set to 1 − reflectance probability, see Fig. 6.7. The type of reflection in the simulation is set to 100% diffuse. All solids within the simulation are set to have surface absorption + surface reflection probabilities = 100% to disallow bulk transmission since all materials in the integrating sphere are virtually opaque. Detection probabilities for the SiPM and APD are set to 100% to assess the total number of incident photons on both detectors.

In the simulation, 2.5 million photons with the peak LED wavelength are injected into the sphere with a maximum number of bounces of 100 for each photon and the photons detected per area are recorded for the SiPM and APD. Photons can be injected all at once, but batches of 50 pulses with 50,000 photons each were used, which seemed to increase performance. The ratio of the photons detected per area from the SiPM and that of the APD is the integrating sphere form factor. Since the position of the SiPM and APD is difficult measure due to

spatial constraints in the real integrating sphere, the simulation is run 250 times with the SiPM and APD insertion depths into the sphere being randomly sampled within a 10 mm window of their expected position, see Fig. 6.8. The form factor is then given as the average within a 3 mm window and the uncertainty is the standard deviation. 3 mm is the estimated precision of determining the position of the detectors in the real integrating sphere by eye, which is the length and width of the SiPM and diameter of the APD active area. The form factor comes out to 1.061 ± 0.0056.

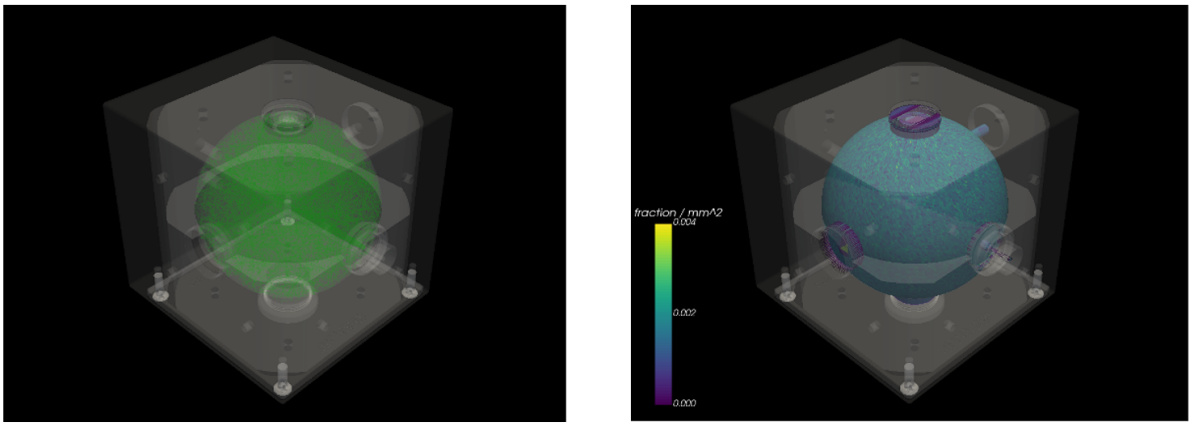

Figure 6.6: (Left) a visualization of the integrating sphere geometry with a sample of ray-traced photon paths. (Right) A hit map showing how uniformly the photons are hitting the integrating sphere expressed in fraction of initial source per mm^2.

6.4 Summary

Chroma proves to be a powerful tool in simulating optical photon propagation through complex mesh geometries. From simulating photon propagation, it was possible to predict the difference in the number of photons received by the SiPM and APD in the SiPM characterization test stand with good performance. A sweep of 250 different location variations for the

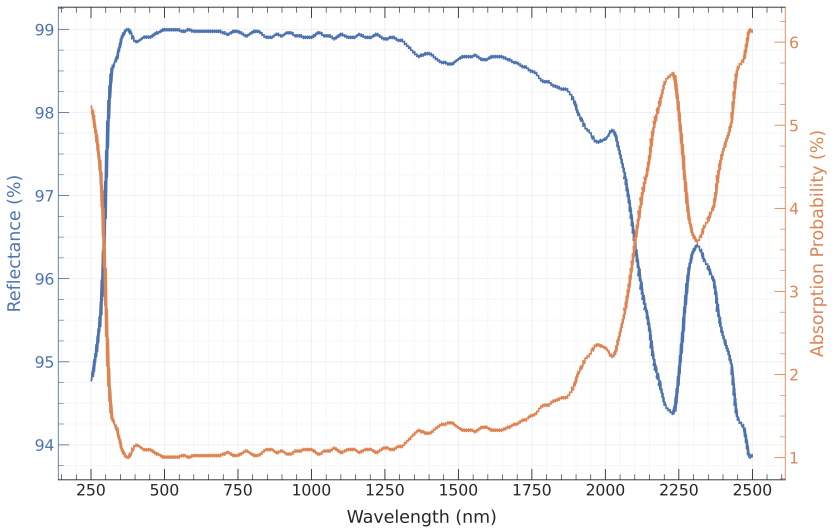

Figure 6.7: A plot of the reflectance and absorption probability set in the Chroma simulation. The reflectivity data is from the ThorLabs datasheet and the absorption probability is set to be 1 - reflectance. The reflection model in the simulation for the PTFE is set to 100% diffuse.

SiPM and APD with a total of 2,500,000 initial photons per location took on average 30 minutes to complete. GPU accelerated optical photon simulations have the potential to greatly increase the performance and accuracy of the LEGEND-1000 optical photon map calculations. Current GEANT4 geometries of LEGEND-1000 are comprised of primitive solids and optical photons are propagated on the CPU. With the usage of triangular mesh geometries, LEGEND-1000 could be modeled to virtual accuracy with widely used open-source computer graphics software such as blender$^{\text{TM}}$. And as background levels are required to decrease for larger ^{76}Ge experiments, more precise and computationally faster estimations of the liquid argon veto efficiency may be necessary to achieve those background goals.

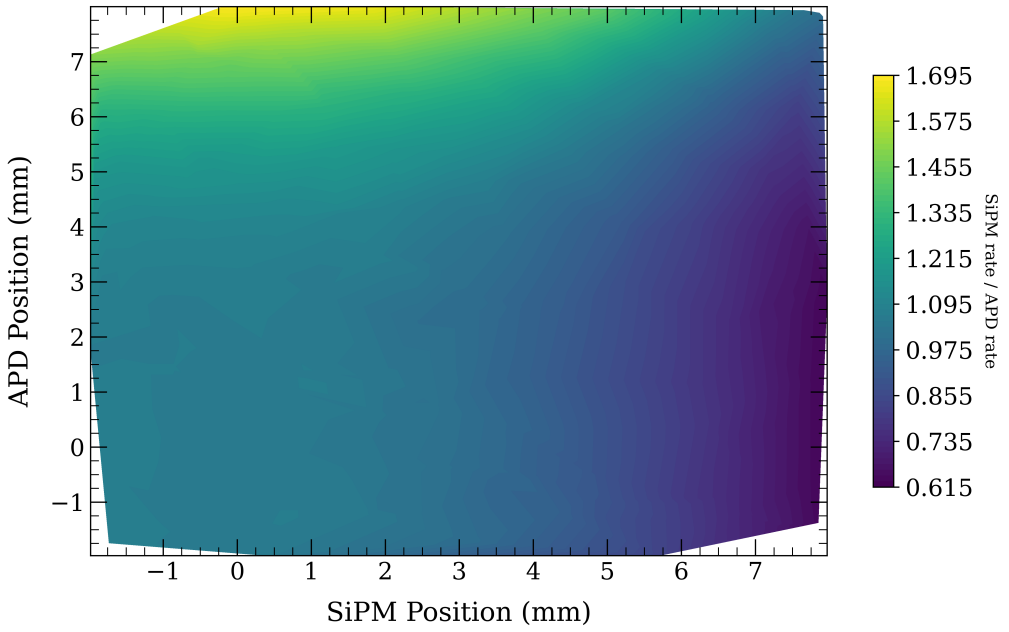

Figure 6.8: The ratio of the SiPM photon rate per area and the APD photon rate per area for varying insertion depths into the integrating sphere. 0 mm corresponds to the device sitting on the integrating sphere surface. The integrating sphere form factor is estimated by taking the average and standard deviation of the values in a 3 x 3 mm box centered at zero which gives a form factor of 1.061 ± 0.0056

Chapter 7

CONCLUSION

The work presented in this thesis is comprised of contributions to the search for $0\nu\beta\beta$ decay in current generation ^{76}Ge experiments and research and development for building the next phases of ^{76}Ge experiments, in particular LEGEND-1000. The two primary projects are designing a multi-site discrimination parameter for the MAJORANA DEMONSTRATOR and measuring the photon detection efficiency (PDE) of silicon photomultipliers (SiPM) at liquid nitrogen temperature for LEGEND 1000. The multi-site discrimination parameter helped the MAJORANA DEMONSTRATOR reach a $0\nu\beta\beta$ decay lower half-life limit in ^{76}Ge of 8.3×10^{25} yr, which corresponds to $m_{\beta\beta}$ limits of 113−269 meV depending on the choice of nuclear matrix elements. The SiPM characterization test stand was able to show a drop in PDE when operating SiPMs close to liquid argon temperature. This suggests that further investigation is necessary to more precisely understand the efficiency of the LAr-Veto readout system, in order to accurately predict background levels in LEGEND-1000 and beyond.

7.1 Multi-site Discrimination Analysis in ^{76}Ge Experiments

The AvsE parameter has proven to be a successful way to reject multi-site events in high purity germanium detector designs with small p^+ contacts. In the final $0\nu\beta\beta$ decay analysis of the MAJORANA DEMONSTRATOR AvsE removed roughly 60% of the background in the background estimation window after the surface event cuts and removed additional bulk detector multi-site events that pass all other analysis cuts. AvsE distinguishes itself from other multi-site discrimination parameters from its nonlinear correction to the energy dependence, which has the advantage of capturing the maximum current dependence with energy to higher order with the disadvantage of being less stable in between long calibration periods.

The most beneficial results coming out of the AvsE analysis is the importance of correcting for extraneous dependencies such as AvsE's width dependence on energy and waveform drift-time. Ideally a multi-site parameter would only depend on the maximum current, but realistically multi-site parameters have acute correlations with other observables that effect where the cut boundary is set. This makes the drift-time correction and width-energy dependence correction derived from ^{56}Co calibration data the most important aspects to be used in the future for further multi-site discrimination parameters.

AvsE has proven to be a very unstable parameter, comparatively to the other analysis parameters. More work can be done to address the instabilities of the non-linear energy dependence correction across short calibrations and whether a non-linear energy dependence correction has an advantage over one with a linear energy dependence when cutting on background data. So far there is no evidence that AvsE out-performs the conventional multi-site cut A/E in a search for $0\nu\beta\beta$ decay in ^{76}Ge. Precisely modeling the energy dependence in the long calibrations may not present much of an advantage when cutting on background data due to the instability of AvsE, but may have advantages in background modeling and other beyond standard model physics searches at energy regions outside of the background averaging window. AvsE also misidentifies multi-site events where one of the energy depositions is near the p^+ point contact, also a features of A/E. Future directions to resume research in AvsE is the study of the width-energy dependence in inverted point contact detectors, analysis methods that correctly identify multi-site events the current AvsE analysis misses, the study of correlations of the AvsE parameter with other analysis parameters, and stability corrections to the energy dependence. All of these research areas have the potential to significantly impact the background suppression capability of LEGEND-1000 and beyond given the more stringent background level requirements.

7.2 LAr-Veto Readout and Optical Simulations for LEGEND 1000

The characterization of SiPMs at liquid nitrogen temperature has shown the PDE decreases under cryogenic temperature conditions. This was shown with a broad LED spectrum and

a more precise and stable light source should be used to scan the photon detection efficiency over several different wavelengths. Multiple SiPMs were tested in the SiPM test stand, but only the KETEK PM3325-WB-D0 was tested in all of the characterization steps with the latest board designs. It would be interesting to see how the PDE at liquid nitrogen temperature varies with the device wavelength sensitivity and pixel pitch. Along with a light source that can narrowly scan many wavelengths, these measurements would be able to point to the optimal SiPM properties derived from experimental results for LEGEND-1000. Another constraint to consider for LEGEND-1000 is the radiopurity, which is why its important that the optimal SiPM be available without any packaging around the active detector material. Determining what the optimal SiPM is for the current LEGEND-1000 design would be interesting to know. It may also be interesting to pursue custom SiPM designs sensitive to visible spectrum that are made to operate at cryogenic temperatures. This study was done with liquid nitrogen to demonstrate feasibility and a PDE measurement at liquid argon temperature would present a better estimate of the PDE in LEGEND-1000.

Studying how photons propagate in the integrating sphere of the SiPM test stand led to the use of chroma. Chroma allowed for the simulation of photon propagation with GPU-accelerated ray tracing on mesh geometries produced from precise CAD models. This showed a promising alternative to the current optical simulations used to estimate the efficiency of the liquid argon veto. Not only does chroma promise better performance, it also has the flexibility of working with mesh geometries that have wide support outside of high energy physics software. An optical simulation of LEGEND 1000 in Chroma would be good to test the accuracy of the current simulations and demonstrate potential performance gains.

BIBLIOGRAPHY

[1] Bécquerel, A H. "Sur Les Radiations Invisibles Émises Par Les Sels d'uranium". In: *C. R. Acad. Sci.* Vol. 122. Paris, 1896, pp. 689–694.

[2] Curie, Pierre and Curie, Marie. "Sur Une Substance Nouvelle Radio-Active, Contenue Dans La Pechblende". In: *C. R. Hebd. Séanc. Acad. Sci.* Vol. 126. Paris, pp. 175–178.

[3] E. Rutherford. "LXXIX. The Scattering of α and β Particles by Matter and the Structure of the Atom". In: *The London, Edinburgh, and Dublin Philosophical Magazine and Journal of Science* 21.125 (May 1911), pp. 669–688. ISSN: 1941-5982. DOI: 10.1080/14786440508637080.

[4] Pauli, Wolfgang. *Open Letter to the Group of Radioactive People at the Gauverein Meeting in Tübingen.* Dec. 1930.

[5] E. Fermi. "Versuch einer Theorie der β-Strahlen. I". In: *Zeitschrift für Physik* 88.3 (Mar. 1934), pp. 161–177. ISSN: 0044-3328. DOI: 10.1007/BF01351864.

[6] H. Bethe and R. Peierls. "The "Neutrino"". In: *Nature* 133.3362 (Apr. 1934), pp. 532–532. ISSN: 1476-4687. DOI: 10.1038/133532a0.

[7] C. L. Cowan et al. "Detection of the Free Neutrino: A Confirmation". In: *Science* 124.3212 (July 1956), pp. 103–104. DOI: 10.1126/science.124.3212.103.

[8] C. S. Wu et al. "Experimental Test of Parity Conservation in Beta Decay". In: *Physical Review* 105.4 (Feb. 1957), pp. 1413–1415. DOI: 10.1103/PhysRev.105.1413.

[9] M. Goldhaber, L. Grodzins, and A. W. Sunyar. "Helicity of Neutrinos". In: *Physical Review* 109.3 (Feb. 1958), pp. 1015–1017. DOI: 10.1103/PhysRev.109.1015.

[10] J. C. Palathingal. "Method of Measuring the Helicity of the Antineutrino". In: *Physical Review Letters* 18.12 (Mar. 1967), pp. 473–474. DOI: 10.1103/PhysRevLett.18.473.

[11] J. C. Palathingal. "Helicity of Antineutrinos Emitted by Nuclei". In: *Physical Review Letters* 24.10 (Mar. 1970), pp. 524–526. DOI: 10.1103/PhysRevLett.24.524.

[12] Abdus Salam. "On Parity Conservation and Neutrino Mass". In: *Il Nuovo Cimento (1955-1965)* 5.1 (Jan. 1957), pp. 299–301. ISSN: 1827-6121. DOI: 10.1007/BF02812841.

[13] L. Landau. "On the Conservation Laws for Weak Interactions". In: *Nuclear Physics* 3.1 (Mar. 1957), pp. 127–131. ISSN: 0029-5582. DOI: 10.1016/0029-5582(57)90061-5.

[14] F. Englert and R. Brout. "Broken Symmetry and the Mass of Gauge Vector Mesons". In: *Physical Review Letters* 13.9 (Aug. 1964), pp. 321–323. DOI: 10.1103/PhysRevLett.13.321.

[15] Peter W. Higgs. "Broken Symmetries and the Masses of Gauge Bosons". In: *Physical Review Letters* 13.16 (Oct. 1964), pp. 508–509. DOI: 10.1103/PhysRevLett.13.508.

[16] G. S. Guralnik, C. R. Hagen, and T. W. B. Kibble. "Global Conservation Laws and Massless Particles". In: *Physical Review Letters* 13.20 (Nov. 1964), pp. 585–587. DOI: 10.1103/PhysRevLett.13.585.

[17] G. Aad et al. "Observation of a New Particle in the Search for the Standard Model Higgs Boson with the ATLAS Detector at the LHC". In: *Physics Letters B* 716.1 (Sept. 2012), pp. 1–29. ISSN: 0370-2693. DOI: 10.1016/j.physletb.2012.08.020.

[18] S. Chatrchyan et al. "Observation of a New Boson at a Mass of 125 GeV with the CMS Experiment at the LHC". In: *Physics Letters B* 716.1 (Sept. 2012), pp. 30–61. ISSN: 0370-2693. DOI: 10.1016/j.physletb.2012.08.021.

[19] G. Danby et al. “Observation of High-Energy Neutrino Reactions and the Existence of Two Kinds of Neutrinos”. In: *Physical Review Letters* 9.1 (July 1962), pp. 36–44. DOI: 10.1103/PhysRevLett.9.36.

[20] M. L. Perl et al. “Evidence for Anomalous Lepton Production in ${e}{\hat{+}}\ensuremath{-}{e}{\hat{\ensuremath{-}}}$ Annihilation”. In: *Physical Review Letters* 35.22 (Dec. 1975), pp. 1489–1492. DOI: 10.1103/PhysRevLett.35.1489.

[21] K. Kodama et al. “Observation of Tau Neutrino Interactions”. In: *Physics Letters B* 504.3 (Apr. 2001), pp. 218–224. ISSN: 0370-2693. DOI: 10.1016/S0370-2693(01)00307-0.

[22] J. N. Bahcall et al. “Solar Neutrino Flux.” In: *The Astrophysical Journal* 137 (Jan. 1963), pp. 344–346. ISSN: 0004-637X. DOI: 10.1086/147513.

[23] Bruce T. Cleveland et al. “Measurement of the Solar Electron Neutrino Flux with the Homestake Chlorine Detector”. In: *The Astrophysical Journal* 496.1 (Mar. 1998), p. 505. ISSN: 0004-637X. DOI: 10.1086/305343.

[24] Ziro Maki, Masami Nakagawa, and Shoichi Sakata. “Remarks on the Unified Model of Elementary Particles”. In: *Progress of Theoretical Physics* 28.5 (Nov. 1962), pp. 870–880. ISSN: 0033-068X. DOI: 10.1143/PTP.28.870.

[25] Ling-Lie Chau and Wai-Yee Keung. “Comments on the Parametrization of the Kobayashi-Maskawa Matrix”. In: *Physical Review Letters* 53.19 (Nov. 1984), pp. 1802–1805. DOI: 10.1103/PhysRevLett.53.1802.

[26] S. M. Bilenky and S. T. Petcov. “Massive Neutrinos and Neutrino Oscillations”. In: *Reviews of Modern Physics* 59.3 (July 1987), pp. 671–754. DOI: 10.1103/RevModPhys.59.671.

[27] K. S. Hirata et al. “Observation of ${\hat{8}}\mathrm{B}$ Solar Neutrinos in the Kamiokande-II Detector”. In: *Physical Review Letters* 63.1 (July 1989), pp. 16–19. DOI: 10.1103/PhysRevLett.63.16.

[28] P. Anselmann et al. “Solar Neutrinos Observed by GALLEX at Gran Sasso”. In: *Physics Letters B* 285.4 (July 1992), pp. 376–389. ISSN: 0370-2693. DOI: 10.1016/0370-2693(92)91521-A.

[29] J. N. Abdurashitov et al. “Results from SAGE (The Russian-American Gallium Solar Neutrino Experiment)”. In: *Physics Letters B* 328.1 (May 1994), pp. 234–248. ISSN: 0370-2693. DOI: 10.1016/0370-2693(94)90454-5.

[30] Super-Kamiokande Collaboration et al. “Evidence for Oscillation of Atmospheric Neutrinos”. In: *Physical Review Letters* 81.8 (Aug. 1998), pp. 1562–1567. DOI: 10.1103/PhysRevLett.81.1562.

[31] M. H. Ahn et al. “Indications of Neutrino Oscillation in a 250 Km Long-Baseline Experiment”. In: *Physical Review Letters* 90.4 (Jan. 2003), p. 041801. DOI: 10.1103/PhysRevLett.90.041801.

[32] SNO Collaboration et al. “Measurement of the Rate of ... Interactions Produced by $\hat{}\{8\}$B$ Solar Neutrinos at the Sudbury Neutrino Observatory”. In: *Physical Review Letters* 87.7 (July 2001), p. 071301. DOI: 10.1103/PhysRevLett.87.071301.

[33] R.L. Workman et al. *(Particle Data Group)*. 2022.

[34] Kevin J. Kelly et al. “Neutrino Mass Ordering in Light of Recent Data”. In: *Physical Review D* 103.1 (Jan. 2021), p. 013004. DOI: 10.1103/PhysRevD.103.013004.

[35] K. Abe et al. “Constraint on the Matter–Antimatter Symmetry-Violating Phase in Neutrino Oscillations”. In: *Nature* 580.7803 (Apr. 2020), pp. 339–344. ISSN: 1476-4687. DOI: 10.1038/s41586-020-2177-0.

[36] Carlo Giunti and Chung Wook Kim. *Fundamentals of Neutrino Physics and Astrophysics*. Oxford ; New York: Oxford University Press, 2007. ISBN: 978-0-19-850871-7.

[37] Ettore Majorana. “Teoria simmetrica dell’elettrone e del positrone”. In: *Il Nuovo Cimento (1924-1942)* 14.4 (Sept. 2008), p. 171. ISSN: 1827-6121. DOI: 10.1007/BF02961314.

[38] M. Aker et al. “Direct Neutrino-Mass Measurement with Sub-Electronvolt Sensitivity”. In: *Nature Physics* 18.2 (Feb. 2022), pp. 160–166. ISSN: 1745-2481. DOI: 10.1038/s41567-021-01463-1.

[39] Lev Kofman, Andrei Linde, and Alexei A. Starobinsky. “Towards the Theory of Reheating after Inflation”. In: *Physical Review D* 56.6 (Sept. 1997), pp. 3258–3295. DOI: 10.1103/PhysRevD.56.3258.

[40] N. Aghanim et al. “Planck 2018 Results - VI. Cosmological Parameters”. In: *Astronomy & Astrophysics* 641 (Sept. 2020), A6. ISSN: 0004-6361, 1432-0746. DOI: 10.1051/0004-6361/201833910.

[41] Ryan J. Cooke, Max Pettini, and Charles C. Steidel. “One Percent Determination of the Primordial Deuterium Abundance*”. In: *The Astrophysical Journal* 855.2 (Mar. 2018), p. 102. ISSN: 0004-637X. DOI: 10.3847/1538-4357/aaab53.

[42] Ling, J. Samuel, Sanny, Jeff, and Moebs, William. “University Physics”. In: vol. 3. Rice University, 2018, p. 539.

[43] Andrei D. Sakharov. “Violation of CP Invariance, C Asymmetry, and Baryon Asymmetry of the Universe”. In: *Soviet Physics Uspekhi* 34.5 (May 1991), p. 392. ISSN: 0038-5670. DOI: 10.1070/PU1991v034n05ABEH002497.

[44] M. Fukugita and T. Yanagida. “Barygenesis without Grand Unification”. In: *Physics Letters B* 174.1 (June 1986), pp. 45–47. ISSN: 0370-2693. DOI: 10.1016/0370-2693(86)91126-3.

[45] Laura Covi, Esteban Roulet, and Francesco Vissani. “CP Violating Decays in Leptogenesis Scenarios”. In: *Physics Letters B* 384.1 (Sept. 1996), pp. 169–174. ISSN: 0370-2693. DOI: 10.1016/0370-2693(96)00817-9.

[46] W. Buchmüller, P. Di Bari, and M. Plümacher. “Leptogenesis for Pedestrians”. In: *Annals of Physics* 315.2 (Feb. 2005), pp. 305–351. ISSN: 0003-4916. DOI: 10.1016/j.aop.2004.02.003.

[47] S. R. Elliott, A. A. Hahn, and M. K. Moe. "Direct Evidence for Two-Neutrino Double-Beta Decay in ${\hat}82}\mathrm{Se}$". In: *Physical Review Letters* 59.18 (Nov. 1987), pp. 2020–2023. DOI: 10.1103/PhysRevLett.59.2020.

[48] E. Aprile et al. "Observation of Two-Neutrino Double Electron Capture in 124Xe with XENON1T". In: *Nature* 568.7753 (Apr. 2019), pp. 532–535. ISSN: 1476-4687. DOI: 10.1038/s41586-019-1124-4.

[49] Matteo Agostini et al. "Toward the Discovery of Matter Creation with Neutrinoless Double-Beta Decay". In: *arXiv:2202.01787 [hep-ex, physics:hep-ph, physics:hep-th, physics:nucl-ex, physics:nucl-th]* (Feb. 2022). arXiv: 2202.01787 [hep-ex, physics:hep-ph, physics:hep-th, physics:nucl-ex, physics:nucl-th].

[50] J. Schechter and J. W. F. Valle. "Neutrinoless Double-$\ensuremath{\beta}$ Decay in SU(2)\ifmmode\times\else\texttimes\fi{}U(1) Theories". In: *Physical Review D* 25.11 (June 1982), pp. 2951–2954. DOI: 10.1103/PhysRevD.25.2951.

[51] Jonathan Engel and Javier Menéndez. "Status and Future of Nuclear Matrix Elements for Neutrinoless Double-Beta Decay: A Review". In: *Reports on Progress in Physics* 80.4 (Mar. 2017), p. 046301. ISSN: 0034-4885. DOI: 10.1088/1361-6633/aa5bc5.

[52] A. Belley et al. "Ab Initio Neutrinoless Double-Beta Decay Matrix Elements for ${\hat}48}\mathrm{Ca}$, ${\hat}76}\mathrm{Ge}$, and ${\hat}82}\mathrm{Se}$". In: *Physical Review Letters* 126.4 (Jan. 2021), p. 042502. DOI: 10.1103/PhysRevLett.126.042502.

[53] V. Cirigliano et al. "A Neutrinoless Double Beta Decay Master Formula from Effective Field Theory". In: *Journal of High Energy Physics* 2018.12 (Dec. 2018), p. 97. ISSN: 1029-8479. DOI: 10.1007/JHEP12(2018)097.

[54] Valerio D'Andrea et al. "Neutrinoless Double Beta Decay with Germanium Detectors: 1026 Yr and Beyond". In: *Universe* 7.9 (Sept. 2021), p. 341. ISSN: 2218-1997. DOI: 10.3390/universe7090341.

[55] Matteo Agostini, Giovanni Benato, and Jason A. Detwiler. "Discovery Probability of Next-Generation Neutrinoless Double-$\ensuremath{\beta}$ Decay Experiments". In: *Physical Review D* 96.5 (Sept. 2017), p. 053001. DOI: 10.1103/PhysRevD.96.053001.

[56] Gary J. Feldman and Robert D. Cousins. "Unified Approach to the Classical Statistical Analysis of Small Signals". In: *Physical Review D* 57.7 (Apr. 1998), pp. 3873–3889. DOI: 10.1103/PhysRevD.57.3873.

[57] KamLAND-Zen Collaboration. "First Search for the Majorana Nature of Neutrinos in the Inverted Mass Ordering Region with KamLAND-Zen". In: *arXiv:2203.02139 [hep-ex, physics:physics]* (Mar. 2022). arXiv: 2203.02139 [hep-ex, physics:physics].

[58] GERDA Collaboration et al. "Final Results of GERDA on the Search for Neutrinoless Double-$\ensuremath{\beta}$ Decay". In: *Physical Review Letters* 125.25 (Dec. 2020), p. 252502. DOI: 10.1103/PhysRevLett.125.252502.

[59] Majorana Collaboration et al. "New Limits on Bosonic Dark Matter, Solar Axions, Pauli Exclusion Principle Violation, and Electron Decay from the Majorana Demonstrator". In: *Physical Review Letters* 118.16 (Apr. 2017), p. 161801. DOI: 10.1103/PhysRevLett.118.161801.

[60] Majorana Collaboration et al. "First Limit on the Direct Detection of Lightly Ionizing Particles for Electric Charge as Low as $e/1000$ with the Majorana Demonstrator". In: *Physical Review Letters* 120.21 (May 2018), p. 211804. DOI: 10.1103/PhysRevLett.120.211804.

[61] Majorana Collaboration et al. "Search for Trinucleon Decay in the Majorana Demonstrator". In: *Physical Review D* 99.7 (Apr. 2019), p. 072004. DOI: 10.1103/PhysRevD.99.072004.

[62] Majorana Collaboration et al. "Search for Double-$\ensuremath{\beta}$ Decay of $\hat{76}\mathrm{Ge}$ to Excited States of $\hat{76}\mathrm{Se}$ with the Majorana

Demonstrator". In: *Physical Review C* 103.1 (Jan. 2021), p. 015501. DOI: 10.1103/PhysRevC.103.015501.

[63] I. J. Arnquist et al. *Final Result of the MAJORANA DEMONSTRATOR's Search for Neutrinoless Double-β Decay in ^{76}Ge*. July 2022. DOI: 10.48550/arXiv.2207.07638. arXiv: 2207.07638 [hep-ex, physics:nucl-ex, physics:physics].

[64] N. Abgrall et al. "The Processing of Enriched Germanium for the Majorana Demonstrator and R&D for a next Generation Double-Beta Decay Experiment". In: *Nuclear Instruments and Methods in Physics Research Section A: Accelerators, Spectrometers, Detectors and Associated Equipment* 877 (Jan. 2018), pp. 314–322. ISSN: 0168-9002. DOI: 10.1016/j.nima.2017.09.036.

[65] W. Shockley. "Currents to Conductors Induced by a Moving Point Charge". In: *Journal of Applied Physics* 9.10 (Oct. 1938), pp. 635–636. ISSN: 0021-8979. DOI: 10.1063/1.1710367.

[66] S. Ramo. "Currents Induced by Electron Motion". In: *Proceedings of the IRE* 27.9 (Sept. 1939), pp. 584–585. ISSN: 2162-6634. DOI: 10.1109/JRPROC.1939.228757.

[67] Tommaso Comellato, Matteo Agostini, and Stefan Schönert. "Charge-Carrier Collective Motion in Germanium Detectors for $$\beta \beta $$-Decay Searches". In: *The European Physical Journal C* 81.1 (Jan. 2021), p. 76. ISSN: 1434-6052. DOI: 10.1140/epjc/s10052-021-08889-0.

[68] N. Abgrall et al. "The Majorana Demonstrator Readout Electronics System". In: *Journal of Instrumentation* 17.05 (May 2022), T05003. ISSN: 1748-0221. DOI: 10.1088/1748-0221/17/05/T05003.

[69] Sergio Zimmermann et al. "Implementation and Performance of the Electronics and Computing System of the Gamma Ray Energy Tracking In-Beam Nuclear Array (GRETINA)". In: *2011 IEEE Nuclear Science Symposium Conference Record*. Oct. 2011, pp. 596–601. DOI: 10.1109/NSSMIC.2011.6154119.

[70] N. Abgrall et al. "The Majorana Demonstrator Calibration System". In: *Nuclear Instruments and Methods in Physics Research Section A: Accelerators, Spectrometers, Detectors and Associated Equipment* 872 (Nov. 2017), pp. 16–22. ISSN: 0168-9002. DOI: 10.1016/j.nima.2017.08.005.

[71] N. Abgrall et al. "ADC Nonlinearity Correction for the Majorana Demonstrator". In: *IEEE Transactions on Nuclear Science* 68.3 (Mar. 2021), pp. 359–367. ISSN: 1558-1578. DOI: 10.1109/TNS.2020.3043671.

[72] I. J. Arnquist et al. *Charge Trapping and Energy Performance of the MAJORANA DEMONSTRATOR*. Aug. 2022. DOI: 10.48550/arXiv.2208.03424. arXiv: 2208.03424 [physics].

[73] Valentin T. Jordanov and Glenn F. Knoll. "Digital Synthesis of Pulse Shapes in Real Time for High Resolution Radiation Spectroscopy". In: *Nuclear Instruments and Methods in Physics Research Section A: Accelerators, Spectrometers, Detectors and Associated Equipment* 345.2 (June 1994), pp. 337–345. ISSN: 0168-9002. DOI: 10.1016/0168-9002(94)91011-1.

[74] Majorana Collaboration et al. "Search for Neutrinoless Double-$\ensuremath{\beta}$ Decay in ${\hat}{76}\mathrm{Ge}$ with 26 Kg Yr of Exposure from the Majorana Demonstrator". In: *Physical Review C* 100.2 (Aug. 2019), p. 025501. DOI: 10.1103/PhysRevC.100.025501.

[75] Helmuth Spieler. *Semiconductor Detector Systems*. Series on Semiconductor Science and Technology 12. Oxford: Oxford University Press, 2005.

[76] Majorana Collaboration et al. "Multisite Event Discrimination for the Majorana Demonstrator". In: *Physical Review C* 99.6 (June 2019), p. 065501. DOI: 10.1103/PhysRevC.99.065501.

[77] I. J. Arnquist et al. "$$\alpha $$-Event Characterization and Rejection in Point-Contact HPGe Detectors". In: *The European Physical Journal C* 82.3 (Mar. 2022), p. 226. ISSN: 1434-6052. DOI: 10.1140/epjc/s10052-022-10161-y.

[78] "P-TYPE POINT CONTACT GERMANIUM DETECTORS AND THEIR APPLICATION IN RARE-EVENT SEARCHES". PhD thesis. University of North Carolina at Chapel Hill, 2015.

[79] Micah James Noecker Buuck. "A Radiogenic Background Model for the MAJORANA DEMONSTRATOR". Thesis. 2019.

[80] M. Agostini et al. "Background-Free Search for Neutrinoless Double-β Decay of 76Ge with GERDA". In: *Nature* 544.7648 (Apr. 2017), pp. 47–52. ISSN: 1476-4687. DOI: 10.1038/nature21717.

[81] Glen Cowan et al. "Asymptotic Formulae for Likelihood-Based Tests of New Physics". In: *The European Physical Journal C* 71.2 (Feb. 2011), p. 1554. ISSN: 1434-6052. DOI: 10.1140/epjc/s10052-011-1554-0.

[82] Mihai Horoi and Andrei Neacsu. "Shell Model Predictions for ${\hat}124}\mathrm{Sn}$ Double-$\ensuremath{\beta}$ Decay". In: *Physical Review C* 93.2 (Feb. 2016), p. 024308. DOI: 10.1103/PhysRevC.93.024308.

[83] L. Coraggio et al. "Calculation of the Neutrinoless Double-$\ensuremath{\beta}$ Decay Matrix Element within the Realistic Shell Model". In: *Physical Review C* 101.4 (Apr. 2020), p. 044315. DOI: 10.1103/PhysRevC.101.044315.

[84] M. T. Mustonen and J. Engel. "Large-Scale Calculations of the Double-$\ensuremath{\beta}$ Decay of ${}{\hat}76}\mathbf{Ge},\phantom{\rule{0.28em}{0ex}}{}{\hat}130}\mathbf{Te},\phantom{\r and ${}{\hat}150}\mathbf{Nd}$ in the Deformed Self-Consistent Skyrme Quasiparticle Random-Phase Approximation". In: *Physical Review C* 87.6 (June 2013), p. 064302. DOI: 10.1103/PhysRevC.87.064302.

[85] Juhani Hyvärinen and Jouni Suhonen. "Nuclear Matrix Elements for $0\ensuremath{\nu}\ensurema Decays with Light or Heavy Majorana-neutrino Exchange". In: *Physical Review C* 91.2 (Feb. 2015), p. 024613. DOI: 10.1103/PhysRevC.91.024613.

[86] Fedor Šimkovic, Adam Smetana, and Petr Vogel. "$0\ensuremath{\nu}\ensuremath{\beta}\ensure and $2\ensuremath{\nu}\ensuremath{\beta}\ensuremath{\beta}$ Nuclear Matrix Elements Evaluated in Closure Approximation, Neutrino Potentials and SU(4) Symmetry". In: *Physical Review C* 98.6 (Dec. 2018), p. 064325. DOI: 10.1103/PhysRevC.98.064325.

[87] Dong-Liang Fang, Amand Faessler, and Fedor Šimkovic. "$0\ensuremath{\nu}\ensuremath{\beta}\ Decay Nuclear Matrix Element for Light and Heavy Neutrino Mass Mechanisms from Deformed Quasiparticle Random-Phase Approximation Calculations for $\hat{76}\mathrm{Ge}, $\hat{82}\mathrm{Se}$, $\hat{130}\mathrm{Te}$, $\hat{136}\mathrm{Xe}$, and $\hat{150}\mathrm{Nd}$ with Isospin Restoration". In: *Physical Review C* 97.4 (Apr. 2018), p. 045503. DOI: 10.1103/PhysRevC.97.045503.

[88] Tomás R. Rodríguez and Gabriel Martínez-Pinedo. "Energy Density Functional Study of Nuclear Matrix Elements for Neutrinoless $\ensuremath{\beta}\ensuremath{\beta}$ Decay". In: *Physical Review Letters* 105.25 (Dec. 2010), p. 252503. DOI: 10.1103/PhysRevLett.105.252503.

[89] Nuria López Vaquero, Tomás R. Rodríguez, and J. Luis Egido. "Shape and Pairing Fluctuation Effects on Neutrinoless Double Beta Decay Nuclear Matrix Elements". In: *Physical Review Letters* 111.14 (Sept. 2013), p. 142501. DOI: 10.1103/PhysRevLett.111.142501.

[90] L. S. Song et al. "Nuclear Matrix Element of Neutrinoless Double-$\ensuremath{\beta}$ Decay: Relativity and Short-Range Correlations". In: *Physical Review C* 95.2 (Feb. 2017), p. 024305. DOI: 10.1103/PhysRevC.95.024305.

[91] J. Menéndez. "Neutrinoless $B\beta$ Decay Mediated by the Exchange of Light and Heavy Neutrinos: The Role of Nuclear Structure Correlations". In: *Journal of Physics G: Nuclear and Particle Physics* 45.1 (Dec. 2017), p. 014003. ISSN: 0954-3899. DOI: 10.1088/1361-6471/aa9bd4.

[92] J. Barea, J. Kotila, and F. Iachello. "$0\ensuremath{\nu}\ensuremath{\beta}\ensuremath{\beta}$ and $2\ensuremath{\nu}\ensuremath{\beta}\ensuremath{\beta}$ Nuclear Matrix Elements in the Interacting Boson Model with Isospin Restoration". In: *Physical Review C* 91.3 (Mar. 2015), p. 034304. DOI: 10.1103/PhysRevC.91.034304.

[93] Frank F. Deppisch et al. "Analysis of Light Neutrino Exchange and Short-Range Mechanisms in $0\ensuremath{\nu}\ensuremath{\beta}\ensuremath{\beta}$ Decay". In: *Physical Review D* 102.9 (Nov. 2020), p. 095016. DOI: 10.1103/PhysRevD.102.095016.

[94] M. Agostini et al. "Pulse Shape Discrimination for Gerda Phase I Data". In: *The European Physical Journal C* 73.10 (Oct. 2013), p. 2583. ISSN: 1434-6052. DOI: 10.1140/epjc/s10052-013-2583-7.

[95] S. J. Meijer. "Precision Modeling of Germanium Detector Waveforms For Rare Event Searches". PhD thesis. University of North Carolina at Chapel Hill, 2019.

[96] LEGEND Collaboration et al. *LEGEND-1000 Preconceptual Design Report*. July 2021. DOI: 10.48550/arXiv.2107.11462. arXiv: 2107.11462 [nucl-ex, physics:physics].

[97] M. Agostini et al. "Probing Majorana Neutrinos with Double-β Decay". In: *Science* 365.6460 (Sept. 2019), pp. 1445–1448. DOI: 10.1126/science.aav8613.

[98] Luis Manzanillas et al. "Usage of PEN as Self-Vetoing Structural Material in Low Background Experiments". In: *Proceedings of 40th International Conference on High Energy Physics — PoS(ICHEP2020)*. Vol. 390. SISSA Medialab, Apr. 2021, p. 163. DOI: 10.22323/1.390.0163.

[99] L. Manzanillas et al. “Usage of PEN as Self-Vetoing Structural Material in the LEGEND Experiment”. In: *Journal of Instrumentation* 17.03 (Mar. 2022), p. C03031. ISSN: 1748-0221. DOI: 10.1088/1748-0221/17/03/C03031.

[100] C. Amsler et al. “Luminescence Quenching of the Triplet Excimer State by Air Traces in Gaseous Argon”. In: *Journal of Instrumentation* 3.02 (Feb. 2008), P02001–P02001. ISSN: 1748-0221. DOI: 10.1088/1748-0221/3/02/P02001.

[101] M. Miyajima et al. “Average Energy Expended per Ion Pair in Liquid Argon”. In: *Physical Review A* 9.3 (Mar. 1974), pp. 1438–1443. DOI: 10.1103/PhysRevA.9.1438.

[102] S. Kubota et al. “Evidence of the Existence of Exciton States in Liquid Argon and Exciton-Enhanced Ionization from Xenon Doping”. In: *Physical Review B* 13.4 (Feb. 1976), pp. 1649–1653. DOI: 10.1103/PhysRevB.13.1649.

[103] Tadayoshi Doke, Kimiaki Masuda, and Eido Shibamura. “Estimation of Absolute Photon Yields in Liquid Argon and Xenon for Relativistic (1 MeV) Electrons”. In: *Nuclear Instruments and Methods in Physics Research Section A: Accelerators, Spectrometers, Detectors and Associated Equipment* 291.3 (June 1990), pp. 617–620. ISSN: 0168-9002. DOI: 10.1016/0168-9002(90)90011-T.

[104] Ettore Segreto. “Properties of Liquid Argon Scintillation Light Emission”. In: *Physical Review D* 103.4 (Feb. 2021), p. 043001. DOI: 10.1103/PhysRevD.103.043001.

[105] R. Acciarri et al. “Effects of Nitrogen Contamination in Liquid Argon”. In: *Journal of Instrumentation* 5.06 (June 2010), P06003–P06003. ISSN: 1748-0221. DOI: 10.1088/1748-0221/5/06/P06003.

[106] R. Acciarri et al. “Oxygen Contamination in Liquid Argon: Combined Effects on Ionization Electron Charge and Scintillation Light”. In: *Journal of Instrumentation* 5.05 (May 2010), P05003–P05003. ISSN: 1748-0221. DOI: 10.1088/1748-0221/5/05/P05003.

[107] Mario Schwarz et al. "Liquid Argon Instrumentation and Monitoring in LEGEND-200". In: *EPJ Web of Conferences* 253 (2021), p. 11014. ISSN: 2100-014X. DOI: 10.1051/epjconf/202125311014.

[108] A. Neumeier et al. "Attenuation of Vacuum Ultraviolet Light in Pure and Xenon-Doped Liquid Argon —An Approach to an Assignment of the near-Infrared Emission from the Mixture". In: *EPL (Europhysics Letters)* 111.1 (July 2015), p. 12001. ISSN: 0295-5075. DOI: 10.1209/0295-5075/111/12001.

[109] Neil McFadden. "Studying Properties Of Xenon Doped Argon and Developing Optical Simulation Techniques for the LEGEND Collaboration, a Neutrinoless Double Beta Decay Experiment". PhD thesis. Feb. 2020.

[110] T. Heindl et al. "The Scintillation of Liquid Argon". In: *EPL (Europhysics Letters)* 91.6 (Sept. 2010), p. 62002. ISSN: 0295-5075. DOI: 10.1209/0295-5075/91/62002.

[111] Marcin Kuźniak and Andrzej M. Szelc. "Wavelength Shifters for Applications in Liquid Argon Detectors". In: *Instruments* 5.1 (Mar. 2021), p. 4. ISSN: 2410-390X. DOI: 10.3390/instruments5010004.

[112] Christopher Benson, Gabriel D. Orebi Gann, and Victor Gehman. "Measurements of the Intrinsic Quantum Efficiency and Absorption Length of Tetraphenyl Butadiene Thin Films in the Vacuum Ultraviolet Regime". In: *The European Physical Journal C* 78.4 (Apr. 2018), p. 329. ISSN: 1434-6052. DOI: 10.1140/epjc/s10052-018-5807-z.

[113] J. Asaadi et al. "Emanation and Bulk Fluorescence in Liquid Argon from Tetraphenyl Butadiene Wavelength Shifting Coatings". In: *Journal of Instrumentation* 14.02 (Feb. 2019), P02021–P02021. ISSN: 1748-0221. DOI: 10.1088/1748-0221/14/02/P02021.

[114] Chirstophe Wiesinger. "No Neutrinos Not Found". PhD thesis. Technical University of Munich, 2020.

[115] Saint-Gobain Ceramics & Plastics, Inc. *Fiber Product Sheet.*

[116] J. Janicskó Csáthy et al. *Optical Fiber Read-out for Liquid Argon Scintillation Light*. June 2016. DOI: 10.48550/arXiv.1606.04254. arXiv: 1606.04254 [hep-ex, physics:physics].

[117] I. Abt et al. "Alpha-Event and Surface Characterisation in Segmented True-Coaxial HPGe Detectors". In: *Nuclear Instruments and Methods in Physics Research Section A: Accelerators, Spectrometers, Detectors and Associated Equipment* 858 (June 2017), pp. 80–89. ISSN: 0168-9002. DOI: 10.1016/j.nima.2017.03.057.

[118] Othman, Gulden. "The CAGE Scanner: Investigating Surface Backgrounds in High-Purity Germanium Detectors". PhD thesis. University of North Carolina at Chapel Hill, 2021.

[119] EXO-200 Collaboration et al. "Search for Neutrinoless Double-$\ensuremath{\beta}$ Decay with the Complete EXO-200 Dataset". In: *Physical Review Letters* 123.16 (Oct. 2019), p. 161802. DOI: 10.1103/PhysRevLett.123.161802.

[120] Yoshihito Gando. "First Results of KamLAND-Zen 800". In: *Journal of Physics: Conference Series* 1468.1 (Feb. 2020), p. 012142. ISSN: 1742-6596. DOI: 10.1088/1742-6596/1468/1/012142.

[121] D. Q. Adams et al. "Search for Majorana Neutrinos Exploiting Millikelvin Cryogenics with CUORE". In: *Nature* 604.7904 (Apr. 2022), pp. 53–58. ISSN: 1476-4687. DOI: 10.1038/s41586-022-04497-4.

[122] The SNO+ collaboration et al. "The SNO+ Experiment". In: *Journal of Instrumentation* 16.08 (Aug. 2021), P08059. ISSN: 1748-0221. DOI: 10.1088/1748-0221/16/08/P08059.

[123] M. H. Lee. "AMoRE: A Search for Neutrinoless Double-Beta Decay of $\less$sup$\greater$100$\less Using Low-Temperature Molybdenum-Containing Crystal Detectors". In: *Journal of Instrumentation* 15.08 (Aug. 2020), pp. C08010–C08010. ISSN: 1748-0221. DOI: 10.1088/1748-0221/15/08/C08010.

[124] R. Arnold et al. "Probing New Physics Models of Neutrinoless Double Beta Decay with SuperNEMO". In: *The European Physical Journal C* 70.4 (Dec. 2010), pp. 927–943. ISSN: 1434-6052. DOI: 10.1140/epjc/s10052-010-1481-5.

[125] Maik Biroth et al. "Characterization of SiPM Properties at Liquid Nitrogen Temperature". In: *2016 IEEE Nuclear Science Symposium, Medical Imaging Conference and Room-Temperature Semiconductor Detector Workshop (NSS/MIC/RTSD)*. Oct. 2016, pp. 1–3. DOI: 10.1109/NSSMIC.2016.8069772.

[126] Fabio Acerbi et al. "Cryogenic Characterization of FBK HD Near-UV Sensitive SiPMs". In: *IEEE Transactions on Electron Devices* 64.2 (Feb. 2017), pp. 521–526. ISSN: 1557-9646. DOI: 10.1109/TED.2016.2641586.

[127] Fang Liu et al. "Characterization of a Mass-Produced SiPM at Liquid Nitrogen Temperature for CsI Neutrino Coherent Detectors". In: *Sensors* 22.3 (Jan. 2022), p. 1099. ISSN: 1424-8220. DOI: 10.3390/s22031099.

[128] R.B. Fair and H.W. Wivell. "Zener and Avalanche Breakdown in As-implanted Low-Voltage Si n-p Junctions". In: *IEEE Transactions on Electron Devices* 23.5 (May 1976), pp. 512–518. ISSN: 1557-9646. DOI: 10.1109/T-ED.1976.18438.

[129] Fabio Acerbi and Stefan Gundacker. "Understanding and Simulating SiPMs". In: *Nuclear Instruments and Methods in Physics Research Section A: Accelerators, Spectrometers, Detectors and Associated Equipment*. Silicon Photomultipliers: Technology, Characterisation and Applications 926 (May 2019), pp. 16–35. ISSN: 0168-9002. DOI: 10.1016/j.nima.2018.11.118.

[130] Emilie Roncali and Simon R. Cherry. "Application of Silicon Photomultipliers to Positron Emission Tomography". In: *Annals of Biomedical Engineering* 39.4 (Apr. 2011), pp. 1358–1377. ISSN: 1573-9686. DOI: 10.1007/s10439-011-0266-9.

[131] Ravil Agishev et al. "Lidar with SiPM: Some Capabilities and Limitations in Real Environment". In: *Optics & Laser Technology* 49 (July 2013), pp. 86–90. ISSN: 0030-3992. DOI: 10.1016/j.optlastec.2012.12.024.

[132] L. Consiglio. "The Cryogenic Electronics for Dark Side-20k SiPM Readout". In: *Journal of Instrumentation* 15.05 (May 2020), pp. C05063–C05063. ISSN: 1748-0221. DOI: 10.1088/1748-0221/15/05/C05063.

[133] Giovanni Chesi et al. "Optimizing Silicon Photomultipliers for Quantum Optics". In: *Scientific Reports* 9.1 (Dec. 2019), p. 7433. ISSN: 2045-2322. DOI: 10.1038/s41598-019-43742-1.

[134] Patrick Eckert et al. "Characterisation Studies of Silicon Photomultipliers". In: *Nuclear Instruments and Methods in Physics Research Section A: Accelerators, Spectrometers, Detectors and Associated Equipment* 620.2 (Aug. 2010), pp. 217–226. ISSN: 0168-9002. DOI: 10.1016/j.nima.2010.03.169.

[135] Glenn F. Knoll. *Radiation Detection and Measurement*. 3rd ed. New York: Wiley, 2000. ISBN: 978-0-471-07338-3.

[136] W. Bludau, A. Onton, and W. Heinke. "Temperature Dependence of the Band Gap of Silicon". In: *Journal of Applied Physics* 45.4 (Apr. 1974), pp. 1846–1848. ISSN: 0021-8979. DOI: 10.1063/1.1663501.

[137] Fabio Acerbi et al. "NUV and VUV Sensitive Silicon Photomultipliers Technologies Optimized for Operation at Cryogenic Temperatures". In: *Nuclear Instruments and Methods in Physics Research Section A: Accelerators, Spectrometers, Detectors and Associated Equipment* 1046 (Jan. 2023), p. 167683. ISSN: 0168-9002. DOI: 10.1016/j.nima.2022.167683.

[138] T. Pershing et al. "Performance of Hamamatsu VUV4 SiPMs for Detecting Liquid Argon Scintillation". In: *Journal of Instrumentation* 17.04 (Apr. 2022), P04017. ISSN: 1748-0221. DOI: 10.1088/1748-0221/17/04/P04017.

[139] G. Gallina et al. *Performance of Novel VUV-sensitive Silicon Photo-Multipliers for nEXO*. Nov. 2022. DOI: 10.48550/arXiv.2209.07765. arXiv: 2209.07765 [physics].

[140] Stanley Seibert and Anthony LaTorre. "Fast Optical Monte Carlo Simulation With Surface-Based Geometries Using Chroma". In: (), p. 28.

Appendix A

ICPC A/E SYSTEMATICS

In the MAJORANA $0\nu\beta\beta$ decay search analysis the multi-site discrimination parameter used for the ICPC detectors is the A/E parameter. This was chosen over the AvsE parameter because it was underestimated how much work would be necessary to investigate whether AvsE is a valid multi-site discrimination parameter or not for an ICPC. AvsE has only been applied to and throughly tested with PPC detectors. Throughly testing AvsE for four ICPCs with approximately 2.5 kg-yrs of exposure was not worth it to delay the release of final results from the experiment. In addition, this may have overlapped with the data-taking schedule for LEGEND-200. In fact, all ICPC detectors use parameters from the collaboration's independent analysis from Oak Ridge National Lab. The set of ICPCs is treated as a separate subset of DS8, DS8(ICPC).

A/E is the ratio of the maximum current to the energy of a particular energy deposition in the detector. The maximum current is calculated by applying a symmetric trapezoidal filter with a 80 ns rise time and no flat time. A/E, like AvsE, is an unstable parameter when measuring the DEP acceptance per calibration. Since A/E uses a linear dependence with energy, the shift in A/E vs time can be corrected for by scaling the parameter so that all DEP peaks between two long calibrations are peaked at the same value. This is defined as an offset in A/E that's linearly interpolated between calibrations. A drift-time correction is applied after. A random correction factor AE_{DT} is sampled 20 times and the value that produces the narrowest A/E DEP peak is chosen.

$$\left(\frac{A}{E}\right)_{DT} = \left(\frac{A}{E}\right)_{Raw} + AE_{DT} \times DT \tag{A.1}$$

DT is the drift-time and $\left(\frac{A}{E}\right)_{Raw}$ is A/E before the drift-time correction. Another correction

is applied similarly to remove some left-over residual energy dependence in A/E.

$$\left(\frac{A}{E}\right)_E = \left(\frac{A}{E}\right)_{DT} + AE_E \times \left(\frac{E_{cal}^{ctc}}{1000\,\mathrm{keV/MeV}} - 2\mathrm{MeV}\right) \tag{A.2}$$

AE_E is sampled to achieve the narrowest A/E distribution and E_{cal}^{ctc} is the calibrated energy. The final A/E parameter is $\left(\frac{A}{E}\right)_E$ multiplied by a number to register A/E > 0 as the cut which returns a 90% acceptance rate at the DEP A/E peak. The calibration of A/E for the ICPC detectors is done externally by collaborators at Oak Ridge National Lab and the efficiencies and systematics are calculated through the main MAJORANA analysis. The A/E efficiencies are computed in an analogous way to the AvsE systematics.

- Signal Acceptance: The signal acceptance is calculated using the AvsE acceptance formula and the same signal and side-band energy windows are used, except with a cut set at A/E > 0. The signal acceptance average among the four ICPC detectors is higher than the PPC detectors. A/E is tuned with a 5 keV window around the DEP and AvsE is tuned with a 10 keV window around the peak. The higher signal acceptance may be coming from the high energy tail in the DEP that comes from the low energy interactions as one of the 511 keV γ's escapes the detector. A/E does not include a correction for determining the $Q_{\beta\beta}$ acceptance and is estimating by incorporating the signal acceptance drop measured in the AvsE analysis without applying a width-energy dependence correction

- Statistical Uncertainty: Calculated by detector as in the AvsE analysis, but also including the 1-σ confidence intervals in the width-energy dependence added in quadrature to the uncertainty.

- ROI energy dependence: Same method as the PPC detectors for AvsE however with different fit ranges to accommodate the wider A/E distribution

- $2\nu\beta\beta$ energy dependence: Same method as the PPC detectors for AvsE however with different fit ranges to accommodate the wider A/E distribution

- $0\nu\beta\beta$ acceptance: Unlike the AvsE parameter, A/E does not include a correction for the width-energy dependence, therefore the difference in acceptance between DEP events and $0\nu\beta\beta$ decay events is expected to be greater. Sufficient data for ICPC simulated waveforms is not available so the simulation systematic difference is taken to be the same as for AvsE plus an additional 50% error to be conservative

- Stability: A/E is rescaled for every calibration and thus the AvsE stability systematic, which measures the acceptance drift over short calibrations, would not capture the uncertainty correctly. For each small calibration the A/E cut value is positioned so that it is the same distance away from the DEP peak in A/E. The change in acceptance over the change in cut value was given by the Oak Ridge analysis for each detector and these were multiplied to the change in calibration over the change in run number to get the change in acceptance per run number. For each ICPC detector an average deviation was fit and the standard deviation of the points is computed, see Fig. A.1. The stability systematic is the average of the average deviations and the average of the standard deviations added in quadrature.

Dataset	DEP efficiency and systematics
DS8 (ICPC)	$0.8520 \pm 0.0221(\text{stat}) \, ^{-0.0031}_{-0.0306}(\text{roi}) \, ^{+0.0112}_{-0.0309} \, (2\nu\beta\beta) \, ^{+0.0338}_{-0.0338} \, (0\nu\beta\beta) \pm 0.0031(\text{stab})$
DS8 (ICPC)	$0.8520^{+0.0421}_{-0.0594}$

Table A.1: *avse cut efficiency and systematic uncertainty for the ICPC detectors in DS8.*

To match the MAJORANA analysis, a high A/E cut is implemented at A/E < 10 to remove α backgrounds that escape the DCR cut. Again the signal acceptance and uncertainties are similar to the AvsE analysis.

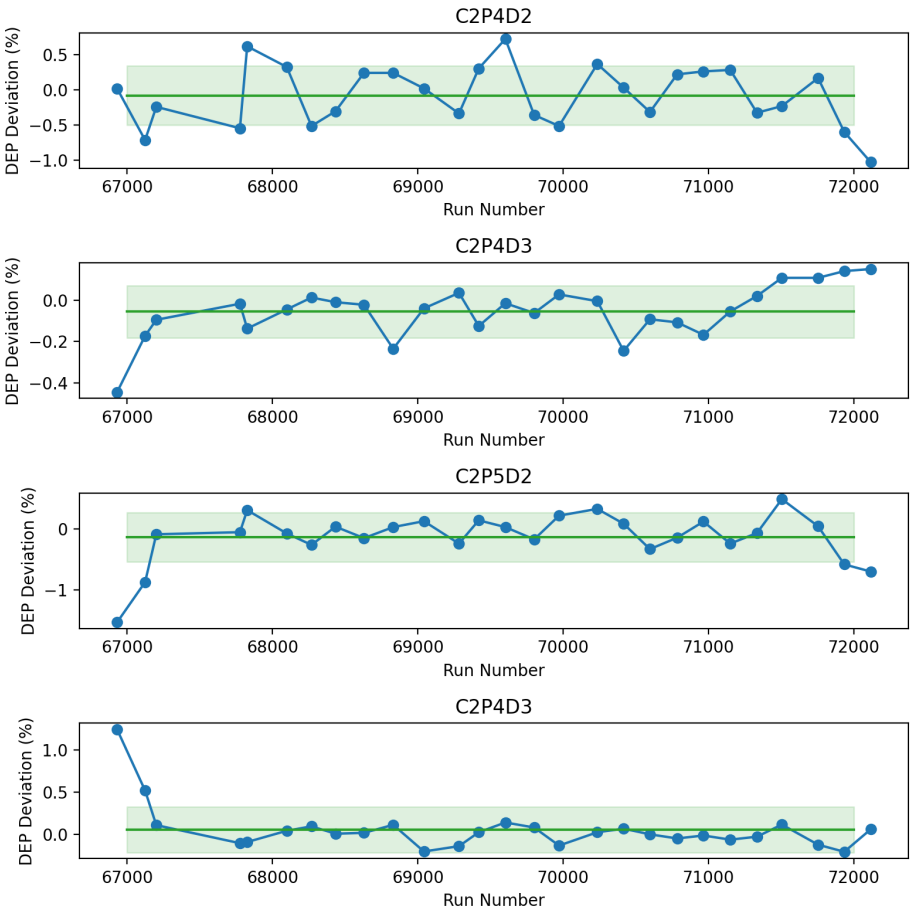

Figure A.1: The acceptance deviation by run number for each of the four ICPC detectors in DS8

- Signal Acceptance: The signal acceptance is computed the same way as the high AvsE cut, however the drop in acceptance at $Q_{\beta\beta}$ is subtracted signal acceptance at the DEP. This effect is several times smaller than for the multi-site cut.

- $2\nu\beta\beta$ Acceptance: The difference in the DEP survival fraction and the survival fraction of events in the energy window of 950−1400 keV in the open background after applying a DCR cut. This is used to account for the difference in high A/E acceptance from calibration data and open background data.

- Stability: The stability of the DEP survival fraction over short calibrations calculated using the same method as the AvsE > -1 cut.

Dataset	DEP efficiency and systematics
DS8 (ICPC)	$0.9781 \pm 0.0015(\text{stat}) \pm 0.0077(2\nu\beta\beta)\ ^{+0.0338}_{-0.0338} \pm 0.0118(\text{stab})$
DS8 (ICPC)	0.9781 ± 0.0142

Table A.2: *High A/E cut efficiency and systematic uncertainty for the ICPC detectors in DS8.*

Appendix B

SIPM AND APD PRE-AMP DESIGNS

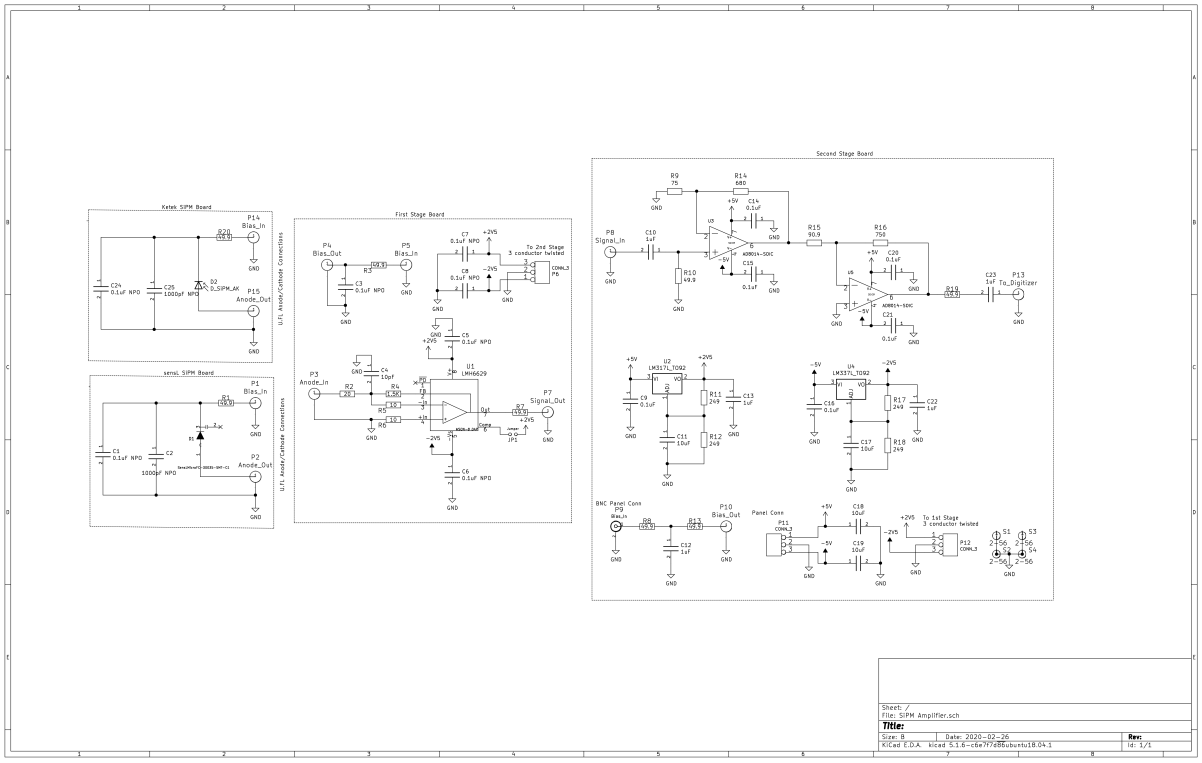

Figure B.1: The SiPM pre-amp has two stages. One stage with a transimpendance amplifier and a second stage with a non-inverting and inverting amplifier. The first stage is used to measure pulses from the LED and the first stage with the second stage connected is used to measure dark count behavior.

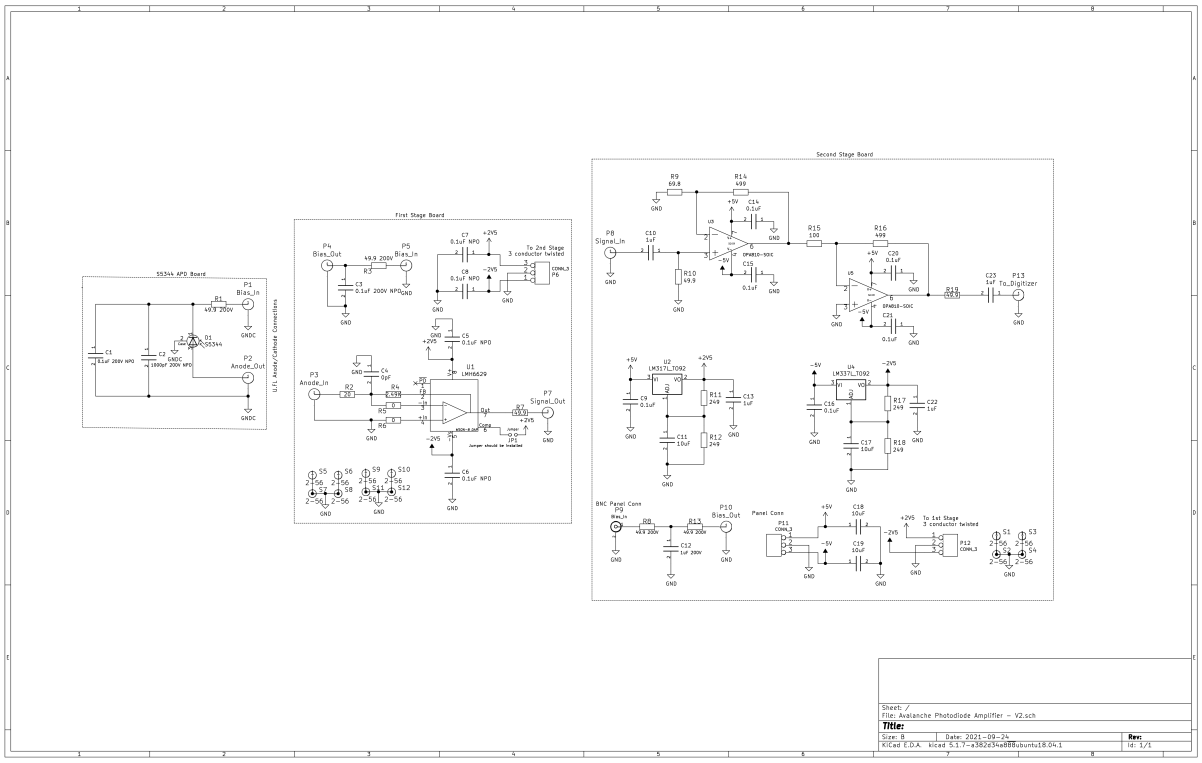

Figure B.2: The APD pre-amp has two stages like the SiPM pre-amp, but with a gain just short of double the SiPM first stage. The first and second stage are always used when measuring light pulses from the APD.

Appendix C

SIPM PDE SYSTEMATICS

This section includes tables of the nominal values and uncertainties for the measurable quantities used to calculate the photon detection efficiency and uncertainty for a set of bias voltages. The area of the SiPM is taken to be 9 mm^2 and the area of the APD is taken to be $\pi(1.5)^2$ mm^2. For the semi-relative liquid nitrogen photon detection efficiency calculation a systematic is added in quadrature that takes the difference in APD received photon count at room temperature and APD received photon count at liquid nitrogen temperature.

bias (V)	N_{SiPM}	P_{DiCT}	P_{AP}	f	N_D	Q_L	Q_D	g_{APD}
25.0	566.696852	0.051	0.0050	1.061	4.032736	5.754032e-14	-1.424693e-15	64.847125
25.5	988.854982	0.104	0.0148	1.061	7.627195	5.689311e-14	-1.410150e-15	64.847125
26.0	1305.938575	0.154	0.0214	1.061	11.328830	5.773429e-14	-1.379671e-15	64.847125
26.5	1627.950116	0.210	0.0257	1.061	14.812371	5.793016e-14	-1.144433e-15	64.847125
27.0	1935.429014	0.274	0.0282	1.061	15.577368	5.819787e-14	-5.636672e-16	64.847125
27.5	2218.478521	0.328	0.0354	1.061	18.057568	5.894254e-14	-4.328139e-16	64.847125
28.0	2534.402459	0.389	0.0320	1.061	22.506279	6.032571e-14	3.039180e-16	64.847125
28.5	2845.761935	0.441	0.0384	1.061	26.157929	6.048479e-14	9.849869e-16	64.847125
29.0	3126.851348	0.503	0.0416	1.061	32.148724	6.178470e-14	1.475968e-15	64.847125
29.5	3349.080027	0.545	0.0409	1.061	36.751899	6.246949e-14	2.460866e-15	64.847125
30.0	3606.604452	0.586	0.0580	1.061	39.130643	6.238542e-14	3.230938e-15	64.847125

Table C.1: Photon detection efficiency measurable quantities for the absolute room temperature measurement

bias (V)	σ_{SiPM}	σ_{DiCT}	σ_{AP}	σ_f	σ_L	σ_D	σ_g	
25.0	0.064997	0.0013	0.005	0.0056	0.006945	2.504467e-16	2.351405e-16	0.097565
25.5	0.516067	0.0019	0.005	0.0056	0.047660	2.406007e-16	2.371154e-16	0.097565
26.0	0.436159	0.0022	0.005	0.0056	0.019961	2.445741e-16	2.412413e-16	0.097565
26.5	0.705617	0.0028	0.005	0.0056	0.052301	2.458625e-16	2.434096e-16	0.097565
27.0	0.759910	0.0035	0.005	0.0056	0.079229	2.383023e-16	2.535903e-16	0.097565
27.5	0.880580	0.0035	0.005	0.0056	0.084114	2.490000e-16	2.479481e-16	0.097565
28.0	1.050104	0.0039	0.005	0.0056	0.093015	2.359639e-16	2.389743e-16	0.097565
28.5	1.123859	0.0042	0.005	0.0056	0.119654	2.336343e-16	2.360655e-16	0.097565
29.0	1.014940	0.0045	0.005	0.0056	0.125907	2.301926e-16	2.358480e-16	0.097565
29.5	0.981862	0.0049	0.005	0.0056	0.130612	2.574854e-16	2.270172e-16	0.097565
30.0	0.867965	0.0062	0.005	0.0056	0.176096	2.444564e-16	2.399819e-16	0.097565

Table C.2: Photon detection efficiency measurable uncertainties for the absolute room temperature measurement

bias (V)	N_{SiPM}	P_{DiCT}	P_{AP}	f	N_D	Q_L	Q_D	g_{APD}
25.0	361.011613	0.051	0.0050	1.061	-0.161739	3.150614e-14	-5.115756e-15	64.847125
25.5	598.075561	0.104	0.0148	1.061	3.225869	3.309016e-14	-2.746159e-15	64.847125
26.0	787.427977	0.154	0.0214	1.061	5.786944	3.161075e-14	-5.079582e-15	64.847125
26.5	975.556443	0.210	0.0257	1.061	7.684266	3.053996e-14	-6.287249e-15	64.847125
27.0	1162.822200	0.274	0.0282	1.061	9.623038	2.959234e-14	-6.688466e-15	64.847125
27.5	1332.059798	0.328	0.0354	1.061	11.631142	2.958379e-14	-5.476273e-15	64.847125
28.0	1523.114432	0.389	0.0320	1.061	13.582417	2.816551e-14	-7.218647e-15	64.847125
28.5	1705.013893	0.441	0.0384	1.061	15.526600	2.728496e-14	-8.184724e-15	64.847125
29.0	1917.331939	0.503	0.0416	1.061	19.255260	2.549749e-14	-9.061627e-15	64.847125
29.5	2163.035820	0.545	0.0409	1.061	22.192731	2.588807e-14	-8.183480e-15	64.847125
30.0	2462.501833	0.586	0.0580	1.061	26.268726	2.451675e-14	-8.448863e-15	64.847125

Table C.3: Photon detection efficiency measurable quantities for the relative room temperature measurement.

bias (V)	σ_{SiPM}	σ_{DiCT}	σ_{AP}	σ_f	σ_L	σ_D	σ_g	
25.0	0.240493	0.0013	0.005	0.0056	0.023575	9.046434e-16	9.795616e-16	0.097565
25.5	0.287743	0.0019	0.005	0.0056	0.028840	9.684044e-16	1.003274e-15	0.097565
26.0	0.370588	0.0022	0.005	0.0056	0.032187	1.013076e-15	1.045600e-15	0.097565
26.5	0.493155	0.0028	0.005	0.0056	0.037050	9.221742e-16	1.003505e-15	0.097565
27.0	0.572711	0.0035	0.005	0.0056	0.039545	9.630659e-16	9.925063e-16	0.097565
27.5	0.660203	0.0035	0.005	0.0056	0.047290	9.650890e-16	9.511878e-16	0.097565
28.0	0.752010	0.0039	0.005	0.0056	0.067448	1.024643e-15	1.086881e-15	0.097565
28.5	0.826023	0.0042	0.005	0.0056	0.077875	9.205214e-16	9.569887e-16	0.097565
29.0	0.954744	0.0045	0.005	0.0056	0.088600	9.388496e-16	9.507549e-16	0.097565
29.5	1.041591	0.0049	0.005	0.0056	0.104670	9.769825e-16	9.850157e-16	0.097565
30.0	1.052894	0.0062	0.005	0.0056	0.121542	1.031064e-15	9.902152e-16	0.097565

Table C.4: Photon detection efficiency measurable quantity uncertainties for the relative room temperature measurement.

bias (V)	N_{SiPM}	P_{DiCT}	P_{AP}	f	N_D	Q_L	Q_D	g_{APD}
22.0	441.002878	0.067	0.0000	1.061	-54.691721	5.541584e-14	-6.693444e-15	64.847125
22.5	573.482647	0.080	0.0000	1.061	-80.550498	5.374791e-14	-8.344266e-15	64.847125
23.0	687.244257	0.128	0.0431	1.061	-111.181304	5.430823e-14	-8.549429e-15	64.847125
23.5	809.707303	0.164	0.0583	1.061	-148.846538	5.379293e-14	-1.022357e-14	64.847125
24.0	938.728439	0.281	0.0759	1.061	-194.556252	5.446988e-14	-8.009001e-15	64.847125
24.5	1042.675406	0.299	0.0756	1.061	-242.391936	5.453188e-14	-1.047197e-14	64.847125
25.0	1173.213210	0.345	0.0862	1.061	-310.771435	5.324946e-14	-1.100089e-14	64.847125
25.5	1330.638613	0.410	0.1240	1.061	-463.038700	5.498468e-14	-1.042150e-14	64.847125
26.0	1498.017876	0.433	0.0917	1.061	-556.409769	5.314507e-14	-1.135517e-14	64.847125
26.5	1575.554291	0.471	0.1190	1.061	-807.544620	5.119602e-14	-1.482534e-14	64.847125
27.0	1611.022822	0.495	0.1150	1.061	-1058.132225	5.067035e-14	-1.726059e-14	64.847125

Table C.5: Photon detection efficiency measurable quantities for the relative liquid nitrogen temperature measurement

bias (V)	σ_{SiPM}	σ_{DiCT}	σ_{AP}	σ_f	σ_L	σ_D	σ_g	
25.0	0.240493	0.0168	0.005	0.0056	0.023575	9.046434e-16	9.795616e-16	0.097565
25.5	0.287743	0.0150	0.005	0.0056	0.028840	9.684044e-16	1.003274e-15	0.097565
26.0	0.370588	0.0176	0.005	0.0056	0.032187	1.013076e-15	1.045600e-15	0.097565
26.5	0.493155	0.0163	0.005	0.0056	0.037050	9.221742e-16	1.003505e-15	0.097565
27.0	0.572711	0.0262	0.005	0.0056	0.039545	9.630659e-16	9.925063e-16	0.097565
27.5	0.660203	0.0259	0.005	0.0056	0.047290	9.650890e-16	9.511878e-16	0.097565
28.0	0.752010	0.0260	0.005	0.0056	0.067448	1.024643e-15	1.086881e-15	0.097565
28.5	0.826023	0.0278	0.005	0.0056	0.077875	9.205214e-16	9.569887e-16	0.097565
29.0	0.954744	0.0288	0.005	0.0056	0.088600	9.388496e-16	9.507549e-16	0.097565
29.5	1.041591	0.0302	0.005	0.0056	0.104670	9.769825e-16	9.850157e-16	0.097565
30.0	1.052894	0.0298	0.005	0.0056	0.121542	1.031064e-15	9.902152e-16	0.097565

Table C.6: Photon detection efficiency measurable quantity uncertainties for the relative liquid nitrogen temperature measurement